Altered bone formation response to mechanical loading in a mouse model of the progeroid disorder gerodermia osteodysplastica

vorgelegt von
M.Sc.
Michael Thelen

Von der Fakultät III - Prozesswissenschaften
der Technischen Universität Berlin
zur Erlangung des akademischen Grades

Doktor der Ingenieurwissenschaften
- Dr. Ing. -

genehmigte Dissertation

Promotionsausschuss:
Vorsitzender: Prof. Dr. Peter Neubauer
Gutachter: Prof. Dr. Roland Lauster
Gutachter: Prof. Dr. Uwe Kornak

Tag der wissenschaftlichen Aussprache: 07. Dezember 2018

Berlin 2019

MEINER FAMILIE

ANNETTE
HANS-WILHELM
JOHN
CHRISTOPH
DANIELA

Acknowledgements

The presented work results from the close collaboration of multiple institutes. Every cooperation partner was essential in contributing important, extraordinary and fundamental fragments for the realization of this dissertation. I would like to acknowledge the groups from all institutes for providing a constructive, creative and pleasant working environment.

Special thanks are dedicated to the people who supported me during the last years facilitating this thesis:

Prof. Dr. Uwe Kornak for giving me the opportunity to work in his laboratory, be part of his amazing team, his scientific guardiancy, his trust and overall support.

Prof. Dr. Bettina Willie for initiating this project, her scientific insights into biomechanics and welcoming me to her laboratory at Shriners Hospital for Children in Montréal, Quebec, Canada.

Prof. Dr. Roland Lauster for supporting my scientific career from my bachelor studies onwards and for supervising my PhD thesis.

Prof. Dr. Richard Weinkamer for accepting my collaboration offer and due to this the proof of my theory about the impaired osteocyte network in $Gorab^{Prx1}$ mutants.

Prof. Dr. Stefan Mundlos for giving me the chance to be his associate research fellow at the MPI for molecular genetics.

Dr. Sabine Bartosch for supporting me in the Berlin-Brandenburg School for Regenerative Therapies, in entitling me as the Project Manager of the 8^{th} BSRT Symposium – Regenerate, Repair, Regrow – Personalized Biomedicine Rises and for the BSRT financial support for finishing my thesis.

Without the will and effort of the people listed above the work on this thesis would have not been possible. Thank you!

Furthermore, I want to thank all the people, who worked with me during the past 3.5 years for generating this piece of work.

Institute for Medical Genetics and Human Genetics

Daniela Keller für die fachliche, freundschaftliche und immerwährende Unterstützung von Tag eins meiner Dissertationszeit bis heute, dem letzten Tag meiner Doktorandenzeit. Ich wünsche dir von ganzem Herzen nur das Beste liebe Dani! Vielen Dank für alles.

Guido Vogt für die unerschöpfliche Hilfsbereitschaft, die Gute Laune und die Fairness, welche du Tag für Tag mit auf die Arbeit gebracht hast.

Dr. Björn Fischer-Zirnsak für die fachlich überragende Einarbeitung, für Hilfestellungen jeglicher Art und für all die Lehrstunden, welche wir zusammen absolviert haben.

Dr. Hardy Chan for the endless discussions about Gorab, mice dissections and immunohistochemistry. Furthermore, I want to thank him for several side-project ideas, like the *in vitro* studies targeting the primary cilium and oxidative stress response in fibroblasts after siRNA knockdown.

Uta Rössler, Miguel Rodriguez, Floriane Hennig, Claire Schlack, Naji el Choubassi, Dr. Magdalena Steiner, Anja Lekaj, Denise Emmerich, Carola Dietrich, Viktoria Dienst, Janina Radszewski, Phillipe Schröter, Fabienne Pritsch, Dr. Heidemarie Neitzel, Lukas Altinbas, Nina Stelzer, Alexej Knaus, Namrata Saha, Gabriele Hildebrand, Susanne Rothe, Bastian Salewsky und Patrick Sauer für eine unglaublich inspirierende, hilfsbereite und fachlich versierte Zusammenarbeit in dem Institut für medizinische Genetik und Humangenetik an der Charité.
Catrin Janetzki und Ulrike Krüger danke ich für die professionelle Durchführung des RNAseq's.

Julius Wolff Institute

Anne Seliger danke ich für die fruchtvolle Zusammenarbeit, und die unzähligen Stunden, welche wir zusammen im Tierhaus verbracht haben, während der vielen Loadings und µCT Scans.

Mario Thiele danke ich für viele technische und praktische Lösungen für ImageJ basierte Auswertungsmethoden, Notfallsupport für das *in vivo* µCT und bei der Aufarbeitung der 3D Modelle der *in vivo* Scans.

Dr. Christine Figge und **Dr. Agnes Ellinghaus** für das Heranführen an tierversuchliches Arbeiten und der vielen Arbeit in Form von Osteotomien an der leider abgebrochenen Knochenheilungsstudie.

Tobias Thiele danke ich für die Einführung in das strain gauging, das mechanical loading und für immer offene Ohren bei auftretenden Problemen.

Max-Planck-Institute for colloids and interfaces

Dr. Andreas Roschger und seinem Team danke ich für die kompetente, zügige und verlässliche Kooperation bezüglich der Osteozyten-Netzwerk-Visualisierung.

McGill – Shriners hospital for children/Canadian center of computational genomics

Catherine Julien for the very warm welcoming in Montréal, the trouble-free collaboration, the qPCR support and for taking care of all the orderings for both projects I was able to undertake at Shriners.

Eloi Mercier for processing the RNAseq raw data and for being available for several years, even when the collaboration was already closed.

Dr. Nicholas Mikolajrwicz for training me in single cell membrane disruption/mechanical loading and for supporting my evaluation of the in vitro calcium flow, gap junction and ATP vesicle formation.

Elizabeth Zimmermann and **Max Rummler** for supporting my everyday work at McGill and the lunch company.

BSRT Symposium

Julia Bergmann, Dr. Krithika Hariharan, Aline Lückgen, Namrata Saha, Alexej Knaus, Sarah Heilmann, Rajiv Kumar Khajuria and Edoardo Borgiani for their support and extraordinary work on the 8th BSRT Symposium.

FACS analysis

Christian Buchner for his inspiring ideas on our fluorescence-activated cell sorting project, which unfortunately was stopped due to the abortion of the osteotomy studies.

Journalistic support

Janina Trebing und **Mike Young** für das zügige, gewissenhafte und selbstlose Korrekturlesen bezüglich Grammatik und Ausdruck des Englischen.

Forschergruppe DFG

Dr. Georg Duda und **Dr. Katharina Schmidt-Bleek** für die herausragende Organisierung und Betreuung der Forschergruppe, welche die Rahmenbedingungen meiner Promotion stellte.

Abstract

Bone tissue has to constantly adapt to changing mechanical requirements. The mechanisms behind mechanosensation, mechanotransduction, signal transmission and the resulting response of bone tissue are, until this day not fully understood. A failure of these processes leads to inappropriate bone architecture, bone mass and reduced mechanical stability as seen in age-related osteoporosis or rare diseases such as *osteogenesis imperfecta* or *gerodermia osteodysplastica* (GO).

GO is a progeroid disorder with wrinkled skin, osteoporosis, and spontaneous fractures caused by loss-of-function mutations in the gene *GORAB (SKYL1BP1)*. The gene product is located in the Golgi-apparatus where it is likely involved in retrograde vesicle trafficking. Our group showed recently that loss of Gorab leads to an impairment of early osteoblast differentiation, low dermatan sulfate levels, altered TGF-β signaling and an impaired proteoglycan (decorin/biglycan) glycosylation in skin and bone resulting in an osteoporosis phenotype and spontaneous fractures in the *Gorab*^{Prx1} mouse model.

Unexpectedly, we observed elevated numbers of abnormally differentiated osteocytes in the mutants. Given that osteocytes are the bone cell type orchestrating the bone's response to mechanical loading we wanted to investigate how Gorab^{Prx1} animals react to mechanical stimulation.

To this end, Gorab^{Prx1} mutants and littermate controls (LC) were subjected to *in vivo* tibial loading for two weeks. Serial microCT registrations, dynamic and static histomorphometry were performed to define the different responses of the two cohorts. The results showed an astonishing complete loss of the physiological anabolic response to mechanical loading in Gorab^{Prx1} mice. This effect was mirrored by altered strain-induced gene expression changes revealed by RNA-sequencing.

In order to find the reason for this phenomenon we investigated the lacunar-canalicular osteocyte network in detail. The results show a reduced canalicular density and connectivity in spite of the higher osteocyte numbers.

In a parallel approach, osteocyte-like cell lines were investigated after Gorab knock-down. The analysis of the primary cilium and mechanisms (ATP vesicle formation, calcium flux and GAP-junction function) important for mechanosensation did not reveal striking

impairments. In summary, we found a loss of mechanosensitivity in Gorab^{Prx1} mutants that is possibly due to a perturbed lacunar-canalicular osteocyte network.

Zusammenfassung

Knochengewebe passt sich kontinuierlich an variable mechanische Anforderungen an. Die verantwortlichen Mechanismen für die Kraftamplifikation, Mechanosensitivität, Signaltransmission und die daraus resultierende Anpassung des Knochengewebes sind bis heute nicht komplett verstanden. Eine Beeinträchtigung dieser Mechanismen führt durch eine unzureichende Knochenarchitektur und -masse zu einer reduzierten Knochenstabilität. Beispiele für Erkrankungen mit einer verminderten Knochenstabilität sind die altersbedingte Osteoporose oder seltenen Erkrankungen wie Osteogenesis imperfecta oder Gerodermia osteodysplastica (GO).

Bei GO handelt es sich um eine progeroide Erkrankung, welche mit faltiger Haut, frühzeitiger Osteoporose und spontanen Knochenfrakturen einhergeht. Sie wird durch „loss-of-function“ Mutationen im Gen *GORAB* (*SKYL1BP1*) verursacht. Das von *GORAB* kodierte Protein ist im Golgi-Apparat lokalisiert und in den retrograden Vesikeltransport des Golgi-Apparates involviert.

Der Verlust von Gorab in mesenchymalen Stammzellen führt im Gorab^{Prx1} Mausmodell zu einer Beeinträchtigung der frühen Osteoblastendifferenzierung, einem verminderten Dermatansulfat-Gehalt und einer beeinträchtigten Glykanierung von Proteoglykanen (Decorin/Biglykan) in Haut und Knochen. Die daraus resultierenden Veränderungen der extrazellulären Matrix und des TGF-β Signalwegs rufen einen Osteoporose Phänotyp und spontane Frakturen hervor.

Unerwartet wurde eine erhöhte Anzahl von abnorm differenzierten Osteozyten in den Mutanten gefunden. Osteozyten sind der für die Umsetzung mechanischer Stimulation in eine anabole zelluläre Antwort des Knochens zuständige Zelltyp. Die Zellen verfügen über eine einzigartige Form der Kommunikation über ein sogenanntes lakuno-kanalikuläres Netzwerk. Es wurde die Hypothese aufgestellt, dass sich der Osteoporose-Phänotyp der Gorab^{Prx1} Mausmutanten durch eine verminderte Sensitivität der veränderten Osteozyten für mechanische Reize verursacht wird.

Um die Reaktion des Knochens auf mechanische Belastung in einem definierten Experiment zu untersuchen, wurde die linke Tibia von Gorab^{Prx1} Mutanten und Kontrolltieren fünfmal wöchentlich über zwei Wochen einer zyklischen, genau definierten

Verformung ausgesetzt. Die stimulierte Tibia wurde fortwährend im Vergleich zur nicht stimulierten Tibia mittels serieller microCT Aufnahmen und durch dynamische und statische Histomorphometrie analysiert. Die Ergebnisse zeigten einen gänzlichen Verlust der physiologisch anabolen Reaktion auf mechanische Belastung in Gorab^{Prx1} Tieren. Dieser Effekt spiegelte sich auch in einem veränderten Genexpressionsmuster wieder, das durch RNAseq ermittelt wurde.

Um den Grund für die fehlende anabole Antwort auf mechanische Belastung zu finden, wurde das lakuno-kanalikuläre Netzwerk der Osteozyten detailliert untersucht. Trotz der erhöhten Anzahl an Osteozyten in Gorab^{Prx1} Mutanten wurde eine reduzierte kanalikuläre Dichte und eine herabgesetzte Konnektivität dokumentiert. Um weitere Ursachen für die fehlende Mechanosensitivität zu erforschen, wurden in Osteozyten ähnlichen Zelllinien die Auswirkung des Gorab-Knockdowns auf das primäre Zilium, die Bildung von ATP-Vesikeln, den Kalzium-Fluss und die Funktion der GAP-Junctions untersucht, ohne deutliche Unterschiede festzustellen.

Zusammengefasst haben wir den Verlust der Mechanosensitivität in Gorab^{Prx1} Mutanten, welcher wahrscheinlich durch ein gestörtes lakuno-kanalikular Netzwerk der Osteozyten zustande kommt, gezeigt.

Table of contents

Table of Figures

List of Tables

1 Introduction

The introduction is tailored to give the reader detailed insights in order to understand and discuss the executed experiments and obtained results. The chapter “Osteoporosis-related disease burden in aging societies“ is used to demonstrate the urge of this study. Therefore, it is the first chapter of the introduction.
A skeletal overview, proceeding to the bones architectural microscopic elements is also included, because the majority of this thesis’ experiments are executed on bone *in vivo*.
The bones characteristic celltypes, osteoblasts, osteoclasts and osteocytes are intensively described.
Lastly, the interaction of the three bone celltypes, resulting in bone homeostasis and remodeling are also explained in detail.
Due to our findings that osteocytes play the main role in this study, their chapter is the most detailed, including a description of their residential area. This environment is entitled as lacunar-canalicular network. The network is the place where mechanical loads are amplified, transduced into cellular signals and transmitted to the bone forming and resorbing cells. In particular, the osteocyte functions in mechanosensation and mechanotransduction are needed to understand diseases in bone formation and homeostasis, especially in GO patients and Gorab^{Prx1} mice.

1.1 Osteoporosis-related disease burden in aging societies

In times, when the human population continuously extends its lifespan, the focus of medical research shifts to the age related dilemma in diseases and healthcare. This is intended to prevent rising patient suffering, the need for care, and offsets the increasing costs to the public health system.
Even today a tremendous effort is needed to cover the bulk of the care needed in the majority of the western world. In particular, the care needed by patients affected by osteoporosis and other bone related diseases, increases proportionally with the ageing

population. The risk of bone fractures for example, is linked to low bone mineral densities, which are symptomatic for osteoporosis and other bone diseases.

In Germany, the daily costs covered by the healthcare-system surpassed the 1 billion €/day disbursements in 2017 (Destasis, Deutsches Statistisches Bundesamt). Preventive therapies, suitable for the maintenance of health in elderly patients are desperately needed.

This study is a non-invasive, regenerative attempt for patients with low mineral density, using mechanical stimulation as a treatment.

Mechanical stimulation in general is known for its capacity for bone formation in healthy individuals. Daily activity and exercise along with genetic, nutritional, and hormonal factors influence bone mass and architecture, allowing for growth and maintenance of the skeleton to resist fracture during habitual loading. Unfortunately, the skeleton's ability to form new bone declines with increasing age. A number of exercise trials have demonstrated that physical stimuli, which enhance bone formation in young people are not as effective in older individuals[1-3].

For this study, as a low bone mineral density model of research, the genetic disorder *Gerodermia osteodysplastica* was chosen. *Gerodermia osteodysplastica* is a progeroid, autosomal, recessive disorder, whose patients exhibit brittle bones and wrinkled skin. GO's pathomechanism is affecting connective tissue elements, like collagen, decorin and biglycane[4].

Mutations resulting in GO occur in the gene *SCYL1BP1*, mapped on 1q24.2 (Ensembl). Phenotype matching, *SCYL1BP1* is massively expressed in osteoblasts, osteocytes and in the skin[5]. As mentioned above genetic modified mice ($Gorab^{Prx1}$) develop an early onset of an osteoporotic phenotype, including a low bone mineral density and idiopathic bone fractions[5]. Due to the obtained results the focus was placed on the investigation of mechanoresponsiveness in the lacunar-canalicular network.

1.2 The skeleton

The human skeleton has basic and complex vital functions in the human organism:

- Basic functions
    - shape giving,
    - locomotion,
    - soft tissue support and protection,
    - mechanical rigidity,
    - storehouse for minerals,
- complex functions
    - housing the bone marrow,
    - hematopoiesis,
    - osteoimmunology and
    - endocrine organ capacities.

The skeleton is composed of 206 bones, but the unpredictable supernumerary e.g. of the hand and feet bones increase that number[6]. Nevertheless, the skeleton is a complex system, composed of many types of tissues covering an overall of 14 % body weight. Bones are classified in five separate categories: Long, short, flat, irregular and sesamoid bones[6]. All bones are under constant remodeling, therefore, the human skeleton is completely renewed every 10 years. Moreover, bone is known to adapt to physical strains, rearranging its architecture and mineral density to mechanical stimuli. Osteoblasts, known for their ability of bone formation and their counterpart, osteoclasts, capable of bone resorption, are needed for the procedure of bone remodeling. Osteocytes are the third division of bone cells. Today osteocytes are mainly known as mechano-sensors and their ability of mechanotransduction[7]. Osteoblasts and Osteoclasts are found on the surface of mineralized bone. The natural habitat of osteocytes are lacunae within the mineralized bone tissue. Osteocytes are capable of forming a network with other osteocytes, and even reaching the surface to orchestrate the bone remodeling process by transmitting the mechanical information via cellular information paths to osteoblast and osteoclasts.

1.2.1 Long bones

All experiments executed *in vivo* during this study were conducted by using the tibia. The tibia belongs to the division of long bones, due to its cylinder-like shape. Moreover, the tibial geometry, which is longer than wide, meets the criteria for classification as a long bone. Therefore, only the long bones structure is explained in detail.

The long bones structure is divided in epiphyseal and diaphyseal regions. Diaphysis hosts the bone marrow cavity which is encased by a layer of dense and hard compact bone. On its endosteal side a small layer of cancellous bone can be found. In adulthood most part of the diaphyseal cavity contains yellow marrow, based on the high percentage of adipocytes. Distal and proximal ends of the long bone represent the epiphysis. These represent the roundish ends of the long bone, which reassemble the connection to joining bones. Furthermore, diaphyseal areas can be subclassified in pressure, traction, atavistic and aberrant diaphysis'. The tibia shows a classic anatomy of pressure diaphysis; connected to the femur via the knee joint, it transmits the weight of the body. They reassemble the parts, where the pressure during locomotion is distributed.

The epiphysis houses red marrow, which is mostly responsible for the production of red blood cells. Between the epiphysis and diaphysis' lies the metaphysis. This narrow part of the long bone contains the growth plate. From childhood until 18-21 years of age, the growth plate is responsible for the lengthening of the bones. Therefore, it synchronizes chondrogenesis and osteogenesis. Afterwards, both ends of the cartilage consisting growth plate connect and undergoes complete ossification.

A more detailed histology of epiphyseal, metaphyseal and diaphyseal compartments are listed in the appendix, during the comparison of human vs rodent (mouse) anatomy and histology of the tibia. Figure 1 shows the basic features of the tibia.

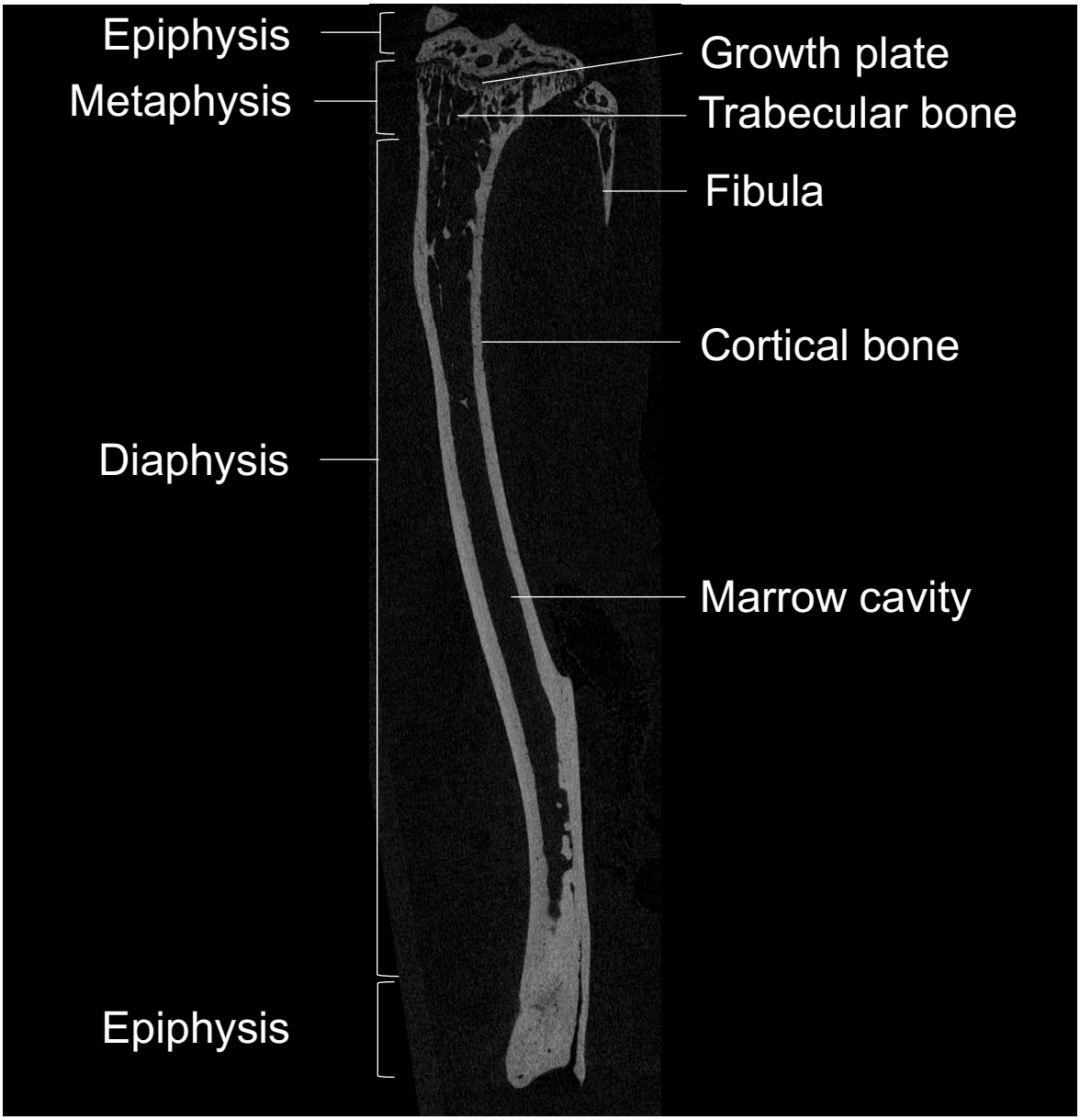

Figure 1 Ex-vivo tibia longitudinal cross section µCT scan of a 10 week old littermate control mouse. Epiphyseal, metaphyseal and diaphyseal regions were marked. Furthermore, growth plate, trabecular and cortical bone, marrow cavity and the cranial part of the fibula are labelled.

1.2.2 Cortical bone

Human cortical bone represents, in comparison to trabecular bone, the denser outer layer of bones. The compact bone consists of single microscopic columns, termed as osteons (180-250 µm in diameter). Osteons do not occur as discrete units, but rather divide, rejoin

and interconnect with other osteons, forming a three dimensional interlinked structure. Each osteon is constructed around a harversian canal. Harversian canals contain blood and lymphatic vessels, nerves and connective tissue. These are surrounded by multiple layers of 3-7 µm thick concentric lamellae, consisting of parallel collagen fiber bundles. Between each lamella is a layer of lacunae containing osteocytes. Harversian canals are metabolically active and undergo remodeling processes. Osteons are transversally connected by Volkmann's canals.

Lamellae can be separated into three types, concentric (described above), interstitial, and circumferential. Interstitial lamellae are located between the neighboring osteons and are irregular in shape. Those were originally part of interstitial lamellae, but were destroyed during bone remodeling. The third type are the circumferential lamellae, which flank, parallel to each other, the outer and inner periphery of the osteons next to the outer periosteum and the inner endosteum.

The outer surface of the cortical bone is covered by the periosteum. It is connected to the bone via collagen fibers bundles, the Sharpey fibers. Long bones inner surfaces are covered by the endosteum, which is more narrow in diameter than the periosteum. Nevertheless, both consist of fibrous connective tissue and are covered with osteoprogenitor cells, which can differentiate to osteoblasts and later, in case of embedding to osteocytes.

1.2.3 Trabecular bone

Trabecular bone, also called cancellous or spongy bone is found in the epiphysis. As mentioned in 1.2.1 the epiphysis is the place for red blood cell production, but also the mechanical joint for the distribution of mechanical loads. If the epiphysis would be completely filled with exclusively bone marrow, lacking any further stabilization, the compact bone would fracture under the immense amount of power, which weighs on the proximal and distal ends. Therefore, a support system is needed to distribute the load equally. Bone tissue is known for its ability to adjust its shape according to mechanical properties, which are dictated by movement. Wolff's law, "Law of the transformation of bones" describes this relation.

Trabecular bone is a sponge like system, which supports the load distribution. Despite, or due to the red marrow filled holes in the cancellous bone this tissue has the maximal strength by minimum mass. Its orientation is dictated, as stated above, by the mechanical strain. Therefore, it is a highly anisotropic tissue with maximal strength and stiffness. Porosity in human trabecular bone accounts around 75–95 % with a density of 0.2 to 0.8 g/cm[38]. Nevertheless, even this specialized and adapted tissue has its limitations, with a Young's modulus of 800-14000 MPa and a strength of failure of 1-100 MPa. The heterogenicity of trabecular bone is the reason why these values are wide ranged.
Trabecular bone, similar to cortical bone is pervaded by a nanoscale network of osteocytes. Like in cortical bone osteoblasts and osteoclasts can be found on the trabecular bone's surface and osteocytes in the trabecular bone's tissue.

1.3 Bone's extracellular matrix

Extracellular matrix (ECM) in bone is an extremely specialized tissue. Composed of 90 % organic structures and 10 % inorganic material, it represents, next to dentin the second hardest tissue in the human body.
Organic matrix contains mostly collagen type I proteins next to non-collagen proteins. The group of non-collagen organic components contain osteocalcin, osteonectin, osteopontin, fibronectin, bone sialoprotein II, bone morphogenic proteins, growth factors and proteoglycans like decorin, biglycan, lumican or osteoaderin[9-11].
Collagen fibers are arranged as bundles, which are stabilized by decorin and other structure giving proteoglycans. Also, collagen fibers are arranged parallel to each other, giving the lamellae their ring like structure.
The non-organic structures consist mainly of phosphates and calcium ions. Furthermore, other minerals are important for the bones metabolism and structure, like bicarbonate, sodium, potassium, citrate, magnesium, carbonate, fluorite, zinc, barium, and strontium[12, 13]. The most abundant ions, phosphate and calcium form hydroxyapatite crystals ($Ca_{10}(PO_4)_6(OH)_2$). Hydroxyapatite crystals are hold in a scaffold formed by collagen and their non-collagenous matrix partners. This architecture gives the bone its characteristic stiffness and resistance[14], but bone is still able to bend to a certain extent. The limit in

flexibility is restricted by symmetry and strain direction. During normal locomotion the deformation of long bones ranges between 0,04 - 0,3 %[15].
Bone matrix is an active tissue, which interacts by releasing molecules or vesicles with bone cells. Furthermore, bone matrix adhesion molecules, which interact with bone cells have a constant impact on bone cells and subsequently bone remodeling. Therefore, the ECM is able to take part in orchestrating bone remodeling to a certain extent[16].

1.4 Bone cells and the bone multicellular unit (BMU)

Three types of cells complete the bone cell compartment. In some literature bone lining cells are described as the fourth department of bone cells[12, 13].
Bone lining cells are lined on inactive remodeling sites of the bone. Their cell processes reach into the canaliculi network. Due to activation via osteocyte signaling, they are able to differentiate into osteogenic lineages and become osteoblasts. Therefore, they will be seen as osteogenic precursors and not as a separate department of bone cells[17] in this thesis. Osteoblasts act as bone forming cells by producing osteoid, which is fresh, unmineralized bone composed by organic bone matrix (mostly type I collagen) and inducing the mineralization process. Osteoclasts act as the osteoblast counterpart due to their capability of bone resorption. Osteocytes are the bone's mechanosensors, which subsequently orchestrate the bone remodeling process. The remodeling process is controlled via local factors produced by the cells, such as growth factors and cytokines, and furthermore by systemic factors, like hormones. A balance between osteoblast and osteoclast activity is needed for a healthy bone homeostasis. Imbalances likely result in bone diseases, such as osteoporosis or osteopetrosis.

In the following chapters the three bone cell compartments and their functions are explained in detail. Their genetic differentiation profiles, will be extensively described, due to the differentiation impairment of young osteoblasts and osteocytes we found in Gorab^{Prx1} animals.

1.4.1 Osteoblasts

Osteoblasts cover 4-6 % of total resident bone cells and are located on the bones inner and outer surface[18]. The main function of osteoblasts is the formation of fresh bone tissue, termed osteoid. Furthermore, the mineralization process is initiated by them. In their cuboid form they reside on active remodeling sites, where the polarized cells secrete osteoid to the bone matrix[19]. Their cell body is comparable to protein forming cells, determined by plentiful of rough endoplasmic reticulum, different secretory vesicles and a prominent Golgi apparatus[18, 20]. Furthermore, osteoblasts are mobile cells, which enables them to move a max. distance of 100 µm in a 24 h period[21].

Their origin are mesenchymal stem cells (MSCs). The differentiation process of MSCs towards the osteogenic lineage has to be orchestrated by several active gene expressions, in a specific symphony.

In the following section only the significant differentiation factors are mentioned, though other factors, such as microRNA's, Connexin 43 or FGF also play their parts[22-25]. For example, FGF is one of the factors, which is significant differential expressed in the 4 wk old female Gorab^{Prx1} osteoblast lineage. Important genes to start the differentiation of MSCs are WNT pathway genes and genes of the BMP family[26]. Runx2 acts as a key-factor of the osteoblast differentiation, because it acts as a transcription factor for many osteoblast related genes, such as *Col1A1*, *ALP*, *BSP*, *BGLAP*, and *OCN*[27]. Also, OSX, which is also differential expressed during Gorab^{Prx1} osteoblast differentiation, and Osf2 are both crucial factors for the osteoblast development[18, 28].

After induced *Col1A1* and *Runx2* expression to a certain amount cells change into a proliferation phase and start to express alkaline phosphatase (ALP). At this point cells can be seen as pre-osteoblast[18]. In the later differentiation process to a mature osteoblast *OSX* expression is elevated, matrix proteins are secreted and the shape of the cell body changes to the characteristic cuboidal type[28, 29]. The mature osteoblast is able to produce bone matrix proteins. During the first step of bone formation organic matrix proteins such as collagen type 1, OCN, osteopontin and osteonectin and furthermore proteoglycans such as decorin and biglycan are produced by the osteoblasts (*osteopontin* and *FGF23* are also differential expressed in 4 wk old female Gorab^{Prx1} osteoblast lineage cells).

After that, a two-step mineralization takes place. Firstly, osteoblasts secrete from the apical membrane matrix-vesicles in the range of 30-200 nm, which bind to organic components of the matrix. At the same time, matrix-proteins bind due to their negative charge calcium ions[30, 31]. In a subsequent step, osteoblasts secrete proteoglycan digesting enzymes. By digesting, calcium ions are released and are channeled into the matrix-vesicles via annexin channels[32]. To enable hydroxyapatite formation in vesicles, osteoblasts secrete ALP to degrade phosphate containing compounds. Phosphate is also channeled into the vesicles and hydroxyapatite crystallization is enabled. Once the crystals grow too large inside the vesicles, the vesicles rupture and release the newly formed hydroxyapatite. At this point, the fibrillar mineralization occurs[33, 34].
It should be noted, that some osteoblasts, who extend their cell processes into the osteoid and the mineralized bone, stay behind in the mineralization process and further differentiate to osteocytes. Therefore, osteoblasts and osteocytes origin from the same progenitor cells.

1.4.2 Osteoclasts

Osteoclasts are multinucleated bone resorbing cells. Unequal to osteoblast and osteocytes, who originate form MSCs, osteoclasts descent from hematopoietic stem cells (HSC's). Nevertheless, osteoclasts also undergo a specific program controlled by differentiation factors to develop their maturity. These factors are secreted by osteogenic progenitor cells, osteoblasts, osteocytes and stroma cells. It seems reasonable to conclude from this recital, that osteoblast and osteoclast differentiation are extremely interlinked (1.5).
Osteoclast precursors express the receptor cFMS, opponent of the macrophage colony-stimulating factor (M-CSF). By binding of M-CSF to cFMS, apoptosis is inhibited and the proliferation process is stimulated[35, 36]. M-CSF is secreted by osteogentic progenitor cells, which will develop simultaneously to osteoblasts[37]. The next important factor for further differentiation is the Receptor Activator of NF-κB Ligand (RANKL), which osteoblasts, osteocytes and stroma cells produce. After binding of RANKL to its receptor RANK, which is expressed by osteoclast precursor cells the formation process is started[38]. This process

is balanced by osteoprotegerin (OPG), a factor, which binds to RANKL as an inhibitor[39]. Similar to RANKL, OPG is also produced by osteoblasts, stromal cells, and additionally by fibroblasts[39-41]. Taken together, the RANKL-RANK-OPG interaction system is the core element of osteoclastogenesis[38, 41, 42].

RANKL-RANK interaction affect the expression of *NFATc1* and *DC-STAMP* amongst others. NFATc1 is needed to induce genes for osteoclast activity, such as *TRAP* and *cathepsin K*[43]. As a notation, in this thesis TRAP is used as osteoclast marker for osteoclast quantification. DC-STAMP is responsible for the fusion of osteoclast precursors in order to form multinucleated osteoclasts[43, 44].

After terminal differentiation, osteoclasts mature and are able to resorb bone tissue, which is part of the remodeling process. Whilst actively resorbing bone, the cells become polarized. The cell's cytoskeleton undergoes crucial remodeling in order to form sealing bonds between the cell and the extracellular matrix. F-Actin rings represent these bonds, which seal the remodeling site[45]. These rings are formed exclusively whilst the cell is in direct ECM contact. This ring induces the ruffled membrane border of the resorption site, because of the dense podosome formation. All podosomes are connected through a higher ring-structure. The attachment to the ECM is primary enabled by integrins and CD44[46-49]. Inside the enclosed resorption site osteoclasts secrete a combination of bone resorbing factors, such as cathepsin K, tartrate resistant acid phosphatase (TRAP) or matrix metallopeptidase 9 (MMP9) which are able to degrade ECM. In combination with a decreased pH, induced by a vacuolar-type H^+-ATPase (V-ATPase), the bone matrix is demineralized and degraded[50, 51].

Filopodia and lamellipodia enable the osteoclasts to migrate further, which results in characteristic resorption trails[52]. In the non-resorbing status the F-Actin ring is not present and the podosomes are in dot-like structures present as a band in the cells periphery[53].

1.4.3 Osteocytes and the lacunar-canalicular network

Osteocytes are the most abundant bone cells with a percentage of 90-95 of total bone cells. Osteocytes are also the longest living bone cells, with a lifespan maximum of 25 years[54]. Nevertheless, the osteocyte function was not understood for a long time; their location inside the mineralized bone matrix being the main obstacle to analysis. Isolation techniques were missing. Therefore, osteocytes were described as passive cells and their functions were misinterpreted[55]. Along with new technologies knowledge and understanding of this cell type rose. Isolation and culture techniques, specific osteocyte marker and *in vivo* models were developed. Nowadays, it is known that osteocytes are heavily interlinked with numerous functions[56]. One of the most important functions of the osteocytes are mechanosensation and mechanotransduction.

As noted previously, osteocytes differentiate from osteoblasts. During bone formation, some osteoblasts remain behind in the osteoid and are cemented into the matrix, after a massive decrease in their mobility. The passive evaluation process or active decision process by which an osteoblast turns into an osteocyte is still not understood.

In general, the act of embedding is understood as a passive process. But several groups have confidence, that the embedding process of the young osteocytes could be an active process. Those researchers argue, that matrix degradation has to be performed actively in order to form canaliculi in the osteoid[57, 58].

Once the osteoblast is encased, the cell undergoes a crucial morphologic transformation, from a polygonal, cubic shape to a highly polarized cell with extending cell processes (dendrites). Osteocyte dendrites form a strict regulated network throughout the whole bone tissue.

Four stages of osteocyte differentiation have been proposed: Osteoid-osteocytes, pre-osteocyte, young-osteocyte and adult osteocyte.

Osteocytes are still able to move their cell body. Furthermore, to a certain extent they are able to enlarge / form new dendrites until the ECM is completely mineralized[59].

During the transformation of the osteoblast to osteocyte, the cytoskeleton has to be heavily remodeled. The osteocyte cytoskeleton is of great importance for the cell's mechanotransduction, therefore the changes will be described briefly; Actin and fimbrin

are the key players in dendrite architecture. Fimbrin and actin are omnipresent in osteoblastic stress fibers, but in osteocytes fimbrin is present on the proximal site of the dendrites and mostly at dendrite branching. Furthermore, fimbrin is suspected to connect the actin fibers, which form the dendrite cytoskeleton. Actin is organized in microtubules along the cell process. The amount of villin in osteocytes is much higher than in osteoblasts, despite only being present in the cell body, and not the cell processes. Another dramatic change in the cytoskeletal structure is the spectrin distribution. Spectrin shows spotty localization in osteoblasts and in osteocytes a filamentous organization, colocalized with actin from the cell center up to the end of the cell processes. Myosin and Tropomyosin are distributed in a similar way in osteoblast stress fibers and osteocyte dendrites[60].

Functions of the osteoblastic cytoskeleton differ massively from the osteoblastic, which is why a massive change in architecture is needed. But the change in cytoskeleton architecture, along with the terminal differentiation of osteocytes is also accompanied by an orchestrated expression pattern of marker genes.

In **osteoid-osteocytes** and **young osteocytes** *Col1* and *ALP* expression is dramatically downregulated. On the other hand, *podopanin* (*E11*) is highly expressed. E11 is known to bind to CD44 and ezrin-radixin-moesin complexes, which would lead to the presumption, that E11 is needed for dendrite formation in early osteocytes[61]. Also E11 was investigated regarding its influence to cytoskeleton rearrangement[62], and in flow induces dendrite elongation in murine long bone osteocyte cell line Y4 (MLO-Y4 cells)[63].

In **pre-osteocytes** *dentin matrix protein 1* (*DMP1*) is highly expressed. Loss of DMP1 leads to an impaired osteocyte differentiation. More early osteocyte markers, like *Col1*, *ALP* or *E11* are also constantly expressed in **young osteocytes**. DMP-null mice show a severe hypophosphatemia and high expression of *FGF23*, which strengthens the evidence that osteocytes are involved in phosphate homeostasis[64]. *Phex* is also a highly expressed gene in osteocytes. Its loss shows a similar phenotype to loss of *DMP1*, regarding phosphate homeostasis and *FGF23* expression.

FGF23 is normally expressed by **mature osteocytes**. Their proteins are involved in phosphate homeostasis[65, 66]. FGF23 is the most prominent osteocyte secreted endocrine

factor. It binds to FGF receptors and influences the musculoskeletal system and the kidney.

Crosstalk of kidney and bone is crucial for phosphate homeostasis, and is enabled on circulating FGF23. Matrix extracellular phosphoglycoprotein (MEPE) is also highly expressed in osteocytes. It is able to increase FGF-23 levels indirectly[67]. MEPE can be proteolytically cleaved by cathepsin B or D while releasing the highly phosphorylated acidic serine aspartate-rich MEPE-associated motif (ASARM) peptide fragment[68]. ASRAM can antagonize the phosphate-regulating gene with homologies to Phex and furthermore bind to hydroxyapatite[69].

Sclerostin the protein product of the *SOST* gene is exclusively expressed in **mature osteocytes**[70]. Sclerostin is likely a negative regulator of bone formation by antagonizing the low-density lipoprotein receptor-related protein 5 (Lrp5), which is an important Wnt/ β-catenin signaling pathway protein[71]. Regularly Lrp5 and Wnt ligands bind and the receptor becomes phosphorylated, which results in the activation of disheveled. Subsequently disheveled repress Glykogensynthase-Kinase 3 (GSK3), which in turn releases axin from its complex with β-catenin. β-catenin accumulates and translocates to the nucleus to bind to transcription factors, activating the expression of Wnt target genes. Nevertheless, sclerostin inhibits the WNT pathway by preventing Lrp5 binding to Wnt ligands, whereas β-catenin is phosphorylated and gets degraded via the proteasome pathway. Proving this overexpression and knockout of *SOST* lead to a decrease and increase of bone mass in mice models[70, 72].

Another difference in gene expression between osteoblasts and osteocytes in evident in their interaction with their environment. Firstly, osteocytes, which are embedded in the bone matrix are restricted to oxygen supply. Therefore, they enrich proteins for hypoxia resistance[73]. Oxygen tension may also be an external factor for osteocyte differentiation[74].

Even, if the gene expression is only a minor part of this thesis, the expression profile and the interaction of the gene products during differentiation had to be explained, due to the differentiation impairment of the osteoblastic lineage in Gorab mutants.

More prominent for the thesis is the network architecture formed by osteocytes within the hard tissue matrix of the skeleton, which is termed osteocyte lacunar-canalicular network. The architectural dimensions and characteristics are explained in the following below.

Mature osteocytes (5-20 µm in diameter) have an ellipsoidal shape and reside in an equally ellipsoidal shaped lacuna (15-20 µm in diameter) within the bone's extracellular matrix with a cell-to-cell distance varying between 20-30 µm[75]. Each osteocyte forms approximately 70 cell processes, also termed dendrites. These cell processes passing through thin "tunnels" and connect osteocytes to each other, but also to other cell types on the surface.

The network is responsible for skeletal structure regulation. In human compact bone osteocytes are lined concentric around the Haversian canals, between every lamella. 90 % of dendrites orientate in the horizontal axis, with only a low percentage forming transversal connections to osteocytes located in a different plain.
Bone is a highly dynamic tissue, which is in a constant remodeling process. As a consequence the lacunar-canalicular network is also under constant remodeling. Based on the average remodeling velocity of bone, 9.1 million osteocytes are replenished in the adult human skeleton per day. In total, approximately 42 billion osteocytes reside in an adult human skeleton, with approximately 2,94 trillion dendrites, forming an incredible 23 trillion connections. In total osteocytes form a 175.000 km long network from end-to-end with a surface area of 215 m^2. With this impressive length and surface area, the lacunar-canalicular network leaves only space for ~24 ml extracellular fluid[76]. The composition of the extracellular fluid is yet not fully illuminated, but an array of macromolecules such as osteopontin, osteocalcin, DMP1, proteoglycans and hyaluronic acid are known to be present[77-79].
Most of the data is based on mathematical models, illustrating how underrated this nano-environment has been over the past decades. This network enables osteocytes to communicate with each other and osteoblasts.
In addition, to the cell communication with other bone cells, osteocytes show cell processes, reaching into the bone marrow, indicating, that a communication to marrow

residing cells is possible[80]. Canaliculi show a diameter of 365 ± 130 nm, but house much thinner dendrites with an estimated cell process of 156 nm in diameter[81, 82]. These measurements leave a lacunar-canalicular space around the cell body of with a width of 0.6 µm[83, 84]. This combined with the free lacunar-canalicular space between the cell processes and the ECM, and multiplied by the number of lacunae and the length of the canaliculi system, means an average free space of 24,207 mm^3 in the entire lacunar-canalicular system[76]. This space is filled with canalicular fluid and organic pericellular matrix, which is still not well analyzed. What is known is, that the pericellular fluid travels through the lacunar-canalicular space, providing oxygen and nutrients to the osteocytes[85].

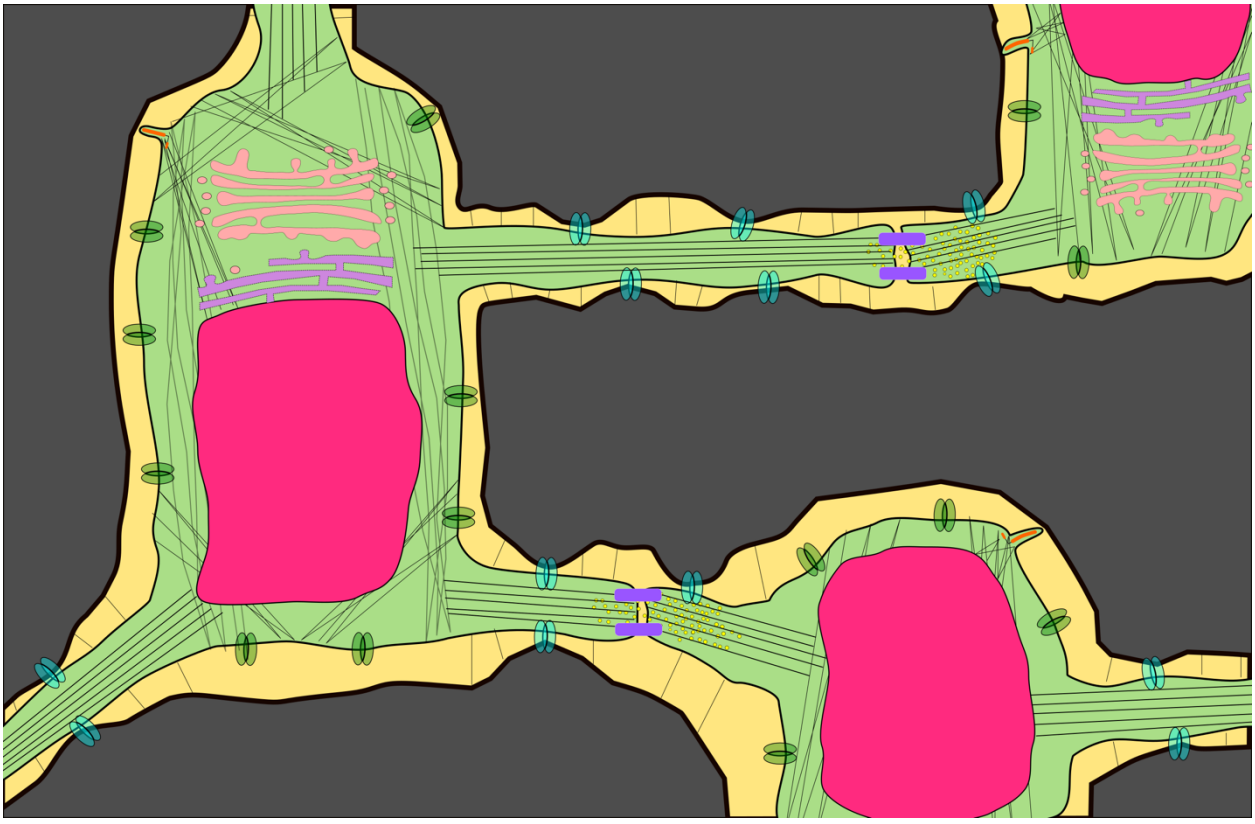

Figure 2 Schematic osteocyte lacunar-canalicular network. Osteocytes including nucleus, endoplasmatic reticulum, Golgi-apparatus and the cytoskeleton. Osteocytes are connected via GAP-junctions indicating calcium signaling. The cell bodies express the primary cilium and $\alpha_5\beta_1$ integrins. Integrin $\alpha_v\beta_3$ originating from the dendrite membrane connect dendrites to the ECM protrusions, tethers spanning the pericellular space from the ECM to the osteocyte dendrite.

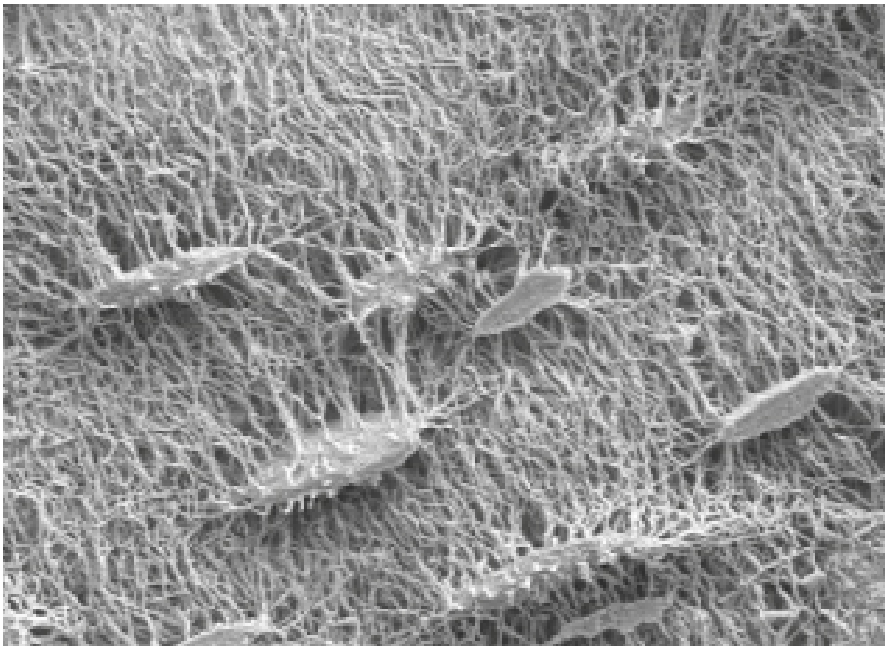

Figure 3 Scanning electron microscopy (SEM) image of cortical bone osteocyte network of LC mice.

As mentioned before the osteocytes are surrounded by the pericellular matrix. Therefore, osteocytes do not reside freely in the network, but are supported by transverse fibrils, which connect the dendrites to the canaliculi walls[12, 86]. Besides their role of biosensors, which will be discussed extensively later, osteocytes also can be classified as a member of the endocrine organs. The bone itself is a highly vascularized tissue, osteocytes produce hormone like factors and secrete them directly into the vascular system which transfers the secreted factors to distant target organs. A hormone like factor produced by osteocytes which matches the afore mentioned criteria would be FGF23, which controls phosphate homeostasis or sclerostin.

1.5 Bone remodeling

Bone remodeling in human is a continuous process, which can be divided in four major, overlapping phases.

Phase 1: Initiation phase at a specific site

Phase 2: Recruitment of MSCs and osteoprogenitor cells, differentiation of osteoclasts and bone resorption

Phase 3: osteoblast differentiation and osteoid synthesis

Phase 4: osteoid mineralization is the final step in bone remodeling

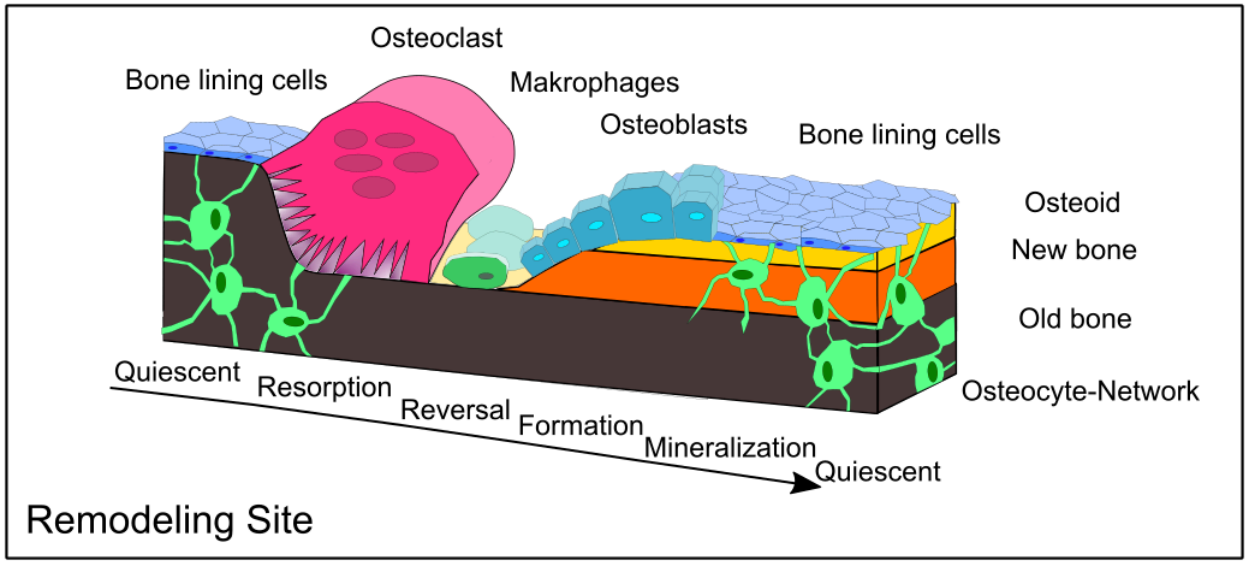

Figure 4 Schematic bone remodeling site. Showing the remodeling process including bone resorption (osteoclast), bone formation (osteoblasts), inactive bone lining cells and the osteocyte network. Old bone indicated in brown, young bone in orange and osteoid in yellow.

During these four phases osteoblasts and osteoclasts closely collaborate by forming the basic multicellular unit (BMU). In trabecular and cortical bone the remodeling process differs, but in a morphological manner rather functional.

In cortical bone the BMU consists of approximately 10 osteoclasts and several thousand osteoblasts. They form a cylindric shaped canal of 2 mm length and 150.200 µm width, which drills through the bone with a general speed of 30 µm/day. Osteoclasts dig a circular tunnel in the main loading direction, followed by the army of osteoblasts, producing osteoid for bone formation[87, 88]. Around 2-5 % of the human cortical bone is replaced per year this way.

Trabecular bone is morphologically equipped with a much larger surface, but lower diameter. Therefore, BMU do not dig through the bone, but rather remodel on the bone surface. Osteoclasts move on the bone surface with a speed of 25 µm/day while digging with a depth of 40-60 µm.
After bone resorption (around 2 weeks) mononuclear cells appear on the bone surface, which send signals for osteoblast differentiation and migration (4-5 weeks). After differentiation osteoblasts fill the resorbed bone volume with osteoid (4 months). After completing the new surface is covered with flat bone lining cells, initiating a resting phase.

1.6 Regulation of the bone multicellular unit

1.6.1 Cell-cell communication

Despite their roles of antagonists, osteoblasts and osteoclasts have a very close interaction profile. It was shown that different pathways as direct cell-cell contact, cytokines or extracellular matrix interaction were used for communication. Cell-cell contact and cytokines are presumable better analyzed by today, than other ways of communication.
The information regarding cell-cell communication is important to understand how closely bone cells work together and that small variances in any factor can impair the balance of osteoblasts, osteoclasts and osteocytes. Any disproportion results in a disbalanced bone remodeling process.
The complexity of interactions between osteoblasts and osteoclasts, which is presented in this work, shows how research focused predominantly on those two bone cell types, based on their executive role. Osteocytes as mechanosensors were neglected for the most time, therefore very little documentation exists regarding the interaction of osteocytes to osteoblasts or osteoclasts. Despite osteoblast-osteoclast interplay is not being the focus of this thesis it is described for the sake of completeness, prior to discussing the role of osteocytes. As previously stated, little is known about the osteocyte communication to the effector cells. Therefore, for the most part, the interaction within the osteocyte network and with the ECM will be described.

1.6.1.1 Osteoblast – Osteoclast cooperation and co-dependence

It has been shown that direct cell-cell contact is an important communication tool between osteoblasts and osteoclasts[89]. Therefore, GAP-junctions are formed to exchange small water-soluble molecules between the cells. Bone lining cells are also known to form cell-cell contacts with osteoclasts in order to induce osteoclastogenesis[89, 90] .

Furthermore, cytokine communication is the most important communication pathway for osteoblasts and osteoclasts. Besides the Wnt/TGF-β pathway (1.5.4) the RANK/RANKL pathway is the most prominent interaction between osteoblasts and osteoclasts.

As an example of the close relationship beside the two opponents, the RANK/RANKL pathway will be described in the following.

Receptor Activator of NF-κB (RANK) is a transmembrane I receptor, part of the TNF receptor superfamily. RANK and its ligand (RANKL) perform as one of the central links in bone homeostasis acting on osteoblasts and osteoclasts. This balance between bone formation and resorption is the key for a dynamic bone homeostasis.

RANKL is primary secreted by osteoblasts and binds to RANK, expressed by mature osteoclasts and osteoclast precursor cells to induce osteoclast differentiation[91]. Therefore, RANKL promotes principal bone resorption. In order to regulate the initiated bone resorption, osteoblasts can secondary secrete osteoprotegerin, also known as osteoclastogenesis inhibition factor (OPG). OPG acts as an RANK antagonist by binding to the receptor on the precursor cells membrane. After binding of RANK to RANKL TNF receptor-associated factors (TRAFs), like TRAFs 2,5 and 6 are activated. TRAF 6 is capable of inducing osteoclastogenesis[92] by activating several intracellular signal transduction pathways like MAPK8/AP-1, IκK/NF-κB, c-myc and calcineurin/NFATc1[93]. Furthermore, TRAF activation activates the freshly matured osteoclasts via Src and MAP2K6/p38/MITF. New studies show LGR4 as another RANK, preventing RANKL from binding in a dose dependent manner[94].

Unlike communication pathways used by osteoblasts, where the focus remains on two communication channels, osteoclasts are able to use at least three different communication trails. Firstly, similarly to osteoblasts they use direct cell-cell contact, forming GAP-junctions and using receptor molecules. Also osteoclasts use diffusible

paracrine factors, like cytokines, growth factors, microRNAs or chemokines. Last but not least, during bone resorption, osteoclasts are able to release growth factors and other molecules from the ECM, which have been composited by osteoblasts[95].

1.6.1.2 The Wnt/β-catenin pathway

As one of the central and most important signaling pathways in bone homeostasis and remodeling the Wnt pathway will be described in detail below. Furthermore, the RNAseq discovery studies revealed several Wnt pathway related genes as dysregulated in Gorab^{Prx1} mutants after mechanical loading in comparison to LC animals. Therefore, this pathway is described in detail.

Historically the Wnt pathway is subdivided in three separate pathways:

- canonical Wnt/β cantenin pathway,
- non-canonical Wnt-planar cell polarity pathway,
- Wnt-calcium pathway.

Wnt protein acts via several pathways for cell growth, differentiation, function and apoptosis, but the canonical Wnt/β-catenin pathway exclusively on bone biology. This fact is why in this thesis only the canonical pathway is described further. The canonical pathway is activated by Wnt ligands binding to the dual receptor complex. The dual receptor complex is consisting of frizzled (FZD) and Lrp5 or Lrp6. This binding leads to the inactivation of the destructive β-catenin complex, releasing β-catenin from proteosomal degradation. Therefore, β-catenin accumulates in the cytoplasm and at a certain point translocates to the nucleus, where it binds to several transcription factors to control target gene expression. Mutations in *Lrp5* or *Lrp6* transmembrane type I receptor genes show osteoporotic phenotypes[96, 97].

Based on this pathway mesenchymal stem cells differentiate to the osteoblastic lineage[96, 98, 99].

Osteoblast and osteocyte Wnt signaling also indirectly represses osteoclast differentiation and moreover bone resorption, via increased OPG secretion[100-102]. Osteoclasts are also directly influenced by Wnt components. Wnt5a stimulates the differentiation of osteoclast precursors by binding to FZD receptor tyrosine kinase like

orphan receptor-2 (ROR2) or the FZD-receptor-like tyrosine kinas (RYK)[103, 104]. Furthermore, β-catenin activates osteoclast precursors in favor of their proliferation [105]. Wnt3a on the other hand inhibits osteoclastogenesis[104]. Osteoclasts themselves activate in return the local differentiation of osteoblasts during the end of the resorption phase, by secreting Wnt ligands among other chemoattractants[106]. This process is also termed the coupling process.

Not only osteoblasts and osteoclasts use the Wnt signaling pathway in bone homeostasis. Bone marrow cells, like T lymphocytes express Wnt10b for example, which can trigger the osteoblast Wnt/β-catenin signaling as a paracrine signaling pathway[106-108].

Osteocytes also interplay with the Wnt pathway. By secreting sclerostin and DKK1 proteins they antagonize the Wnt signaling by occupying Lrp5/6. DKK1 is mostly known for early bone growth and bone regeneration[109]. Furthermore, Krm2 also plays its part in bone formation and resorption by binding to DKK1[110].

In addition mouse studies revealed Wnt signaling as a crucial player in osteocytic mechanosensation[111]. Sclerostin expression is also known to be regulated by mechanobiology[112]. Therefore, the repression of sclerostin is induced by mechanical loading in mice[111]. *Lrp5* loss of function mutations show less mechanoresponsiveness in mice[113-115].

PTH is known to repress several Wnt antagonists, like DKK1, Sost and others[116-118]. Furthermore, PTH-PTH1R complex can associate with Lrp6 and therefore trigger the Wnt signal in the absence of Wnt ligands[119].

BMP signals can be synergistic or antagonistic for bone[120, 121]. Wnt/β-catenin pathway induces osteoblast differentiation and proliferation, but once initiated the osteoprogenitors stay at this differentiation state. BMP signaling is needed for further differentiation[122, 123]. Once the cells evolved to mature osteoblasts, BMP and Wnt start to cooperate for example NMP2 and Wnt/β-catenin are needed for ALP expression and mineralization[124].

1.6.2 Cell-Matrix interaction

1.6.2.1 Integrins and adhesion molecules

As briefly mentioned in 1.2.4 bone matrix acts actively on bone cells via adhesion molecules, ECM-vesicles and other molecules[16]. Most important adhesion molecules for matrix-cell communication are integrins[125]. Osteoblasts for example use integrin $\alpha_1ß_1$, $\alpha_2ß_1$, $\alpha_5ß_1$ integrins for matrix connection by binding to RGD and other amino acid sequences presented by the bone matrix proteins. Those are needed for osteoblast arrangement during osteoid production[125].

As stated, the interaction between matrix and cells is important for bone formation, but it is also important for bone resorption. Osteoclasts express $\alpha_5\beta_3$ integrins to bind to enriched RGD-containing proteins, like sialoprotein or osteopontin and $\alpha_2\beta_1$ integrins, which bind to collagen fibrils[126, 127]. In spite of these connections to the ECM, osteoclasts are very motile cells, who do not express cadherins. Cadherins are only expressed by their progenitor cells to get in contact with growth factor producing stromal cells[128].
During bone resorption by osteoclasts, ECM bound transforming growth factor beta (TGF-ß) or insulin-like growth factor 1 (IGF-1) are released and affects osteoblast activity, which is another example of the close cooperation of osteoclasts and osteoblasts.

Perhaps the most important cell-matrix interaction for osteocytes with the ECM are integrin connections, which are crucial for mechanosensation in bone. Not only is the cell body of osteocytes connected to the lacunae walls by integrins, but their dendrites are linked to the canaliculi walls by integrins and additionally by fine fibrous connections which are termed “tethers”[77,84] (Figure 2). Having not been defined yet by previous research, it is proposed that perlecan is part of these structures[79]. Osteocytes have to balance the insurance of fluid flow for mechanosensation, distribution of nutrients in the network and connections for stability in the extracellular space. It is proposed, that in periodical intervals “hillocks” of the ECM reach into the pericellular space (Figure 5). Integrin $\alpha_v\beta_3$ most probably play a role in the connection to these structures. Integrins are connected

via integrin intracellular anchoring proteins (IIAP) directly to one of the actin fibers[129]. These hillocks were termed canalicular protrusions by Wang et al., who also theorized that these hillock-integrin structures take the place of otherwise one tethering element. Canalicular protrusions are randomly and asymmetrically distributed and their base width spans 75 nm [77]. The general apex to apex distance of neighboring hillocks is 131 ± 40 nm[84].

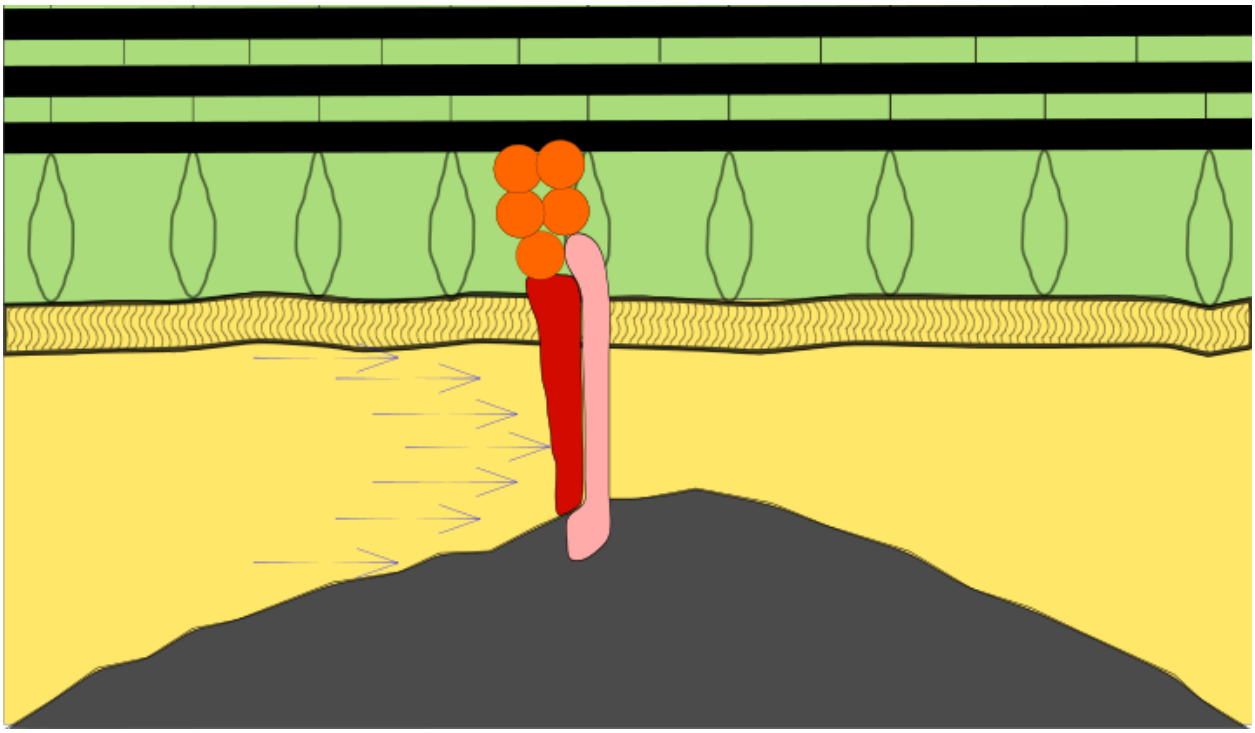

Figure 5 Schematic visualization of flow activated integrin αvβ3, connecting ECM protrusion (grey) and the peripheral part osteocyte process (green, including cross filaments and actin-fimbrin cytoskeleton). Integrin is bound to downstream molecules in orange and furthermore the actin cytoskeleton.

Furthermore, some researchers assume additional periodically interruptions of the pericellular space by collagen fibrils, which attach directly to the cell membrane via integrins[84], but this will not be taken into account in the further discussion.

In general, the described structures are suspected to play a major part in mechanotransduction by sensing fluid flow in the pericellular space, which is induced by mechanical loading[130]. Another function of the fluid flux movement is the bidirectional information exchange via solute transport as an osteocyte signaling channel[131, 132]. The mechanotransduction process will be discussed in detail in 1.7.

1.6.2.2 ECM architecture & stiffness

Aside from the afore mentioned characteristics, the stiffness and elasticity of the ECM is an important parameter influencing morphogenetic processes in embryonic development, defining tissue architecture and driving specific cell differentiation programs[133]. One of the translational pathways bridging ECM conditions to the cell nucleus is the Yes-associated protein / transcriptional coactivator with PDZ-binding motif (YAP/TAZ) pathway, which will be explained below, as this pathway is also important for bone homeostasis[134]. In bone cells, as well as mesenchymal stem cells, muscle stem cells and endothelial cells, this bridge between ECM structural information and nucleus response is important[135-138]. In the case of bone, the stiff ECM upregulates YAP/TAZ and induces its nuclear accumulation and thereby induces osteocyte differentiation. YAP, encoded by *Yap1* gene and TAZ, encoded by *Wwtr1* gene are transcriptional cofactors influencing osteoblast differentiation and bone homeostasis by interacting with the Wnt/β-catenin pathway. In detail, cytoplasmic YAP/TAZ bind axin, which lead proteosomal degradation of β-catenin[139]. Cytoplasmic TAZ also inhibits the phosphorylation of disheveled, which in turn inhibits the release of β-catenin of the destruction complex[140]. These findings support the theory of YAP/TAZ inhibiting Wnt/β-catenin pathway and therefore, osteoblast differentiation.

Stiff ECM also influences the cytoskeleton via bidirectional Rho, Rock signaling and integrin / myosin activity F-actin cytoskeleton is developed. F-actin is able to sustain YAP/TAZ dimers in the nucleus, acting as transcription factors[141]. Unfortunately, the role of YAP/TAZ in osteoblast differentiation may seem not as unidirectional as these studies presume. Xiong et al. used different conditional knockout models to knock out YAP/TAZ at different stages of osteoblast differentiation. They concluded that an early knockout in mesenchymal progenitor cells induces an increase in osteoblast differentiation and Wnt signaling. Therefore, inhibits YAP/TAZ the osteoblastogenesis and bone formation. Loss of YAP/TAZ in mature osteoblasts and osteocytes showed a reduction in number of osteoblasts, increase in osteoclast number and therefore a decrease in bone formation. This means that mature osteoblasts and osteocytes promote osteoblastogenesis and bone formation[142].

Due to the YAP/TAZ effect on osteoblast / osteocyte differentiation and the documented differentiation impairment in Gorab^{Prx1} animals the assumption was made that the lower stiffness of the bone in mutants could induce a lower YAP/TAZ level in osteocytes.
The RNAseq discovery studies did not reveal any changes in the expression patterns of YAP/TAZ related genes, therefore this pathway was not under further investigation.

1.6.2.3 Extracellular matrix vesicles

Extracellular vesicles are membrane derived vesicles, produced by nearly all cell types of the human body. In bone, extracellular vesicles play an important role in the mineralization process, which will not be further discussed in this chapter.
Actual findings suggest that matrix vesicles (MV) have a wider function spectrum than believed. Not only that MVs once in the extracellular matrix are processed in a differential manner[143], but that MV activate growth factors which are stored by them in the matrix, like MMPs. Furthermore, that MVs contain morphogenic proteins, like BMPs and vascular endothelial growth factor (VEGF)[144].
These findings suggest an intercellular information exchange character. In addition to growth factors MVs ,originated from growth plate chondrocytes, are now known to contain massive amount of miRNA as conserved cell-cell communication[145]. The amount of RNA in MV in *in vitro* chondrocyte cultures is measured with the amount of 1.93 ± 0.78 ng RNA/10^4 cells, which was approximately 0.1% of the parent cell's total RNA[146]. miRNAs found in MVs are predicted to target important pathways like focal adhesion, TGF-ß and WNT amongst others[147-150].

1.6.2.4 Chemokines and growth factors released by the ECM

As stated previously, a certain proportion of TGF-β is stored in the bone ECM. During bone resorption, this stored TGF-β is released. Once free, activated molecules are set to recruit osteoprogenitor cells[151]. Approaching the resorption site osteoblasts differentiation is induced. For a terminal osteoblast differentiation low TGF-β signals are needed[152]. Therefore, continuous high TGF-β levels impair the osteoblast differentiation, even after

induction. Besides TGF-β's interaction with osteoblastogenesis, it is known to support osteoclastogenesis via RANKL[153].

Interestingly, our group found elevated active TGF-β levels in Gorab^{Prx1} mutants, which matches the elevated regular bone turnover in 10-12 week old Gorab^{Prx1} animals.

1.7 Mechanosensation and mechanotransduction within the osteocyte network

The unique feature of bone tissue being able to adapt its architecture to mechanical loading is based on the still not well understood mechanisms of mechanosensation and mechanotransduction. Although notably, bone cells are not the only cells capable of mechanosensation, fibroblasts, chondrocytes, cardiomyocytes, endothelial cells and rhabdomyocytes also have this ability[154-158]. External mechanical stimulation acting on bone has to overcome a certain threshold in order to be sensed by cells within the bone. Osteocytes are the key players for mechanosensation in bone. Several mechanisms have been proposed acting in an extremely complex manner to detect mechanical strain by osteocytes. A single responsible mechanoreceptor in osteocytes does not exist. Therefore, by measuring mechanical strain the cells have to transform the mechanical information into cellular / chemical information and distribute the information within the osteocyte network leading to osteoblasts and other cells within the bone marrow cavity. Resultingly, mechanotransduction can be interpreted as the process of converting the mechanical signals in biochemical signals.

In the next chapter the different defined mechanisms, several models and GO related hypothesis regarding mechanosensation will be introduced.

1.7.1 Strain amplification

As described in 1.3.3 the osteocyte network is mainly responsible for mechanosensation, mechanotransduction and therefore orchestrating the bone remodeling process. Bone itself has the ability to deform 0,04 up to 0,3 %[15] and exceeds by only 0,1 %[159]. Deformation limitations also limit the force acting on the cells.

One of the most famous models for mechano-multiplication is predicted by You/Weinbaum et al.. Their model explains, how the limited stress acting on the osteocytes can be multiplied 10-100 x.
In vitro experiments have shown that this multiplication is needed to reach a cellular deformation that activates a response to mechanical stimulation (1-10 %)[160]. If the same mechanical load were to be applied to bone, it would fracture immediately[86]. Osteocytes are known for their embedment in extracellular matrix, surrounded by pericellular fluid. The fluid fills the lacunar-canalicular system as previously described. Mechanical loads acting on bone leads to tissue deformation and subsequently compromises the lacunar-canalicular space. Therefore, a pressure gradient is formed and the extracellular fluid is forced to move along the osteocyte dendrites and cell bodies. While moving through the canalicular system the bone liquid produces shear stress and drag forces. These occur mainly at the pericellular matrix tether elements, which span the osteocyte dendrite in the canalicular space. The moving liquid creates drag forces as a result of frictional forces at these matrix elements (Figure 6).
The bone's physiology (the tangential adjustment of tethers between the cell process and canalicular wall) is enabling circumferential deformations, fed by the drag forces. These hoop strains are acting on the dendrite in a 20-100 x higher force than the fluid flow enabling stress (Figure 6). In Figure 6 the large blue arrow (F_p) indicates the force direction of the fluid flow. Drag forces pointing in the same direction at the flexible tether elements are shown by small blue arrows (F_d). Most important for the strain amplification, shown by red small arrows (F_a) are the amplified forces pulling the cell membrane and therefore the intracellular transversal elements. The conversion from F_p to F_a reassembles the strain amplification. F_a, which is now acting via the transversal elements

on the actin cytoskeleton, is able to activate the cells response. Physics dictate an amplification of force acting on the process by higher frequency or amplitude of mechanical stimulation. As fluid flow occurs within the network in a high amplitude or frequency, membrane disruptions of osteocytes are possible. Membrane disruptions also initiating different cell responses to mechanical stimulation, which will be discussed in a later chapter. Peak strains acting on osteocytes are predicted to reach up to 5 Mpa[161]. Furthermore, this thesis considers also shear stress, induced by shear forces should. You et al. do not consider shear stress for magnitude amplification, but nonetheless it is an important mechanism of cell deformation for mechanosensation[160, 162].

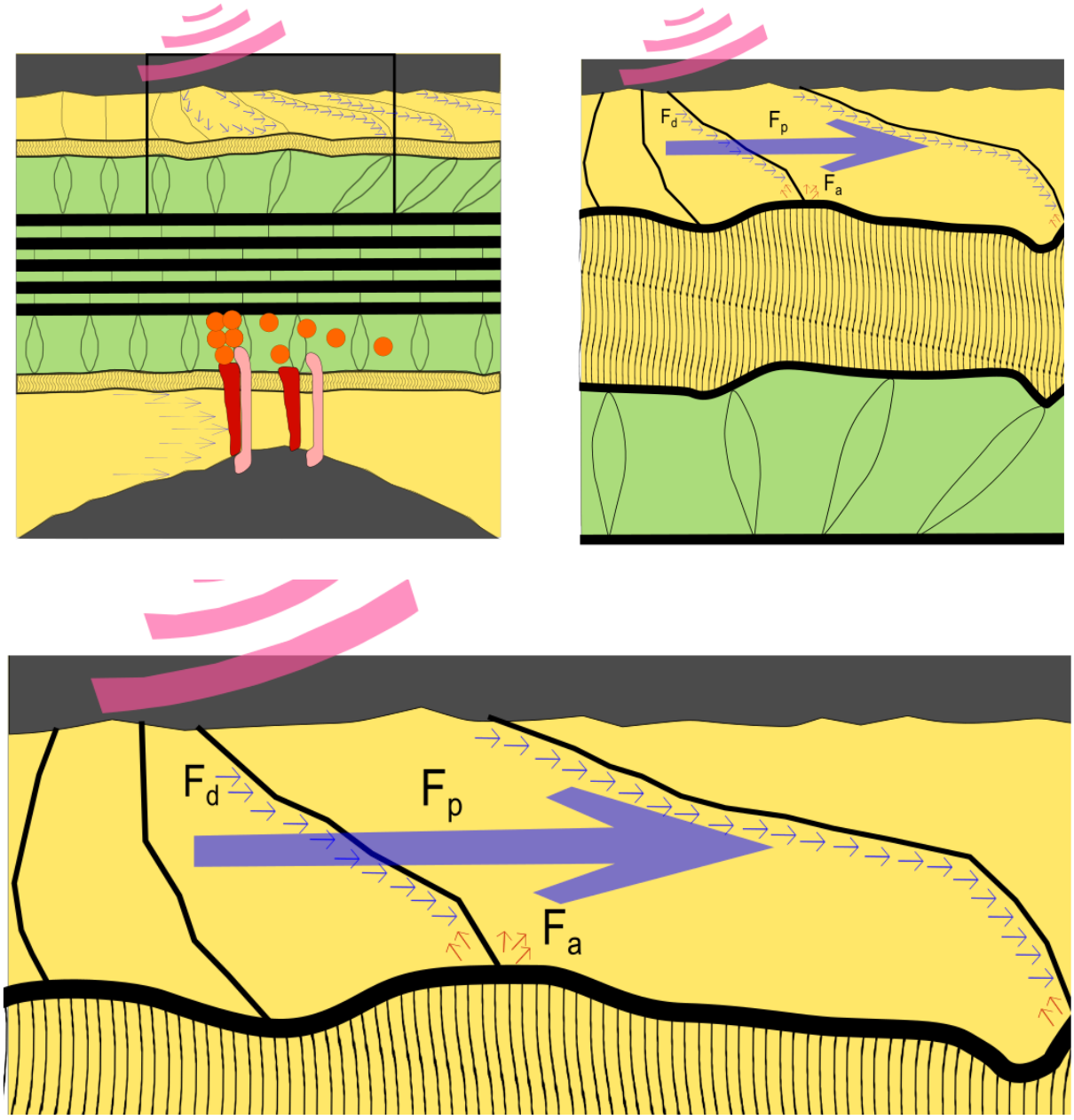

Figure 6 Mechanical strain amplification. ***Top left*** *Overview of fluid flow within the canaliculus around a cross sectioned dendrite. Upper half represents the tether element spanning and lower half the integrin activation.* ***Top right*** *and* ***Bottom*** *model shows more detailed the circumferential drag forces on the membrane. Fd = drag force at tether elements, Fp = Force of the fluid flow induced by pressure, Fa = Amplified force circumferential to the tether elements. In addition, the fluid flow exerts a tangential force on the plasma membrane of osteocytes, producing shear stress*[163]

1.7.2 Mechanosensation

Osteocytes possess a broad variety of mechanosensors. Integrins, cytoskeleton, focal adhesion proteins and the primary cilium are known to sense mechanical stress in different levels. This thesis will explain the most discussed theories and mechanisms for mechanosensation in order to present a broad overview of the decoupled possibilities. Several mechanisms, such as GAP-junctions, calcium flux, the primary cilium and ATP-vesicle formation were investigated during the *in vitro* studies executed for this study.

1.7.2.1 Integrins

Integrins act as mechanosensors, whilst being the kick-off cell component after mechanical stimulation for a cellular response. Being part of the so called “Pericellular matrix-integrin-cytoskeleton-nucleus system” integrins are heterodimeric transmembrane cell adhesion glycoproteins, consisting of a smaller α and larger β subunit. In the pericellular space integrins are connected to ECM proteins such as fibronectin, vitronectin, and osteopontin[130]. The wide variety in human integrins is a result of the combination potential of 18 different α and eight β units. The different combinations determine their binding partner intracellular at the cytoskeleton and extracellular of the ECM. In osteoblasts α2, αν, β1, and β3 are known taking part in mechanosensation.

Heterodimer combination αvβ1 and αvβ3 have been shown to take part in mechanotransduction.

It was shown that by blocking of β1, and β3 integrin units the production of COX-2, prostaglandin E_2 (bone formation) and COX-3 or other osteogenic markers is halted in *in vitro* studies[164, 165]. COX-2 is known to induce PGE_2 formation, which results in a bone formation response[166, 167]. Additionally, *in vitro* studies showed that an alteration of RANKL and OPG expression is induced via shear stress.

In proposed models, the plasma membrane deformation induced by mechanical stimulation initiates integrin conformation changes, which creates high-affinity sites for chemical reactions. This attracts neighboring integrins or other structures of the cytoskeleton to connect with the activated heterodimer. Integrin clusters, bound to the

cytoskeleton and inducing its remodeling to a specialized structure is termed focal adhesion. This special structure is only present during mechanical stimulation. The focal adhesion is bridging from the actin cytoskeleton to the ECM[168]. During its presence the complex recruits several molecules, which are needed for mechanotransduction, like tyrosine kinases, ion channels, phospholipase C or MAPK[169-173]. In absence of the stimulation the complex breaks immediately apart.

Still, downstream mechanisms of the integrin mechanosensation is yet not fully understood.

New studies exhibit evidence, that the event of mechanosensation is mostly present locally at the osteocyte cell processes, not the cell body. McNamara et al. showed that $\beta1$ is mainly found on the osteocyte cell body and $\beta5$ on the osteocyte processes[84]. Therefore, mechanical properties of these two compartments can be assumed. Integrin β_1 and β_5 mostly bind to proteoglycans like versican, syndecan, and fibronectin[174]. Mostly integrin subunit β_1 is paired with α_5[175] and it has been shown that on the cell processes $\alpha_v\beta_3$ integrin heterodimers are hosted[165]. Therefore, this thesis will refer to $\alpha_5\beta_1$ (cell-body) and $\alpha_v\beta_3$[165] (cell process).

Thi et al. showed, that discrete integrin attachment sites along the dendrites are responsible for mechanical induced changes within the osteocytes[176]. This evidence is supported by computational fluid dynamic models, which predict an extremely high wall shear stress at the integrin connections[177].

Wang et al. proposed a model wherein integrins are connected directly to the central actin bundle via the integrin intracellular anchoring protein (IIPA) without commenting on whether the IIPA connects to the integrin after mechanical activation, or if the IIPA enables a constant connection of the actin filament and the transmembrane proteins[77].

In vitro studies and computational models show evidence, but do not prove the actual mechanosensation *in vivo*.

Integrins are not the only membrane receptors in osteocytes for mechanosensation. Caveolin - lipid rafts and other also play along the mechanosensation process. Calveolae are 50-100 nm membrane invaginations with their main component caveolin-1. Caveolin-1 is known to interact with ERKs and integrin $\beta1$, indicating their role in mechanotransduction[178].

1.7.2.2 Focal adhesion

The Focal adhesion kinase (FAK) is likely essential for the conversion of mechanical stimulation to biochemical signals. FAK, part of the tyrosine kinase group, acts as an adapter protein. FAK enables the interaction with several proteins for multiple protein complexes, as described above. Either way, integrins can already be linked to each other, or after activation integrins form focal adhesion. The FAK undergoes an activation by autophosphorylation at tyrosine 397, inducing a high affinity site for proteins containing a Src-homology-2 domain. Src and PI3K now connect to FAK, activating downstream either the FAK-Src/Grb2/Sos/Ras-Raf/MAP2K1/ERK-1/2 or FAK/PI3K/Akt pathways. It is proposed, that the effector proteins of these pathways, extracellular signal-regulated kinase 1/2 (ERK-1/2) and Akt induce the induction of migration, cell proliferation and differentiation and on the other hand inhibit apoptosis[156, 160, 162, 179-182]. Besides FAK multiple actin-associated proteins like paxillin, vinculin, talin and zyxin are binding partner of the focal adhesion[183, 184]. Focal adhesions are assumed to be formed in direction of principle strains within the bone[185].

1.7.2.3 Primary cilium

The primary cilium is a specialized cell organelle, which is derived from the mother centriole of the centrosome, which is surrounded by a specialized domain extension of the cell membrane, termed ciliary membrane[186]. Within the ciliary membrane a circular construction of an axoneme of nine doublet microtubules extending from the basal body can be found. Primary cilia are unable to move on the cell membrane, unlike their relatives, the motile cilia. Amongst other external stimuli, depending on the tissue and cell type, it has been established that primary cilia can act as flow sensor, mostly in kidney cells[187]. *In vitro* experiments, removing the primary cilium from bone cells induced a reduction of protein production, related to osteogenic response to fluid flow[188]. Furthermore, by an osteoblast and osteocyte specific knockout of *Kif5* mice showed a reduction in bone formation[189]. Still, the function as mechanosensor *in vivo* has not been proven. In 2012 transmission electron microscopy studies revealed, that 94 % of all osteocytes develop a

primary cilium. Moreover, the same group measured the *in vivo* length of 0.2 µm, which is compared to other cilia, with a length of 4-9 µm *in vitro rather small*[190]. The small size of the cilium would match the geometric space the lacunar-canalicular network provides the osteocytes and the pericellular fluid to move.

In 2014 Vaughan et al. published a mathematical model for wall shear stress and equivalent elastic strain distribution on osteoblasts and osteocytes under several fluid conditions. In an *in vitro* attempt they placed osteocytes in a simplified lacunar-canalicular system and showed, that the highest shear stress and highest equivalent elastic strain occurs on integrins, connecting cell processes to the ECM. Therefore, they concluded, that they most likely play a role in mechanosensation and mechanotransduction processes (Figure 5).
Furthermore, the primary cilium was incorporated in their simulation. The role of the primary cilium in mechanosensation, referring to their calculations, depends on its configuration with the lacunar ECM. Just in case of a loosely connection to the ECM the equivalent elastic strain reaches levels of activation potential, also the strain increases proportional to the length of the cilium[191].

1.7.2.4 ATP release

ATP release as a reaction to reversible membrane disruption as a novel revealed mechanism of mechanotransduction, was investigated amongst others investigated by Mikolajewicz et al. in 2018. Designing *in vitro* circumstances, inducing a cell disruption of 2-30 %, which was subsequently repaired by the cell itself within 10-100 s. Mechanical loading in treadmill studies induced membrane disruptions in 20-60 % of the osteocytes residing in long bones[192], which emphasizes the importance of ATP release as a signaling pathway in bone. Osteocytes showed ATP-filled quinacrine positive vesicles release due to mechanical stimulation *in vitro*. Hemichannels, P2X7 and T-type voltage sensitive calcium channels (VSCC) give evidence to be responsible for non-membrane-lesion mediated ATP release in osteocytes[193, 194].

In Mikolajewicz studies it was shown, that vesicular ATP release was only a minor part of the total released ATP[195]. Measured ATP was proportional to the membrane injury. Still several studies give evidence that vesicular ATP or hemichannel mediated ATP are the main sources[196].

After membrane injury, vesicle exocytosis is used as a repair mechanism by enlarging the membrane surface. The vesicle exocytosis is normally regulated via Ca^{2+} / phospholipase C (PLC) / phosphokinase C (PKC) in osteoblasts. Therefore, calcium is the first mediator initiating exocytosis driven membrane repair[197]. These *in vitro* findings have been enforced by *in vivo* cyclic loading experiments, which showed that calcium levels in osteocytes increased proportionally to the magnitude of loading[198]. Summing up all these results, mechanical loading in bone induces membrane disruptions coupled with an ATP release, Ca^{2+} uptake and inducing exocytotic vesicle release for membrane repair. Furthermore, mechanical stimulated Hemichannels also enforce the pericellular ATP release. Proteins important in the ATP-vesicle exocytosis are Dysferlin and Myoferlin. Dysferlin and Myoferlin are hypothesized to act as a calcium sensor to trigger exocytosis[199]. According to another hypothesis ferlins actively take part in fusion of vesicles with the membrane[200].

Vesicle fusion for membrane repair is under heavy discussion. Traditionally it was hypothesized, that vesicular originating ATP, or *via* hemichannels released ATP is the main source of purinergic signaling ATP, which acts as signaling molecules for neighboring cells[201]. New studies showed controversial to that stigma, that free intracellular ATP could be the main source of pericellular ATP. Vesicle based membrane repair would therefore limit the amount of ATP leaving the cell, even by releasing their ATP-rich cargo to the pericellular space[195].

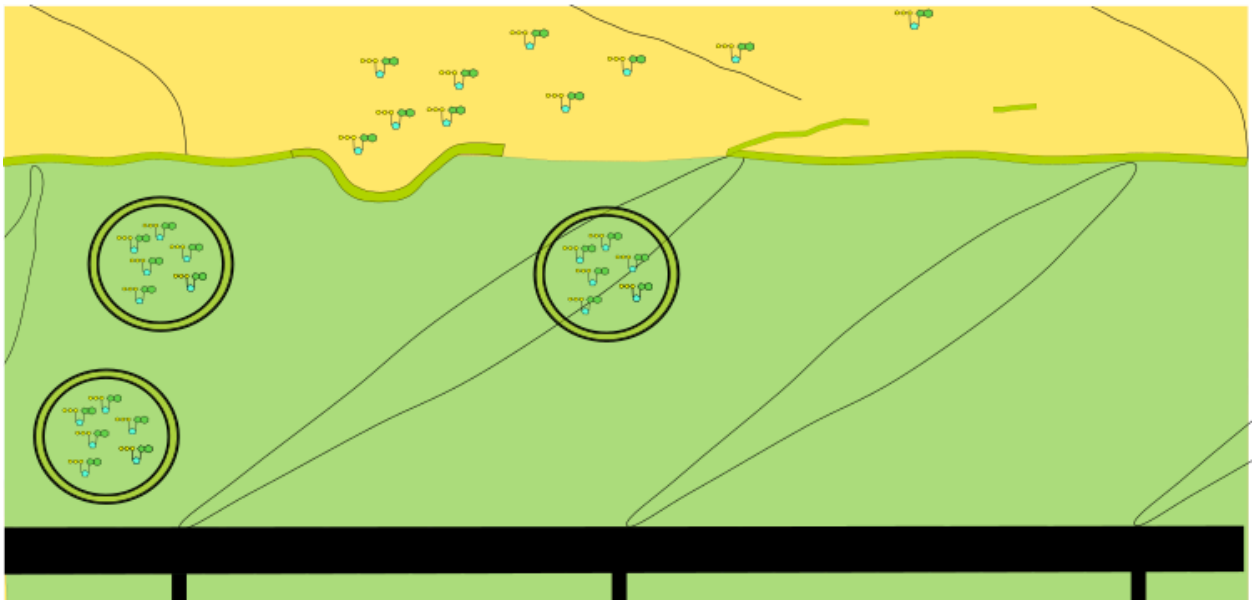

Figure 7 Membrane disruption induce by fluid flow. Pericellular free ATP molecules get washed away with the fluid flow and intracellular ATP filled vesicles sealing the membrane leakage, releasing additional ATP molecules.

1.7.2.5 Calcium signaling

It has been shown, that osteoblasts and osteocytes *in vitro* elevate their intracellular calcium level and release signaling molecules like ATP, nitric oxide or PGE_2 under shear stress[202].

Besides calcium uptake, intracellular release of calcium takes place during mechanotransduction. Two main calcium release channels are present in intracellular calcium release, inositol-1,4,5-triphosphate receptors (IP3R) and ryanodine receptors (RyR). During mechanical loading both channels are associated with, or even regulated via different receptors like mTOR or polycistin-1/2. The endoplasmic reticulum is the biggest and most important intracellular calcium store, which is tapped via IP3R and RyR signaling. IP3R induced intracellular calcium release is mediated by purinergic receptors (ATP induced)[203]. After the cytosolic calcium concentration is elevated to a critical level, the calcium reservoirs recover to their normal concentration, readying for a new mechanical impulse[204].

For the sake of completeness it should be mentioned, that in early osteocytes PTH signaling for Ca^{2+} influx via PKA signaling pathways for downstream production of IGF-1

and osteocalcin is used. In that case, the calcium uptake takes place exclusively at the dendrites of young osteocytes[205].

1.7.2.6 Ion channels and GAP-junctions

GAP-junctions are membrane-spanning channels and can be found at every dendrite-dendrite connection within the osteocyte network. Each pair of connexons form a cylindric tube with a pore in its center. This pore enables a molecule exchange between the cells with a molecule size up to 1kDa[206]. These connections are widely accepted as playing a significant role in the osteocyte network information exchange. Calcium and other signaling molecules like IP3 can be channeled to neighboring cells inducing the pursuing calcium signal[207]. Furthermore, osteocytes under shear stress open their hemichannel GAP-junctions (connexin 43) releasing ATP and thereby activating the neighboring osteocyte calcium uptake via purinergic receptors[196].
Stretch activated ion channels may also play a role in mechanotransduction. It was shown that shear stresses between 1 and 10 pN activate integrin neighboring ion channels[77].

1.7.2.7 Cytoskeleton

The cytoskeleton is a central part in mechanotransduction. As it is connected to the ECM via integrins and tether elements the cytoskeleton is able to react to pericellular fluid flow. In osteocytes the cytoskeleton differs in the cell body and their processes in composition, function and architecture[208, 209].
Dendrites are known to form 19 actin filament bundles at the center of the dendrite in a hexagonal array. These bundles, with 12 nm in distance, are periodically crosslinked by fimbrin. Fimbrin cross-links rotate 60° counterclockwise and advance 12.5 nm axially in successive cross-linking positions[210]. The central actin filament hexoganon is anchored by cross filaments (supposedly similar to myosin-I in the brush border filaments of intestinal microvilli) to transmembrane proteins (e.g. CD44 or osteopontin[211, 212]) in the dendrite membrane[213]. The cross filaments are double helix shaped, surrounding the central actin filament bundle in 37,5 nm distance. At the same time in the pericellular

space tethering elements anchor to these proteins, which form a connection from the ECM to the cytoskeleton. These tether elements are assumed to be proteoglycans originating from the ECM and are also arranged in a double helix structure[81].

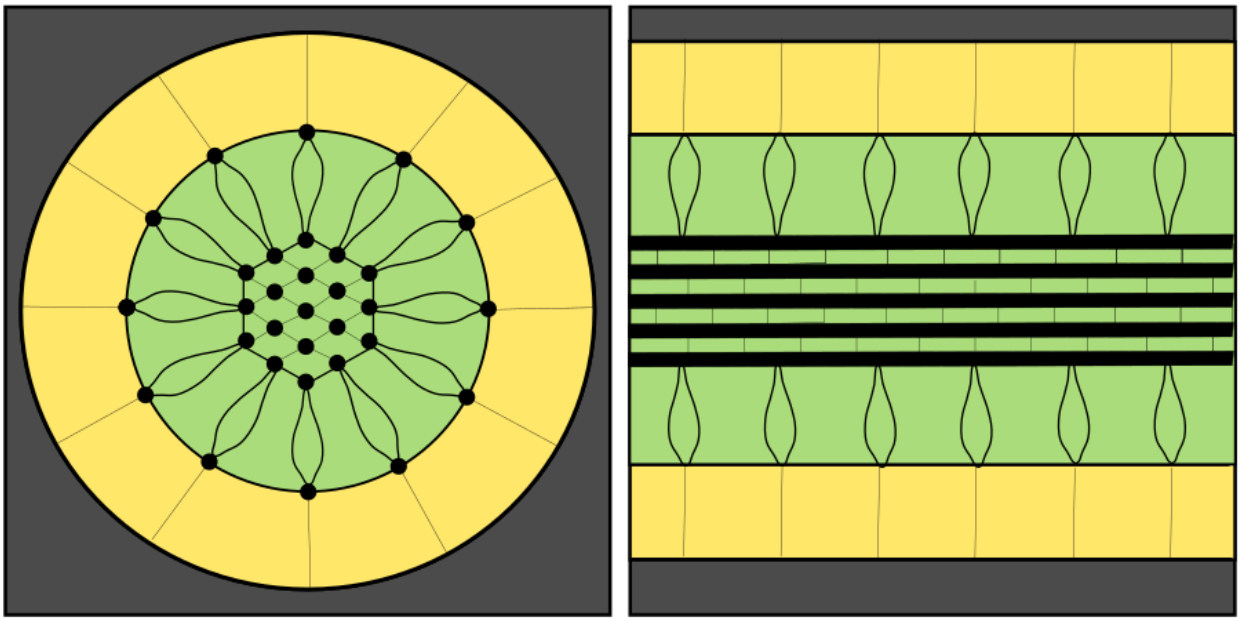

Figure 8 ***Left*** *The transversal cross section of a osteocyte dendrite, showing in green the dendrite with the central hexagonal architecture of actin microtubules, connected among themselves by fimbrin molecules. Actin microtubules are attached to integral membrane proteins via cross filaments in the cell membrane. In yellow the pericellular space is including transversal tethering elements connecting the dendrite to the in grey visualized ECM* ***Right*** *Dendrite architecture in axial direction with identical components.*

Osteocyte cell bodies show an architecture of anti-parallel actin filaments, which are cross-linked by α-actin. This difference in cytoskeleton composition leads to the estimation that processes are up to several hundred times stiffer than the cell body[214]. Stiffness of the processes are crucial for transfer of mechanical forces. Fluid flow induces shear stress in the lacunar-canalicular system. Those are predicted not to reach the threshold for mechanical stimulation of the cell body[129]. Direct substrate deformation *in vivo* may be sufficient to be sensed by the cell body. Furthermore, integrin based sensors are present on the cell bodies membrane, resulting in mechanosensitivity of the cell body[215]. Within the dendrites long actin microtubules are hypothesized to produce axial stress by sliding along the fixed attachments to the ECM (Figure 9). The predicted cytoskeletal reactions to mechanical strain by You et al. are illustrated in Figure 9. Blue elements are forced in flow direction, red elements contra directional. The left graphic shows an universal axial fluid flow, induced by mechanical strain. The shear forces, which

appear by the strain amplification, spans the transversal tether elements. Therefore, the cross filaments, which are connected via integral membrane elements to the transversal elements simultaneously bend. Furthermore, the outer actin microtubules (blue) are pulled in strain direction by the cross filaments and on the other side hold back by the intermediate actin microtubules. Fimbrin elements connect the intermediate actin filaments with the core element, which is supposedly not moving. In this model actin microtubules show no flexibility and slide stiff and contrary to each other, activating downstream mechanisms via movement. Furthermore, a direct activation via actin microtubule movement of the cell body cytoskeleton and therefore the nucleus could be hypothesized. Moreover, stretch activated ion channels may be opened[77]. In case of actin cytoskeleton flexibility all actin microtubules span like a net in peripheral direction, connected and hold back by stiff fimbrin connection molecules, which are pulled bidirectional to the peripheral and central structures.

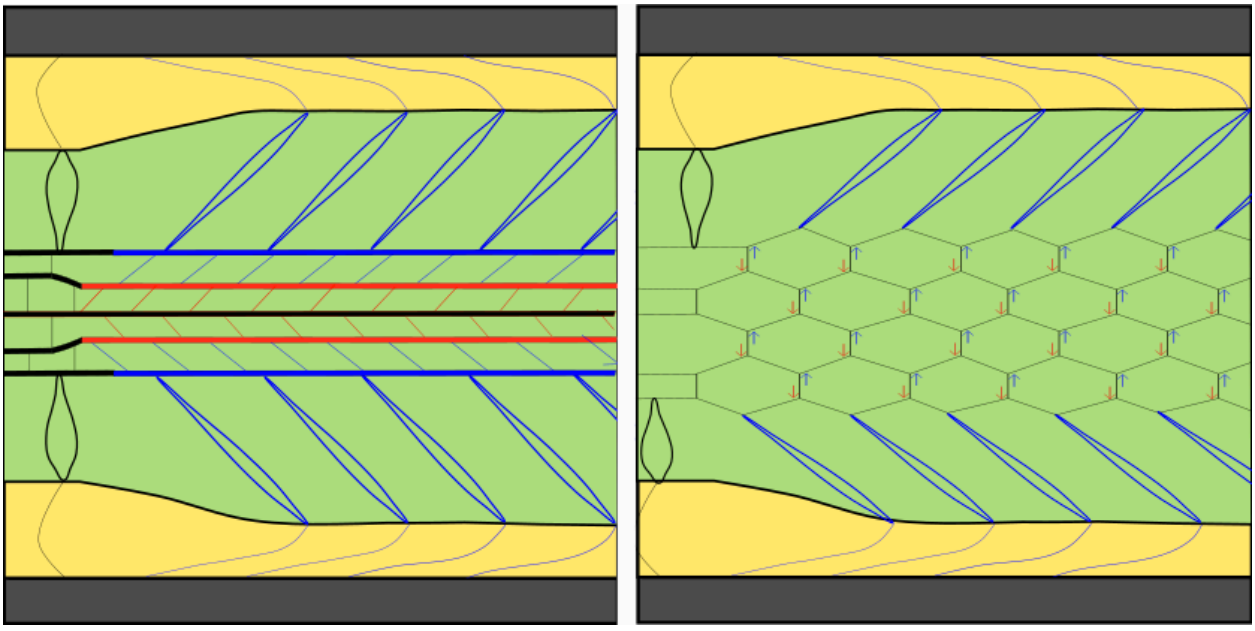

Figure 9 Predicted cytoskeletal reactions to mechanical strain by You et al. ***Left*** *Cytoskeletal deformation including stiff actin microtubules, sliding contrary to each other, activating downstream mechanisms via movement. Universal axial fluid flow spans the transversal tether elements. Therefore, simultaneously the integral membrane elements connected by cross filaments bend. As a consequence, the outer actin microtubules (blue) are pulled in strain direction by the cross filaments and on the other side hold back by the intermediate actin microtubules, connected by fimbrin elements. The core element is supposedly not moving* ***Right*** *In a flexible actin cytoskeleton all actin microtubules span like a net, connected by stiff fimbrin connection molecules, which are pulled bidirectional to the peripheral and central structures. The same color-code as in left picture is used.*

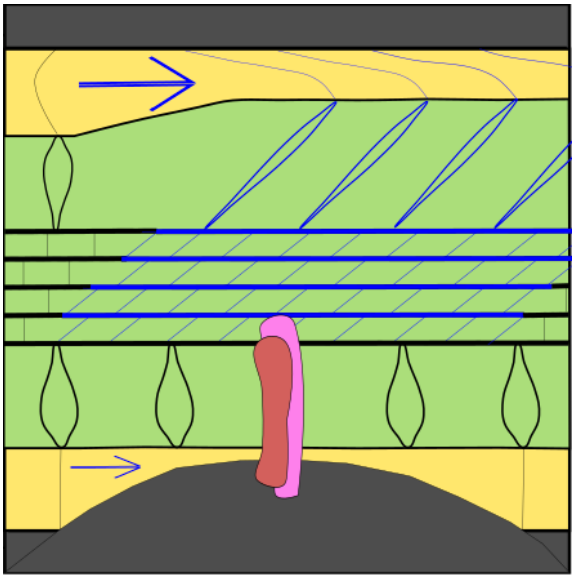

Figure 10 Integrin based connection of the actin cytoskeleton and ECM protrusions. Those prevent the spanning of tether elements in the pericellular space and therefore unilateral movement of the peripheral neighboring actin microtubule. Universal span still proceeds in the non-blocked areas of the canaliculus.

Figure 10 shows the predicted case of cytoskeleton structural changes to mechanical strain near an extracellular matrix protrusion. ECM protrusions are suspected to be connected via integrins to the dendrites cytoskeleton, and therefore not only impair the fluid flow in the pericellular space, but also stop regional the actin microtubule movement in flow direction. As a result, only the unconnected actin microtubules are being dragged in flow direction and the center of contra directional force is in the attached microtubule. However, all of these theories are still not proved *in vitro* or *in vivo*.

Besides actin, also spectrin counts as a mechanosensitive element of the cytoskeleton. Disruption of the spectrin network leads to calcium influx and nitric oxide secretion as a result of reduced cell stiffness[216]. Spectrin is located between nucleus and plasma membrane. In cooperation with F-actin, ankyrin, protein 4.1 and others spectrin forms a scaffold throughout the cytoplasm[217]. Spectrin's PH domain is targeted at the plasma membrane, on the other side it directly binds to F-actin and microtubules[218]. Spectrin contributes to the stiffness of the cell cortex and the overall elasticity of osteocytes[219].

1.7.2.8 Piezoelectricity

Piezoelectricity was a hot topic in the 1950/60's describing the phenomenon of negative electrical charge in bone areas of compression and positive charge in areas of traction[220, 221].

After identifying this phenomenon, scientists tried to explain the differences in charge via power current, produced by the fluid flow, modulating the cellular response.

Nowadays, it is known that piezoelectricity is only a marker for fluid flow/mechanical compression, not an effect of mechanotransduction. The fluid flow itself activates ion channels on the cell membrane, especially calcium and potassium channels. Opening the ion channels induces an ion flux, changing the membrane potential. Depending on the quantity and type of ion channels activated by different mechanical stimulation the membrane can be hyperpolarized or depolarized, resulting in different downstream signals in the cell. Hyperpolarization, which can be found in compressed bone areas leads to osteogenesis, whereas depolarization leads to bone resorption. A possible information transmission within the osteocyte network could be the biochemical activation of ion channels[222-224].

1.8 Diseases in bone formation and homeostasis

Bone as a complex and dynamic organ with a highly complex metabolism shows many weak point for diseases. Beside genetic disorders external factors such as trauma, nutrition and other environmental factors possible have a negative effect on bone health and homeostasis.

The most prominent bone disease worldwide is probably osteoporosis with approximately 200 million affected individuals. Osteoporotic bone is characterized by low bone mass, microarchitectural changes, leading to enhanced bone fragility and increased fracture risk. Increased bone resorption and inadequate replacement of lost bone result in a decreased bone formation.

Causes for osteoporosis can be separated into two categories.

The primary osteoporosis can be subdivided into type I, the postmenopausal osteoporosis, which is based on the massive hormonal estrogen deficiency and type II, which is the age-related osteoporosis, affecting elderly men and women from the age of 70. Secondary causes show a broad spectrum including medication, endocrine disorders, chronic renal diseases, hematopoietic disorders, nutrition or immobilization.

1.8.1 Gerodermia osteodysplastica

Gerodermia osteodysplastica (GO) is an autosomal recessive disorder, and a member of the group of autosomal recessive cutis laxa (ARCL), whose patients show lax, wrinkled skin, joint laxity, and typically a face with a prematurely aged appearance. Furthermore, patients exhibit pronounced osteoporosis with low bone mineral density resulting in frequent fractures, malar and mandibular hypoplasia and an accompanying varying growth deficit[225, 226]. Fractures, which already appear at young age, are caused by the low mineral density appear mostly long bones and vertebrae[5].
Genetically the progeroid disorder is caused by loss of function mutations in the gene *SCYL1BP1*. Several kinds of mutations have been detected until today causing GO, nonsense, frameshift, splice mutations, and variations in the start codon triplet were found[5]. For the gene a reading frame 394 exons have been predicted by Hennies et al. (GenBank accession no. NM_152281).

Matching the GO phenotype, *SCYL1BP1* is massively expressed in connective tissue and especially in osteoblasts. Its gene product, Gorab, a soluble peripheral membrane protein, showing coiled coin domains for protein-protein interactions. It is located extranuclear at the Golgi apparatus and closely interacts with the active golgin Rab6 and ARF5. Therefore, Gorab also defines as a golgin[5]. The Golgi-apparatus is known for its post-translational processing of proteins and as the central hub for protein trafficking[227]. Rab6 is known to be a central part of cellular membrane trafficking in the trans-Golgi network[228]. In the Golgi-network Rab6 is responsible for motor protein recruitment, which are needed for vesicle motion, retrograde transport of endosomes to the Golgi-apparatus and has a huge impact on the secretory pathway to plasma membrane traffic from the Golgi[229, 230]. Recently, our group has shown that the loss of Gorab is impairing early osteoblast

differentiation, reducing dermatan sulfate levels and proteoglycan glycosylation in skin and bone. Furthermore, it is reasonable to assume that decorin is kept back at the Golgi, based on a reduction of GAG attachment to the proteoglycan core protein and thereby an incomplete glycosylation. This is supported by a strong reduction of dermatan sulfate in the Golgi-apparatus.

As described before in 1.5.2 the ECM plays a crucial role in bone homeostasis. Small leucin rich proteoglycans (SLRP) are needed to keep ECM structures in order. Their role in collagen fibrillogenesis and interaction with TGF-β and other matrix ligands is undisputed[231]. SLRP's without their capability of binding to matrix proteins are speculated, due to the resulting loose ECM to endorse free TGF-β[232]. Unbound TGF-β definitely intervenes with osteoblast and osteoclast differentiation activity, and therefore, with the bone homeostasis. Decorin and biglycan are known to bind to collagen and TGF-β via their core protein. Proteoglycans with lower dermatan sulfate proportion show a lower TGF-β binding capacity, which could explain the detected increase of active TGF-β, found by our group in Gorab^{Prx1} mutants. On the other hand, dermatan sulfate is shown to bind to collagen[4]. Gorab's location within the medial/trans Golgi perfectly overlaps with the localization of GAG elongation[233]. Therefore, my group proposed that the alterations in proteoglycan glycosylation plays a major role in the GO pathomechanism. An impairment of proteoglycan transport of glycosylation factors to the glycosylation site is likely. Unfortunately more detailed information about the function of Gorab is still not available.

1.8.1.1 Differences in morphological and mechanical properties in Gorab^{Prx1} tibia

To characterize the mechanical properties of a bone, several properties have to be taken into account. As a mechanical stressed, mineralized tissue basic parameters like, body measurements, bone geometry, tissue level strain distribution, tissue composition or elasticity have to be measured. Our group characterized mice tibiae properties of Gorab^{Prx1} mice, comparing to their littermate control mice (LC). Gorab^{Prx1} mice represent the *Gerodermia osteodystplastica* mouse model, which is Gorab deficient in Prx1 expressing cells in the limbs. The conditional cre knockout model is further explained in the materials and methods chapter. Our group published the following describing data on

bone tibia morphology and mechanical properties in the Journal of Biomechanics, entitled “Examining tissue composition, whole-bone morphology and mechanical behavior of GorabPrx1mice tibiae: A mouse model of premature aging”.

For greater understanding the Finite Element graphic in Figure 11 taken from the above mentioned publication shows the differences in geometry and strain distributional of 10 week old LC mice and Gorab^{Prx1} tibiae. The most significant differences are the length, the altering cross-section geometry and the predicted strain distribution. The growth defect which can be seen here, was consistently observed it Gorab^{Prx1} animals, together with a lower bodyweight.

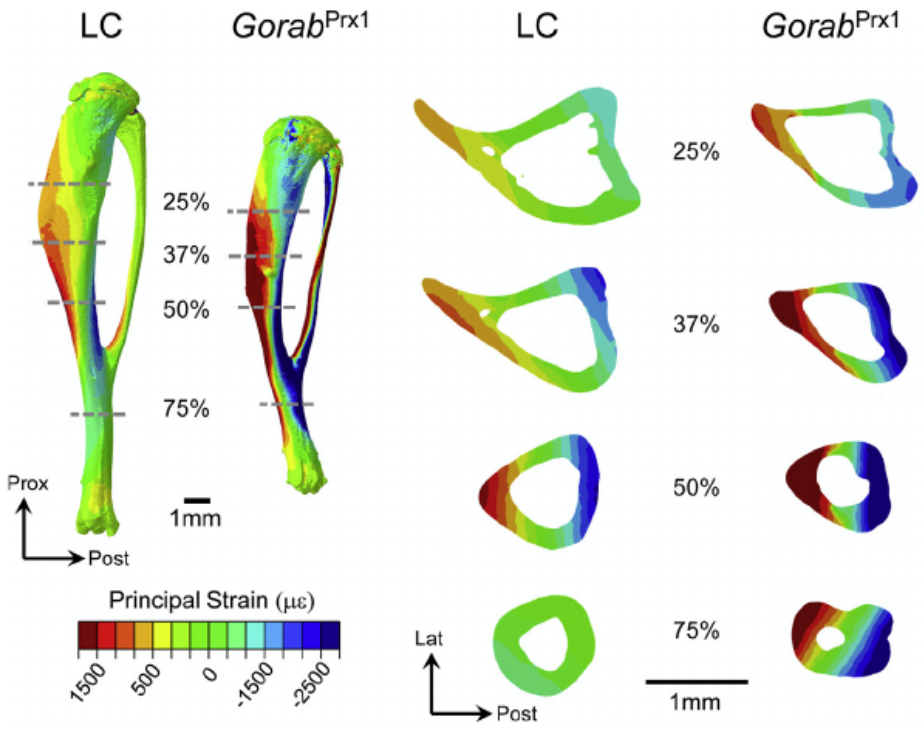

Figure 11 Computationally predicted principal strain distributions throughout the entire tibia and at multiple representative cross-sections (25%, 37%, 50% and 75% relative to the proximal end) for the LC and Gorab^{Prx1} limbs loaded with 5 N in uniaxial compression in vivo. Red and blue indicate tensile and compressive strains, respectively. Strain gauge was attached on the medial surface of the tibial midshaft to measure the longitudinal strain there experimentally. (For interpretation of the references to color in this figure legend, the reader is referred to the web version of this article.) The figure was published under Yang et al. in 2017.

Gorab^{Prx1} show a smaller total area, cortical area, cortical thickness measured at the midshaft and the metaphysis. The total mineral density in cortical bone was not changed in midshaft, only 2 % lower in the metaphyseal area in Gorab^{Prx1}. Moments of inertia, also measured at midshaft and metaphysis were both decreased in Gorab^{Prx1} compared to LC. Trabecular bone in Gorab^{Prx1} was also decreased in volume and number; interestingly the total mineral density was 10 % higher in Gorab^{Prx1} compared to LC. After bodyweight adjustment only the minimum moment of inertia was changed, implementing, that the body weight difference is not responsible for the differences in bone length (Gorab^{Prx1} 17,9 ± 1,2 g and LC 23,3 ± 1,7 g).

Further differences in geometry show an increased anterior convexity of Gorab^{Prx1} tibiae. This curvature leads to higher strain in the bone tissue and a resultant more predictable direction of bending while loading[234].

Mechanical properties like whole – bone strength, stiffness and work-to-fracture of Gorab^{Prx1} are also reduced. Based on FE modeling increased tissue-level strains within the tibiae of Gorab^{Prx1} compared to LC, in case of axial compression of the same magnitude. The overall strain distribution pattern in control mice and Gorab^{Prx1} mice was similar. Strain amplitude throughout the whole tibia was higher in Gorab^{Prx1} tibiae than in LC tibiae. For example, at 50 % length the minimum and maximum principal strain was 73 % and 128 % higher under -5 N mechanical axial load.

Mineral composition were analyzed via Furier-transform infrared spectroscopy and shows signs of a delayed mineralization process.

Therefore, loss of *Gorab* results in weaker and more brittle bone structures, which is shown by a reduction of work-to-break of 6% in Gorab^{Prx1}. These observations represent the human phenotype of GO patients, who also exhibit short brittle long bones and spontaneous fractures, and with aged patient[5, 235, 236].

2 Material & Methods

If not mentioned otherwise the doctoral student M.Sc. Michael Thelen executed the listed experiments.

2.1 *SCYL1BP1* conditional knockout mice

The mouse model was chosen for these studies, due to exhibiting a severe osteoporosis phenotype. Dr. Wing-Lee Chan, who designed this mouse model designed several conditional knockout models for *SCYL1BP1.*

Prx1Cre, Col2a1Cre and *Dmp1Cre* knockout models were analyzed by our group in this attempt. Therefore, different developmental stages of the osteoblastic lineage were examined *in vivo* by knocking them out conditionally. *Dmp1* (highly expressed in late osteoblasts and osteocytes) as well as *Col2a1* (expressed in early chondrocytes) driven knockout models did not show such a severe osteoporosis phenotype as the *Prx1* driven model. *Prx1* is expressed in mesenchymal progenitor cells, which have the ability to differentiate into osteoblasts/osteocytes and chondrocytes.

All mice used in this study were Gorab^{Prx1} mice (Gorab^{Prx1}) and their homozygous cre negative littermates (LC). Gorab^{Prx1} mouse model was generated, as described by Chan et.al [237].

Briefly, a BAC clone containing the mouse *SCYL1BP1* gene was used to extract exon 2-3 including their flanking introns into a pBluescript vector by recombination. LoxP sites, flanking exon 2-3 of *SCYL1BP1* were inserted by homologous combination. The neomycin cassette was subsequently removed. Mouse ES cells were transfected and correctly targeted clones were injected into C57BL/6 blastocysts. In the last step the resulting animals were mated with Prx1-cre mice with the result of Gorab^{Prx1} animals.

2.2 Animal housing

10 week old female Gorab^{Prx1} and homozygous cre^{-} (LC) mice obtained from the Max-Planck-Institut für molekulare Genetik (Berlin, Germany) were housed in groups of 3 to 5

per cage with *ad libitum* access to food and water. Overall 45 mice were used for this study. Mice were transferred to the Forschungseinrichtung für Experimentelle Medizin (FEM) via FEM animal transport one week ahead of the experiments. Housing and all experiments were performed in line with the policies from the local legal research animal welfare representative (LAGeSo Berlin, G0321/12).

2.3 *In vivo* mechanical loading

In vivo cyclic compression of the left tibia was used to induce an anabolic response of the bone. The loading protocol of the mouse tibia was performed by our group as previously described[238].

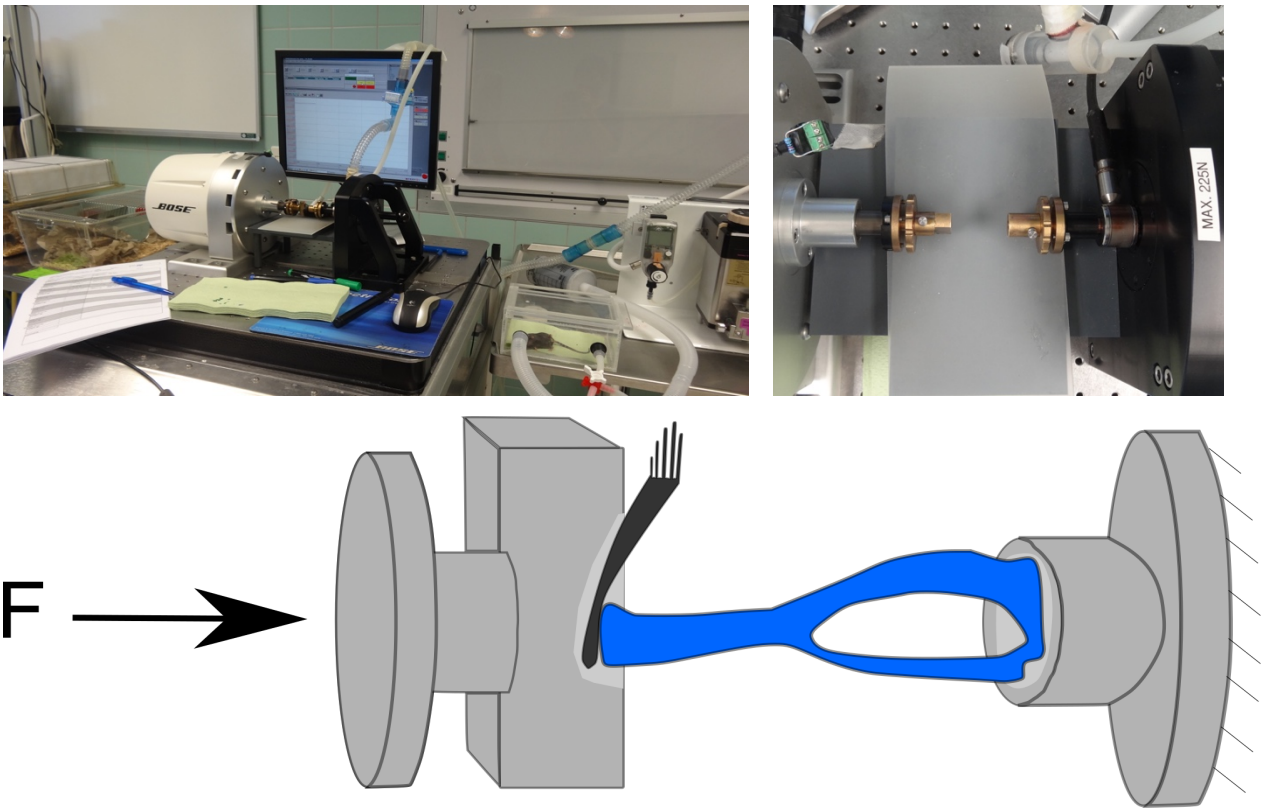

Figure 12 ***Top left*** *Loading device while loading a littermate control mouse, neighboring the isoflurane narcosis device.* ***Top right*** *shows the loading device close up, more detailed the knee and angle fixation sites.* ***Bottom*** *Schematic loading, showing tibia orientation.*

The left ankle and knee were fixed in the loading device concave cups with - 1 N of preload (Testbench ElectroForce LM1, Bose, Framingham, USA). The loading protocol included: 216 cycles applied daily with a frequency of 4 Hz, 5 days/week (M-F), for two weeks,

delivering - 11 N for LC animals and - 5,4 N peak amplitudes for Gorab^{Prx1} animals (data were published as “Examining tissue composition, whole-bone morphology and mechanical behavior of Gorab^{Prx1} mice tibiae: A mouse model of premature aging, Yang et al. in the Journal of Biomechanics, 2017, Michael Thelen was listed as a co-author). Compressions were applied in triangular waveforms alternating 0.15 sec active loading and 0.1 sec rest insertion at - 1 N, followed by a 5 sec break. A maximal microstrain of 1200 με was measured for these peak loads in the tibial midshaft through *in vivo* strain gauging[238, 239]. The animals’ right tibia was used as an internal, unloaded control. Three days after the last loading cycle, at day 15 of the experiment, mice were sacrificed via cervical dislocation while being under Isoflurane induced anesthesia. Afterwards both, left and right tibiae were dissected from the surrounded soft tissue and were treated accordingly to the destined experimental setups.

The *in vivo* loadings were executed in close cooperation of the projects technical assistant M.Sc. Anne Seliger.

2.4 *In vivo* strain gauging

For physiologic comparable effects in LC and Gorab^{Prx1} animas due to mechanical loading, a common strain within the bone tissue was set. 1200 με were chosen for the peak load in the loading protocol. Previous loading experiments, executed by Willie et at. showed that 11 N applied force induce 1200 με in C57BL/6. 1200 με was chosen, because it is known to induce an osteogenic response in mouse tibiae[240, 241]. 1200 με represents approximately 2-3 times the strains tibiae undergo during normal locomotion in mice[242, 243].

LC which have the cre^{-} genotype are similar to C57BL/6 mice, therefore 11 N were used for control animals.

Gorab^{Prx1} animals premiered for loading experiments, therefore we had to determine the force needed to induce a comparable deformation and therefore, a comparable strain in the tibia.

To determine the needed force to induce 1200 με, single element stain gauges were prepared beforehand. Mice were put under isoflurane inhalation anesthesia and got a subcutaneous injection of Carprofen (5 mg/kg). Skin and surrounding muscle tissue were removed and the tibial bone exposed. The single element strain gauge was attached to the medial surface of the tibial midshaft and aligned with the bone's long axis. After connecting the strain gauge to the sensor and the computer a range of dynamic compressive loads from -2 N to -6 N were applied as previously described. WinTest software simultaneously recorded the induced strains. As a result - 5.4 N was needed to induce 1200 με in Gorab^{Prx1} tibia.
Strain gauging experiments were executed in cooperation with M.Sc. Tobias Thiele.

2.5 *In vivo* µCT

Prior to the *in vivo* µCT scans mice were put under anesthesia via an intraperitoneal injection of a 1:1 mixture of Sedan and Ketamine to prevent moving artefacts. Mice were scanned at day 0, 5, 10 and 15. The scanned areas were the tibial midshaft and diaphyseal growth plate area. The diaphyseal VOI was set individually from the midpoint of each tibia, with in total 213 voxel slices (2237 µm). Metaphyseal VOI was also adjusted during each scan for each mouse. The selected VOI starts directly at the growth plate, which due to lower mineralization is visible in the X-ray pre-scan and extends 432 slices (4536 µm) along the bone's long axis.
To ensure a reproducible position of the tibia, mice were placed in a customized plastic mouse bed during imaging. Images were taken *in vivo* in a microCT (VivaCT 40, Scanco, Switzerland; nominal isotropic image resolution 10.5 µm, 55 kVp, 145 µA, 600 ms integration time, no frame averaging). A more detailed scanning protocol was published previously by our group[238].
The *in vivo* µCT scans were executed in close cooperation of the projects technical assistant M.Sc. Anne Seliger.

2.6 3D - Image registration, contouring, fusion and automatic segmentation

All four static µCT scans were aligned and reconstructed to a 3 dimensional model, as each slice (single scan) had to be contoured, fused and segmented).
In the reconstructed µCT for both regions, trabecular and cortical, a ROI is defined. For the trabecular areal the VOI included the secondary spongiosa in the proximal metaphysis, which was defined from 250 µm below the growth plate spanning over the following 5 % of the whole tibial length. To exclude the cortical shell, the trabecular bone was contoured manually using the µCT Evaluation Program V6, provided by Scanco. The threshold of 424 mg HA/cc was used to segment the bone from surrounding soft tissue.
VOI of the cortical bone was chosen at the midpoint of the tibia and was spanned 2.5 % of the tibial length along the tibia's long axis. For cortical bone a threshold of 409 mg HA/cc was used. As a result from the static µCT investigation the following parameters were included, as recommended:

Trabecular VOI

- Bone volume fraction (Tb. BV/TV) [mm^3/m^3],
- Trabecular thickness (Tb.Th) [µm],
- Average number of trabeculae per unit length (Tb.N) [1/mm],
- Trabecular separation (Tb.Sp) [µm] and
- Trabecular volumetric tissue mineral density (Tb.vTMD) [mg HA/cm^3].

Cortical VOI

- Principal moments of inertia (I_{max}, I_{min}) [mm^4],
- Cortical bone area (Ct.Ar) [mm^2],
- Total cross-sectional area inside the periosteal envelope (Tt. Ar) [mm^2],
- Cortical area fraction (Ct.Ar/Tt.Ar) [mm^2/mm^2],
- Cortical thickness (Ct.Th) [µm] and
- Cortical volumetric tissue mineral density (Ct.vTMD) [mg HA/cm^3].

For the principal moments of inertia, a coordinate transformation was used to align the scans in a common coordinate system. Therefore, the z-axis was defined by two midpoints of the cortical ring and the yx-plane was defined according to the position of the fibula.
The 3D image registration, contouring, fusion and automated segmentation were executed in close cooperation of the projects technical assistant M.Sc. Anne Seliger.

2.7 4D analysis of spatio-temporal remodeling

Due to missing supervision based on the professorship, Prof. Dr. Bettina Willie earned at McGill university in Montréal, Canada, Anne Seliger and me were not able to finish the whole creation of the 3D time-lapse morphometry. Dr. Haisheng Young, a postdoc in the newly formed laboratory in Canada executed 2.7.

In order to track spatio-temporal changes based on the cyclic compressive mechanical loading within the bone structure the data of the four µCT time points have to be geometrically aligned. Subsequently structural changes between the different images can be identified and quantified.
Therefore, the data had to be pre-processes, fused, segmented and features had to be extracted and classified.
Detailed description on the transfer function regarding the 4D modeling can be found in Birkhold et al., and the process will be briefly described in chapter 2.7.1- 2.7.5.

2.7.1 Image pre-processing

Artifacts from the µCT imaging had to be removed and furthermore filtering had to be applied to ensure an optimal quality for data fusion. Lastly the ROI for each image had to be adapted (cropped) to reduce computation time of data fusion.

2.7.2 Image fusion

To ensure a correct identification of (re)modeling processes during the analyzed timeframe the imaging data had to be registered in one fixed coordinate system. For this purpose the reference coordinate system of time point 0 has been used. When transforming the data of a later time point, a transformation matrix had been used. The included data is comprised of the temporal changes of the dynamic bone structures, therefore a registration approach is applied. This enables the local mineralization dynamics of the changing bone to be utilized to include the dynamics of the structures into the registration approach. After registration and transformation to the reference coordinate system the data were used to create the desired 4D model.

2.7.3 Image segmentation

After creating the 4D model, volumes of bone formation and bone resorption had to be identified and highlighted in the model. Therefore, the data sets had to be segmented. The segmentation algorithm differs between the trabecular compartment and the cortical compartment.
Nonetheless, before applying any algorithm a thresholding for all data had to be implemented in order to eliminate signals from soft tissue and artefacts.
Thresholding is followed on the one hand (metaphyseal trabecular bone) by segmentation into trabecular and cortical shell and on the other hand (diaphyseal cortical bone) into endocortical and periosteal compartment. (Re)modeling sequences were identified via surface position tracking as a function of time. Therefore, the surfaces are extracted and transformed into a cylinder coordinate system.

2.7.4 Feature extraction and classification

The registered and segmented data sets were used for identification of temporal-structural changes. Using the common coordinate system, points of the same region of bone have been compared. In case of structural changes over time the changes were

classified into formation, resorption and quiescent sites. Classification of resorbing or forming bone tissue is equal to voxels disappearing or appearing over time. Voxel changes to background were classified as bone resorption and voxel changes to bone were identified as bone formation. Voxels, being identified as bone over time were classified as quiescent bone.

2.7.5 Visualization

To visualize bone formation and resorption sites within the temporal frame, color codes were used. Quiescent bone was marked yellow, newly formed bone marked as blue and resorbed bone as red.

2.8 Polymethylmethacrylate embedding and sample preparation

Sample embedding and sectioning for PMMA embedded calcein stainings were executed by M.Sc. Anne Seliger.

Bones were harvested at day 15 of the loading protocol. Muscles and adjacent tissues were removed and bone were placed in a 15 ml Falcon tube, containing 70 % ethanol on a horizontal shaker at RT overnight. The samples were always covered with aluminum foil, due to the light sensitivity of calcein (from now on samples were always covered in aluminum foil). On the following day the bones were transferred into labelled histology cassettes, which were placed in 80 % ethanol ON on a horizontal shaker. From this step on after every exchange, the samples were kept for 10 min at 0.6 bar in an exsiccator. Under these conditions, the bones have to stay in increasing ethanol concentrations. Ethanol has to be exchanged on a daily basis, three times 80 % ethanol, three times 96 % and three times 100 % ethanol.

For pre-infiltration of the tissue, ethanol was exchanged with Xylene. Exsiccator was followed by a 4 h horizontal shake at RT. Subsequently Xylene was exchanged with already prepared pre-infiltration solution (chromatography destabilized Technovit 9100 NEU solution plus aluminiumoxide (Al_2O_3) and hardener). Samples were kept as they were for 1-3 days at 4 °C.

Samples were transferred into the infiltration solution for 5-7 days at 4 °C (chromatography destabilized Technovit 9100 NEU solution plus PMMA powder and hardener), with this step being repeated once. For the embedding PE, forms were prepared by sticking a pair of earplugs to each pair of tibiae. Also the bottom of the PE forms were oiled before the forms were connected via coating with parafilm.

For the polymerization two stock solutions were prepared:

Table 1 Polymerization stock solution recipe for polymerization stock solution A and B

Polymerization solution A	Polymerization solution B
500 ml Technovit 9100 NEU solution	50 ml Technovit 9100 NEU solution
80 g PMMA powder	4 ml “hardener 2”
3 g “hardener 1”	2 ml regulator

Solution A was prepared beforehand, and solution B shortly before use. For the polymerization both stock solutions were mixed 9:1. Bones were placed for embedding into the earplugs and embedded with the polymerization solution mix. One last time the samples were placed for 10 min at 0.6 bar vacuum in the exsiccator. Closed PE forms were stored at -4 °C for at least two days.

2.9 PMMA sectioning

After a minimum of 2 days at -4 °C PMMA blocks were glued onto pre-grinded object slides. Technovit 4000 glue was prepared and used to glue PMMA blocks onto the object slides. For 5-10 min the glued slide-block combination had to be fixated in a press in a planar position until the glue was cured.

In order to get a longitudinal sections of the midshaft cortical bone and axial sections of the metaphyseal trabecular bone the tibia was sawn into diaphysis- and metaphysis parts. After separation the surfaces of the cut were grinded to guarantee a smooth surface. In the next step, via a sandwich method a second object slide is glued to the freshly grinded surface. The dimensions of the new object slide and the grinded object slide-sample combination were measured beforehand in order to calculate the correct sewing position to guarantee a constant height of the final section. The second object slide was glued with the help of a precision adhesive and a light polymerization machine. After slowly pressing the sample to the object slide the light was turned on for 8 min. The sandwich was kept in the dark for at least 6 h. The thickness of the sandwich was measured afterwards and the saw was prepared accordingly to the measures. The archived thickness was 500 µm.

After getting the final thickness of 80 µm using grinding and polishing the object slide should be stored in the dark until evaluation.

2.10 Dynamic histomorphometry – Calcein based of bone formation labeling

For Gorab^{Prx1} and LC 9 mice each were treated with the prior described 14 day long loading program. Intraperitoneal injections of calcein at a dose of 30 µg/g at day 12 and day 3 before euthanasia were given to each mouse. Three days subsequently to the last loading cycle the tibiae were dissected from the surrounding soft tissue and directly embedded in polymethyl methacrylate (PMMA) (Technovit 9100, Wehreim, Germany). Endosteal and periosteal bone formation in Gorab^{Prx1} and LC mice *in vivo* loaded and non-loaded tibiae were analyzed. The calcein labeled sections were imaged and analyzed

by fluorescent microscopy (Leica DMRB, Munich, Germany and AxioCam MRc, Zeiss, Oberkochen, Germany) at a magnification of 200x. Metaphyseal section was made vertical, showing the proximal tibia, including growth plate and trabecular bone reaching the upper diaphysis. Furthermore, a horizontal section was made in the diaphyseal midshaft. Bone formation was measured at the entire endocortical (Ec) and periosteal (Ps) surfaces. Images were processed via the commercial available software AxioVision. The following parameters were analyzed, recommended by the American Society for Bone and Mineral Research[244]:

- Single labeled surface per bone surface (sLS/BS) [%],
- Double labeled surface per bone surface (dLS/BS) [%],
- Mineralizing surface per bone surface (MS/BS) [%],
- Mineral apposition rate (MAR) [µm/d] and
- Bone formation rate per bone surface (BFR/BS) [µm/d].

BS, sLS, dLS and MS were measured in µm, recorded by hand. Random distant measures between related inner and outer labeled surfaces were measured by the algorithm shown in Figure 13. From these measurements the mean surface distance was calculated. Based on these parameters the others were calculated as follows:

- MS/BS [%] = Mineralizing Surface [µm] / Total Bone Surface [µm],
- MAR [µm/d] = Mean Surface distance [µm] / 7 [d],
- BFR [μm^2/d] = MAR [µm/d] * MS/BS [%] and
- BFR/BS [µm/d] = BFR [μm^2/d] / Total bone surface [µm].

Values for cortical trabecular bone were analyzed via ImageJ, using an especially written macro, which calculates sLS/BS, dLS/BS MS/BS, MAR and BFR/BS based on measured total volume, inner and outer layer. The macro was written by Mario Thiele.

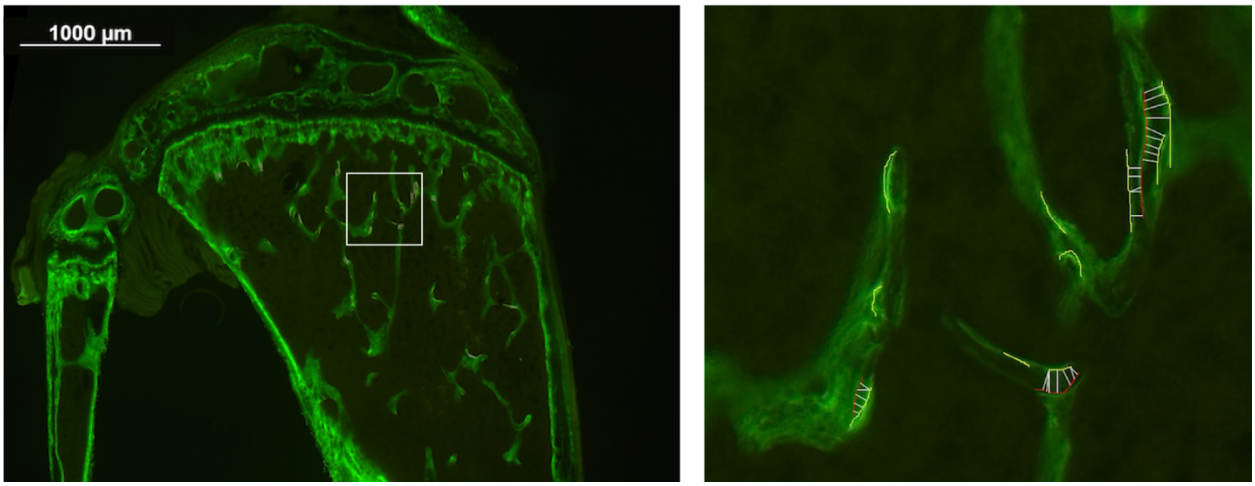

Figure 13 Calcein evaluation of double labeled Gorab^{Prx1} loaded diaphyseal tibia. Label distances (white), inner surfaced (red) and outer surfaces (yellow) marked in ImageJ. Tibiae were dissected at day 15 of mice exposed to axial compression of 1200 με and (left tibia dynamically loaded, right tibia non-loaded control)

2.11 Quantification of osteocyte canaliculi network using rhodamine staining

The purpose of these experiments was to analyze the phenotype of the lacunar-canalicular network in diaphyseal cortical bone of Gorab^{Prx1} tibiae. This was carried out by our collaboration partners from the Max Planck Institut für Kolloid- und Grenzflächenforschung, Department for Biomaterials (Potsdam, Germany). The mice used for this analysis were not mechanically loaded.

At the age of 12 weeks tibiae were dissected from 6 euthanized, female Gorab^{Prx1} and 6 homozygous cre^{-} LC mice. Bones were fixed in 4 % PFA for 48 h at 4°C. PFA was exchanged to 70 % alcohol for storage at 4°C.

Sample preparation and imaging were described before by Roschger et al. (Dissertation: ” Quantitative Analysis of Local Mineral Content and Composition During Bone Growth and Remodeling”).

Briefly, before embedding, a cross-section was cut from the tibia midshaft. It was dehydrated by a series of increasing ethanol concentrations. Subsequently, the staining using Rhodamine 6G was completed. As a staining reagent a mixture of ethanol and Rhodamine was used (1.25 g Rhodamine per 300 ml ethanol). Samples were exposed to

the Rhodamine ethanol mixture (10 ml per sample) over night on a shaker. The staining solution was exchanged once. Stained sections were embedded in PMMA.

Embedded sections were cut and polished to reveal the desired cross-section area. A Leica SP8 was used for confocal laser scanning measurements. 2D overview and 3D stacks of rhodamine fluorescence were imaged.

Therefore, per sample, 4-6 ROI were defined, as shown in Figure 14. In these regions ca. 100 pictures were taken in 0.3 µm stepsize. These were used for 3D visualization and quantification of the lacunar-canalicular network. The network has been skeletonized and quantified in the following using the python-based TINA script package[245].

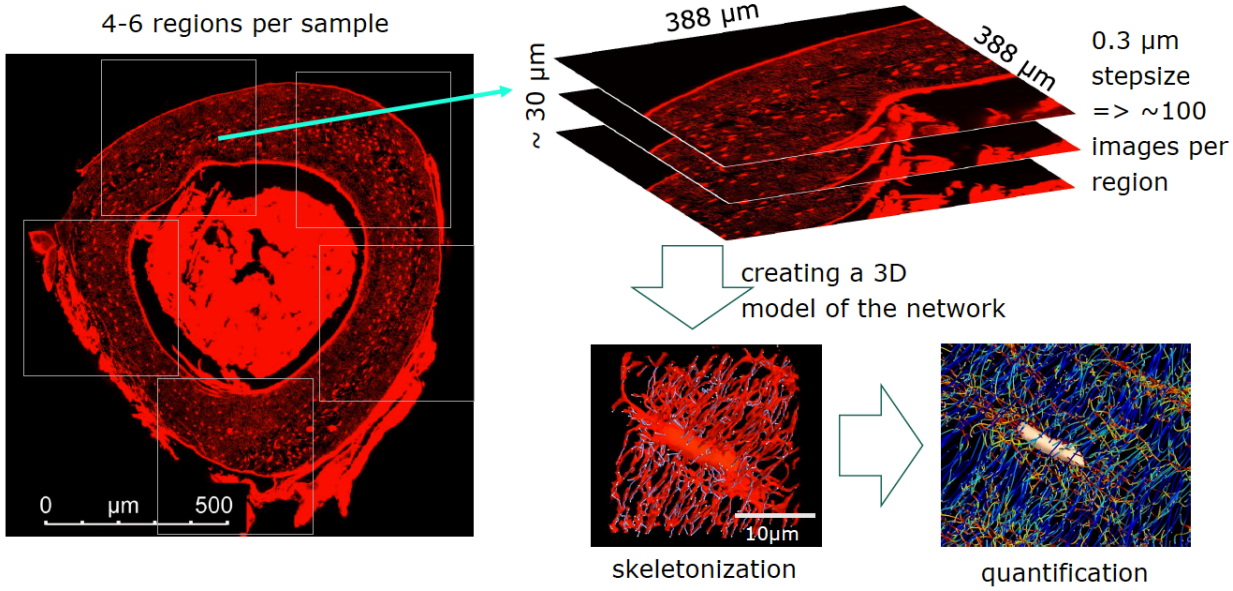

Figure 14 Workflow of creating the 3D models of the lacunar-canalicular network using the confocal laser scanning microscope creating 100 images per ROI in 0.3 µm step-size for skeletonization and the final quantification

2.12 Histology of paraffin embedded demineralized bone

After loading procedures, 5 Gorab^{Prx1} and 5 LC animals were used for histologic stainings to ensure a statistic standard. All were included in the final evaluation. All histologic analysis were executed subsequent to the loading protocol. On day 15 both, left and right tibiae were dissected from the surrounded soft tissue and fixated for 2 days in 4 % paraformaldehyde (PFA) at room temperature (RT). Following the fixation, the bones

were kept in a saturated EDTA solution (EDTA Entkalkungslösung; Herbeta Arzneimittel; Berlin, Germany) for 10 days under exchange of EDTA every second day. After 10 days decalcification, the samples were placed for 20 min under running water. Bones were dehydrated in the Leica TP1020 (Leica Biosystems, Nussloch, Germany) for automatic tissue infiltration using several ethanol incubations with an increasing concentration, finishing with two times xylene bath. Embedding of the samples was done with 60°C preheated paraffin.
5 µm thick longitudinal sections were produced using a rotation microtome (Microm HM 355 S; Thermo Fisher Scientific; Hennigsdorf, Germany). Sections have been deparaffinized by 30 min incubation at 70°C, 2 x 5 min Xylene bath, followed by decreasing alcohol concentrations (100% - 70%) and a final bath in a.dest..

All following histological stainings were executed to characterize the bone cellular compartments, osteoblasts, osteocytes and osteoclasts. Furthermore, PicrosiriusRed was used to analyze the collagen composition of the different phenotypes and loading conditions.

2.13Osterix 3,3'-Diaminobenzidine (DAB) staining

Paraffin embedded sections were incubated for 30 min at 70°C to melt the paraffin. Xylene incubation followed by a decreasing ethanol row ending in *aqua destillata* ensured a complete deparaffination of the bone tissue. The tissue was pretreated with H_2O_2 (Merck, Darmstadt, Germany) for 10 min at room temperature followed with two times 5 min PBS wash and a 60 min blocking with serum free protein blocking solution (DAKO Corporation; Protein Block Serum-Free; California, USA).
Osterix antibody (Vector, California, USA) was diluted 1:2000 in 3 % BSA in 4 % PBS. Per sample 75 µl antibody dilution was added. Antibody incubation was provided in a wet chamber over night at 4°C. Subsequently, the samples were washed twice for 5 min with PBS. Biotinylated anti rabbit antibody was diluted 1:2000 and again 75 µl per section was placed on the samples for 30 min at room temperature. PBS wash to release the not bound AB from the cover slides was performed twice, and was followed by a 30 min

incubation of ABC reagent and a 2 min incubation with DAB to develop the staining (DAB substrate Kit peroxidase, Vector, California, USA). The samples were flushed with PBS and afterwards incubated for 10 min in PBS at room temperature. Finally the samples were washed in a.dest. and air dried overnight. The following morning the stained sections were washed in 50 % ethanol, 100 % ethanol and 2 times in xylene before they were covered in entellan (Merck, Darmstadt, Germany).

2.14Tartrate-resistant acid phosphatase staining

Paraffin embedded sections were incubated for 30 min at 70°C in order to melt the paraffin. Xylene incubation followed by a decreasing ethanol row ending in *aqua destillata* ensured a complete deparaffination of the bone tissue. Sections were immersed with PBS before an 1 hour incubation with the TRAP staining solution (Table 2). During incubation the samples were frequently checked for positive reactions to stop the process, in order to prevent false positive signals. Before counterstaining with hematoxylin (Vector, California, USA) for 5-10 sec the samples were rinsed with PBS and secondly with a.dest. Counterstaining was stopped by washing again with PBS for a couple of seconds. Before drying the counterstaining was also checked via microscopy. Finally, the samples were washed in a.dest and air-dried overnight (ON). On the following day the sections were covered with entellan.

Table 2 TRAP staining solution recipe showing fast red concentration, naphthol concentration and TRAP buffer solvents concentrations

TRAP staining solution		
Fast red solution (200 µl)	Naphthol-AS-TR-phosphate solution (300 µl)	TRAP buffer (1500 µl)
10 mg/ml fast red	10 mg/ml naphtol	9.7 g/l sodium tartrate
		4.1 g/l sodium acetate
in *aqua destillata*	in 2-Ethoxyethanol	in *aqua destillata* (pH 5.2)

2.15Picrosirius red

Sections were incubated in Picrosirius red staining solution (ScyTek Laboratories, Utah, USA) for 1 h. Subsequently flushed two times in 0,5 % acidic acid, followed by a single wash with a.dest.. Afterwards the sections were air dried ON. Next day the sections were flushed with xylene and covered in entellan.

2.16Histology evaluation

For every histologic evaluation three sections per tibia were analyzed, to obtain an average per bone for a representative overview. Histology sections were imaged in a 100 x magnification using an upright compound microscope Olympus BX60. Resolution was set to 1388x1040 standard color to guarantee maximal visualization of cells in the sections. Osterix and TRAP stained sections were analyzed via OsteoMatrix (OsteoMeasure, 2007). OsteoMatrix is a digital supported evaluation tool based on algorithms for cell and bone tissue quantification. Calculated units were based on manually taken values such as cell numbers and bone areas in a specific ROI, which is identical to *in vivo* microCT ROI targeting the metaphyseal trabecular bone. Picrosirius Red stained bones were imaged in polarizing light using the AxioCam MRc microscope. The analysis, differentiation and quantification of young (greenish) and mature (reddish) fibers were performed using ImageJ.

2.17RNAseq

RNAseq was used as a discovery study to identify target genes which could lead to a possible mechanism behind the loss of mechanoresponsiveness in Gorab^{Prx1} animals. A single load session (216 cycles applied with a frequency of 4 Hz, delivering - 11 N for control animals and - 5,4 N peak amplitudes for Gorab^{Prx1} animals. Compressions were applied with triangular waveforms alternating 0.15 sec active loading and 0.1 sec rest insertion at - 1 N, followed by a 5 sec break.) was applied to the left tibia. After 8 h the tibiae were dissected, bone marrow was flushed with PBS and the bones were directly

flash frozen in liquid nitrogen. When not instantly processed, samples were stored at -80°C.

2.18RNA Isolation

Frozen bones were pulverized by hammering. Material was transferred into 1,5 ml RNase and DNase free Eppendorf tubes. Trizol chloroform extraction was performed for all samples. Briefly, 1 ml Trizol (Invitrogen, Carlsbad, USA) was added. Chloroform and Isopropyl alcohol were used to separate proteins and DNA from the RNA. After the final centrifugation, pellets were air dried and resuspended with 20 µl of RNase and DNase free water. Total RNA was quantified using a Bioanalyzer and diluted accordingly.

2.19mRNA library preparation

mRNA Isolation, fragmentation, cDNA synthesis, as well as PCR Library Enrichment has been executed followed the protocol for use with NEBNext Poly(A) mRNA Magnetic Isolation Module (NEB#E7490).
Briefly, after mRNA isolation and fragmentation, first strand cDNA was generated from ~100 ng total RNA using ProtoScript II Reverse Transcriptase, followed by the second strand cDNA synthesis, by adding the second strand synthesis enzyme mix. Magnetic beads were used for purification. NEBNext Adaptor for Illumina was added to ensure the feasibility of the library for Illumina sequencing after PCR library enrichment and a final AMPure XP Bead based purification step.

2.20Illumina HiSeq – Sequencing

Sequencing of the samples was achieved using the Illumina Hiseq flowcell system. Samples were sequenced on 2 Lanes in single-read mode with 50 cycle read length.

2.21RNAseq Evaluation

RNAseq data processing executed by the Canadian Centre for Computational Genomics. The RNAseq analysis report shows in detail how the data was processed and can be found in the appendix of this thesis. The received data were analyzed further using Excel.

2.22IDG-SW3 and MLO-Y4 culturing conditions

IDG-SW3 cells were cultured in 0,01 % Collagen coated 10 cm in diameter petri dishes. Before seeding, dishes were flushed one time with PBS.
IDG-SW3 were expanded at 33°C, 5 % CO_2 and 21 % O_2. Expansion medium containing α-MEM, 10 % FBS, 2,5 µl INF-γ was prepared as needed.
IDG-SW3 differentiation medium is composed of α-MEM, 25 mg ascorbic acid and 4mM β-Glycerolphosphate.
MLO-Y4 cells were cultured at 37°C, 5 % CO_2 and 21 % O_2. Culture medium containing α-MEM and 10 % FBS was prepared as needed.

2.23IDG-SW3/MLO-Y4 siRNA knockdown

IDG-SW3 cells were seeded in a glass bottom culture dishes with 35 mm diameter for 4 days prior mechanical stimulation. 100.000 cells / dish were seeded on day 0 and got cultured in differentiation medium over night at 37°C, 5 % CO_2 and 21 % O_2 for a proper cell settlement and network formation. siRNA knockdown was done from day 1-3. Per batch three conditions were prepared:

- not treated with any siRNA / transfection reagents,
- transfected with non-coding siRNA as a negative control and
- transfected with siRNA targeting *SKYL1BP1* mRNA.

The final siRNA concentration was 25 nm.

MLO-Y4 cells were cultured as described. 100.000 cells per 6-Well were seeded on day 0 and were cultured for settlement overnight. On day 1-3 siRNA knockdown was fulfilled

under the same conditions described as above. In Table 3 knockdown conditions are listed in greater detailed.

Table 3 siRNA knockdown transfection solution preparation table

siGorab	siNonCoding
siRNA pre-dilution	
6 µl Gorab mRNA-targeting siRNA 18 µl RNase free water siRNA ready to use dilution	6 µl non-targeting siRNA 18 µl RNase free water
20 µl siRNA dilution 380 µl serum free α-MEM Transfection reagent ready to use dilution	20 µl siRNA dilution 380 µl serum free α-MEM
24 µl Interferin 379 µl serum free α-MEM	24 µl Interferin 379 µl serum free α-MEM

400 µl siRNA ready to use dilution was pipetted to the transfection reagent ready to use dilution and shake for 10 s, and subsequently incubated for 10 min at RT.
Medium from desired 6-Wells were exchanged with 1,8 ml antibiotic free, serum including α-MEM. After a 10 min incubation 400 µl of the transfection reagent was added dropwise into the wells. The procedure was repeated daily for three days.

2.24 Single cell mechanical stimulation by local membrane deformation of IDG-SW3 cells after siRNA knockdown

A Sutter Pipette Puller (Flaming/Brown, model P-87) was used to customize glass micropipettes from glass capillary tubes (1.5 mm outer diameter, King Precision Glass Inc.). The micropipette tip was placed approximately 10 nm above the IDG-SW3 membrane at a 45° angle from horizontal. Cell membrane deformation/disruption was induced by a FemtoJet microinjector N12 (Eppendorf Inc.) at a speed of 250 µm/s , resulting in a cell contact of 60 ms. In order to minimize the impairment of diffusion

processes, which were induced by the stimulation, the micropipette was left unmoved for the remainder of the recording.

2.25Intracellular calcium recording and analysis

Approximately 80 % confluent IDG-SW3 cells in a glass-bottom 35 mm dish were loaded with a ratiometric fluorescent calcium dye, Fura2-AM. 20 min incubation at room temperature followed by a single wash with physiologic solution. Final volume for mechanical stimulation of 1 ml physiologic solution was added. To obtain an imaging field of view of 220 µm x 168 µm a 40 x objective was used. Subsequently to 10 sec baseline calcium signal recording a single cell was mechanical stimulated. 170 sec of reaction was recorded subsequently with a sampling rate of 2 images per second (2 Hz) by a Nikon T2000 fluorescent inverting microscope. 340 and 380 nm were the alternating wavelengths, which were switched by an ultra-high-speed wavelength switching illumination system (Lambda DG-4, Quorum Technologies). ROI were defined manually and the fluorescent emission at 510 nm was calculated and exported using the imaging software Volocity (Volocity, Improvision).
Data was exported into an Excel spreadsheet, and for characterization a MATLAB algorithm was used, which has been described by Mikolajewicz et al.. As an (Ca^{2+}) outcome measure, a 340/380 ratio was equated. Amplitude (amp; magnitude of response), activation time ($t_{10\%-90\%}$; time between 10% and 90% of maximum response), and decay constant (τ_{decay}) of exponential decay region of deactivation phase of transient response, were the parameters, which were used for statistical analysis. Secondary responsiveness was calculated as the percentage of non-stimulated neighboring cells in the ROI in which (Ca^{2+}) changes were detected.

2.26Vesicle labeling, imaging and analysis

In order to investigate the role of Gorab in ATP mediated cell communication ATP filled vesicles in IDG-SW3 cells were visualized imaged and quantified. Therefore, cells were plated and treated with siRNA as previously described. Prior imaging cells were washed

once with PS, incubated with 10 mM quinacrine at RT for 15 min followed by another washing step. Imaging was executed with a Zeiss LSM 780 laser scanning confocal microscope. Quinacrine was excited at 458 nm using a diode laser. Emission signals were detected in the range of 490-570 nm. Imaging was performed using a Zeiss Plan-Apochromat 63x/1.40 oil immersion objective lens. Analysis was achieved using ImageJ (National Institutes of Health, USA).
Vesicular density was calculated by number of quinacrine positive puncta per cell area.

2.27Primary cilia staining

For the primary cilium staining, 4 - 5 glass cover slips (10 mm in diameter) were attached per 6-Well to the bottom of the plate before cell seeding, in order to multiply the staining combinations per Well. Visualizing the basal ring of the primary cilium and furthermore the elongation proteins of the cilium, two different antibodies were used (Table 4).

Table 4 Primary cilium antibody target scheme

Primary cilium target	Antibody
Primary cilium basis	Anti-γ-Tubulin (Sigma Aldrich, 4D11)
Primary cilium elongation proteins	Anti-α acetylated Tubulin (Sigma Aldrich, T7451)

Subsequent to the siRNA knockdown the cells were 3x washed with PBS (Dulbecco's DPBS, no calcium, no magnesium, Gibco, Carlsbad, California) and fixated with 4 % PFA for 10 min at RT. Fixation was followed again by 3x DPBS wash.
Washing was followed by cell permeabilization and protein blocking. 20 min incubation at RT with 0.1 % Triton in 4 % BSA solution was used for permeabilization and blocking. Subsequently, primary antibody incubation was conducted. For every tubulin staining Gorab was co-stained to visualize the primary cilium target and Gorab in every stain.
After an overnight incubation of the primary antibodies at 4°C cover slips were 3 times washed with DPBS and afterwards incubated for 1 h at RT with the secondary antibody in the given value (Table 5)

Table 5 Primary Cilium antibody dilution and combination table including the primary and secondary antibodies.

Primary Antibody	Primary Antibody	Secondary Antibodies
Anti-γ-Tubulin (mouse)	Anti-Gorab (rabbit)	Anti-mouse flour 488 Anti-rabbit flour 555
Anti-α acetylated Tubulin (mouse)	Anti-Gorab (rabbit)	Anti-mouse flour 488 Anti-rabbit flour 555

All antibodies were diluted 1:1000 in 4 % BSA

In addition the double stains, before inundation with fluoromount (DAPI Fluoromount-G, SouthernBiotech, Birmingham, Alabama), cells were treated with DAPI (Invitrogen, Oregon, USA) for nucleus visualization followed by a final washing procedure 3 times DPBS and 3 times *aqua distillata*.

The cilium length was evaluated using ImageJ and Excel.

3 Results

In the result and the following discussion section of this thesis the experiments are split in five different parts:

I – *In vivo* bone matrix adaption to mechanical loading in cortical bone

II – *In vivo* bone matrix and cellular adaption to mechanical loading in trabecular bone

III – Investigation of the lacunar-canalicular network in Gorab^{Prx1} and LC mice

IV - RNAseq studies to discover possible target gene dysregulation in mechanotransduction

V – *In vitro* approaches for mechanotransduction investigation in IDW-SW3 and MLO-Y4 cells.

Section I-II are exclusively dealing with adaptions to mechanical loading in mice tibiae. All conducted *in vivo* experiments were executed in 10 week old, female Gorab^{Prx1} mice and their littermate control counterpart. All mice underwent the two week mechanical loading program, otherwise it is explicitly mentioned.

In every experiment the left tibia was loaded and the right served as an internal non-loaded control. Consequently, most experiments compare the following four groups (Table 6). ANOVA investigated the effects of several characteristics.

- a = phenotype difference - non-loaded LC and non-loaded Gorab^{Prx1}
- b = loading difference – non-loaded LC and loaded LC
- c = phenotype*loading difference – loaded LC and loaded Gorab^{Prx1}

Table 6 Scheme for genotype, treatment and comparison groups.

LC		Gorab^{Prx1}	
homozygous cre negative		homozygous cre positive	
right tibia	left tibia	right tibia	left tibia
non-loaded	loaded	non-loaded	loaded

Within section I and II an astonishing loss of mechanoresponsiveness in Gorab^{Prx1} animals was detected. In order to explain this striking phenotype, we examined the

cellular histomorphometry and found a significant enhanced number of osteocytes per bone area in Gorab^{Prx1} trabecular bone, in both, non-loaded and loaded tibiae. I hypothesized an altered, either significantly less connected, or chaotic ordered lacunar-canalicular network. In both scenarios osteocytes would be unable to react to the mechanical load. Furthermore, I was interested in the differentiation status of the in number elevated osteocytes, found in the static histomorphometry and the impaired early osteoblast differentiation, previously found by our group[4].
I hypothesized an altered lacunar-canalicular system being responsible for the loss of mechanoresponsiveness, which was investigated in section III.

Section III shows the differences in the lacunar-canalicular network of the diaphyseal cortical bone in 12 week old female Gorab^{Prx1} and LC mice, uncoupled from loading. We chose 12 weeks of age because of the time-point of the tibial extraction after loading. Histology and dynamic histomorphometry should be in line with the developmental timepoint of the lacunar-canalicular evaluation.
The differentiation status was also investigated indirect by lacunar-shape characterization and RNAseq studies.
RNAseq studies in section IV were executed after a single load at 10 weeks. Despite the approach to set all experiment-end-timepoints to 12 weeks of age we decided to do these at 10 weeks of age, because the loading procedure for the 2 week analysis of bone formation starts at 10 weeks and therefore we wanted to examine the response to loading at the initial loading time point. The last section deals with the main mechanotransduction mechanisms known in osteocytes by day. Based on the RNAseq results we focused on pathways and mechanisms which were probably impaired due to changed mRNA expression patterns. For section V osteocyte like cell lines, IDG-SW3 and MLO-Y4 cells were used. IDG-SW3 cells were used for calcium flux, ATP vesicle and GAP-junction function investigations. MLO-Y4 were used for primary cilium analysis. Unfortunately the *in vitro* investigations did not give any proof of a cellular impairment due to the loss of Gorab.

3.1 Section I – *In vivo* bone matrix adaption to mechanical loading in cortical bone

3.1.1 Investigation of the diaphyseal cortical bone

Diaphyseal cortical bone was investigated using *in vivo* µCT and calcein based dynamic histomorphometry. For a consistent, comparable tibial volume the VOI was set individually from the midpoint of each tibia, which was in total 213 voxel slices (2237 µm) in the µCT. The same region was used for the ROI of the mineral apposition rate and bone formation rate, analyzed in PMMA embedded calcein double label analysis and the rhodamine based lacunar-canalicular network investigations in chapter 3.3.

3.1.1.1 In vivo 3D time lapse morphometry – diaphyseal midshaft

In vivo cyclic compressive mechanical loading with a deformation of 1200 με resulted in a clear anabolic response in LC mice. Gorab^{Prx1} mice showed no change in bone remodeling process.

Figure 15 represents the three dimensional *in vivo* time lapse morphometry of the cortical bone of LC and Gorab^{Prx1} mice tibiae. *In vivo* µCT scans were performed on day 0, 5, 10 and 15. The last scans were executed three days post the mechanical loading cycle. Yellow areas show quiescent bone, which was consistent during the two weeks. Blue areas represent bone formation and red areas bone resorption.

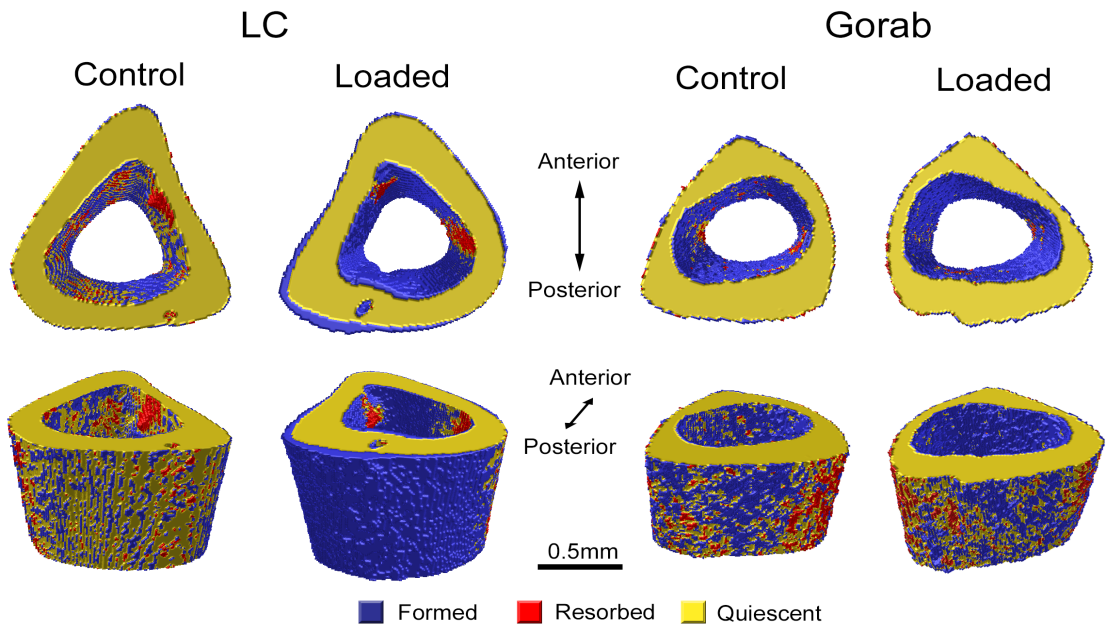

Figure 15 3D in vivo time-lapse morphometry showing areas of bone formation and resorption in a 15 day time frame of mechanical loading in diaphyseal cortical bone of Control (LC) mice and Gorab^{Prx1} (Gorab) mice. µCT image registration was executed on day 0, 5, 10 and 15 of the loading protocol.

The tibial midshaft in Gorab^{Prx1} mice exhibits an atypical geometry when comparing the VOI of the middle diaphysis . Anterior and lateral sites of the cortex demonstrate a thinning in diameter. The VOI's axial plain exhibits a more triangular geometry compared to the LC midshaft. The tibial ridge appears to be not as expressed as in LC mice. Nevertheless, the medial marrow cavity is of similar diameter, but more oval than the LC triangular endosteal site.

LC non-loaded tibial midshaft shows a balanced pattern of bone formation and resorption sites on the mostly quiescent endosteal and periosteal side. Bone formation sites documented in non-loaded LC midshaft shows a strain oriented pattern.

As stated above, LC mice exhibit a significant change in bone formation after loading. The LC periosteum demonstrates universal bone formation due to mechanical loading. The main bone formation takes place in the posterior site of the midshaft. LC endosteum also exhibits a clear increase of bone formation after loading, which in volume is not as high as periosteal, but is still a comprehensive layer of freshly formed bone. Presumable comparable to the non-loaded LC mouse, two bone resorption sites in the anterior endosteal area are visible.

Comparing Gorab^{Prx1} mice to the responding LC mice, it is quite clear, that responses to mechanical loading are rarely visible in the time lapse for tibial cortical bone. Comparing the non-loaded LC scans to the Gorab^{Prx1} scans indeed a higher turnover is visible.
Furthermore, the LC non-loaded patterns of bone remodeling and the LC loaded formation pattern appear to align strain directed.
Gorab^{Prx1} non-loaded and loaded periosteal surface exhibit equal, non-directional formation and resorption patterns. Still, it appears that the resorption is dominantly placed on the outer posterior sites. Interestingly the endosteum seems to exhibit slightly more bone formation patterns, but these changes are not significant. Only both lateral areas show active resorption sites.

Table 7 shows the cortical bone parameters, determined by *in vivo* microCT at day 0, 5, 10 and 15, resulting from the same scans as the time lapse overlay.
Cortical bone outcome parameters are as recommended (Guidelines for assessment of bone microstructure in rodents using micro-computed tomography.):

- Principal moments of inertia
    - Maximal moment of inertia (Imax) [mm^4],
    - Minimal moment of inertia (Imin) [mm^4],
- Cortical bone area (Ct.Ar) [mm^2]
  = Cortical volume / (number of slices*slice thickness),
- Total cross sectional area inside the periosteal envelope (Tt.Ar) [mm^2],
- Cortical area fraction (Ct.Ar/Tt.Ar) [mm^2/mm^2],
- Cortical thickness (Ct.Th) [µm] and
- Cortical volumetric tissue mineral density (Ct.vTMD) [mg HA/cm^3].

Ttest and ANOVA were exclusively calculated for the scans of day 15.
In general, results documented at day 0 represent the differences between the genotypes at the age of 10 weeks without any treatment.
Moments of inertia are biomechanical parameters for bending in tibial bone volume, which in turn are functions of the area moment of inertia about the axis of bending for the

particular cross-section of bone. Respectively **Imax** and **Imin** represent the directions of the greatest and least bending resistance (rigidity).
Imax and Imin show lower values for Gorab^{Prx1} mice, unrelated to loading. Moment of inertia parameters are calculated based on the geometry of the diaphyseal ROI, around the tibia's midpoint. Also, **Ct.Ar**, **Tt.Ar** and **Ct.Th** show lower values for Gorab^{Prx1} animals, representing a smaller bone in the region of interest. **Ct.vTMD** demonstrates no severe differences between the genotypes.

Progressing in the loading protocol bone parameters in the LC show the already described bone formation process in a significant increase of Ct.Ar, Tt.Ar and Ct.Th. Gorab^{Prx1} mice show, the steady bone formation not related to loading by increasing their Ct.Th in approximal 0,01- 0,02 µm.
TMD increased in loaded LC mice around 4 %, resulting in a more compact bone. Both Gorab^{Prx1} ROIs show a non-significant increase over time, aiming to align with the TMD of LC non-loaded bone with a difference of about 2 % at day 15.
The sum of Imin and Imax, representing the tubular structure's torsional rigidity, which is proportional to the polar moment of inertia (J). Therefore, the torsional rigidity in the diaphyseal midshaft is lower in Gorab^{Prx1} diaphyseal cortical bone in general, but the robustness of the bone in this ROI shows similar values around 0.8. It must to be kept in mind that these values are calculated for this specific ROI in mm^2/mm^2, not including the whole bone geometry and strain distribution.
The cortical area increasing in proportion to the total area gives the bone a higher robustness. Comparing LC bone to Gorab^{Prx1} bone, the robustness in LC is in general higher, but neither LC nor Gorab^{Prx1} diaphyseal tibiae exhibit significant increases due to loading. LC robustness (Ct.Ar./Tt.Ar) increases 0.05 from 0.79 to 0.84 mm^4 and in Gorab^{Prx1} diaphyseal cortical bone from 0.82 to 0.85 mm^4. Normally the bones ellipticity can be calculated by I_y/I_x. I_y and I_x are transformed by adjusting the coordinate system. Z-axis is positioned to the midpoint of the cortical ring. Yx-plane is defined by the position of the fibula with respect to the tibia. Therefore, the less elliptic shape, observed in the 3D *in vivo* time lapse morphometry in Gorab^{Prx1} is reproduced by 1.17 (Σ Imax/Imin

Gorab^{Prx1}) to 1.2 (Σ Imax/Imin LC). 1.17 is closer to 1, which would represent a perfect circle.

When summarizing these results, it was observed that in Gorab^{Prx1} animals a general higher bone turnover in the less rigid bone without any significant response to mechanical loading. Seemingly, the mutant's organism tries to catch up the developmental deficiency. In LC tibial midshaft, a straight bone formation response was detected due to mechanical loading.

Table 7 Cortical (Ct) bone parameters of the tibial midshaft, determined by in vivo microCT at days 0, 5, 10 and 15 in mice exposed to axial compression of 1200 με (left tibia dynamically loaded, right tibia non-loaded control) (mean ± SD); ANOVA for day 15: indicates an effect of (a) genotype, (b) loading, (c) genotype and loading, $p < 0.05$. Asterisk indicates a significant difference between loaded and control tibiae for each genotype (Paired t-test; $p < 0.05$).

	LC		Gorab^{Prx1}	
Outcome	Non-Loaded	Loaded	Non-Loaded	Loaded
Day 0	n = 9	n = 9	n = 9	n = 9
Imax (mm^4)	0.06 ± 0.01	0.06 ± 0.01	0.04 ± 0.01	0.03 ± 0.01
Imin (mm^4)	0.05 ± 0.01	0.05 ± 0.01	0.03 ± 0.01	0.03 ± 0.01
Ct.Ar (mm^2)	0.55 ± 0.04	0.54 ± 0.04	0.41 ± 0.08	0.39 ± 0.07
Tt.Ar (mm^2)	0.68 ± 0.06	0.69 ± 0.05	0.49 ± 0.08	0.48 ± 0.08
Ct.Ar./Tt.Ar (mm^2/mm^2)	0.81 ± 0.03	0.79 ± 0.01	0.83 ± 0.06	0.82 ± 0.07
Ct.Th (µm)	0.20 ± 0.01	0.19 ± 0.01	0.17 ± 0.04	0.16 ± 0.04
TMD (mg HA/cm^3)	1292.92 ± 13.23	1258.23 ± 21.55	1240.83 ± 53.73	1227.94 ± 58.31
Day 5	n = 9	n = 9	n = 9	n = 9
Imax (mm^4)	0.06 ± 0.01	0.06 ± 0.01	0.04 ± 0.01	0.04 ± 0.02
Imin (mm^4)	0.04 ± 0.01	0.05 ± 0.01	0.03 ± 0.01	0.03 ± 0.01
Ct.Ar (mm^2)	0.55 ± 0.04	0.55 ± 0.04	0.42 ± 0.06	0.43 ± 0.09
Tt.Ar (mm^2)	0.67 ± 0.05	0.69 ± 0.05	0.50 ± 0.07	0.51 ± 0.12
Ct.Ar./Tt.Ar (mm^2/mm^2)	0.82 ± 0.04	0.80 ± 0.01	0.84 ± 0.06	0.84 ± 0.05
Ct.Th (µm)	0.20 ± 0.01	0.20 ± 0.01	0.17 ± 0.04	0.17 ± 0.03
TMD (mg HA/cm^3)	1278.50 ± 28.06	1274.66 ± 20.27	1252.59 ± 32.49	1237.25 ± 22.35
Day 10	n = 9	n = 9	n = 9	n = 9

Imax (mm^4)	0.06 ± 0.01	0.06 ± 0.01	0.03 ± 0.01	0.03 ± 0.01
Imin (mm^4)	0.04 ± 0.01	0.05 ± 0.01	0.03 ± 0.01	0.03 ± 0.01
Ct.Ar (mm^2)	0.55 ± 0.04	0.58 ± 0.05	0.43 ± 0.08	0.43 ± 0.07
Tt.Ar (mm^2)	0.65 ± 0.08	0.71 ± 0.07	0.51 ± 0.08	0.50 ± 0.08
Ct.Ar./Tt.Ar (mm^2/mm^2)	0.85 ± 0.05	0.82 ± 0.04	0.84 ± 0.06	0.85 ± 0.04
Ct.Th (µm)	0.20 ± 0.02	0.21 ± 0.01	0.18 ± 0.04	0.18 ± 0.03
TMD (mg HA/cm^3)	1294.49 ± 22.74	1293.88 ± 12.18	1359.05 ± 43.95	1243.27 ± 16.29
Day 15	n = 9	n = 9	n = 9	n = 9
Imax (mm^4)[a]	0.06 ± 0.01	0.07 ± 0.01*	0.04 ± 0.01	0.04 ± 0.01
Imin (mm^4)[a]	0.04 ± 0.01	0.05 ± 0.01	0.03 ± 0.01	0.03 ± 0.01
Ct.Ar (mm^2)[a, b, c]	0.55 ± 0.04	0.61 ± 0.03*	0.44 ± 0.06	0.44 ± 0.06
Tt.Ar (mm^2)[a, b, c]	0.65 ± 0.07	0.73 ± 0.06*	0.52 ± 0.06	0.52 ± 0.08
Ct.Ar./Tt.Ar (mm^2/mm^2)	0.85 ± 0.04	0.84 ± 0.04	0.85 ± 0.05	0.85 ± 0.04
Ct.Th (µm) [a, b ,c]	0.20 ± 0.02	0.23 ± 0.01*	0.18 ± 0.03	0.18 ± 0.02
TMD (mg HA/cm3) [a, c]	1293.87 ± 18.58	1310.23 ± 17.98	1268.27 ± 29.90	1254.02 19.56

3.1.1.2 In vivo histomorphometry of mineral apposition rate and bone formation rate – diaphyseal midshaft

To determine the mineral apposition rate (MAR) and bone formation rate (BFR), $Gorab^{Prx1}$ and LC mice received two calcein injections. The first injection was administered on day 3 of the mechanical loading protocol, with the second seven days later, on day 10. This resulted in a single or double labeled surface in the endosteum and periosteum at bone formation sites.

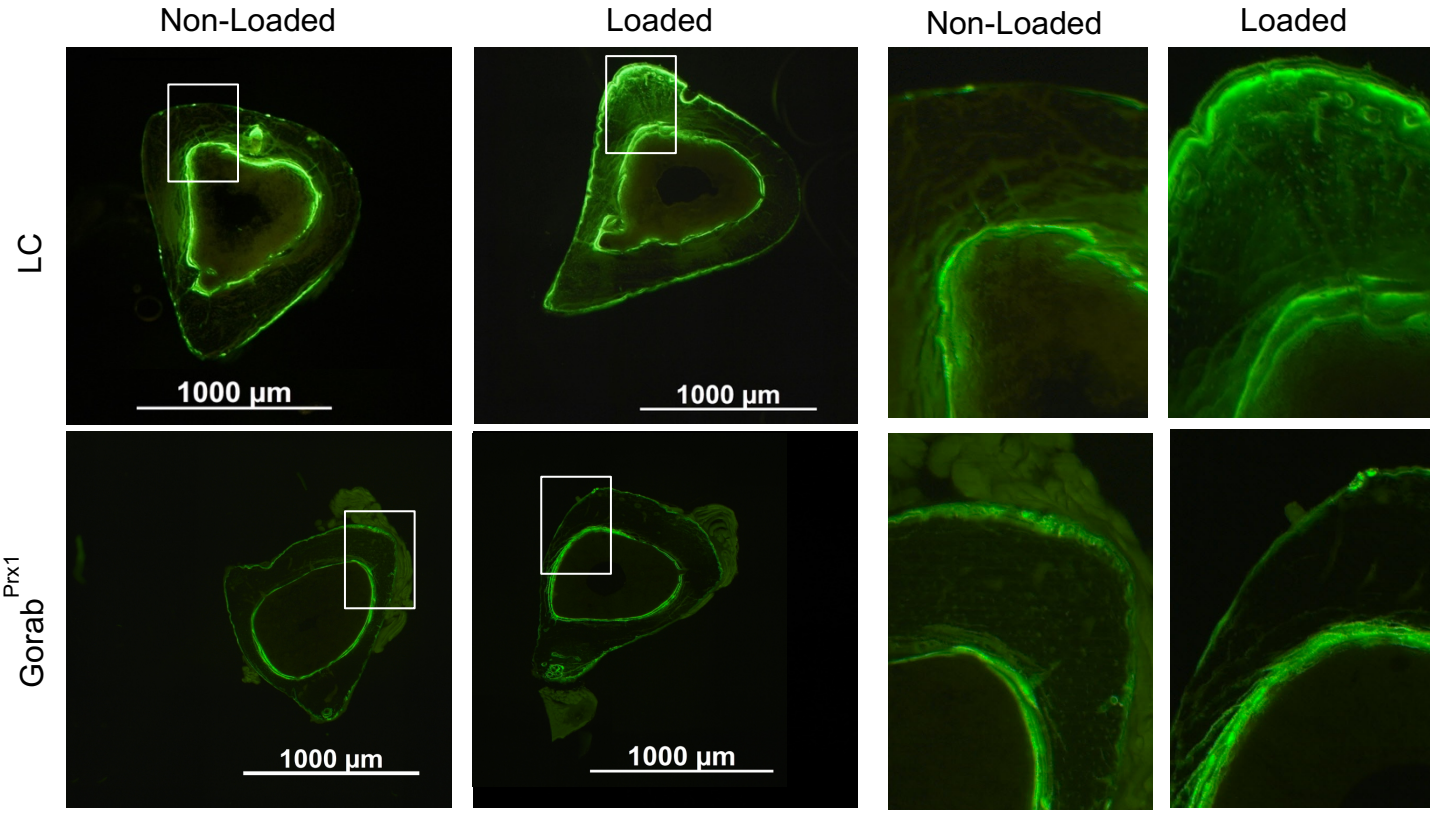

Figure 16 Calcein double labeled tibial midshaft of 12 week old female LC and Gorab^{Prx1} animals. 0,1 ml Calcein injected at day 3 and 10 of the 14 day mechanical loading protocol, pictures taken at a Leica DMRB fluorescence microscope at a 100 x magnification, filter for the wavelength spectrum of 488 λ. Tibiae were dissected at day 15 of mice exposed to axial compression of 1200 με (left tibia dynamically loaded, right tibia non-loaded control)

Figure 16 represents calcein labeled LC and Gorab^{Prx1} tibial midshaft bone sections. Fluorescent dye pattern show a strong and consistent endocortical signal over the surface in non-loaded and loaded LC animals. The periosteal midshaft in loaded LC tibiae exhibits the highest signal. Almost the complete edge shows at least a single labeled surface. The only exception is the medial side of the loaded (left) periosteum, showing short segments without any formation. These can be compared to the regions of bone resorption, seen in the 3D *in vivo* time lapse overlay model. Non-loaded LC shows only isolated regions of single label spanning at the edge of the periosteum. The gap between the first and second label in double labeled surface areas is the most widened in the loaded LC bone. **MAR** was increased due to loading in LC mice from 0.88 to 2.56 µm/d periosteal and from 1.10 to 2.41 µm/d endosteal. Along with a periosteal **BFR** increase from 0.18 to 1.49 µm/d and endosteal 0.48 up to 1.64 µm/d the massive response in bone formation is portrayed.

Gorab^{Prx1} mice show in non-loaded and loaded similar signal patterns in single and double labeled surfaces, mineral apposition rates and bone formation rates. In comparison to LC loaded bone the signals are weaker, but steady in the endocortical and the periosteal surface coverage. Double labeled surface is double the amount on both evaluated surfaces compared to LC non-loaded mice. Still, periosteal MAR and BFR show similar values to LC mice. The only difference between non-loaded LC and both Gorab^{Prx1} groups is the doubled value of endocortical BFR. The Ec. BFR/BS in non-loaded and loaded Gorab^{Prx1} mice ranges in the middle of LC non-loaded and loaded bone. All calcein based dynamic histomorphometry results of the tibial midshaft are presented in Table 8, additionally all parameters for day 15 are shown in bar diagrams in Figure 17.

Table 8 Cortical (Ct) bone histomorphometry of mineral apposition rate (MAR) and bone formation rate normalized to bone surface (BFR/BS) of the tibial midshaft, endocortical and periosteal, determined by double labeled fluorochrome (calcein) labeling, calcein injected at day 3 and 10 in mice exposed to axial compression of 1200 με (left tibia dynamically loaded, right tibia non-loaded control) (mean ± SD); ANOVA for day 15: indicates a periosteal effect of (a) genotype, (b) loading, (c) genotype and loading and endosteal effects of (d) genotype, (e) loading, (f) genotype and loading, $p < 0.05$. Asterisk indicates a significant difference between loaded and control tibiae for each genotype (Paired t-test; $p < 0.05$).

	LC		Gorab^{Prx1}	
Outcome	Non-Loaded	Loaded	Non-Loaded	Loaded
Day 15	n = 9	n = 9	n = 8	n = 8
Ps sLS/BS (%) [c]	24.54 ± 9.61	44.58 ± 15.84*	40.95 ± 11.72	34.68 ± 18.84
Ps dLS/BS (%) [a, b, c]	5.74 ± 7.18	39.07 ± 16.14 *	9.10 ± 8.06	12.37 ± 10.40
Ps MS/BS (%) [a, b, c]	18.01 ± 9.51	61.35 ± 14.22 *	29.57 ± 10.36	29.71 ± 11.95
Ps. MAR (µm/d) [a, b, c]	0.88 ± 0.41	2.56 ± 1.00 *	0.72 ± 0.21	0.72 ± 0.13
Ps. BFR/BS (µm/d) [a, b, c]	0.18 ± 0.15	1.49 ± 0.44 *	0.22 ± 0.11	0.22 ± 0.11
Ec sLS/BS (%)	28.62 ± 24.30	24.83 ± 14.33	21.14 ± 15.56	20.74 ± 18.00
Ec dLS/BS (%) [d, e]	28.46 ± 20.73	56.85 ± 14.90 *	66.32 ± 21.00	78.30 ± 16.36 *
Ec MS/BS (%) [d, e, f]	42.77 ± 14.92	69.27 ± 9.99 *	76.89 ± 13.62	88.67 ± 8.11 *
Ec. MAR (µm/d) [d, e, f]	1.10 ± 0.26	2.41 ± 0.53 *	1.26 ± 0.35	1.19 ± 0.31
Ec. BFR/BS (µm/d) [e, f]	0.48 ± 0.23	1.64 ± 0.28 *	0.97 ± 0.34	1.06 ± 0.28

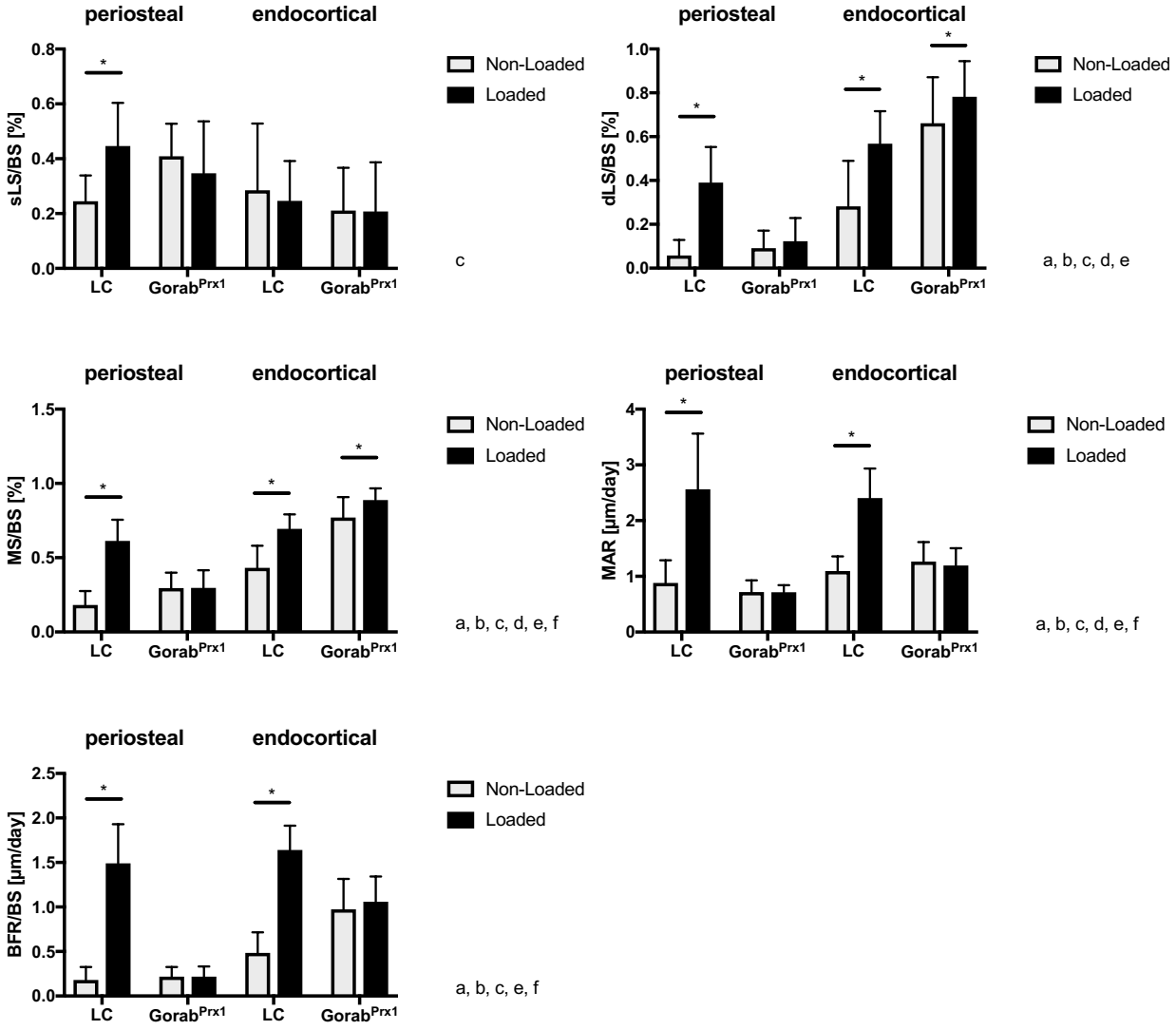

Figure 17 Cortical (Ct) bone histomorphometry of single labeled surface per bone surface (sLS/BS, double labeled surface per bone surface (dLS/BS), mineralized surface per bone surface (MS/BS), mineral apposition rate (MAR) and bone formation rate normalized to bone surface (BFR/BS) of the tibial midshaft, endocortical and periosteal, determined by double labeled fluorochrome (Calcein) labeling, Calcein injected at day 3 and 10 in mice exposed to axial compression of 1200 με (left tibia dynamically loaded, right tibia non-loaded control) (mean ± SD); ANOVA for day 15: indicates a periosteal effect of (a) genotype, (b) loading, (c) genotype and loading and endosteal effects of (d) genotype, (e) loading, (f) genotype and loading, $p < 0.05$. Asterisk indicates a significant difference between loaded and control tibiae for each genotype (Paired t-test; $p < 0.05$).

The calcein based histomorphometry consistently represent the via *in vivo* µCT collected data, uncovering the loss of mechanoresponsiveness in Gorab^{Prx1} diaphyseal cortical bone.

3.1.2 Metaphyseal cortical bone

Metaphyseal cortical bone has been analyzed by *in vivo* µCT scanning. Similar to the diaphyseal area the VOI has been adjusted during every scan for each mouse. The selected VOI starts at the caudal end of the growth plate, which due to lower mineralization is visible in the X-ray pre-scan. ROI extends 432 slices (4536 µm) along the bone's long axis. This cortical VOI was analyzed as a by-product of the trabecular metaphyseal bone of the tibia. Therefore, the VOI are identical. Nonetheless, it is advantageous investigating an additional VOI to cover two different volumes of interest in cortical bone exposed to different mechanical strains and demands.

3.1.2.1 In vivo 3D time lapse morphometry – metaphysis

Metaphyseal cortical bone parameters differ from the diaphyseal values based on the bones natural geometry. The head of the tibia is naturally thicker than the midshaft, because of the strain distribution properties of the bone, housing of the trabecular bone and the red bone marrow.
The initial moments of inertia **Imax** and **Imin** at day 0, without any loading treatment show with 0.36 mm^4 and 0.25 mm^4 in LC non-loaded and 0.19 mm^4 and 0.08 mm^4 in $Gorab^{Prx1}$ non-loaded tibiae higher values compared to the diaphyseal midshaft. Therefore, the rigidity, represented by the sum of both, the **polar moment of inertia** (J) is higher in this area (J = 0.61 mm^4 LC non-loaded and J = 0.27 $Gorab^{Prx1}$ non-loaded). This emphasizes the extreme low rigidity of the metaphyseal cortical bone in mutants. The robustness (**Ct.Ar./Tt.Ar**) is lower compared to the midshaft in both groups. Keeping in mind that the cortical bone is analyzed separately from the trabecular bone relativizes the reduced robustness. The geometry of the metaphyseal cortical bone is in LC animals with a value of 1.44 relative roundish, compared to the $Gorab^{Prx1}$ bone, which is quite deformed with a value of 2.38.

During the treatment all cortical bone parameters in LC mice for the metaphyseal area except TMD increase significantly. This indicates a universal bone formation response in

cortical bone due to mechanical loading in LC mice. Gorab^{Prx1} mice however do not show any response to loading in Imax, Imin, Ct.Ar, Tt.Ar, or TMD. Table 9 shows all values collected by *in vivo* µCT from day 0, 5, 10 and 15.

Table 9 Cortical (Ct) bone parameters of the tibial, metaphyseal area , determined by in vivo microCT at days 0, 5, 10 and 15 in mice exposed to axial compression of 1200 με (left tibia dynamically loaded, right tibia non-loaded control) (mean ± SD); ANOVA for day 15: indicates an effect of (a) genotype, (b) loading, (c) genotype and loading, $p < 0.05$. Asterisk indicates a significant difference between loaded and control tibiae for each genotype (Paired t-test; $p < 0.05$).

	LC		Gorab^{Prx1}	
Outcome	Non-Loaded	Loaded	Non-Loaded	Loaded
Day 0	n = 9	n = 9	n = 9	n = 9
Imax (mm^4)	0.36 ± 0.09	0.38 ± 0.07	0.19 ± 0.08	0.25 ± 0.04
Imin (mm^4)	0.25 ± 0.05	0.26 ± 0.05	0.08 ± 0.03	0.08 ±0.03
Ct.Ar (mm^2)	0.88 ± 0.11	0.9 ± 0.09	0.34 ± 0.1	0.36 ±0.08
Tt.Ar (mm^2)	1.37 ± 0.14	1.41 ± 0.12	0.9 ± 0.17	1.25 ± 0.71
Ct.Ar./Tt.Ar (mm^2/mm^2)	0.64 ± 0.03	0.63 ± 0.05	0.37 ± 0.06	0.33 ± 0.1
Ct.Th (µm)	0.11 ± 0.01	0.11 ± 0.02	0.05 ± 0.01	0.05 ± 0.01
TMD (mg HA/cm^3)	1107.63 ± 18.31	1075 ± 20.26	1056.76 ± 20.94	1052.34 ± 17.39
Day 5	n = 9	n = 9	n = 9	n = 9
Imax (mm^4)	0.36 ± 0.1	0.4 ± 0.09	0.2 ±0.08	0.23 ± 0.08
Imin (mm^4)	0.26 ± 0.05	0.29 ± 0.06	0.08 ± 0.03	0.09 ±0.05
Ct.Ar (mm^2)	0.88 ± 0.09	0.97 ± 0.1	0.36 ± 0.1	0.4 ± 0.12
Tt.Ar (mm^2)	1.36 ± 0.19	1.43 ± 0.16	0.9 ± 0.17	1.01 ± 0.28
Ct.Ar./Tt.Ar (mm^2/mm^2)	0.66 ± 0.03	0.68 ± 0.04	0.4 ± 0.05	0.38 ± 0.06
Ct.Th (µm)	0.17 ± 0.01	0.12 ± 0.015	0.055 ± 0.01	0.06 ± 0.01
TMD (mg HA/cm^3)	1113.27 ± 19.55	1093.71 ± 20.2	1059.38 ± 23.63	1054.61 ± 15.14
Day 10	n = 9	n = 9	n = 9	n = 9
Imax (mm^4)	0.34 ± 0.05	0.49 ± 0.09	0.22 ± 0.1	0.25 ± 0.08
Imin (mm^4)	0.26 ± 0.04	0.33 ± 0.05	0.09 ± 0.03	0.1 ± 0.05
Ct.Ar (mm^2)	0.89 ± 0.06	1.13 ± 0.08	0.39 ± 0.11	0.43 ± 0.12
Tt.Ar (mm^2)	1.34 ± 0.1	1.6 ± 0.1	0.94 ± 0.18	1.01 ± 0.21
Ct.Ar./Tt.Ar (mm^2/mm^2)	0.67 ± 0.02	0.7 ± 0.03	0.41 ± 0.07	0.42 ± 0.06

Ct.Th (µm)	0.12 ± 0.01	0.14 ± 0.01	0.06 ± 0.1	0.06 ± 0.01
TMD (mg HA/cm^3)	1127.5 ± 15.76	1104.88 ± 19.5	1069.35 ± 25.15	1058.64 ± 18.81
Day 15	n = 9	n = 9	n = 9	n = 9
Imax (mm^4)$^{a, b, c}$	0.38 ± 0.08	0.52 ± 0.08*	0.24 ± 0.1	0.28 ± 0.11
Imin (mm^4)$^{a, b, c}$	0.27 ± 0.05	0.36 ± 0.06*	0.1 ± 0.04	0.11 ± 0.06
Ct.Ar (mm^2)$^{a, b, c}$	0.95 ± 0.07	1.19 ± 0.07*	0.44 ± 0.11	0.46 ± 0.14
Tt.Ar (mm^2)$^{a, b, c}$	1.4 ± 0.13	1.68 ± 0.11*	0.96 ± 0.14	1.05 ± 0.21
Ct.Ar./Tt.Ar (mm^2/mm^2)^{a}	0.68 ± 0.02	0.71 ± 0.04*	0.45 ± 0.07	0.43 ± 0.054
Ct.Th (µm)$^{a, b, c}$	0.13 ± 0.01	0.14 ± 0.02*	0.06 ± 0.01	0.06 ± 0.01
TMD (mg HA/cm^3)$^{a, b}$	1131.49 ± 17.84	1123.50 ± 23.61	1077.26 ± 17.00	1063.85 ± 13.04*

Summarizing the additional cortical bone VOI in the distal metaphyseal area, a loss of mechanoresponsiveness is observed, comparable to the diaphyseal cortical bone.

3.2 Section II – *In vivo* bone matrix adaption to mechanical loading in trabecular bone

After characterizing the bone formation response in cortical bone, the trabecular bone formation response in LC and Gorab^{Prx1} tibiae was also analyzed. For this, besides dynamic in vivo µCT and calcein based dynamic histmorphometry, static histomorphometry of the cellular compartments and the bone architecture were executed.

3.2.1 Dynamic Histomorphometry metaphyseal trabecular bone

VOI is identical to the one chosen for the metaphyseal cortical bone. Both analyses were performed on the same scan.

3.2.1.1 In vivo 3D time lapse morphometry – metaphyseal trabecular bone

Due to critical differences in trabecular bone morphology and function compared to cortical bone, different parameters are needed to describe the dynamic histomorphometry in this section. Therefore, the evaluation of metaphyseal trabecular bone does not show the initial moments of inertia, based on the sponge like morphometry throughout the trabecular bone network. The following parameters were chosen, based on official recommendations[244]:

- Trabecular bone volume per total volume (Tb.BV/TV) [mm^3/mm^3],
- Trabecular thickness (Tb.Th) [mm],
- Trabecular number (Tb.N) [1/mm],
- Trabecular separation (Tb.Sp) [mm] and
- Trabecular volumetric tissue mineral density (Tb.vTMD) [mg HA/cm^3].

Bone volume over total volume (BV/TV) shows pre-treatment, based on the phenotype differences significant lower values in Gorab^{Prx1} mice with 50% less BV/TV of 0.05 mm^3/mm^3 compared to 0.1 mm^3/mm^3 in LC mice. After completing the mechanical loading protocol LC mice showed an increase of 0.06 mm^3/mm^3, whereas Gorab^{Prx1} mice showed

no increase in BV/TV. Surprisingly, BV/TV in non-loaded bone increased from 0.1 to 0.13 mm^3/mm^3 in LC during the mechanical loading protocol before returning to 0.09 mm^3/mm^3.
Trabecular thickness (Tb.Th) did increase during the loading protocol in $Gorab^{Prx1}$ mice slightly, but the increase was also similar in LC mice with an increase of 0.01 mm reaching 0.06 mm.
As a consequence of a reduction in **trabecular number**, **trabecular separation** increased in both groups.
Tb.Th in LC increased with 10 µm up to 0.06 mm, whereas $Gorab^{Prx1}$ mice showed the same increase in Tb.Th reaching 0.05 mm due to loading. Reminding that the trabecular bone is a three dimensional environment, the increase of 0.01 mm in Tb.Th induces the massive increase in BV/TV, based on the proportion and in combination to the reduction of **Tb.N**, which takes place in both compartments, the increase from 0.05 to 0.06 mm weights more than an increase from 0.04 - 0.05 mm.
The **total mineral density** shows in $Gorab^{Prx1}$ mice a higher increase in the trabecular bone compartment in general. Pre-loading and after two weeks of mechanical stimulation mutant trabecular bone shows quite constant 80 $mgHA/cm^3$ higher values. Table 10 summarizes the dynamic trabecular bone parameters collected via *in vivo* µCT, furthermore Figure 18 showing BV/VT, Tb.N and Tr.Th.

Table 10 Trabecular (Tb) bone parameters of the tibial, metaphyseal area , determined by in vivo microCT at days 0, 5, 10 and 15 in mice exposed to axial compression of 1200 με (left tibia dynamically loaded, right tibia non-loaded control) (mean ± SD); ANOVA for day 15: indicates an effect of (a) genotype, (b) loading, (c) genotype and loading, $p < 0.05$. Asterisk indicates a significant difference between loaded and control tibiae for each genotype (Paired t-test; $p < 0.05$).

	LC		$Gorab^{Prx1}$	
Outcome	Non-Loaded	Loaded	Non-Loaded	Loaded
Day 0	n = 9	n = 9	n = 9	n = 9
BV/TV (mm^3/mm^3)	0.10 ± 0.04	0.10 ± 0.03	0.05 ± 0.02	0.05 ± 0.02
Tb.Th (mm)	0.05 ± 0.01	0.05 ± 0.00	0.04 ± 0.00	0.04 ± 0.01
Tb.Sp (mm)	0.24 ± 0.026	0.24 ± 0.03	0.27 ± 0.04	0.28 ± 0.04
Tb.N (1/mm)	4.31 ± 0.48	4.20 ± 0.47	3.70 ± 0.57	3.60 ± 0.52
TMD (mgHA/ccm)	801.91 ± 31.43	790.91 ± 20.73	874.29 ± 24.17	869.56 ± 32.07
Day 5	n = 9	n = 9	n = 9	n = 9
BV/TV (mm^3/mm^3)	0.13 ± 0.04	0.14 ± 0.06	0.05 ± 0.02	0.05 ± 0.02

Tb.Th (mm)	0.05 ± 0.01	0.06 ± 0.01	0.46 ± 0.00	0.46 ± 0.00
Tb.Sp (mm)	0.24 ± 0.02	0.25 ± 0.03	0.28 ± 0.04	0.29 ± 0.04
Tb.N (1/mm)	4.26 ± 0.44	4.11 ± 0.60	3.63 ± 0.55	3.48 ± 0.53
TMD (mgHA/ccm)	822.22 ± 30.29	813.82 ± 23.56	882.68 ± 28.06	870.30 ± 39.20
Day 10	n = 9	n = 9	n = 9	n = 9
BV/TV (mm^3/mm^3)	0.12 ± 0.04	0.15 ± 0.06	0.05 ± 0.013	0.04 ± 0.013
Tb.Th (mm)	0.05 ± 0.01	0.06 ± 0.01	0.05 ± 0.00	0.05 ± 0.01
Tb.Sp (mm)	0.26 ± 0.03	0.27 ± 0.03	0.29 ± 0.04	0.3 ± 0.05
Tb.N (1/mm)	4.00 ± 0.49	3.9 ± 0.48	3.49 ± 0.48	3.33 ± 0.47
TMD (mgHA/ccm)	823.33 ± 32.21	828.98 ± 26.34	896.7 ± 25.75	900.98 ± 31.36
Day 15	n = 9	n = 9	n = 9	n = 9
BV/TV (mm^3/mm^3) [a, b ,c]	0.09 ± 0.03	0.16 ± 0.06*	0.04 ± 0.01	0.05 ± 0.01
Tb.Th (mm) [a, b ,c]	0.05 ± 0.00	0.06 ± 0.01*	0.05 ± 0.00	0.05 ± 0.01
Tb.Sp (mm)	0.28 ± 0.03	0.28 ± 0.04	0.31 ± 0.06	0.31 ± 0.53
Tb.N (1/mm) [a, c]	3.70 ± 0.40	3.86 ± 0.56	3.21 ± 0.53	3.21 ± 0.49
TMD (mgHA/ccm) [a, b]	812.57 ± 21.54	833.54 ± 30.53*	904.72 ± 23.84	908.0 21.93

Trabecular bone also shows an anabolic response in LC tibiae after mechanical stimulation, similar to the already shown bone formation response in cortical bone. Gorab^{Prx1} animals again show no significant response to loading, reinforcing the loss of mechanoresponsiveness throughout the whole tibia. Only TMD shows higher values in mutant trabecular bone, perhaps indicating the cortical bone examined catching up based on the developmental delay.

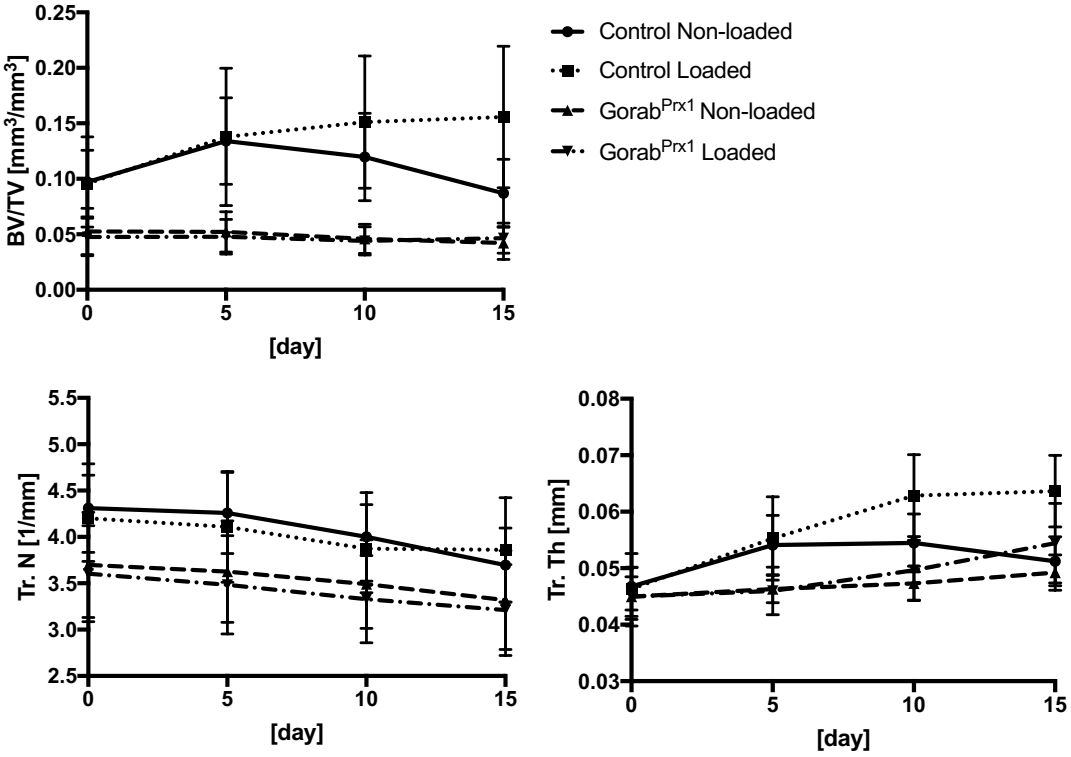

Figure 18 BV/TV, Tb.N and Tb.Th in trabecular (Tb) bone of the tibial, metaphyseal area, determined by in vivo microCT at days 0, 5, 10 and 15 in mice exposed to axial compression of 1200 με (left tibia dynamically loaded, right tibia non-loaded control) (mean ± SD).

3.2.1.2 In vivo histomorphometry of mineral apposition rate and bone formation rate – metaphyseal trabecular bone

Trabecular mineral apposition rate (Tb.MAR) and bone formation rate (Tb.BFR) were measured in the same Gorab^{Prx1} and LC bones as the cortical MAR and BFR were measured. After two injections of calcein with a seven day gap a single or double labeled surface was examined regions of bone formation. To examine the trabecular bone the

metaphyseal secondary spongiosa was prepared in axial sections. As recommended, the following trabecular bone parameters were measured:

- Trabecular single labeled surface per bone surface (Tb. sLS/BS) [%],
- Trabecular double labeled surface per bone surface (Tb. dLS/BS) [%],
- Trabecular mineralized surface per bone surface (Tb. MS/BS) [%],
- Trabecular mineral apposition rate (Tb. MAR) [µm/d] and
- Trabecular bone formation rate (Tb.BFR) [μm^2/d].

In Table 11 all data of the calcein based histomorphometry were summarized and in Figure 19 data are shown in bar diagrams.

Tb.sLS/BS showed no significant differences within all comparisons. LC mice showed no changes regarding mechanical loading similar to Gorab^{Prx1} mice, which also did not show significant changes in the non-loaded and loaded limb. Furthermore, no significant changes are measured between LC and Gorab^{Prx1} mice.

Tb.dLS/BS in LC mice exhibited 7.55 ± 5.04 % double labeled surface per bone surface in the non-loaded limb, and after loading the trabecular bone exhibited twice the amount of double labeled surface of 15.86 ± 4.87 %. In Gorab^{Prx1} mice a similar effect was evident via Anova, but with only an increase from 4.46 ± 2.05 to 6.25 ± 2.68 % no significance was given.

Tb.MS/BS also showed a significant increase after loading in LC mice with an increase of 7.78 %. Gorab^{Prx1} again demonstrated a tendency for an increased mineralized surface after loading, but 1.48 % increase to 7.52 % did not provide significant results within the paired ttest. Anova also indicates an effect between LC and Gorab^{Prx1} mice and also for loading.

Tb.MAR shows no significances between the loaded and non-loaded tibiae, neither in LC, nor in Gorab^{Prx1} mice. Anova revealed an effect between the genotypes.

Anova of **Tb. BFR** shows effects for genotype, loading and their combination, but only Tb.BFR differences of loaded and non-loaded LC tibiae showed a significant effect.

Table 11 Trabecular (Tb) bone histomorphometry of mineral apposition rate (MAR) and bone formation rate normalized to bone surface (BFR/BS) of the metaphyseal secondary spongiosa, determined by double labeled fluorochrome (calcein) labeling, calcein injected at day 3 and 10 in mice exposed to axial compression of 1200 με (left tibia dynamically loaded, right tibia non-loaded control) (mean ± SD); ANOVA for day 15: indicates the effect of (a) genotype, (b) loading, (c) genotype and loading, $p < 0.05$. Asterisks indicate a significant difference between loaded and control tibiae for each genotype (Paired t-test; $p < 0.05$).

	Control		Gorab^{Prx1}	
Outcome	Non-Loaded	Loaded	Non-Loaded	Loaded
Day 15	n = 7	n = 7	n = 7	n = 7
Tb. sLS/BS [%]	5.26 ± 6.20	4.23 ± 2.71	3.16 ± 1.94	2.52 ± 1.67
Tb. dLS/BS [%] $_{a, b, c}$	7.55 ± 5.04	15.86 ± 4.87 *	4.46 ± 2.05	6.25 ± 2.68
Tb. MS/BS [%] $_{a, b}$	10.19 ± 4.73	17.97 ± 5.14 *	6.04 ± 2.28	7.52 ± 3.00
Tb. MAR [µm/d] $_{a}$	3.18 ± 0.25	3.52 ± 0.49	2.28 ± 0.59	2.45 ± 0.25
Tb. BFR [µm^2/d] $_{a, b, c}$	0.32 ± 0.14	0.62 ± 0.16 *	0.15 ± 0.07	0.18 ± 0.07

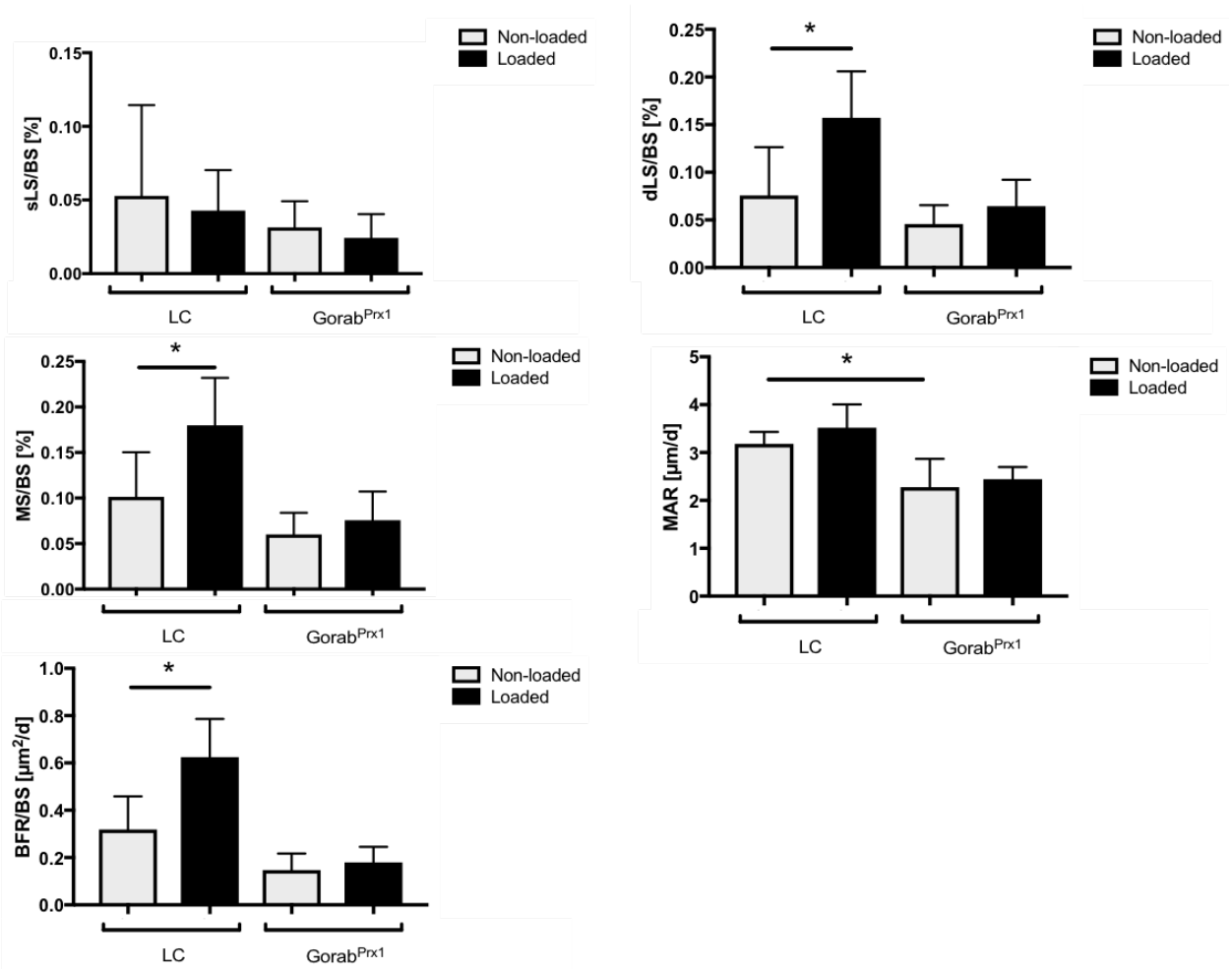

Figure 19 Trabecular (Tb) bone dynamic histomorphometry of single labeled surface per bone surface (sLS/BS, double labeled surface per bone surface (dLS/BS), mineralized surface per bone surface (MS/BS), mineral apposition rate (MAR) and bone formation rate normalized to bone surface (BFR/BS) of the metaphyseal trabecular bone, determined by double labeled fluorochrome (calcein) labeling, calcein injected at day 3 and 10 in mice exposed to axial compression of 1200 με (left tibia dynamically loaded, right tibia non-loaded control) (mean ± SD); ANOVA for day 15: indicates a periosteal effect of (a) genotype, (b) loading, (c) genotype and loading and endosteal effects of (d) genotype, (e) loading, (f) genotype and loading, $p < 0.05$. Asterisk indicates a significant difference between loaded and control tibiae for each genotype (Paired t-test; $p < 0.05$).

3.2.2 Static histology trabecular bone

Besides *in vivo* µCT based evaluation of the trabecular bone n=7 LC mice and n=5 Gorab^{Prx1} mice were treated with the described two week protocol of mechanical loading. Afterwards, tibiae were extracted, decalcified, paraffin embedded, and subsequently used for immunohistology. Several staining procedures such as Osterix 3,3'-Diaminobenzidine (DAB), Tartrate-resistant acid phosphatase staining (TRAP), Picrosirius Red among others were conducted for the following results. The stainings were conducted to shed some light into the cellular compartments of Gorab^{Prx1} trabecular bone, in order to gain indications as to why in mutant bone the mechanoresponsiveness is lost.

3.2.2.1 Trabecular bone parameters static histomorphometry

Trabecular bone parameters measured in histologic sections overall resemble the data obtained by the *in vivo* µCT on d 15.
The following trabecular bone parameters were measured in the static histomorphology:

- Trabecular bone volume per total volume (Tb.BV/TV) [mm^3/mm^3],
- Trabecular bone area (Tb.B.Ar) [mm^2],
- Trabecular bone perimeter (Tb.B.Pm) [mm],
- Trabecular thickness (Tb.Th) [mm],
- Trabecular number (Tb.N) [1/mm] and
- Trabecular separation (Tb.Sp) [µm].

Tb.BV/TV shows in LC and Gorab^{Prx1} mice the same difference between non-loaded and loaded trabecular bone compared to data collected by using *in vivo* µCT of 0.07 mm^3/mm^3 and 0.01 mm^3/mm^3. Therefore, the obtained effect of significant higher Tb.BV/TV in LC mice and no significant change in Gorab^{Prx1} tibiae can be seen as consistent throughout different methods. Anova indicates effects for genotype, loading and it's combination.

Tb.Th shows also no significant differences in Gorab^{Prx1} non-loaded and loaded bone, but in LC mice, loaded trabecular bone showed a 50 % higher value compared to loaded bone. Anova indicates effects for genotype, loading and it's combination.
In contrast to the *in vivo* µCT, **Tb.N** is non-significant higher in LC mice in the loaded (3.80 1/mm) compartment than in the non-loaded (2.98 1/mm). In both groups trabecular bone did show higher area (**Tb.B.Ar**) and perimeter (**Tb.B.Pm**) values in the loaded leg, whereas Gorab^{Prx1} mice showed less difference after loading. **Tb.Sp** shows only ANOVA effects regarding phenotype and furthermore the ttest indicates a significant reduction in LC after loading. Table 12 and Figure 20 summarize the data, obtained by the static bone histomorphometry.

Table 12 Static histomorphometry, Trabecular (Tb) bone parameters of the tibial, metaphyseal area , determined in decalcified bone sections via OsteoMetrics,, tibiae dissected at day 15 of the axial compression protocol (left tibia dynamically loaded, right tibia non-loaded control) (mean ± SD); ANOVA for day 15: indicates an effect of (a) genotype, (b) loading, (c) genotype and loading, $p < 0.05$. Asterisk indicates a significant difference between loaded and control tibiae for each genotype (Paired t-test; $p < 0.05$).

	LC		Gorab^{Prx1}	
Outcome	Non-Loaded	Loaded	Non-Loaded	Loaded
Day 15	n=7	n=7	n=5	n=5
Tb.BV/TV(mm^3/mm^3) [a,b,c]	0.07 ± 0.02	0.14 ± 0.05*	0.05 ± 0.01	0.06 ± 0.03
Tb.B.Ar (mm^2) [a,b,c]	0.03 ± 0.01	0.06 ± 0.02	0.02 ± 0.00	0.03 ± 0.01
Tb.B.Pm (mm)	2.63 ± 0.49	3.31 ± 0.78	2.14 ± 0.37	2.44 ± 0.86
Tb.Th (µm) [a, b, c]	24.36 ± 2.08	37.39 ± 8.15*	20.37 ± 1.95	22.62 ± 3.48
Tb.N (1/mm) [a, b]	2.98 ± 0.56	3.80 ± 0.88	2.42 ± 0.40	2.69 ± 0.86
Tb.Sp (µm) [a]	323.26 ± 64.26	239.92 ± 66.28*	403.07 ± 64.43	395.48 ± 153.48

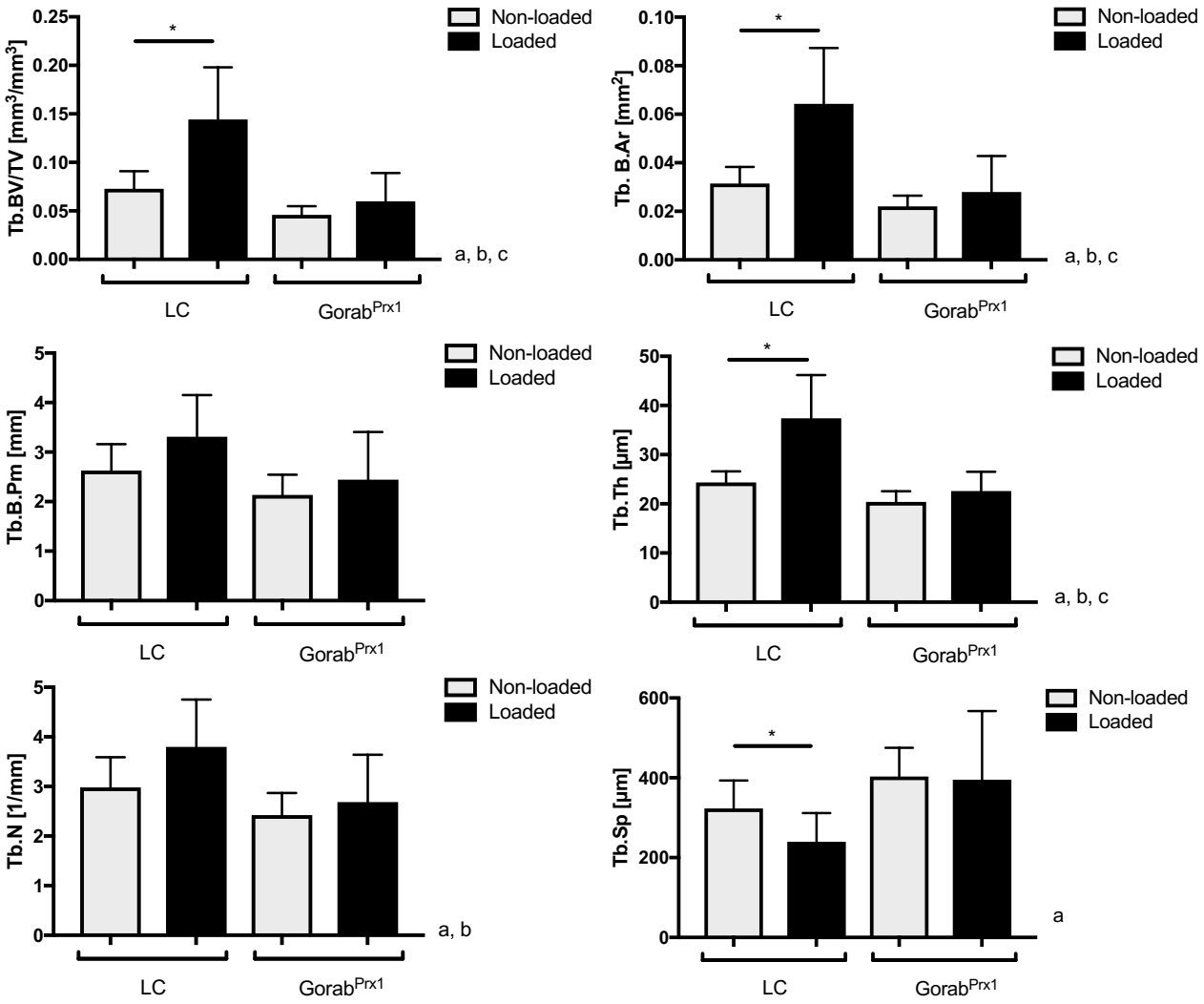

Figure 20 Trabecular Bone Volume per Total Volume (Tb. BV/TV), Trabecular Bone Area (Tb. B.Ar), Trabecular Bone Perimeter (Tb. B.Pm), Trabecular Thickness (Tb.Th), Trabecular Number (Tb.N) and Trabecular Separation (Tb.Sp), determined in decalcified bone sections via OsteoMetrics. Tibia was dissected at day 15 of mice exposed to axial compression of 1200 με (left tibia dynamically loaded, right tibia non-loaded control) (mean ± SD); ANOVA for day 15: indicates an effect of (a) genotype, (b) loading, (c) genotype and loading, $p < 0.05$. Asterisk indicates a significant difference between loaded and control tibiae for each genotype (Paired t-test; $p < 0.05$).

Picrosirius red staining for collagen fiber characterization

Using picrosirius red staining, the composition of reddish and greenish collagen fibers can be visualized and quantified. Green fibers represent weak, thin or young collagen bundles, whereas red fibers show mature, thick strong fibers. Depending on which study is followed even collagen types are associated with the fiber color of the tissue under

polarized light. Some researchers associate collagen type I with red color and collagen type IV with greenish colors[246]. However, the differentiation of green and red fibers shows is consistent throughout the literature. In earlier studies, our group demonstrated crucial differences in young (4 week old) animals using picrosirius red, in the collagen composition in cortical bone[4]. It was shown that control animals show a strong red signal and Gorab^{Prx1} mice show mostly green signal throughout the compact bone. Two major conditions are different in this study, in that we used 10 week old animals for the 2 week loading protocol and subsequently analyzed the trabecular bone, which is a different compartment compared to cortical bone.

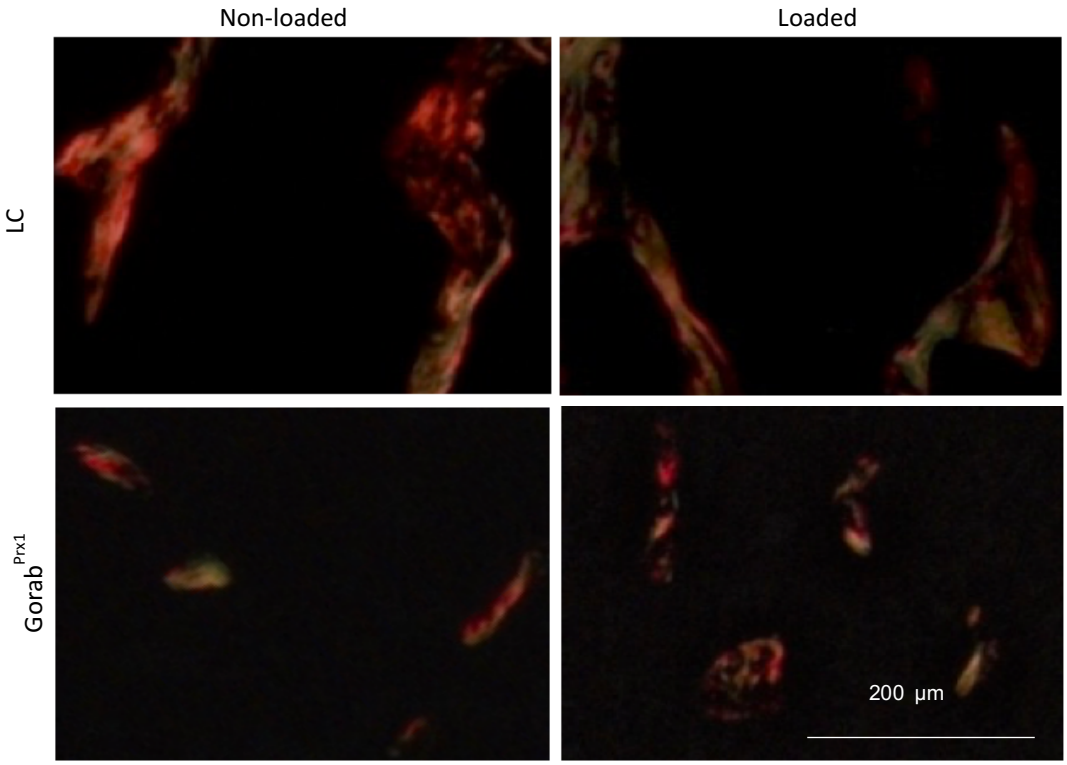

Figure 21 Picrosirius red stained longitudinal tibial cross sections in polarizing light microscopy, showing primary spongiosa trabecular bone in the ROI of 12 wk old LC and Gorab^{Prx1} animals. Tibiae were dissected at day 15 of mice exposed to axial compression of 1200 με (left tibia dynamically loaded, right tibia non-loaded control)

We found in the non-loaded LC and Gorab^{Prx1} tibiae similar percentages of green and red fibers. Interestingly, after loading the amount of red fibers in LC mice was reduced and the balance favored green fibers, young fibers. In Gorab^{Prx1} mice only the percentage of

red fibers per bone area was decrease, but green fibers showed similar amount. The change in green and red fibers represent the bone formation, which led to a significant increase of BV/TV. Tendencies of bone formation, associated with green fibers can be found in LC mice, but not in Gorab^{Prx1} animals. By obtaining the ratio of green fibers per bone area per red fibers per bone, the effect is more clear [(Green fibers/B.Ar) / (Red fibers / B.Ar)]. In LC mice this ratio increased after loading from 75 % to 102 %. In Gorab^{Prx1} animals the balance between red and green fibers stays mostly the same, from 75 to 80 %. Table 13 shows the evaluated quantifications of collagen fibers *by* ImageJ.

Table 13 Static histomorphometry, picrosirius red indicated quantification of red and green fibers under polarizing light in the metaphyseal trabecular bone, determined in decalcified bone sections via OsteoMetrics,, tibia dissected at day 15 of mice exposed to axial compression of 1200 με and (left tibia dynamically loaded, right tibia non-loaded control) (mean ± SD); ANOVA for day 15: indicates an effect of (a) genotype, (b) loading, (c) genotype and loading, $p < 0.05$. Asterisk indicates a significant difference between loaded and control tibiae for each genotype (Paired t-test; $p < 0.05$).

	LC		Gorab^{Prx1}	
Outcome	Non-Loaded	Loaded	Non-Loaded	Loaded
Day 15	n=5	n=5	n=5	n=5
Green fibers/B.Ar (mm^2/mm^2)	0.40 ± 0.10	0.44 ± 0.09	0.40 ± 0.04	0.40 ± 0.13
Red fibers /B.Ar (mm^2/mm^2)	0.53 ± 0.06	0.43 ± 0.08	0.53 ± 0.07	0.50 ± 0.07
Green fibers/Red fibers [%]	75	102	75	80

3.2.2.2 Trabecular bone cellular static histomorphometry

Cellular histomorphometry was also evaluated in n = 7 LC and n = 5 Gorab^{Prx1} mice. The left tibia underwent the 14 d mechanical loading protocol, which already demonstrated in LC mice an increase in BV/TV, whereas the effect of loading on the bone was missing in mutant mice. Therefore, the bone cell compartment was investigated.

DAB staining was used for immunohistochemical antibody staining of Osterix expressing cells. Osteoblasts were identified with the help of Osterix expression. Same sections were used for osteocyte quantification. They were identified by their characteristic environment, trapped in the mineralized bone matrix. TRAP staining was used to identify osteoclasts. All collected data are summarized in Table 14.

Firstly **osteoblasts** (Ob), **osteoclasts** (Oc) and **osteocytes** (Ot) were quantified in total per section. It was shown that Ob were present in all four groups in similar quantities. In non-loaded mice **N.Ob** was around 70 cells per section and in sections of loaded bone the number of osteoblasts was a little lower. This was presumable based on the increased bone perimeter and differentiation to osteocytes which occurred. **N.Oc** showed in LC mice no significant changes to loading, ranging between 18-20 cells per ROI. In Gorab^{Prx1} mice number of osteoclasts is in non-loaded mice around 10 cells and after loading around 13 cells per ROI.

N.Ot increased in LC mice with loading from 26 to 41 cells per ROI. In Gorab^{Prx1} bone the number of osteocytes did not change and stayed at 46 cells per ROI. **Number of Lacunae** (N.Lc) in LC bone is increasing with loading, proportionally to osteocytes. Still number of counted lacunae is higher as the number of osteocytes. Also, in Gorab^{Prx1} N.Lc is higher in loaded bone tissue than in non-loaded trabecular bone, even if the number of counted osteocytes is not changed (Figure 22).

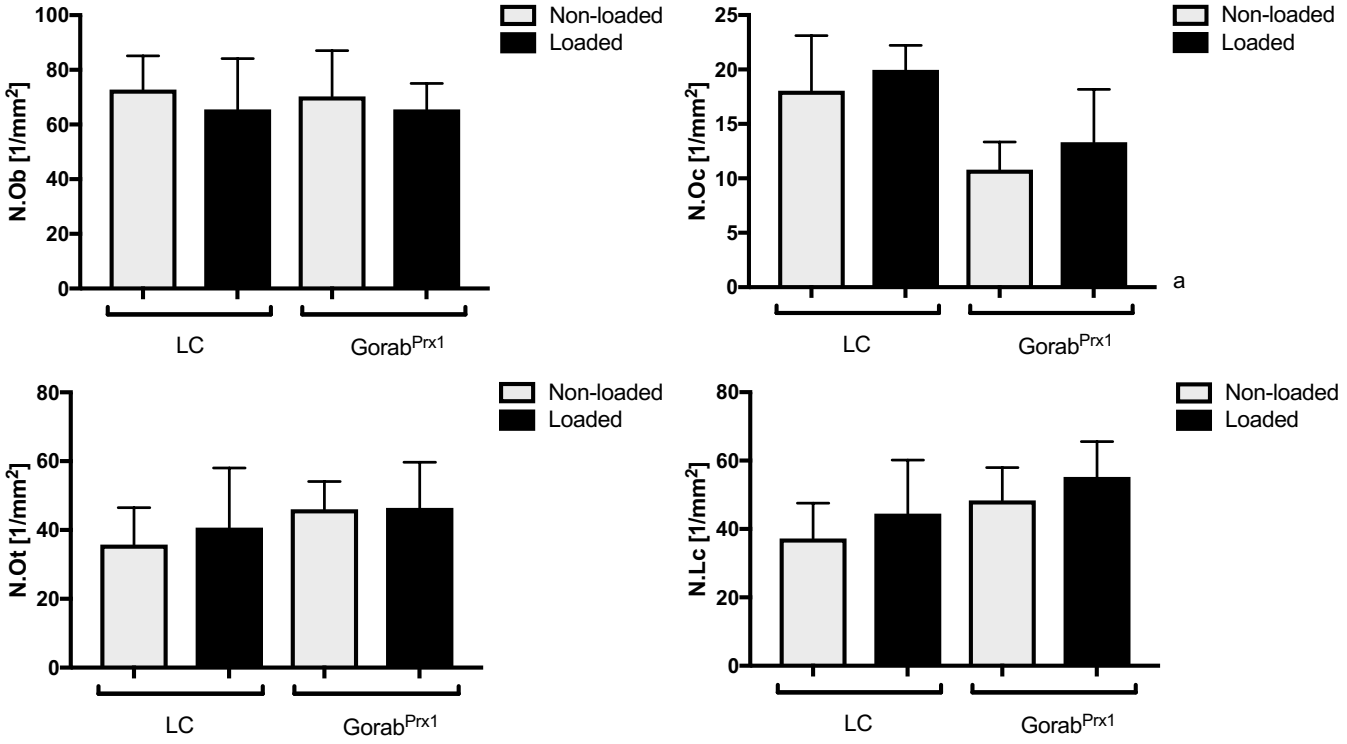

Figure 22 Cellular Histomorphometry in trabecular bone. Number of Osteoblasts (N.Ob), Number of Osteoclasts (N.Oc), Number of Osteocytes (N.Ot) and Number of Lacunae (N.Lc), determined in decalcified bone sections via OsteoMetrics, tibia dissected at day 15 of mice exposed to axial compression of 1200 με (left tibia dynamically loaded, right tibia non-loaded control) (mean ± SD); ANOVA for day 15: indicates an effect of (a) genotype, (b) loading, (c) genotype and loading, $p < 0.05$. Asterisk indicates a significant difference between loaded and control tibiae for each genotype (Paired t-test; $p < 0.05$).

N.Ad indicated controversial results in LC and mutants. N.Ad did not change significantly in any group, but tendencies displayed an decrease with loading in LC and an increase in Gorab^{Prx1} mice.

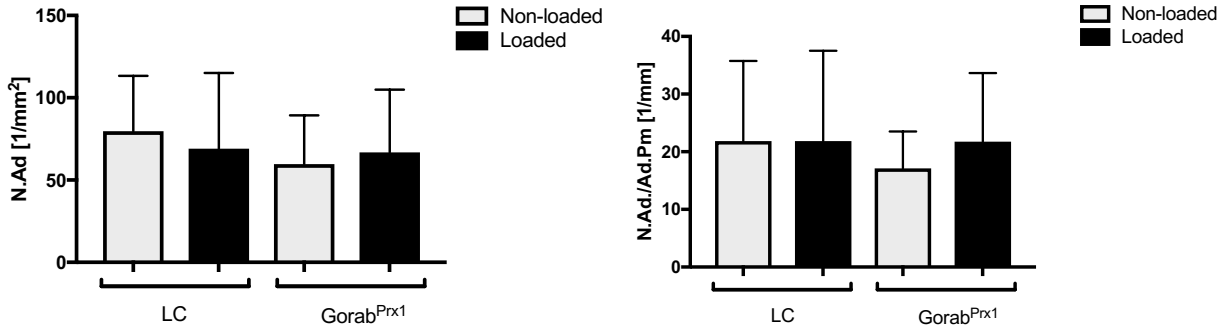

Figure 23 Cellular Histomorphometry in trabecular bone. Number of Adipocytes (N.Ad) and Number of Adipocytes per Adipocyte Perimeter (N.Ad./B.Pm) determined in decalcified bone sections via OsteoMetrics, tibia dissected at day 15 of mice exposed to axial compression of 1200 με (left tibia dynamically loaded, right tibia non-loaded control) (mean ± SD); ANOVA for day 15: indicates an effect of (a) genotype, (b) loading, (c) genotype and loading, $p < 0.05$. Asterisk indicates a significant difference between loaded and control tibiae for each genotype (Paired t-test; $p < 0.05$).

Focusing on the lipid metabolism in the bone marrow cavity adipocytes were quantified and their perimeter was measured. No significant changes were conducted in quantity of adipocytes per ROI. Moreover, the number of adipocytes per adipocyte perimeter also did not vary significantly with regards to genotype or loading (Figure 23). Due to the unsuspicious data regarding the lipid metabolism, no further investigations were executed.

What is more enlightening than the total numbers are the cell count per bone perimeter or bone area, due to the differences of bone tissue found in the genotypes and in their reaction regarding loading. All data are shown in Figure 25. Furthermore, Figure 24 shows DAB stained osteoblasts of LC and Gorab^{Prx1} non-loaded and loaded in metaphyseal trabecular bone.

Number of osteoblasts per bone area (N.Ob./B.Ar) demonstrate a value 30 % less in loaded trabecular bone than in non-loaded bone in LC animals. In non-loaded sections, 28.24 N.Ob./B.Ar were found and in loaded only 19.84 N.Ob./B.Ar. In comparison, the number of osteoblasts per bone area in Gorab^{Prx1} animals in the loaded limb was 29.31 1/mm, whereas in non-loaded bone only 19.83 1/mm. LC mice again demonstrate an increase in BV/TV, therefore the bone perimeter is increasing and the number of osteoblasts stays at a similar level, shown in N.Ob. Osteoblast perimeter, also seen as eroded surface per bone perimeter (**Ob.Pm./B.Pm**), also shows lower values in loaded bone (0.22 mm/mm non-loaded and 0.15 mm/mm in loaded bone), therefore the formation sites are similar, and seemingly highly effective, based on the elevated bone formation seen in *in vivo* µCT morphometry and the static histomorphometry due to loading in LC mice.

In case of Gorab^{Prx1} **number of osteoblasts per bone perimeter** an inversed phenomenon was observed. In non-loaded sections 19.83 1/mm were found, but in loaded sections an average of 29.31 1/mm. Partwise, this could be based on the impaired osteoblast differentiation, as illustrated by our group. Mechanical loading could trigger the differentiation process. Still, Ob.Pm./B.Pm did not change significantly in Gorab^{Prx1} mice. The average width of osteoblasts, proportional to N.Ob/Ob.Pm, was in loaded LC bone slightly reduced, whereas in Gorab^{Prx1} mice basically not changed.

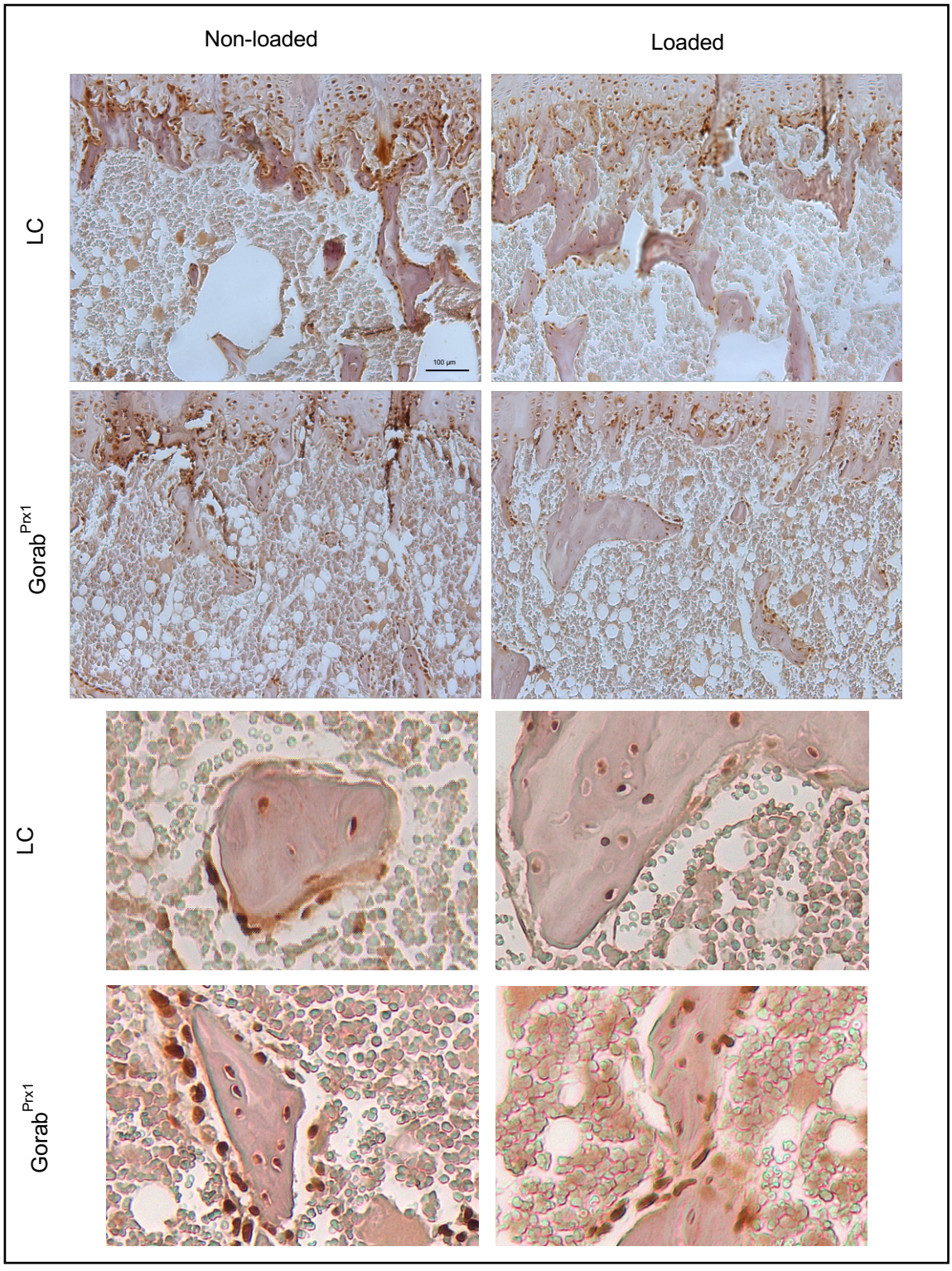

Figure 24 Osterix protein AB-DAB stained longitudinal tibiae cross sections showing non-loaded and loaded trabecular bone of 12 wk old LC and Gorab^{Prx1} mice. Imaging was executed in a 100 x magnification at an Olympus BS60 microscope. Tibiae were dissected at day 15 of mice exposed to axial compression of 1200 με (left tibia dynamically loaded, right tibia non-loaded control).

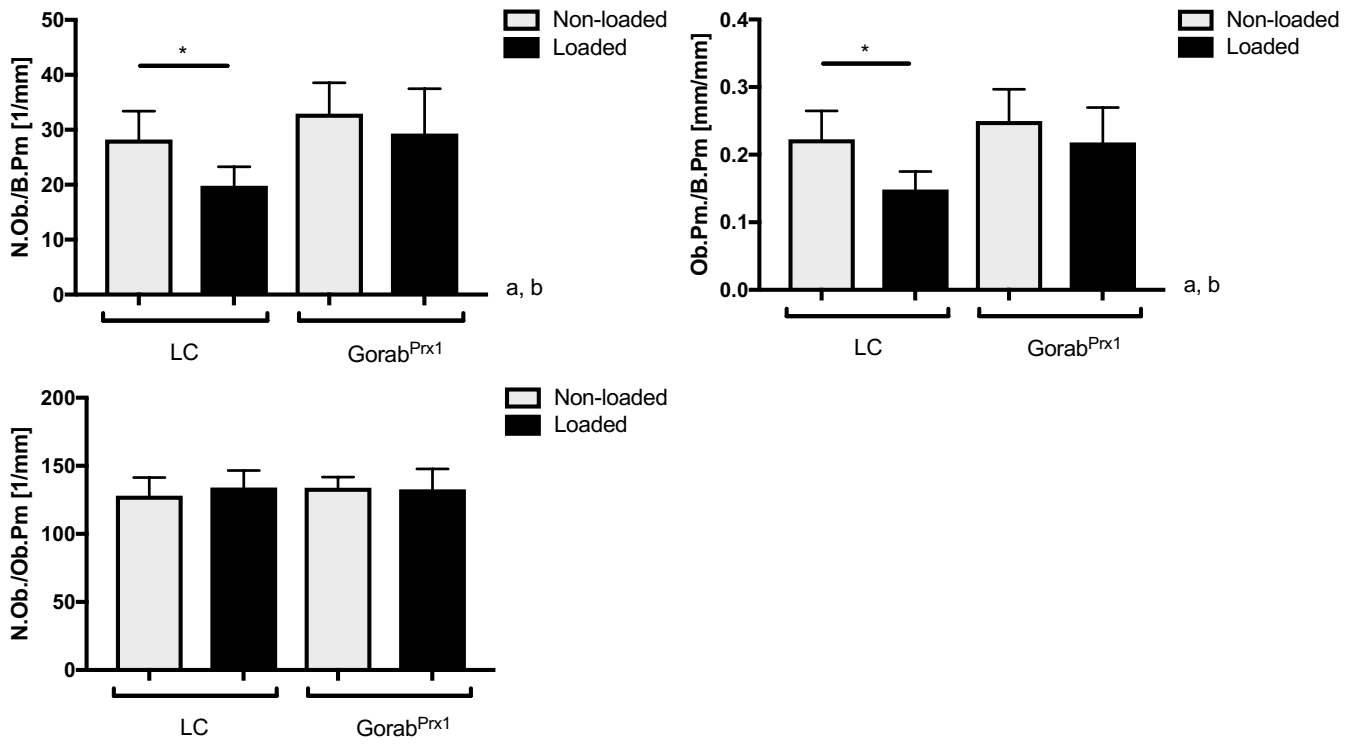

Figure 25 Cellular Histomorphometry in trabecular bone. Number of Osteoblasts per Bone Perimeter (N.Ob./B.Pm), Osteoblast Perimeter per Bone Perimeter (Ob.Pm./B.Pm) and Number of Osteoblasts per Osteoblast Perimeter (N.Ob./Ob.Pm) determined in decalcified bone sections via OsteoMetrics, tibia dissected at day 15 of mice exposed to axial compression of 1200 με (left tibia dynamically loaded, right tibia non-loaded control) (mean ± SD); ANOVA for day 15: indicates an effect of (a) genotype, (b) loading, (c) genotype and loading, $p < 0.05$. Asterisk indicates a significant difference between loaded and control tibiae for each genotype (Paired t-test; $p < 0.05$).

The number of osteoclasts per bone perimeter (N.Oc./B.Pm) showed no significant changes in LC and Gorab^{Prx1} mice with regards to loading. LC exhibited 4.47 1/mm in non-loaded and 5.89 1/mm in loaded trabecular bone. Similar results were obtained in mutants, with 4.66 1/mm in non-loaded and 5.47 1/mm in loaded animals (Figure 26). TRAP stained osteocytes in LC and Gorab^{Prx1} non-loaded and loaded diaphyseal trabecular bone are visualized in Figure 27.

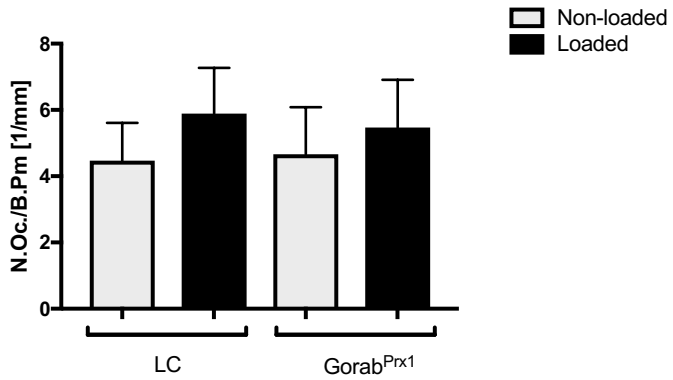

Figure 26 Cellular Histomorphometry in trabecular bone. Number of Osteoclasts per Bone Perimeter (N.Oc./B.Pm) determined in decalcified bone sections via OsteoMetrics, tibia dissected at day 15 of mice exposed to axial compression of 1200 με (left tibia dynamically loaded, right tibia non-loaded control) (mean ± SD); ANOVA for day 15: indicates an effect of (a) genotype, (b) loading, (c) genotype and loading, $p < 0.05$. Asterisk indicates a significant difference between loaded and control tibiae for each genotype (Paired t-test; $p < 0.05$).

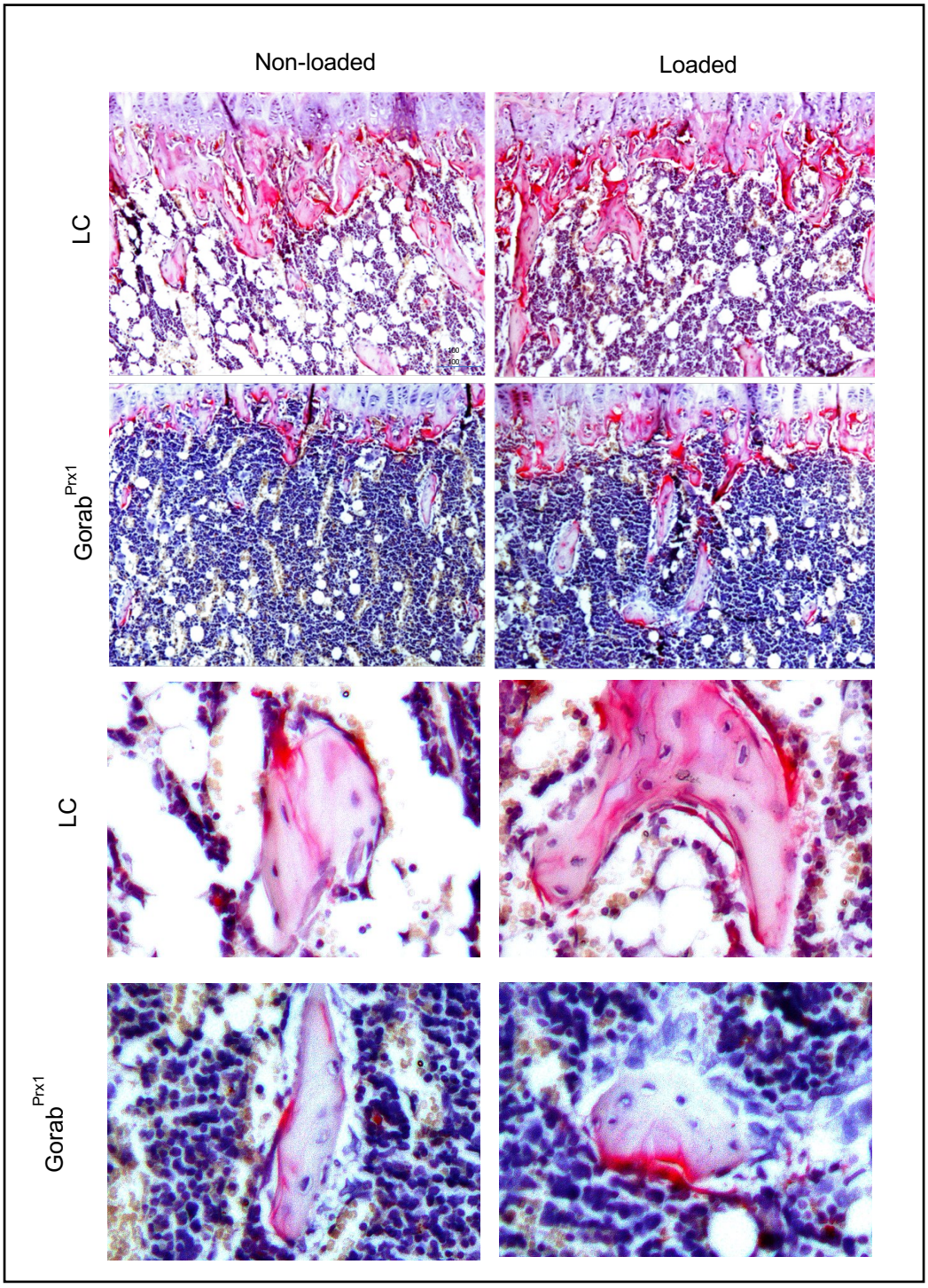

Figure 27 Tartrate-resistant acid phosphatase (TRAP), Hemalaun counterstained longitudinal tibiae cross sections showing the growth plate of 12 wk old Gorab^{Prx1} and Control animals. Imaging was executed in a 100 x magnification at an Olympus BS60 microscope. Tibiae were dissected at day 15 of mice exposed to axial compression of 1200 με (left tibia dynamically loaded, right tibia non-loaded control).

Interestingly, comparing the **number of osteocytes per bone area** (N.Ot./B.Ar) revealed a significant difference in non-loaded and loaded LC mice. Non-loaded bone had 1133.55

1/mm^2, and loaded bone only 641.92 1/mm^2. In Gorab^{Prx1} trabecular bone, significantly higher values were obtained. 2130.4 1/mm^2 N.Ot./B.Ar in non-loaded sections and a non-significant smaller number of osteocytes were found in loaded trabecular bone area 1819.43 1/mm^2 (Figure 28).

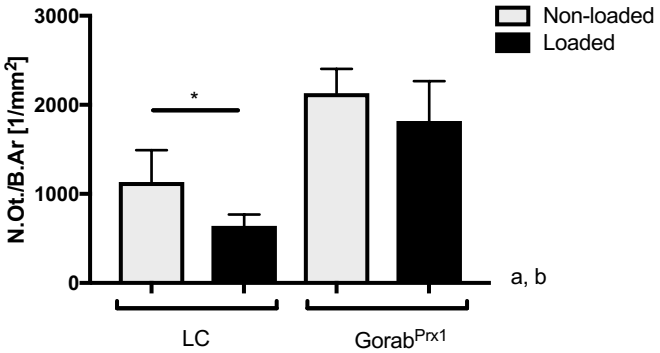

Figure 28 Cellular Histomorphometry in trabecular bone. Number of Osteocytes per Bone Area (N.Ot./B.Ar) determined in decalcified bone sections via OsteoMetrics, tibia dissected at day 15 of mice exposed to axial compression of 1200 με (left tibia dynamically loaded, right tibia non-loaded control) (mean ± SD); ANOVA for day 15: indicates an effect of (a) genotype, (b) loading, (c) genotype and loading, $p < 0.05$. Asterisk indicates a significant difference between loaded and control tibiae for each genotype (Paired t-test; $p < 0.05$).

The reduction in both groups with loaded limbs can also be explained by the increased bone volume. LC mice exhibit significantly higher bone volume with significant reduced osteocytes per bone area. In Gorab^{Prx1} animals a similar, but much weaker response to mechanical loading was observed. Bone volume increased only slightly, accompanied by a non-significant reduction in osteocytes per bone area.

Table 14 Static cellular histomorphometry, trabecular (Tb) bone osteogenic cell parameters in the tibial, metaphyseal area , determined in decalcified bone sections via OsteoMetrics, tibia dissected at day 15 of mice exposed to axial compression of 1200 με and (left tibia dynamically loaded, right tibia non-loaded control) (mean ± SD); ANOVA for day 15: indicates an effect of (a) genotype, (b) loading, (c) genotype and loading, $p < 0.05$. Asterisk indicates a significant difference between loaded and control tibiae for each genotype (Paired t-test; $p < 0.05$).

	LC		Gorab^{Prx1}	
Outcome	Non-Loaded	Loaded	Non-Loaded	Loaded
Day 15	n=7	n=7	n=5	n=5
N.Ob	72.83 ± 11.41	65.57 ± 17.16	70.30 ± 14.99	65.53 ± 8.53
N.Oc [a]	18.06 ± 4.62	19.97 ± 2.04	10.80 ± 2.27	13.33 ± 4.34
N.Ot	25.79 ± 9,93	40.67 ± 16.05	46.03 ± 7.24	46.40 ± 11.89
N.Ad	79.74 ± 31.09	69.10 ± 42.58	59.73 ± 26.50	66.80 ± 34.08
N.Lc	37.24 ± 9.55	44.52 ± 14.49	48.37 ± 8.56	55.20 ± 9.25
Ob.Pm./B.Pm (mm/mm) [a, b]	0.22 ± 0.04	0.15 ± 0.02*	0.25 ± 0.04	0.22 ± 0.05
N.Ob./B.Pm (1/mm) [a, b]	28.24 ± 4.77	19.83 ± 3.19*	19.83 ± 5.05	29.31 ± 13.37
N.Ob./Ob.Pm (1/mm)	128.02 ± 12.35	134.15 ± 11.46	133.90 ± 6.96	132.80 ± 13.37
N.Ot./B.Ar (1/mm^2) [a, b]	1133.55 ± 332.00	641.92 ± 117.50*	2130.40 ± 244.06	1819.43 ± 400.06
N.Oc./B.Pm (1/mm)	4.47 ± 10.4	5.89 ± 1.26	4.66 ± 1.27	5.47 1.28

3.3 Section III - Investigation of the lacunar-canalicular network in Gorab^{Prx1} and LC mice

In previous studies our group observed an irregular and disordered ECM in Gorab^{Prx1} bone, based on the glycosylation deficiency of proteoglycans. These findings were already published by Chan et al.[4]. Due to these findings and the high number of osteocytes found in Gorab^{Prx1} tibial trabecular bone we hypothesized an impairment of the lacunar-canalicular network. With this impairment the loss of mechanoresponse could be, at least partly, explained. All following investigations were executed on the tibia diaphyseal midshaft. The VOI was chosen, similar to the VOI of *in vivo* µCT and calcein based histomorphometry in the diaphyseal cortical bone.

Furthermore, vascular porosity was evaluated, due to the impact of the porosity on bone rigidity and strength.

The following data describes the phenotypical differences of Gorab^{Prx1} and LC mice without loading.

Examination of the following lacunar-canalicular network and vascular porosity parameter was performed:

Lacuna parameters:

- Lacuna volume [µm^3],
- Lacuna oblateness,
- Lacuna stretch,
- Lacuna number density [1/mm^3],
- Volume occupied by lacuna [%],

Canaliculus parameters:

- Canaliculi density [µm/µm^3],
- Number of canaliculi per lacuna [number of canaliculi/lacuna],

Vascular porosity parameters:

- Vascular canal number density [1/mm^3] and
- Volume occupied by vascular canals [%].

In order to analyze the above listed parameters the Leica SP8 confocal laser scanning microscope was used for overview scans and subsequently 4-5 ROIs per sample were scanned in 0.3 µm steps to create 3D models for evaluation and quantification.

3.3.1 Overview images of rhodamine stained cortical bone of the tibial diaphyseal midshaft

When comparing overview images (Figure 29) of the lacunar-canalicular network in LC and Gorab^{Prx1} cortical bone, a lack of connectivity and roundish lacunae can be supposed. Additionally, in the peripheral area of mutant bone less canaliculi can be observed, which connect the lacunar-canalicular network to the effector cells.

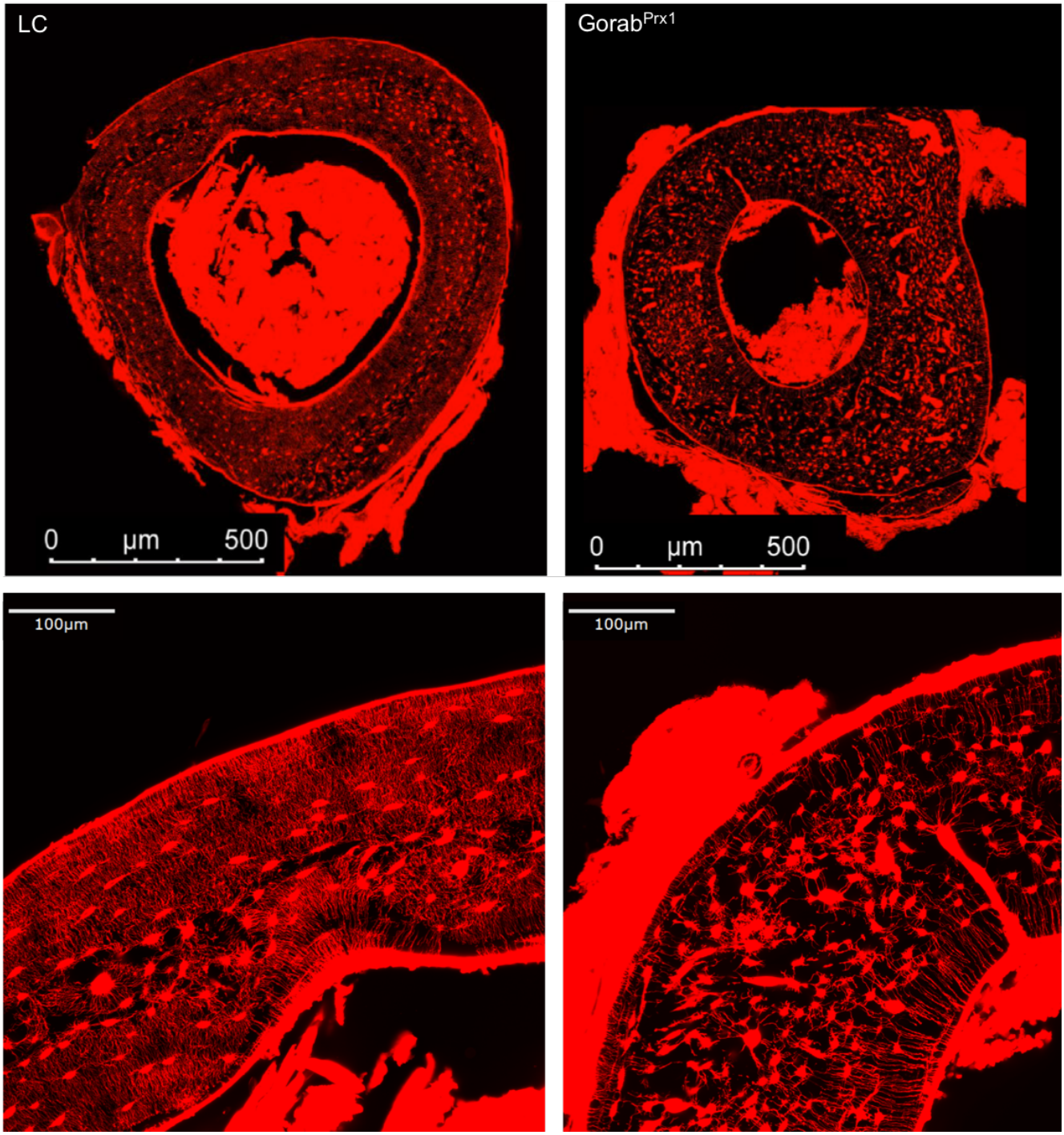

Figure 29 Rhodamine stained tibial diaphyseal midshaft showing cortical bone lacunar-canalicular network in LC and Gorab^{Prx1} mice using the Leica SP8 Confocal Laser Scanning Microscope.

3.3.2 Lacuna characterization of Gorab^{Prx1} and LC mice in diaphyseal cortical long bone

For lacuna characterization, several parameters must be defined.

An idealized lacuna in its physiological form shows an ellipsoidal shape with a > b > c, as seen in Figure 30.

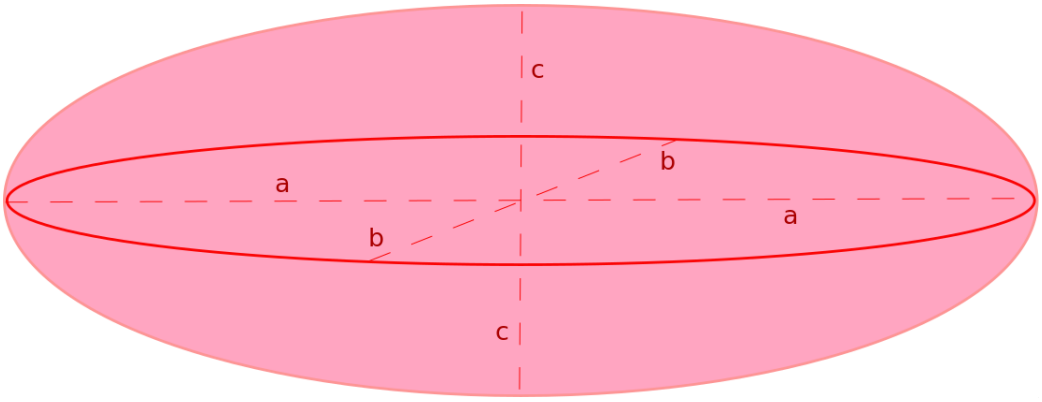

Figure 30 Idealized lacuna shape in a unitless coordinate system representing the long axis a, height of the lacunar body c and the width of the lacunar body in b.

Lacuna stretch

$$(a - c)/a$$

The lacuna stretch parameter is characterized as follows, with 0 as a minimum, representing a spherical shape and ~1 as a maximum representing a large difference between the longest axis to the shorter.

Lacuna oblateness

$$\frac{2(b - c)}{a - c} - 1$$

The lacuna oblateness parameter can be compared to three different geometries; 1 equals a frisbee, 0 equals an almond and -1 equals a cigar.

Lacunae in Gorab^{Prx1} exhibit a lower volume for each individual lacunae with an average of 290 µm^3/lacuna, in contrast to LC lacunae which have an average of 352 µm^3/lacuna. Their geometry also differs significantly regarding the lacunar stretch. With 0 as spherical, Gorab^{Prx1} lacunae are significant more rounded in shape, with a lacunar stretch value of 0.77, compared to LC lacunae with a value of 0.89.

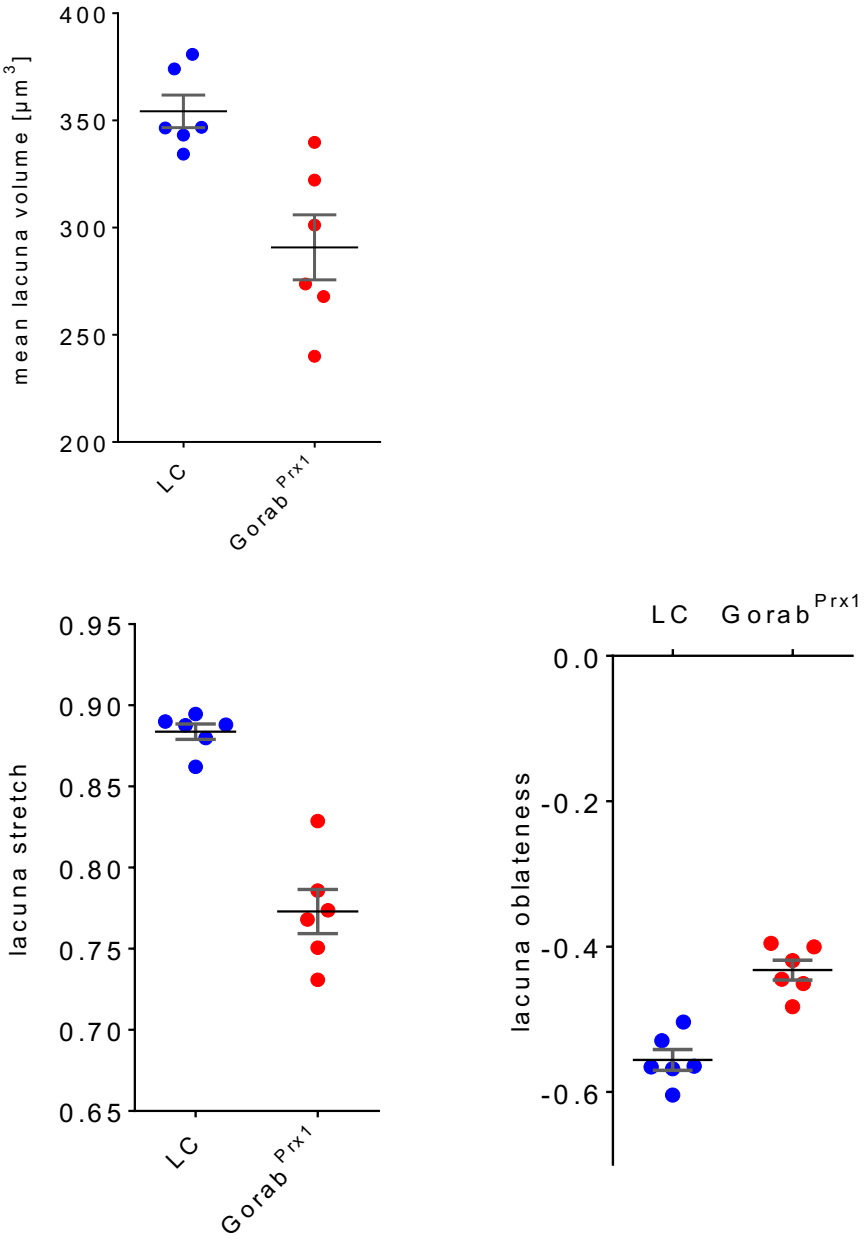

Figure 31 Lacuna geometry in 12 week old female GorabPrx1 and LC mice in tibial diaphyseal midshaft cortical bone showing the mean lacuna volume [µm³], lacuna stretch and the lacuna oblateness.

The oblateness does differ significantly, lacunae in mutant cortical show a value of -0.43 to LC lacunae with an average oblateness of -0.57 (Figure 31).

Therefore, lacunae in Gorab^{Prx1} tibial, diaphyseal cortical bone are smaller in volume and show a more spherical geometry in comparison to lacunae in the same region of LC tibiae (Figure 32).

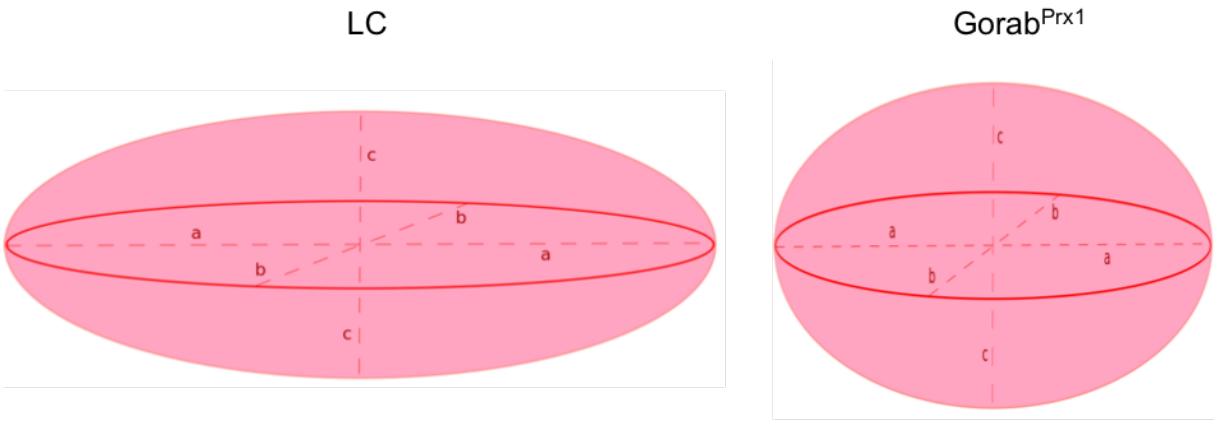

Figure 32 Model of the predicted lacuna geometry in a unitless coordinate system, of a LC lacuna and a Gorab^{Prx1} lacuna.

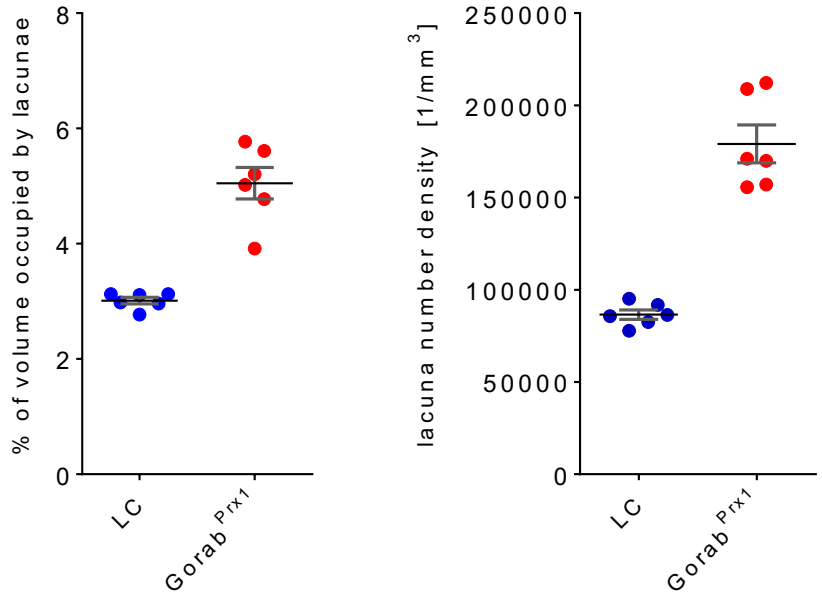

Figure 33 % of volume occupied by lacunae and lacuna number density [1/mm^3]in 12 week old female LC and Gorab^{Prx1} tibial diaphyseal midshaft cortical bone.

Besides the single lacuna geometry, additional key features were analyzed, e.g. the total volume occupied by lacunae in the VOI, lacunae number density and the average number of canaliculi evolving from a single lacuna (Figure 33, 34).

Despite the smaller average volume the lacuna in Gorab^{Prx1} cortical bone, the % of occupied volume by lacunae is significantly higher with an occupied volume of around 5 % compared to 3 % in LC mice. This paradox is based on the considerable increase of the number of lacunae found in the VOI. An average density of 180.000 lacunae per mm^3 were found in the VOI of the Gorab^{Prx1} cohort, compared to 95.000 lacunae per mm^3 in the comparable VOI of LC mice.
Those findings are consistent to the findings of the static cellular histomorphometry, where an enormous high number of osteocytes were also found in Gorab^{Prx1} trabecular metaphyseal bone. Therefore, high numbers in osteocytes/lacunae were found in both trabecular and cortical bone compartments. They exhibited similar phenotypic characteristics, with the loss of mechanoresponsiveness, and high number in osteocytes. Furthermore, the more spherical lacunar geometry found in Gorab^{Prx1} cortical bone could hint towards an impaired osteocyte differentiation process. Based on the impaired differentiation process osteoblasts, which were encased in osteoid are not able to terminal differentiate into osteocytes and therefore, not undergo the crucial cytoskeleton reassemble, which the cells undergo during differentiation.

3.3.3 Canaliculus network characterization of Gorab^{Prx1} and LC mice in diaphyseal cortical long bone

Characterization of the canalicular network includes the mean canaliculi density within the bone, the evolving canaliculi per lacuna, average edge (canaliculus) length and node degree. This chapter describes perhaps the most striking findings of section III.

Figure 34 shows that, in Gorab^{Prx1} animals, only half of the average 80 canaliculi evolved from the lacuna in the VOI. Therefore, the individual osteocyte connection to the network is massively impaired in Gorab^{Prx1} cortical bone.

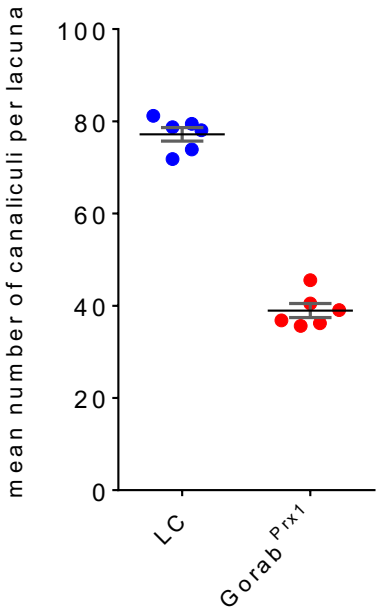

Figure 34 Mean number of canaliculi per lacuna in 12 week old female Gorab^{Prx1} and LC mouse tibiae, measured in the diaphyseal cortical bone VOI.

Figure 35 shows the canaliculi network density distributions of Gorab^{Prx1} and LC mice based on the evaluation of subvolumina of around 400µm^3. Gorab^{Prx1} exhibit a narrower distribution shifted to the left (lower canaliculi density) compared to the LC mice. The average peak maximum for Gorab^{Prx1} is around 0.1 µm/µm^3 while it is around 0.22 µm/µm^3 for the controls. The second peak of the in the Gorab^{Prx1} distributions at 0 µm/µm^3 corresponds to subvolumina without any network.

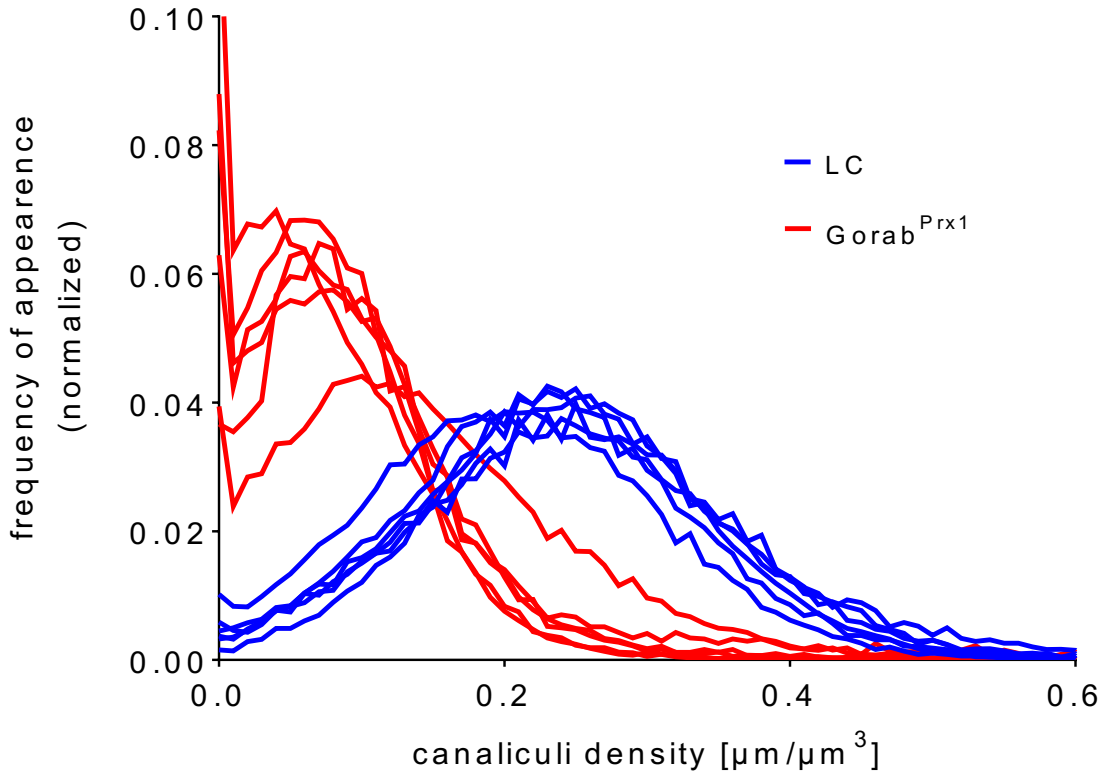

Figure 35 Canaliculi density [µm/µm³] plotted against their frequency of appearance in 12 week old female Gorab^{Prx1} and LC mouse tibiae, measured in the diaphyseal cortical bone VOI.

The high amount of semi-homogeneous distributed osteocytes leads to changes in the edge length distribution representing the length of canaliculi. Figure 36 plots the length of canaliculi in Gorab^{Prx1} tibiae vs. their frequency of appearance. Compared to LC mice, Gorab^{Prx1} animals exhibit more short edges but also an increased number of long edges. These shorter canaliculi also differ in their node degree. In the Gorab^{Prx1} lacunar-canalicular network a high amount of degree 3 nodes are detected. Therefore, the percentage of high degree nodes are lower compared to LC cortical bone, which has a reduced branching as a result.

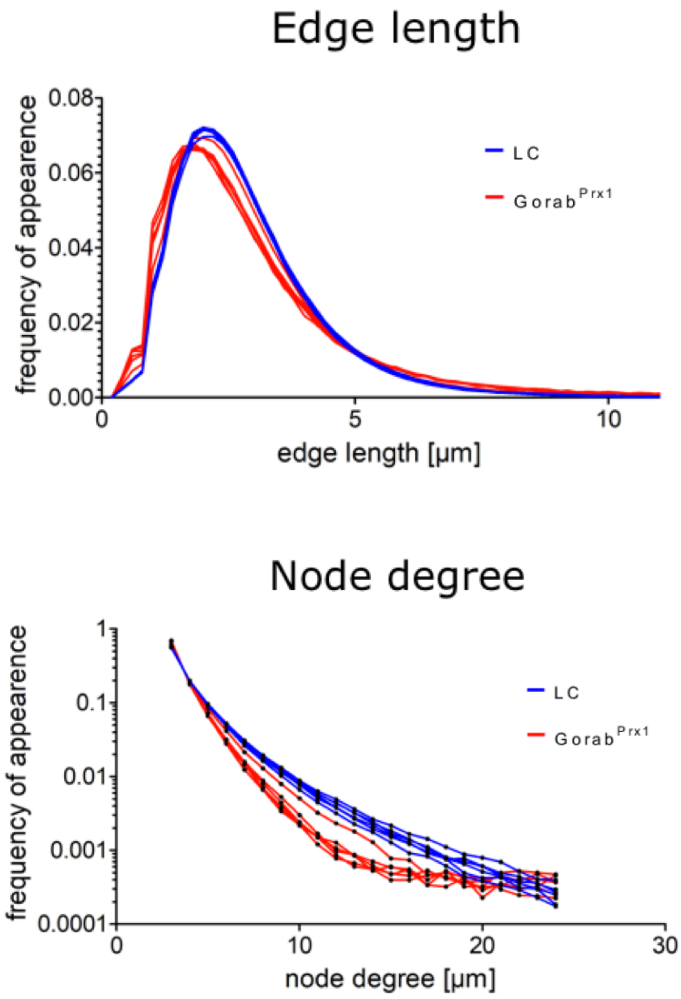

Figure 36 Edge length and node degree in 12 week old female Gorab^{Prx1} and LC mouse tibiae, measured in the diaphyseal cortical bone VOI. The areas under the individual curves is normalized to 1.

Based on all data regarding the lacunar-canalicular network, modeling a representing lacuna for LC and Gorab^{Prx1} visualizes the differences of the two mouse models.

In LC mice an ellipsoidal, cigar shaped lacuna body with numerous rising canaliculi can be remodeled. In the Gorab^{Prx1} model significant less canaliculi were detected and furthermore the more spherical cell body can be observed (Figure 37).

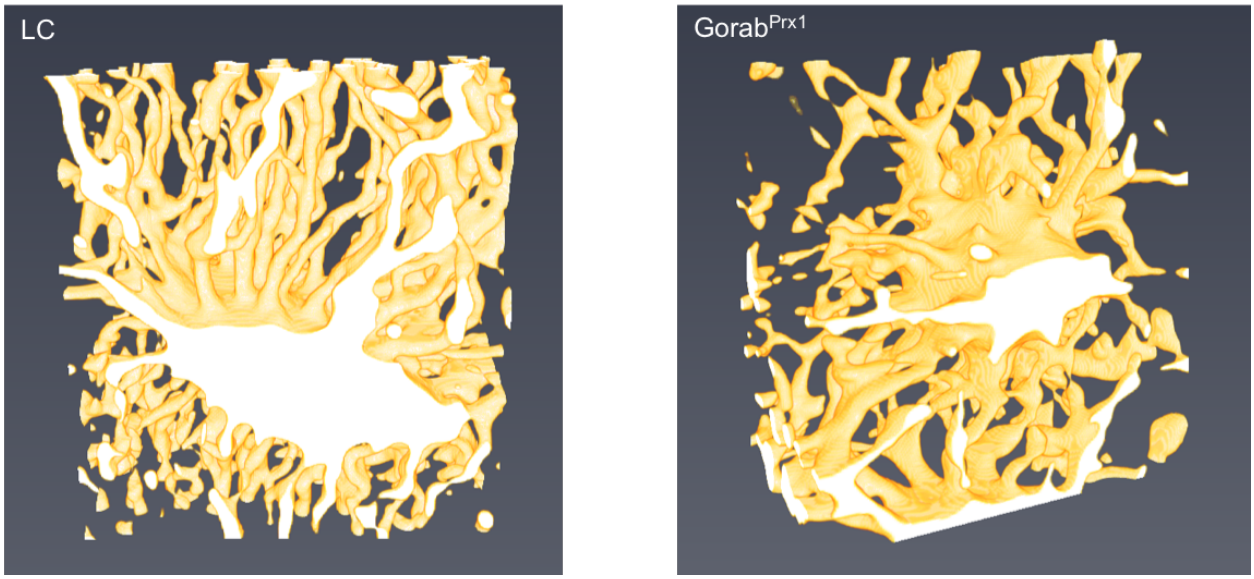

Figure 37 3D model of a LC and Gorab^{Prx1} lacuna and their spreading canaliculi in the modeled from Leica SP8 confocal laser scanning microscopy pictures after stacking and skeletonization.

3.3.4 Vascularization of cortical diaphyseal bone in LC and Gorab^{Prx1} tibiae

Vascular canal number density and % of volume occupied by vascular canals show significant differences between LC and Gorab^{Prx1}. The impressive 8-fold vascular porosity is consistently to the number of vascular canals. Therefore, the vascularization increases the bone's porosity (Figure 38).

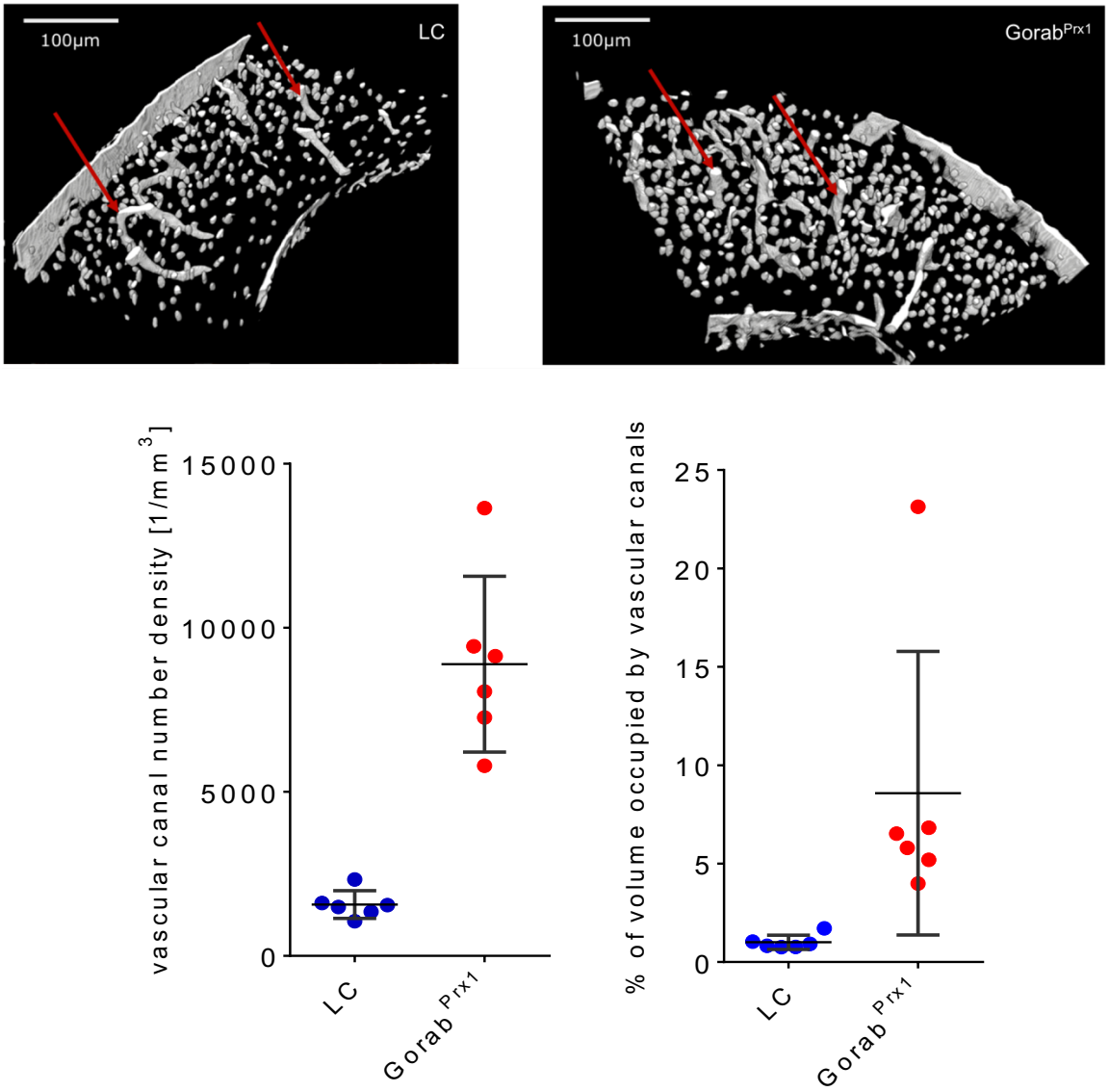

Figure 38 ***Top*** *3D models showing rendering of the CLSM images (Rhodamine image) without canaliculi in LC and Gorab^{Prx1} diaphyseal cortical bone, red arrows indicating vascularization canals.* ***Bottom*** *Vascular canal number density [1/mm^3] and % of volume occupied by vascular canals.*

3.4 Section IV – RNAseq studies to discover possible target gene dysregulation in mechanotransduction

RNAseq studies were planned to investigate altered pathways in loaded tibiae of Gorab^{Prx1} compared to the internal non-loaded control tibia, the loaded LC tibia and the according non-loaded LC control.

Therefore, a single loading session was applied and 8 h after loading tibiae were dissected from the mice, cleaned from surrounding muscle and other soft tissue, flash frozen in liquid nitrogen and stored at -80°C.

Experimental design planned 3 animals per group to ensure statistical relevance. Unfortunately, two out of twelve samples showed degraded RNA's after isolation. Final cohort numbers are shown in Table 15.

Table 15 Number of animals used for RNAseq analysis.

Cohort	Number of mice
LC Non-Loaded tibia	n = 2
LC Loaded tibia	n = 2
Gorab^{Prx1} Non-Loaded tibia	n = 3
Gorab^{Prx1} Loaded tibia	n = 3

This explains the low n number, and therefore the missing significance the RNAseq study was used only as a discovery study to find possible target genes, dysregulated after loading. The following results will be proved by qPCR with higher number of samples in later studies.

A holistic approach was applied to screen for possible target genes, dysregulated after loading in Gorab^{Prx1} mice. This holistic approach is covering ECM proteins (collagen), the Wnt / TGF-β pathway and proteins relevant in mechanotransduction, more precise proteins relevant in intracellular calcium release, ATP release, membrane repair, GAP-junctions, primary cilium, tether elements and fimbrin. Therefore, this study aimed to find dysregulations on mRNA level which could explain the loss of mechanoresponsiveness.

Relevant target genes are presented in the following.

Wnt / TGF-β pathway

The Wnt pathway has been analyzed in more detail, because our group found significant differences between Gorab^{Prx1} and LC mice regarding the Wnt / TGF-β pathway in previously published studies[4]. All Wnt / TGF-β pathway related gen expressions are shown in Figure 39.

Smad9 is indicating an increase in LC after loading of around 50%, whereas in Gorab^{Prx1} RNA isolates do not show a comparable increase in the expression profile.

Wnt7b shows a tenfold increase of transcripts after loading in LC mice. Gorab^{Prx1} mice show no change, but a general higher expression in non-loaded LC condition.

Dkk1 shows a mean increase of 46 % after loading in LC mice. Gorab^{Prx1} mice show no change in Dkk1 expression regarding loading, but also shows in general a high expression level, similar to the loaded LC condition.

Wnt4 also shows an upregulation on mRNA level after loading in LC mice. Gorab^{Prx1} again shows no response due to loading.

Lrp5 also gets upregulated after loading in LC mice, but shows no response to loading in Gorab^{Prx1} mice.

Sost, an important osteocyte marker shows no response to loading in both, LC and Gorab^{Prx1} expression profiles. All conditions show similar expression profiles.

Ctnnb1 shows an upregulation due to loading in LC of 25 %. Gorab^{Prx1} shows no response to loading.

Axin1 shows in LC and Gorab^{Prx1} mice a minimal upregulation after loading.

GSK3a/b show similar expression patterns with a minimal upregulation after loading in LC mice and with no change in Gorab^{Prx1} mice.

The following genes are nominated for an qPCR validation to reach significance and statistical relevance: ***Lrp5***, ***Smad9***, ***Wnt4*** and ***Wnt7b***.The selection is based on their importance related to mechanotransduction and their grade of difference in the expression pattern in LC and Gorab^{Prx1} after a single session of mechanical loading.

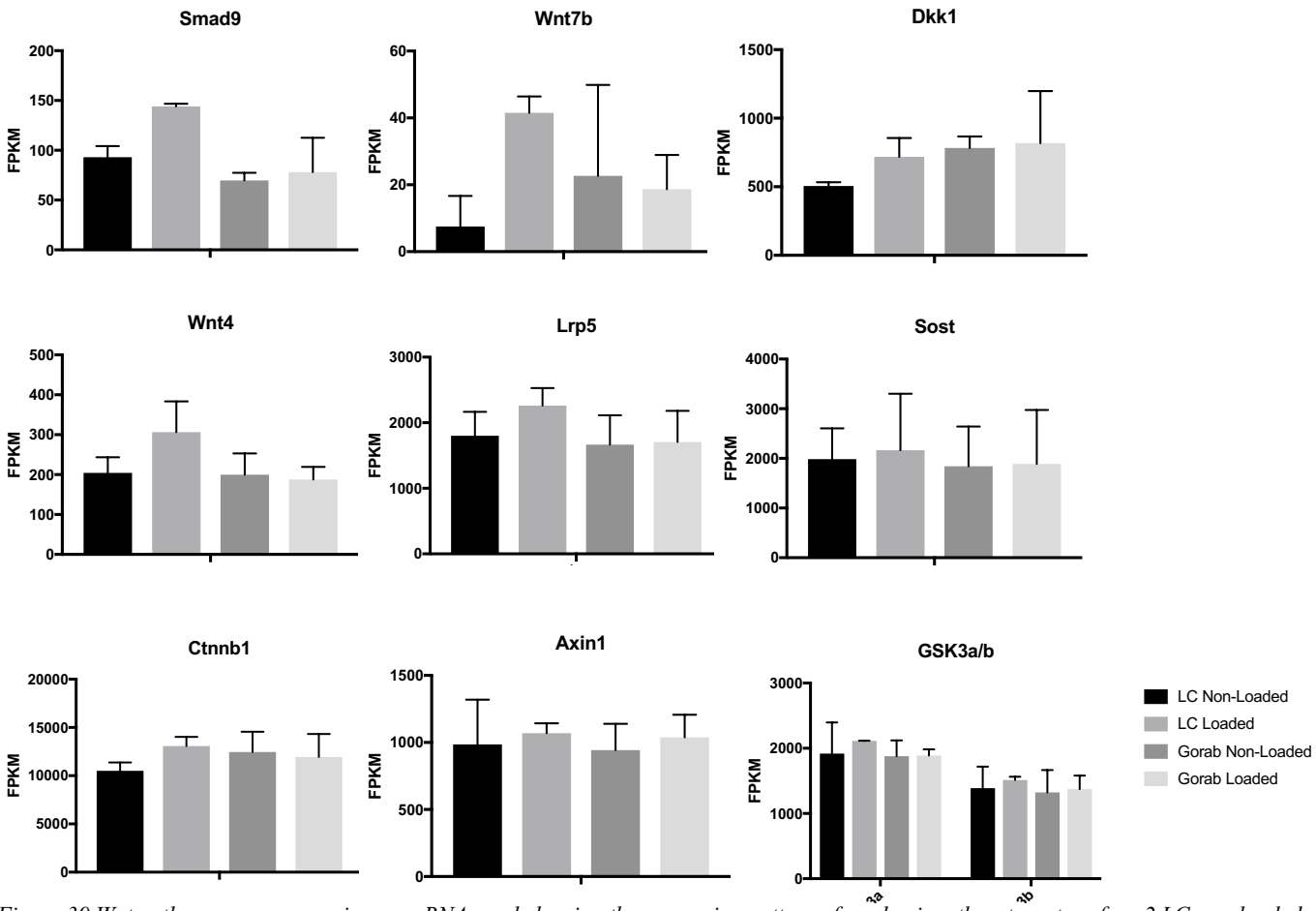

Figure 39 Wnt pathway gene expression on mRNA revel showing the expression pattern of predominantly osteocytes of n =2 LC non-loaded, n = 2 LC loaded, n = 3 Gorab^{Prx1} non-loaded and n = 3 Gorab^{Prx1} loaded tibiae. All animals were 10 weeks of age at the time the single loading procedure was applied and female. Reads were normalized to fragments per kilobase million (FPKM).

Collagen

ECM proteins were also investigated via RNAseq analysis. Only differential expressed genes were *Col1a1* and *Col1a2*. Col1a1 and Col1a2 showed similar expression profiles in LC mice.

Col1a1 sows an incredible increase of 95 % mRNA transcripts after loading in LC mice, similar to ***Col1a2***'s 70 % increased expression. Gorab^{Prx1} mice show no elevated expression after loading, tendencies to a little decreased pattern can be observed. The level of expression shows a similar level to non-loaded LC values (Figure 40). The collagen expression levels show the bone formation response in ECM proteins on mRNA level, which is not induced by mechanical loading in Gorab^{Prx1} tibial bone.

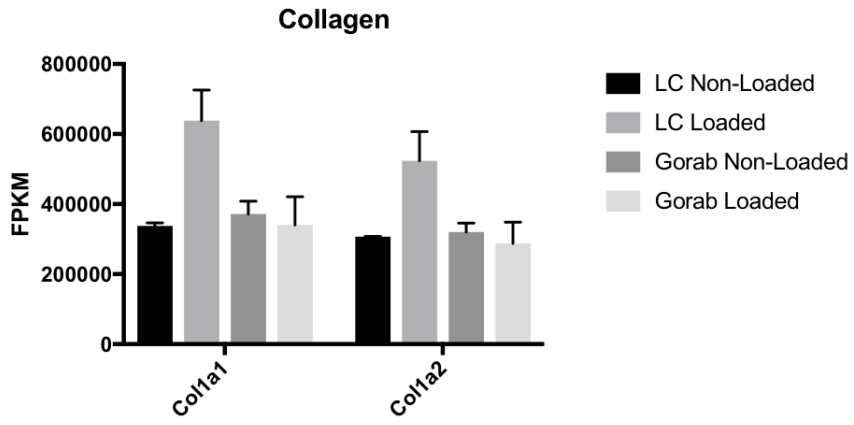

Figure 40 Col1a1 and Col1a2 gene expression on mRNA revel showing the expression pattern of predominantly osteocytes of n = 2 LC non-loaded, n = 2 LC loaded, n = 3 Gorab^{Prx1} non-loaded and n = 3 Gorab^{Prx1} loaded tibiae. All animals were 10 weeks of age at the time the single loading procedure was applied and female. Reads were normalized to fragments per kilobase million (FPKM).

Calcium channels needed for mechanical induced ATP release

Cacna1g and ***P2RX7*** coding for Calcium Voltage-Gated Channel Subunit Alpha1 G (*Cacna1g*) and Purinergic Receptor P2X 7 (*P2RX7*), proteins which are needed for calcium channels. These channel ATP to the pericellular space due to mechanical loading in osteocytes. Unfortunately, these genes did not show any relevant change due to loading in LC and Gorab^{Prx1} mice (Figure 41).

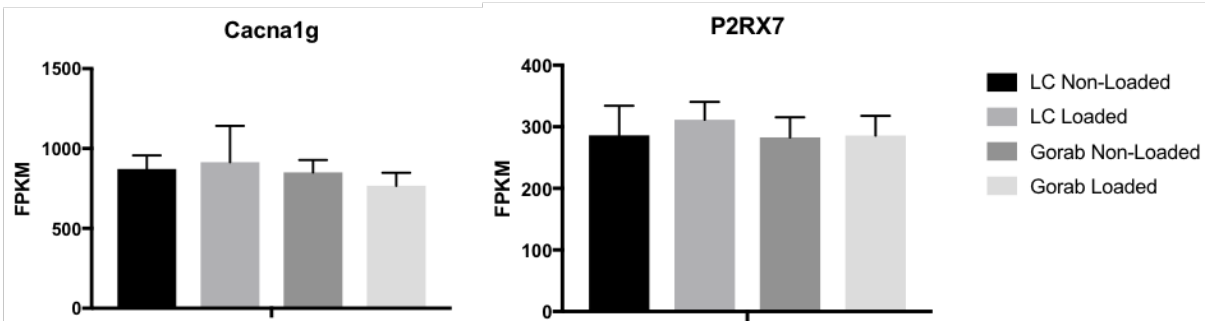

Figure 41 Cacna1g and P2RX7 gene expression on mRNA revel showing the expression pattern of predominantly osteocytes of n = 2 LC non-loaded, n = 2 LC loaded, n = 3 Gorab^{Prx1} non-loaded and n = 3 Gorab^{Prx1} loaded tibiae. All animals were 10 weeks of age at the time the single loading procedure was applied and female. Reads were normalized to fragments per kilobase million (FPKM).

Primary Cilium

Tubulinα1a (*Tuba1a),* which encodes the elongation proteins of the primary cilium and *Tubulinγ1* (*Tubg1*), which encodes the proteins needed for the basis of primary ciliae were also checked for mRNA expression levels after a single loading session (Figure 42).

Tuba1a shows in LC mice after loading a 27 % increase of transcripts, but in Gorab^{Prx1} animals a 4 % decrease was detected.

Tubg1 shows in LC mice an 13 % increase due to mechanical loading, but also Gorab^{Prx1} mice show an 9 % increase.

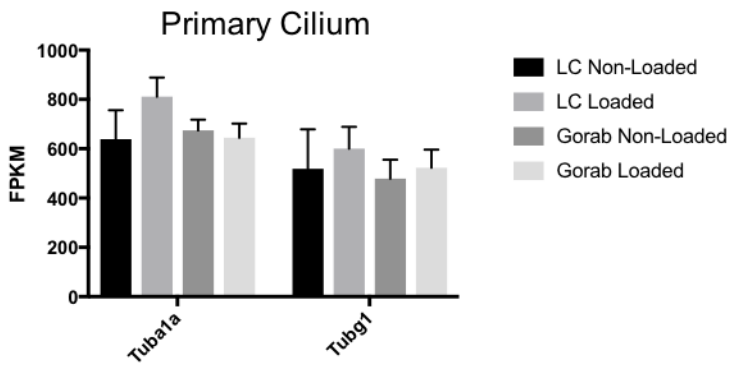

Figure 42 Tuba1a and Tubg1 gene expression on mRNA revel showing the expression pattern of predominantly osteocytes of n = 2 LC non-loaded, n = 2 LC loaded, n = 3 Gorab^{Prx1} non-loaded and n = 3 Gorab^{Prx1} loaded tibiae. All animals were 10 weeks of age at the time the single loading procedure was applied and female. Reads were normalized to fragments per kilobase million (FPKM).

Integrins, which are needed to connect osteocyte to the ECM protrusions and to the lacunae walls.

Itgb1, found on the osteocyte cell body showed a 17 % increase in mRNA transcription due to loading in LC mice. In Gorab^{Prx1} bone, on the other hand, the expression level without loading was on the level of the loaded LC, and decreases around 5 % after loading.

Itgb3, connecting the osteocyte dendrite at ECM protrusions, showed an interesting expression profile. In LC mice, the expression decreases due to loading around 85 % and in Gorab^{Prx1} mice around 82 %. Therefore, the effect shows similar patterns (Figure 43).

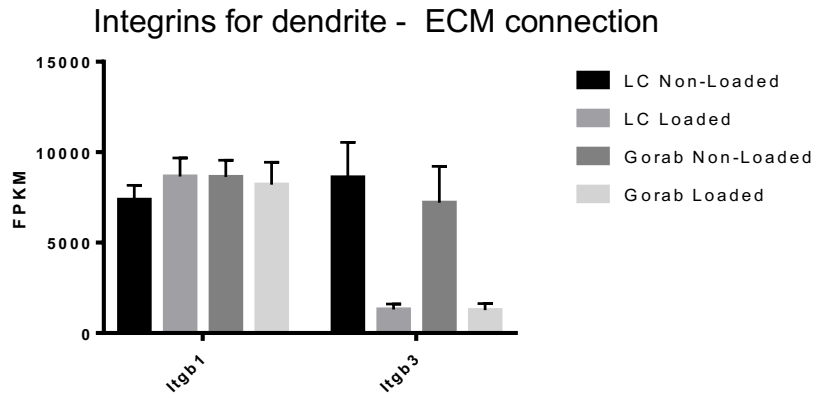

Figure 43 Itgb1and Itgb3 gene expression on mRNA revel showing the expression pattern of predominantly osteocytes of n =2 LC non-loaded, n = 2 LC loaded, n = 3 Gorab^{Prx1} non-loaded and n = 3 Gorab^{Prx1} loaded tibiae. All animals were 10 weeks of age at the time the single loading procedure was applied and female. Reads were normalized to fragments per kilobase million (FPKM).

Calveolin

Calveolin1 (*Cav1*), which is known to form sack-like structures in the plasma membrane of numerous cells is suspected to play a role in mechanotransduction. Our siRNA results show a clear increasing effect on the expression pattern of *Cav1* due to loading in LC and Gorab^{Prx1} mice. Therefore, no indication for further investigations were found (Figure 44).

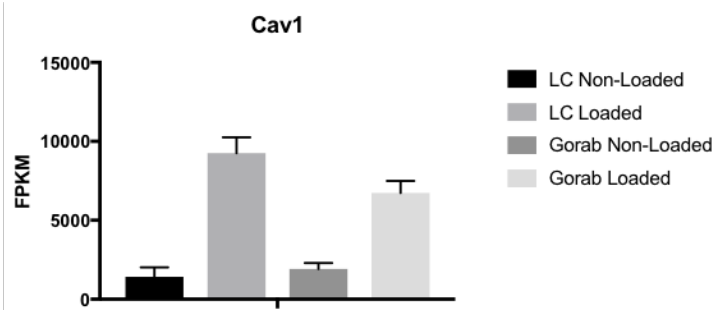

Figure 44 Cav1 gene expression on mRNA revel showing the expression pattern of predominantly osteocytes of n =2 LC non-loaded, n = 2 LC loaded, n = 3 Gorab^{Prx1} non-loaded and n = 3 Gorab^{Prx1} loaded tibiae. All animals were 10 weeks of age at the time the single loading procedure was applied and female. Reads were normalized to fragments per kilobase million (FPKM).

Intracellular calcium signaling

Important proteins for intracellular calcium release were evaluated to check for abnormalities on mRNA levels. ***Ryanodine Receptor 1*** (*Ryr1*) and ***Inositol 1,4,5-Trisphosphate Receptor Type 3*** (*Itpr3*) are two of the most important genes encoding for proteins needed for intracellular calcium release. Due to the high expectations for

these candidates, no mentioning differences between LC and Gorab^{Prx1} animals were detected due to loading. Ryr1 showed a decrease after loading in LC and Gorab^{Prx1}. Furthermore, Itpr3 showed a minimal increase after loading in LC mice to the expression level Gorab^{Prx1} animals showed with and without loading (Figure 45).

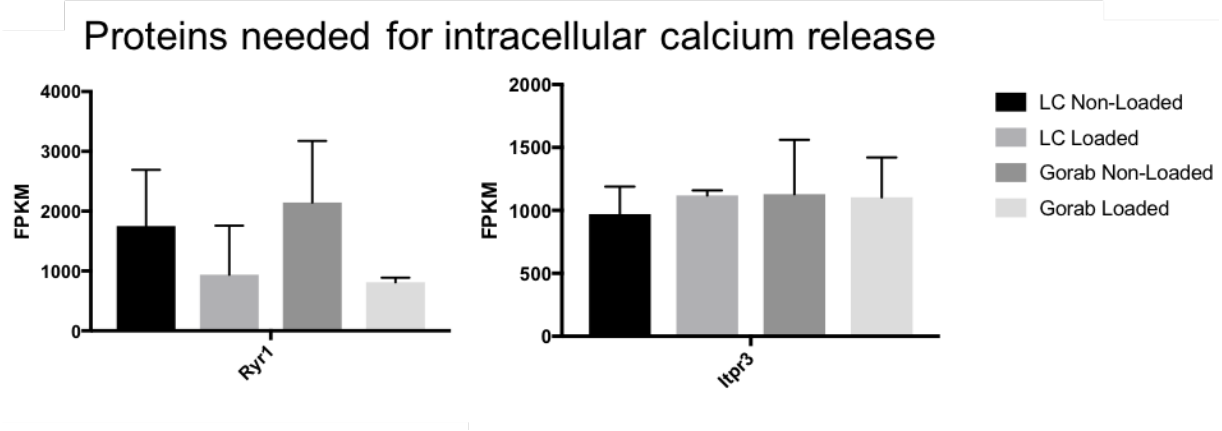

Figure 45 Ryr1 and Itpr3 gene expression on mRNA revel showing the expression pattern of predominantly osteocytes of n =2 LC non-loaded, n = 2 LC loaded, n = 3 Gorab^{Prx1} non-loaded and n = 3 Gorab^{Prx1} loaded tibiae. All animals were 10 weeks of age at the time the single loading procedure was applied and female. Reads were normalized to fragments per kilobase million (FPKM).

GAP-Junction

GAP Junction Protein Alpha 1 (*Gja1*) did show a 42 % increase in transcription rate in LC mice after loading. Whereas in Gorab^{Prx1} animals, only a slight tendency for upregulation due to loading was detected (Figure 46).

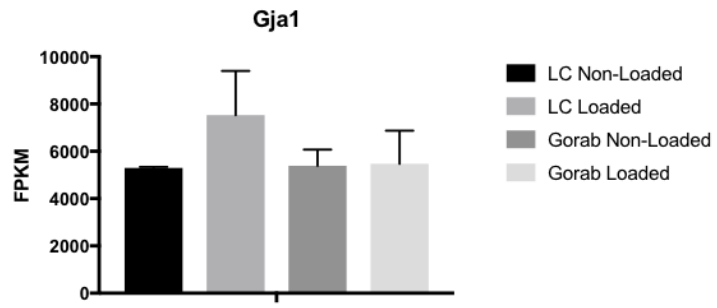

Figure 46 Gja1 gene expression on mRNA revel showing the expression pattern of predominantly osteocytes of n =2 LC non-loaded, n = 2 LC loaded, n = 3 Gorab^{Prx1} non-loaded and n = 3 Gorab^{Prx1} loaded tibiae. All animals were 10 weeks of age at the time the single loading procedure was applied and female. Reads were normalized to fragments per kilobase million (FPKM).

Fimbrin

As part of the osteocyte dendrite cytoskeleton Plastin1 (Pls1), decoding for the protein fimbrin, showed in both, LC mice and Gorab^{Prx1} animals in the loaded limb a reduction in mRNA transcription patterns (Figure 47).

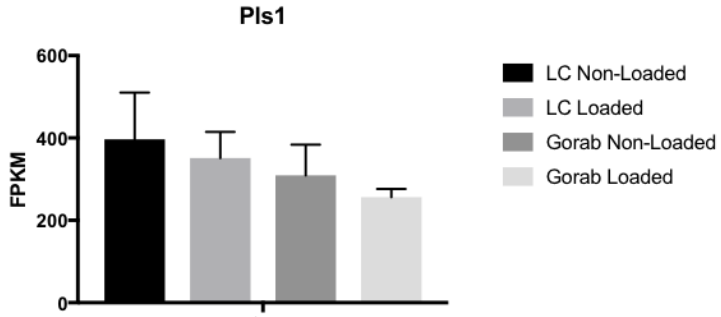

Figure 47 Pls1 gene expression on mRNA revel showing the expression pattern of predominantly osteocytes of n =2 LC non-loaded, n = 2 LC loaded, n = 3 Gorab^{Prx1} non-loaded and n = 3 Gorab^{Prx1} loaded tibiae. All animals were 10 weeks of age at the time the single loading procedure was applied and female. Reads were normalized to fragments per kilobase million (FPKM).

Membrane repair

Due to membrane disruption events during mechanical loading process the membrane repair mechanism was investigated. Interestingly ***Dysferlin*** (*Dysf*) was 33 % upregulated due to mechanical loading in LC tibiae, but in Gorab^{Prx1} tibiae no changes were detected regarding loading. Furthermore, ***Myoferlin*** (*Myof*) was also upregulated due to loading in LC mice. Contrary to the LC observations *Myof* was downregulated in loaded Gorab^{Prx1} tibiae (Figure 48). Protein Kinase C (Prkd1), which is under investigation to play a role in membrane repair, did show similar expression patterns in all cohorts (data not shown).

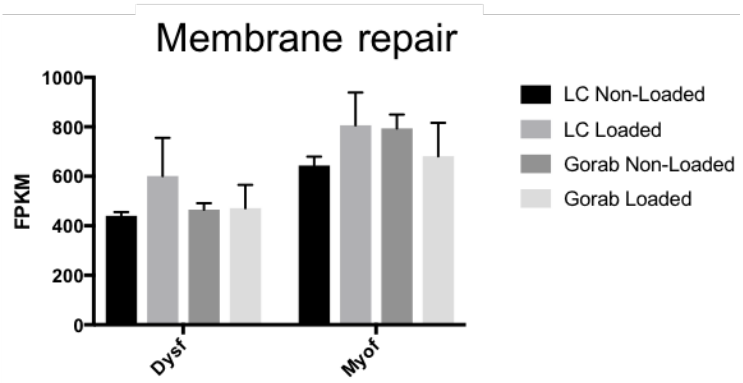

Figure 48 Dysf and Myof gene expression on mRNA revel showing the expression pattern of predominantly osteocytes of n =2 LC non-loaded, n = 2 LC loaded, n = 3 Gorab^{Prx1} non-loaded and n = 3 Gorab^{Prx1} loaded tibiae. All animals were 10 weeks of age at the time the single loading procedure was applied and female. Reads were normalized to fragments per kilobase million (FPKM).

3.5 Section V – *In vitro* approaches for mechanotransduction investigation in IDW-SW3 and MLO-Y4 cells.

IDG-SW3 a cell line, introduced by Lynda Bonewald is known to represent the late osteoblast, early osteocyte state[247]. IDG-SW3 cells were cultured to 80 % of confluence under differentiation conditions previous to siRNA driven knockdown of *Gorab* mRNA, which was executed in order to investigate the loss of Gorab *in vitro*.
Therefore, the ATP filled vesicle formation has been analyzed, as these vesicles also serve as a signaling pathway in mechanotransduction. Additionally, vesicle formation is conducted via the Golgi-apparatus, where the localization and function of Gorab protein is within the cell.
Furthermore, the calcium flux as intracellular signaling in general and under GAP-junction blocking conditions has been investigated.

3.5.1 ATP-filled vesicle formation *in vitro*

The number of vesicles, counted via ImageJ was neither impaired by the non-coding siRNA, nor the target siRNA for Gorab. Beside the number of vesicles per cell, number of vesicles per cell area was calculated and therefore the cell area has been measured. Area, covered by the cell also did not vary between the different siRNA transfections. As a result the mechanotransduction seems not be impaired by the ATP vesicle formation via the Golgi-apparatus (Figure 49).

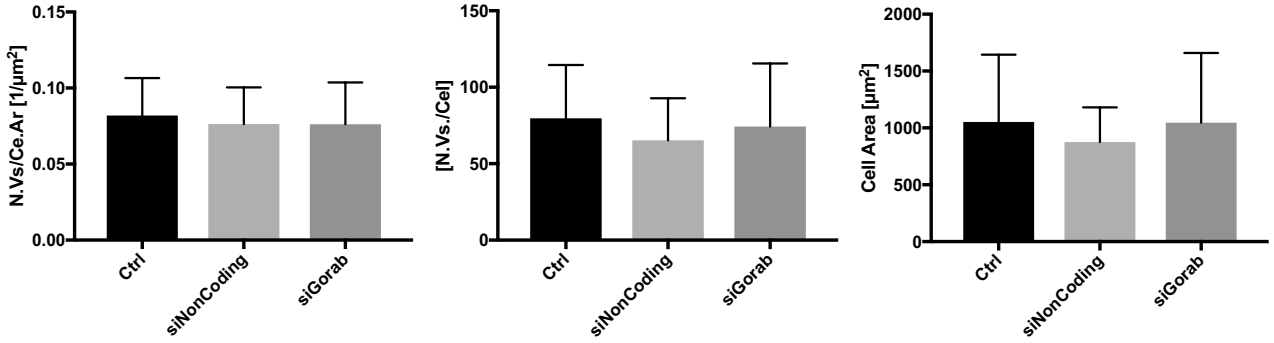

Figure 49 IDG-SW3 cells at 80 % confluency cultured in exclusively differentiation medium,(control), with additional siRNA targeting Scyl1bp1 mRNA or non-coding siRNA for three days, pictures taken subsequently to 30 min quinacrine staining for visualization of ATP storage sites.

3.5.2 Calcium signaling *in vitro* to mechanical stimulation

Calcium signaling is an important information pathway for cells to distribute information. It has been examined in neuronal system[248], gastrointestinal epithelium[249], bone and other tissues.

For the calcium signaling analysis IDG-SW3 cells were cultured up to 80 % of confluence under differentiation conditions and subsequently treated with siRNA transfection reagents. Ctrl was not treated with any transfection reagents, siNonCoding was treated with non-target siRNA and serves as another negative control and siGorab was treated with siRNA targeting the mRNA of *Scyl1bp1* (*Gorab*).

The number of activated cells in the ROI did not change between the non-transfected, non-target siRNA transfected and the Gorab-target siRNA transfected cells. Even after GAP-junction blocking with Octanol the number of activated neighboring cells did not change significantly (Figure 50). A possibility for this phenomenon would be a reduced connectivity in Gorab deficient cells, in keeping with the data found in the canalicular connectivity. However, due to the non-significance of the *in vitro* data this is pure speculation and likely based on the 2D cultivation conditions.

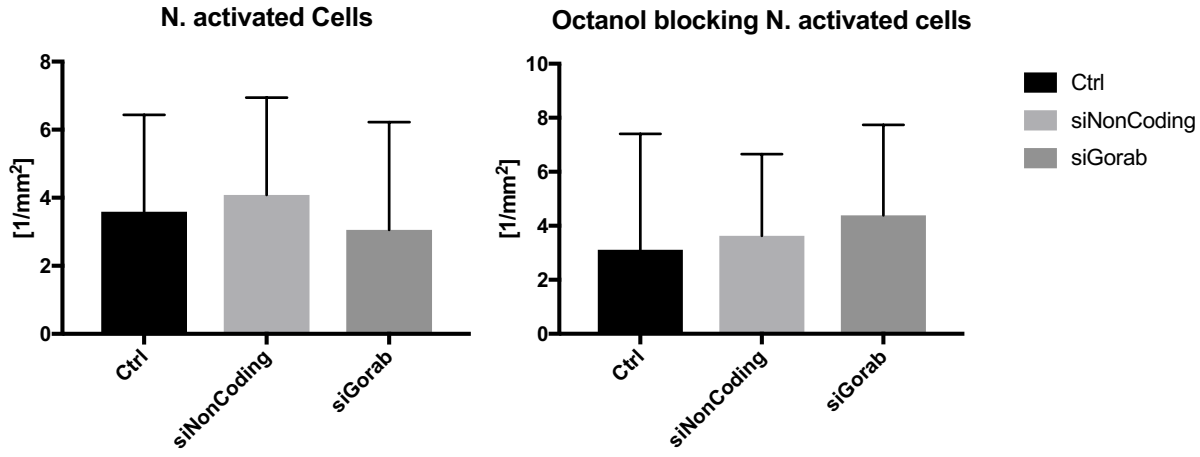

Figure 50 Number of calcium activated cells [1/mm²] and Number of calcium activated cells after octanol blocking [1/mm²] quantified after mechanical stimulation of a single cell in a 80 % confluent IDG-SW3 cultured in exclusively differentiation medium,(Ctrl), with additional siRNA targeting Scyl1bp1 mRNA or non-coding siRNA for three.

Mechanical stimulated cell reactions including membrane disruptions are categorized in a primary and secondary responses. Those are described by the following parameters, describing the intracellular calcium concentration:

Primary response parameters of the initially stimulated cell (Figure 51):

- Amplitude [A.U.],
- Full width at half maximum (FWHM) and
- Area under curve (AUC)

Secondary response of surrounding cells:

- Amplitude [A.U.],
- Percentage of activated cells within the ROI [%],
- Signaling radius within the ROI [µm] and
- Propagation velocity [s/µm].

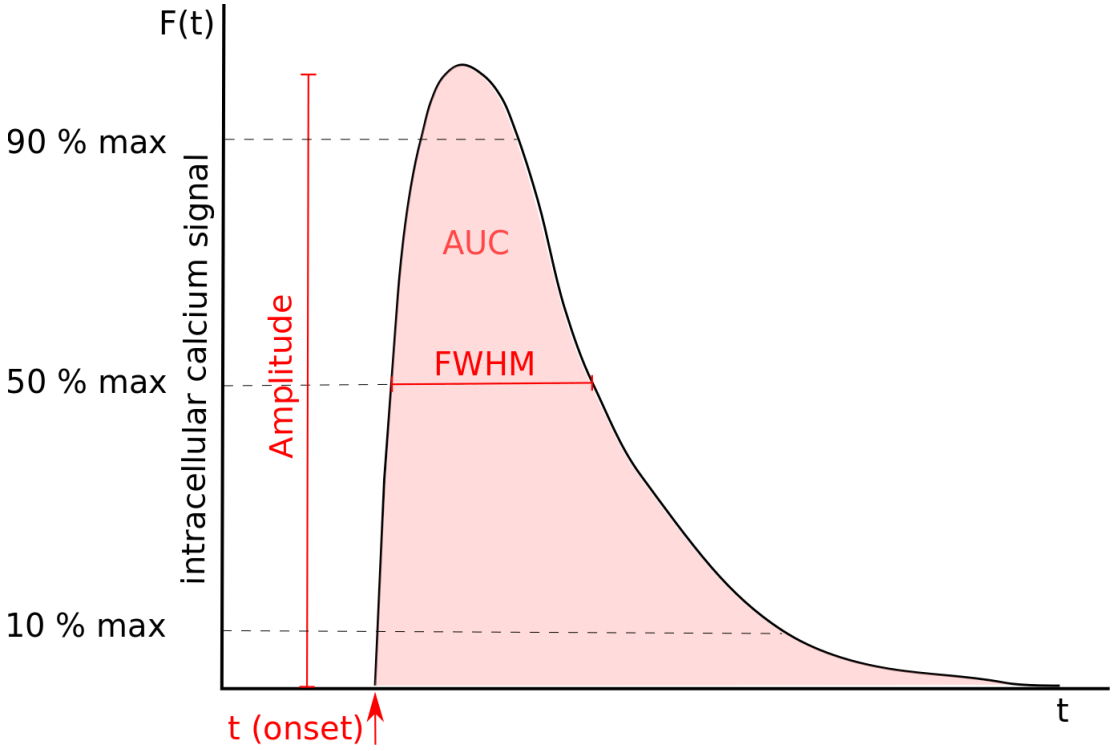

Figure 51 Graph of an idealized intracellular calcium signal after mechanical stimulation, showing the amplitude, area under curve (AUC), full width half maximum (FWHM) and the time of onset.

Primary response in IDG-SW3 cells did not change regarding knockdown of Gorab. Primary amplitude, FWHM and AUC did not change significantly in calcium signaling. Primary response after GAP-junction blocking was not impaired due to the reduced Gorab transcription. Significances due to non-target siRNA transfection were observed, but not comparing Gorab mRNA targeting siRNA transfection to non-transfected cells (Figure 52).

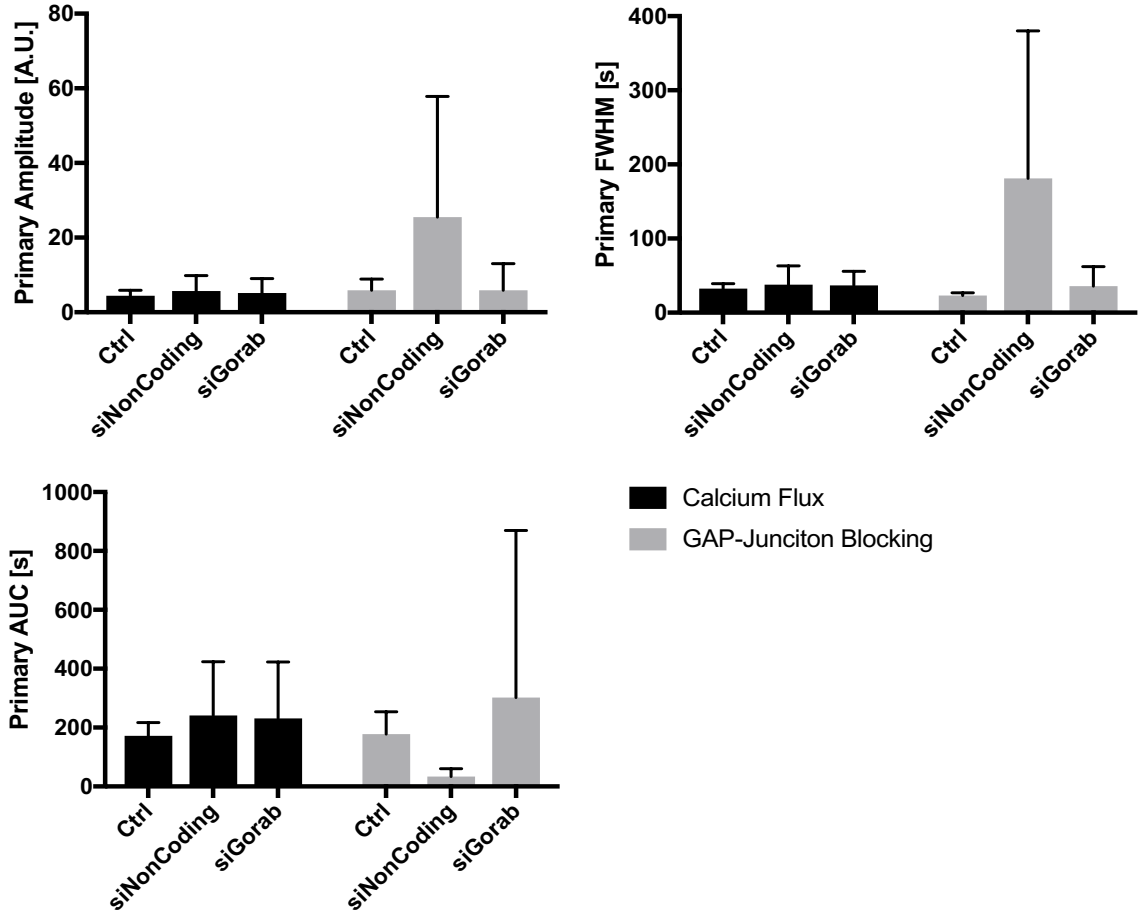

Figure 52 Calcium response in IDG-SW3 cells at 80 % confluency cultured in exclusively differentiation medium, or with additional siRNA targeting Scyl1bp1 mRNA or no target siRNA for 3 days, at day 4 single cells got mechanical stimulated by local membrane stimulation via a 10 µm deep micropipette poke, calcium flux response in the primary stimulated cells was measured using a ratiometric fluorescent calcium dye indicated in black, measured at f340/f380, cells additionally treated with the GAP-junction blocker Octanol are indicated in grey.*

Secondary response did not show any changes, neither in calcium flux, nor after GAP-junction blocking. Secondary amplitude, responsiveness, signaling radius and propagation velocity did not show significant reactions to transfection of non-target siRNA

or Gorab siRNA. Matching to its treatment the propagation velocity is reduced after GAP-junction blocking in all three groups (Figure 53).

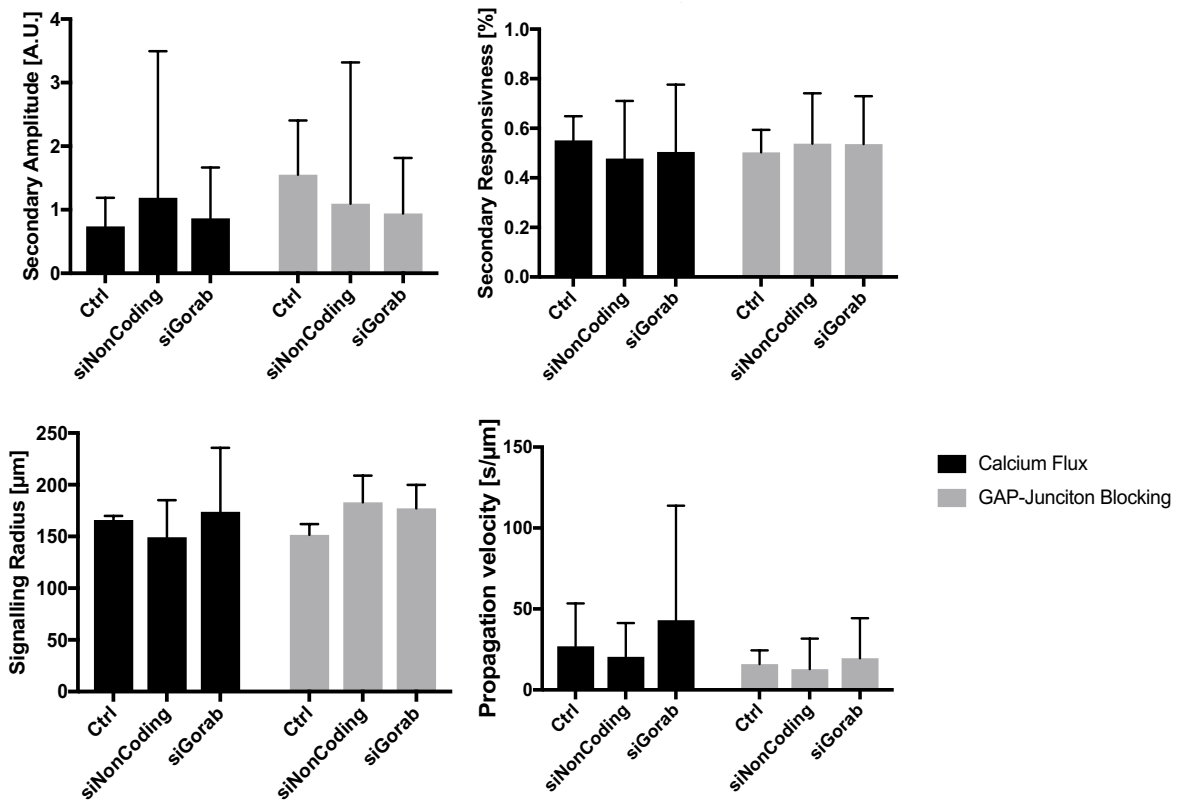

Figure 53 Secondary calcium response (secondary amplitude, responsiveness, signaling radius and propagation velocity) in IDG-SW3 cells at 80 % confluency cultured in exclusively differentiation medium, or with additional siRNA targeting Scyl1bp1 mRNA or no target siRNA for 3 days, at day 4 single cells got mechanical stimulated by local membrane stimulation via a 10 µm deep micropipette poke, calcium flux response in the secondary activated cells, and activation pattern parameters were measured using a ratiometric fluorescent calcium dye indicated in black, cells additionally treated with the GAP-junction blocker Octanol are indicated in grey.*

Summarizing the data regarding the calcium flux and the octanol blocking studies, no significant differences were found. In some cases with increase number of experiments some significances could be revealed.

3.5.3 Primary cilium characterization and quantification

The primary cilium is under intensive discussion to be a mechanosensory tool in the osteocyte network in bone. Therefore, the primary cilium was investigated in quantity and length. Quantity of the cilium did not show any changes after siRNA driven knockdown of *Gorab* mRNA (data not shown). Due to the relevance of the cilium length, assuming its connection to the lacuna wall the length was quantified via α-tubulin (Figure 54).

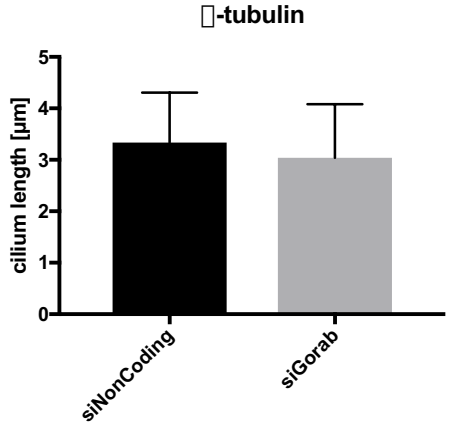

Figure 54 Primary cilium length measurements in 80 % confluent MLO-Y4 cells via α-tubulin immunofluorescense coupled with a ImageJ evaluation.

α-tubulin staining did show a 10 % relevant shortening in the length of the primary cilium. Regarding the estimations of the length of the osteocytic primary cilium *in vivo* the change reduces the length of 0.2 µm to 0.18 µm. It is very unlikely that the reduction in length explains the drastic loss of bone formation response in Gorab^{Prx1} animals on its own. Nonetheless, it could play a subordinated role.

4 Discussion

Bone mass declines with increasing age, due to a shift in the balance between bone formation by osteoblasts, and bone resorption by osteoclasts. This shift can be partially explained by a reduced anabolic response of the aging bone to mechanical stimulation. Since *gerodermia osteodysplastica* is a progeroid connective tissue disease with early onset osteoporosis we wanted to know whether a) an early loss of osseous mechanosensitivity is involved in the pathogenesis, and b) whether supraphysiological mechanical stimulation could rescue the bone phenotype. To our surprise, we found a complete loss of mechanosensitivity in Gorab-deficient bone tissue. Even though supraphysiological strains were applied, no anabolic effect could be induced. Higher strains were precluded due to the increased fragility of the mutant bone, meaning that for GO, other treatment options have to be considered.

4.1 Methodological aspects of the *in vivo* tibia loading model

This study is based on an *in vivo* tibia loading model, in which a maximum of 1200 με was induced for two weeks five times per week at a frequency of 4 Hz. This protocol was previously established after a series of optimization experiments[238, 250]. A strain magnitude of 1200 με is 3-4 times higher than the physiological strain experienced by mouse bones due to normal locomotion.

The anabolic response of *in vivo* mechanical loading has been shown in previous experiments, to depend upon both the strain amplitude and the strain frequency[251]. In some models a strain amplitude of 1200 με did not have a significant anabolic effect at 5 Hz, but only at 10 Hz[252].

The application of even higher frequencies is questionable. By applying higher frequencies, the pericellular fluid in the lacunar-canalicular network does not receive the necessary relaxation time (Relaxation time: τ = 0.005 s[253, 254]) needed to flow back to its starting position; if the frequencies are too high the fluid stays continuously at its endpoint[255]. Models suggested a response plateau around 10 Hz[256, 257]. With increasing frequency, the amplitude can be decreased for a proper bone formation reaction. Studies

found that 1820 με is efficient for 1 Hz, dropping to 1180 με at 5 Hz, and 650 με at 10 Hz[252].

Warden et al. also showed that 20 to 30 Hz frequencies result in only half of the induced periosteal rBFR/BS, after loading with identical stain amplitudes[257].

It is therefore possible that the missing anabolic response of *Gorab*^{Prx1} tibia was not due to a diminished sensitivity towards maximum strain, but to altered sensitivity towards frequency. In order to clarify this point, additional experiments would be needed in which the strain frequency is varied.

Prior strain gauging measurements allowed for a determination of the forces needed to cause this deformation in the two experimental groups of littermate controls and *Gorab*^{Prx1} mutants. However, due to experimental restrictions, it was not possible to determine the required force for each animal undergoing the 2 week loading protocol. The bone phenotype of *Gorab*^{Prx1} animals shows a variability, which may depend on individually different knockout efficiencies and on the absence or presence and timepoint of occasional tibia fractures, which could lead to changes in the curvature. For most bone parameters the variability in the tibia was 35-40% of the mean in *Gorab*^{Prx1} mutant mice compared to 15-25% in littermate controls[4, 258]. Theoretically, this could lead to an underestimation of the required force and thereby to insufficient loading.

4.2 Methodological aspects of bone adaption registration

The registration of bone adaption to supraphysiological mechanical stimulation was completed using a combination of methodological attempts, which investigated the reaction on several levels. Every method has its drawbacks, but due to the variety of methods used to discover the consistent, tremendous loss of mechanosensation in mutant animals, they do not impair the result reliability. Nevertheless, these drawbacks should be discussed.

The *in vivo* µCT picture registration holds a few minor weakpoints. The global threshold, which was chosen for the trabecular compartment and the cortical bone, did not vary between mutant and control animals. During the lacunar-canalicular network studies Paul

Roschger from the Ludwig Boltzmann Institute for Osteology executed quantitative backscattered electron microscopy (qBEI) on the samples, used for the network investigation. He found differences in the calcium composition of mutant and control animal cortical bone. Enforcing the different mineral composition in Gorab^{Prx1} mice TMD shows significant differences in mutant and control mice (3.1, 3.2.1.1). This could have led to exclusion of minor or non-mineralized bone tissue. Therefore, it would be beneficial to stain mineralized bone sections to distinguish if Gorab^{Prx1} animals show a high degree of unmineralized bone. Osteoid accumulations can inversely correlate with bone mineral density, assessed by µCT[259].

Furthermore, the continuous dose of radiation, is currently a point of debate as to whether it induces irreparable damages on the cellular level. This cellular damage is furthermore suspected to lower the ALP activity *in vitro*, an indicator for bone formation capacity[260].

Picrosirius red staining could be affected by the orientation of the collagen fibers, after sectioning. In general, color based evaluations completed using computational software are variable, although picrosirius red is a general stain for collagen fibers, and the evaluation by ImageJ is well established[261, 262]. Without a specific programmed macro, the evaluating person has to set an individual threshold for every picture, based on the orientation and polarization of the bone structure. Also for computational programmed macros several variabilities have to be considered during programming[263]. Variable color, owing to polychromatic staining of collagen fibers, variable background, fiber orientation in the section and the overall bone architecture are the main important factors, which must be taken into account.

RNAseq studies, which were executed to illuminate the cellular genetic response to supraphysiological strains have two main drawbacks. Firstly, unfortunately two RNA samples showed non-interpretable results in the bioanalyzer. Therefore, those samples were excluded from the RNAseq. This sample suspension led to insufficient n numbers, thus no statistical significant evaluation was possible. Two additional animals were already single loaded and the RNA is shipped to an external laboratory for RNAseq. Those results will be included in the planned publication.

Still, this study was used to identify target genes, which showed different expression profiles in mutant and control animals under loaded or non-loaded conditions.

Based on those qPCR will be executed for a selection of 11 target genes to validate the RNAseq results. By picking specific primer pairs the sample contamination can be ignored mostly.
Overall, it must to be kept in mind that RNA quantification is not representing the protein levels of target genes, but it is still a trustworthy insight to the cellular response.

4.3 Methodological aspects of lacunar-canalicular network investigation

By applying the methods used for the lacunar-canalicular network investigation, one can only grasp the phenotype and speculate on the mechanism behind the phenotype. Nontheless, the description of the network is of inestimable value on the way to mechanism elucidation. It does, however, only show the architectural result of the knockout. The chicken/egg problem, of whether the mechanosensation is impaired by the loss of Gorab, or the resulting network, is therefore not answered.
Unfortunately, from our experimental setup, is not possible to say how the adapted network affects strain amplification, mechanotransduction and signal transmission. It can only be stated that the network, which provides the framework for the mechanoresponse, is massively impaired. Modelling the effects of the network changes requires higher mathematical modelling to determine parameters such as Reynolds number, microflow velocity, pressure, frictional forces and shear stress[77, 86, 129].

4.4 Methodological aspects of mechanistic *in vitro* studies

In vitro models are generally only a very simplified attempt to simulate mechanisms and reactions of actually *in vivo* networked cells[264]. Three dimensional structure, interactions with other celltypes, different oxygen levels and tension, soluble factors and microRNAs of foreign origin, extracellular matrices and many other factors are not considered in the experimental setups used in this thesis.
In addition to the general limitations, the chosen cell types are only close to the original osteocyte, which is residential *in vivo*. Genetically modified imitations of osteocytes were used, which are only described as osteocyte-like cell lines[247, 265].

Furthermore, due to time limitations, a siRNA knockdown was used for the knockdown of Gorab. Compared to Crispr/Cas9 technology, which generates a stable knockout cell line, the knockdown efficiency achieved by siRNA technologies is not as functional[266].
Unfortunately, the cooperation partners have not yet managed to determine the knockdown efficiency of the trials. For a trustworthy interpretation of the experiments the knockdown efficiency should be min. around 70 %.
Furthermore, it must be kept in mind that single cell studies require a high number of experiments, due to the variability of reactions. Minimal divergences can lead to completely different outcomes.
The ATP-vesicle quantification showed that the number of vesicles is not affected. A possible explanation could lie in the non-stressed condition of the cells. No mechanical stimulation is applied to the cells before or during the experiment. Mechanical stress in the non-poked cells does not exist. The medium, however, contains enough nutrients to maintain vesicle production. If there is no consumption of ATP vesicles due to mechanical stress, no time related production impairment can be detected. Further studies should be carried out in a constant fluid flow over the entire plate to examine the cells for ATP vesicles after a short resting phase. This should provide information about the ATP vesicle production. Also, by measuring the released ATP and the vanished vesicle number, Myoferlin and Dysferlin functions could have been measured indirectly.
GAP junction function could only be investigated superficially in the chosen *in vivo* model. The cell connectivity can be reduced rapidly in the different cell types. Before and after Gorab knockdown, the connection ability of the cells can change. The effect of different GAP junction expressions after knockdown was also observed in other studies[195].

4.5 Changes in mechanosensitivity and bone structure in *Gorab*^{Prx1} mice vs. chronologically aged mice

Wolff's law, and later more definitively Harold Frost's mechanostat model, predict the adaption of bone tissue to mechanical loads[267, 268]. To give more detail: Frost predicts a

negative feedback system in which the input is local mechanical strain, induced by functional mechanical loading, and the output is a structurally appropriate bone[269]. Following this theory in areas of supraphyseological mechanical strains, the bone produces a stiffer construct in order to reduce the strains and reset the set point strains. On the other hand, during time experiencing lower strains than the set point, the tissue reacts with bone resorption, followed by a decrease of bone mass, and a newly set point in mass and architecture[269].

Several studies have investigated the effects of mechanical loading *in vivo* for different purposes[15, 236, 240, 241, 262]. The age related effects to mechanical strain was investigated by Willie et al.[238, 250] amongst others. In her study, young (10 wk), adult (26 wk), and geriatric mice (78 wk), underwent a loading procedure that was identical to that applied in the presented studies[238, 250]. Trabecular and cortical reactions in young and adult age showed similarities and differences to supraphysiological strain. But overall both cohorts showed anabolic responses, while 26 wk old mice reacted later with less pronounced osteogenic reactions[238].

A constant negative trend with age in endocortical and periosteal BFR/BS and MAR were detected. In the oldest cohort, the anabolic response was completely missing. This effect can be compared to Gorab^{Prx1}'s missing response to mechanical loading (3.1.1.2). Even so, the loading induced adaptive changes in the mineral and matrix properties in elderly mice, which shows, that loading has a positive effect on collagen maturity and mineral:matrix ratio[250]. Those effects were not evaluated in mutant animals during our loading studies.

Nonetheless, several studies showed, that the bone mineralization depends in the maturity of the collagen network[270, 271]. Picrosirius red staining indicates no changes in collagen composition regarding maturity in mutant mice. Therefore, the mineral content seemingly did not change with loading.

Since GO is a progeroid disorder, it seems reasonable to expect similar effects to loading in young mutant mice, comparable to those observed in adult C57Bl/6J mice. Namely a reduced anabolic response.

Our results show even a more severe phenotype for Gorab^{Prx1} animals. We found a complete loss of mechanoresponsiveness in µCT, dynamic/static histomorphometric

parameters and RNA based experiments showed no expression adaptions on mRNA level due to mechanical loading.

The reduced anabolic response in aged bone can be correlated with several age dependent changes in bone matrix architecture and cell status.

With increasing age, the trabecular bone in men and women shows reduction in BV/TV, Tb.Th and Tb.N[272-274]. Furthermore, the percentage area of trabecular resorbing surface increases significantly with age[275]. This can be correlated to a reduced osteoblast and/or increased osteoclast activity, which is different to the effect we discovered. No evidence in osteoclast or osteoblast activity changes were found in mutant animals (3.2.2.2). Cortical bone declines in Ct.Th and increases in Ct.Po, two main factors, which run bone fragility with age[276-279]. Comparing those changes to the GO model, many similar effects can be found. BV/TV, Tr.N, Ct.Th, Ct.Ar are all reduced in mutant animals.

Consequently we faced the question of whether the corresponding and dissimilar parameters in chronologically aged individuals, and the GO model, originate from similar reasons. In order to answer this question the origin for the loss of anabolic response had to be examined. It had to be discerned whether matrix related or cellular factors lead to the dramatic results.

4.6 Changes in ECM structure in Gorab^{Prx1} mutants and chronologically aged animals

Gorab^{Prx1} animals have a unique but unordered extracellular matrix in their Gorab deficient bone tissue. With *Gorab*'s loss of function, proteoglycans are not correctly processed in the Golgi-apparatus. As a result, collagen organization ends up in a less alternating orientation. Collagen fibers seem to be unordered without proper proteoglycan cross-linking. In contrast to disorganized collagen structures in Gorab^{Prx1} animals, in chronologically aged bone tissue collagen content reduces in men and women alike[280]. This reduction is correlated to an increased mineralization process in bone. Therefore, elasticity and resistance on both nano and micro levels change dramatically. This leads to ever decreasing bone strength, with the risk of fracture

increasing steadily. It has been shown that the non-enzymatic linkage of collagen fibers increases with age, contrary to the reduced cross linkage capacities in Gorab^{Prx1} mutants. Non-enzymatic advanced glycation end products are increasingly used for the inter- and intra-fibrillary linkage of collagen fibers[281-283]. This leads to an increased stiffness of the tissue, and consequently reduced boiling strength and fracture resistance[284-286]. Based on the increased stiffness, microcracks occur more frequently, which in turn leads to fracture bridges. These also lead to bone hardening. The enzymatic cross-linking between collagen fibers is not affected with age.

4.7 Abnormal extracellular matrix in *Gorab*^{Prx1} mutants – primary or secondary effect?

In general, laboratory mice have a lifespan of 2 years. Accordingly, animals are classified as “old” between 18-24 months[287]. The bone structure of laboratory mice develops extremely rapid in the first two months of life, with peak BMD and cortical size being reached between 3-6 months. Trabecular bone volume reaches its maximum after about 8 weeks in C57Bl/6 mice[288-292]. Taking this into account, in the current study young bone formation response is investigated.

The effect in chronologically aged bone is the opposite to that of bone weakening observed in Gorab^{Prx1}. In mutant animals a low mineralization and low cross-linking capability is observed. Nevertheless, a fracture risk is documented in patients and Gorab deficient mice. Investigating 4 week old animals, Chan et al. hypothesized that the phenotype occurs when embryonic woven bone is converted into mature lamellar bone. MAR was reduced in 4 and 12 wk old mutants, and in 4 wk old state an increased osteoid formation was observed. Additionally, qBEI analysis exhibited significantly greater regions of low mineralized bone, indicating an increased number of regions of primary mineralization in 12 week old mutants (data not shown).

The Gorab^{Prx1} bone phenotype is much more severe in 4 week old animals than in 12 week old animals. Presumably, Gorab deficient tissue is not able to stand the extreme amount of required cross linking proteoglycans in bone formation and development. Therefore, the produced collagens are not in an architectural physiological setup.

Afterwards, in 12 week old animals, seen in results of dynamic histomorphometry, µCT time lapse and N.Ob/B.Pm, the mutant skeleton tries to compensate the deficient bone by showing a high bone turnover (3.1.1.1, 3.1.1.2, 3.1.2.1, 3.2.1.1, 3.2.1.2, 3.2.2.2). Even if the phenotypes exhibits opposing characteristics in chronologically aged and progeroid bone, the effects result in a similar weak bone structure.

Seemingly, the skeleton attempts to gradually rejuvenate the aged skeleton after it has overjumped adulthood and is catapulted directly into a geriatric bone-strength (3.1.1.1, 3.1.1.2, 3.1.2.1, 3.2.1).

With age, the porosity increases and therefore the net loading area on a micro level decreases accordingly[293, 294]. This is a phenomenon shared in both chronologically aged bone, and in the here described progeroid bone. Mutant porosity is also elevated compared to control animals (3.3.4, 3.3.2, 3.3.3). Therefore, this also contributes to the low fracture toughness seen in mutants.

The ECM effects, are in my opinion, primary effects based on the loss of Gorab. As a secondary effect resulting from the altered ECM architecture the loss of mechanoresponsiveness was found.

If the knockdown efficiency is sufficient, *in vitro* experiments give additional indications for this theory, because no significant differences in mechanotransduction in Gorab deficient osteocyte like cell lines were observed.

Other progeroid disorders also exhibit fragile bone structures.

Marfan syndrome is the most common connective tissue syndrome. Patients exhibit dysregulated linear bone growth, reduced bone mass and also modulations in endogenous TGF-β activity[295]. To our knowledge no mechanical loading studies on bone of fibrillin-1 deficient mice have taken place at the time of writing. This is most likely because fibrillins represent only a minor component of bone matrix proteins (1-3 %)[296]. Only mechanical stimulation in aorta connective tissue has been investigated and described[297]. The studies showed that fibrillin-1 takes part in the mechanoresponse of cardiomyocytes[297]. I assume, that osteopenia in Marfan patients could also face problems in mechanotransduction. The long bones deformations already impair the physiological strain distribution and also TGF-β hyperactivity can also lead to osteoblastic differentiation impairments, such as those seen in our mouse model[4, 298].

Mutations in Lamin A/C exhibit reduced bone strength as a result of increasing fat infiltration[299]. Lipocytes did not reveal any abnormalities in Gorab^{Prx1} bone.
Zinc metalloprotease Zmpste deficient mice also exhibit spontaneous fractures and a dramatic reduction in cortical and trabecular bone volume. In contrast to our mouse model no increased bone turnover was manifest[300].

4.8 Cellular changes in *Gorab*^{Prx1} mutants

N.Ob/B.Pm shows a significant difference between LC non-loaded and loaded limbs, which is likely due to the increase Tb.BV/TV. Therefore, the number of osteoblasts per bone perimeter is more distributed/diluted in loaded bone. In LC mice, no bone formation defect is known, therefore the function of osteoblasts should be unaffected. The level of bone formation, requested by the mechanical loading, seemingly does not threshold further osteoblast recruitment and differentiation, because the already differentiated osteoblasts are able to process the initiated bone formation request.
A similar but definitely not as drastic effect can be observed in Gorab^{Prx1} metaphyseal trabecular bone. The effect of loading does not show significant changes in N.Ob/B.PM or BV/TV, only tendencies can be observed.
If these tendencies were to be questioned; based on the similarity to the in LC described significant effect, no impairment of Gorab^{Prx1} osteoblast function would be described.
Interestingly, N.Ob/B.Pm shows in the ANOVA an effect in phenotype. Therefore, those elevated numbers in osteoblasts per bone perimeter resemble the skeletons try of rejuvenation. The higher, not strain directed bone formation in Gorab^{Prx1} bone tissue is likely the effect of the elevated osteoblast numbers.
Supposable osteocytes transmit much less but widely distributed signals (not as concrete as in LC bone), which they sense and translate from mechanical loading, or other effectors, like microcracks[301-303].
Interestingly, N.Ot/B.Ar uncoupled from loading mutant animals show a massively higher number of osteocytes per bone area. Even the N.Ot counted in Gorab^{Prx1} sections, in both loaded and non-loaded, is slightly higher compared to both non-loaded and loaded sections of LC tibiae. After completing the cellular histomorphometry, the massive amount

of osteocytes in Gorab^{Prx1} tibiae was the strongest and only documented anomaly in the cellular investigation, matching the phenotype (explained *via* an impairment of the mechanoresponse).

4.9 Changes in the osteocyte lacunar-canalicular network

Analyzing the lacunar geometry gave insights into the osteocyte residential space within the bone structure. In Gorab^{Prx1} diaphyseal, cortical bone lacunae with a significant reduced volume and a spherical geometry were found. These findings match the morphology of old osteocytes in human and mice, or osteocytes which did not differentiate properly[304, 305]. A differentiation defect of the osteoblastic cell line found in 4 week old mutant animals is already known to exist[4]. Additionally, RNAseq data executed during these studies also illustrated a similar expression pattern in 10 week old animals, indicating a dysregulated differentiation process (3.4).

Osteocytes evolve from osteoblasts, which show a cubical morphology on the bone's surface. While being embedded in the newly formed bone matrix, osteocytes undergo a crucial morphological reassemble of the cytoskeleton[21]. In the following osteocytes form the shape of their lacuna and cleave their way through the bone matrix in order to connect *via* cell processes to the lacunar-canalicular network[58].

Therefore, the osteocyte likely defines the shape of their lacuna. With an altered shape of the bone sensing cells, their cytoskeleton should in turn also indicate an altered architecture. As the most important intracellular mechanical strain distribution system the cytoskeleton has within the osteocyte dendrites and the cell body specific functions, which are directly linked to their architecture[306, 307]. The osteocyte cytoskeleton within the osteocyte cell body is needed to transmit information, received from the actin-fimbrin cytoskeleton in the dendrite to the nucleus, where the mechanical signals get transduced into gene expression profiles[308-311]. Another function of the cytoskeleton is the activation of mechanical inducible membrane channels, integrins, and other proteins[306, 307]. With a change in architecture the cell specific function in mechanotransduction is also changed and therefore, maybe impaired.

Due to the high amount of lacunae and non-terminal differentiated osteocytes found in cortical mutant bone, it appears that the organism tries to compensate the lack of mechanoresponsiveness, as observed in the dynamic histomorphometry (3.2.2.2).
Investigation of the canalicular network showed a cruel reduction in number of canaliculi per lacuna in Gorab^{Prx1} diaphyseal cortical bone. Matching these findings, the canaliculi density is drastically lower compared to LC bone. The reduced connectivity, which results from these findings, can partly explain the lack of mechanoresponsiveness.
With a reduced number of canaliculi a reduced mechanotransduction is associated[312]. Additionally, a reduced edge length documented the decrease in overall length of the network, which reduces the sum of available volume of mechanotransduction. Zhou et al. showed that convective transport rate is proportional to the canalicular density and inversely related to the canalicular length[313]. After ATP and other signal molecules are released, the convective transport plays an important role in transmission of the signal, therefore the signal distribution is massively impaired in Gorab^{Prx1} animals.
Additionally, the length and anatomy of the lacunar-canalicular network has a great effect on the diffusion rate and transport in the network. Rate of transport due to pure diffusion is proportional to the canalicular density, which is much lower in Gorab^{Prx1} cortical bone[314]. The reduced connectivity could be the reason why the vascularization is more than 8 times higher in Gorab^{Prx1} cortical bone compared to LC animals.
Osteocytes show an orientation of connectivity to the peripheral regions, the endosteum and periosteum, where osteoblasts and osteoclasts reside (Figure 29). In Gorab^{Prx1} less connected lacunae can be observed. In the case of a mechanical originated tissue deformation, signals originating from the central cortical bone are increasingly diluted/weakened from osteocyte to osteocyte due to the decrease in dendrite connections (intracellular calcium signaling). Additionally, the lower number of canaliculi reduce extracellular signals (convective ATP signaling) until they reach the surface.
Taking the altered ECM composition into account, further impairments of the mechanotransduction process could be possible. For example, ECM hillocks, which are needed for integrin connection and therefore activation of FAK, could be reduced in size or number or composition. Dramatic proteoglycans changes, which are needed as binding

partners of integrins, could be reduced or altered. Also ECM tethers, which span the dendrites in the canaliculi, could be impaired.

4.10Possible roles of changes in vascularization

As implied previously, the vascularization in Gorab^{Prx1} diaphyseal cortical bone is significantly higher compared to LC mice. Reduced diffusion conditions for nutrient and oxygen supply, based on the short length of canaliculi and the increased number of cells to be supplied, justify the high vascularization. Furthermore, osteocytes are under discussion of soluble factor secretion, such as the vascular endothelial growth factor (VEGF) in order to induce vascularization[315]. The high vascular porosity also equating to large decrease in bone mass and density. Furthermore, high porosity leads to weakening of cortical bone resulting in loss of stiffness and reduced load tolerability[316-319], which can be seen in spontaneous fractures of both GO patients and also Gorab^{Prx1} animals.

4.11 May Gorab play a role in mechanotransduction through the primary cilium?

It has been reported, that due to the loss of Gorab in hair follicle morphogenesis, the primary cilium formation is significantly reduced[320].

Due to the primary cilium's broad sensory function, it became an important candidate for taking a notable role in mechanosensation in bone. As described by Vaughan et al. if the primary cilium forms a loosely connection to the ECM wall it would play a role in osteocytic mechanosensation. Furthermore, they calculated that the mechanosensation capability grows proportional to the length of the cilium[191]. Those two hints lead to the analysis of the expression profile of the two most abundant structure proteins of the primary cilium, *Tuba1a* and *Tubg1*. Tuba1a, which illustrates the length of the cilium exhibits higher expression profiles in loaded LC tibiae. Gorab^{Prx1} tibiae show no response in the Tuba1a expression profile.

It is possible that primary cilia are damaged or destroyed during the mechanical load induced fluid flow. Subsequently, the cilium is repaired, or renewed. If the network in Gorab^{Prx1} bone does not give the fluid enough volume to form a proper flow, there is no

chance of damaging the primary cilium, and no need for upregulating *Tuba1a*. Otherwise, if the primary cilium is indeed damaged, and the loss of Gorab impairs the expression of *Tuba1a*, the mechanoresponsiveness could be impaired, but this is very unlikely based on the current knowledge of Gorab's function in the Golgi-apparatus.

Tubg1 shows similar expression profiles in LC and Gorab^{Prx1} tibiae. In loaded limbs a slight increase was detected. The position of γ-tubulin, which forms the base of the primary cilium indicates that in non-loaded and loaded limbs the quantity should be comparable in LC and mutant bone.

What caught the attention is the not elevated expression in loaded Gorab^{Prx1} bone of *Tuba1a*. It appears that the length of the cilium is a very sensitive parameter for the mechanosensation process. Therefore, in mechanical stressed osteocytes *Tuba1* should be expressed on comparable levels, especially if in control animals the expression increases.

Therefore, the primary cilium was chosen for further *in vitro* investigation. Even, if non-response in expression levels in Gorab^{Prx1} also could be based on an upstream impairment.

Since the measured difference between mutant and control cilia is only 10%, it cannot be assumed that the loss of Gorab could cause biological effects. Possibly the 10 fold length difference between *in vivo* osteocyte primary cilia and *in vitro* cilia is evoked by the cell-type difference, or the culture conditions, and the environment would change the mutant and control osteocyte cilia ratio. To quantify the length difference *in vivo* immunohistology stainings of alpha tubulin should be executed. Unfortunately, no sections are available at the time of writing.

4.12 Possible calcium regulation changes in Gorab

Ryr1 and *Itpr3* gene products are presented as model proteins, based on their importance in intracellular calcium release. Their expression does not raise any assumption for an impairment or anomaly in intracellular calcium signaling. But it has to be kept in mind, that proteins like Ryr1 and Itpr3 are not the only factors who could impair the calcium signaling. Membrane channels and membrane disruptions also provide calcium to the cells.

Therefore, the intracellular calcium signaling, which acts as mechanotransmission pathway within the osteocyte network was investigated by *in vitro* studies.

The primary response shows in intracellular calcium levels no significance comparing Gorab deficient and control cells. Therefore, the initial reaction of ER calcium release and uptake from the surrounding environment seems unimpaired, like shown on mRNA levels. Interestingly *GAP-junction protein Alpha 1* (*Gja1*) shows a 42 % increase of their mRNA transcripts (FPKM) in LC bone. This response to mechanical load is missing in Gorab^{Prx1} tibae. Based on those results GAP-junctions came under suspicion to play a role in the loss of mechanoresponsiveness. *GJA1* is highly expressed in heart cells and are thought to have a crucial role in the synchronized contraction of the heart. This implies a mechanical high stability of the protein, leading to the conclusion, that it is unlikely they will be destroyed or damaged due to mechanical stress.

Even so, a higher expression is detected in loaded LC bone. Therefore, for some reason a loaded healthy bone has a higher requirement of GAP-junction proteins.

In vitro mechanical loading studies testing for calcium flux within the culture plate did not reveal any, significant changes in Gorab deficient and control cells. Both GAP-junction blocked and non-blocked experiments did reveal any impairment.

From those data an unimpaired calcium communication within the network can be suspected. A final prove that the calcium flux and GAP-junction function is unaffected a higher number of experiments have to be executed.

4.13 ATP-containing vesicle formation for membrane repair and information transmission

ATP release is a signaling pathway for mechanical stressed osteocytes. Due to mechanical strain, ATP is released *via* membrane channels to the pericellular space. These molecules are washed away with the pericellular flow, inducing a response in neighboring osteocytes.

Also due to the pericellular fluid flow induced by mechanical deformation of bone, the osteocyte membrane usually disrupts under high shear stress, while losing free ATP molecules by the damage.

This mechanism acts as a double pathway. In order to repair the membrane disruption the cell provides ATP containing vesicles, which fuse with the cell membrane, under the assistance of ferlins, to fill the membrane damage. On the other hand, the vesicle cargo, in this case ATP molecules, undergo exocytosis and are washed away to neighboring cells, which receive the ATP signal and react with elevated calcium intake for further signal transmission[321].

Based on the altered expression profile of exocytosis proteins (Myoferlin and Dysferlin) in loaded mutant bone, the above described mechanism became a point of focus.

Studies revealed that mutations in the Dysferlin encoding gene lead to vesicle accumulations beneath mechanical induced membrane disruption sites without vesicle-membrane fusion[322]. Therefore, they are essential for exocytosis.

To rule out the possibility of an overall affected ATP vesicle formation, the number of ATP filled vesicles was estimated in IDG-SW3 cells after siRNA driven knockdown of *Gorab* mRNA.

Due to higher expression profiles in loaded LC tibiae, it seems reasonable that ferlins are consumed during downstream processes induced by mechanical stress. For both genes, no upregulation in loaded Gorab^{Prx1} tibiae was documented. One possible explanation could be that, the fluid flow is not as strong to lead to membrane disruptions in Gorab deficient bone. Therefore, not only the pericellular ATP concentration would be massively reduced, but the strain amplification would be impaired.

If Dysf and Myof take actively part in the fusion of vesicles and membrane the focus should be shifted to the original function of Gorab in the Golgi-apparatus:

Gorab takes part in the retrograde vesicle transport and furthermore in the posttranslational processes of several proteins. Vesicles fusing with the membrane often express signal molecules on the surface. If those surface molecules are altered or missing in the vesicle membrane as an effect of the loss of Gorab, vesicles cannot fuse properly with the cell membrane and the cell cannot regenerate properly.

This mechanism could be a possible impairment, leading to the loss of mechanoresponsiveness.
Unfortunately, no differences in number of vesicles per cell were detected. Therefore, we concluded that vesicle formation is not impaired due to the loss of Gorab.

Cacna1g and *P2RX7* are proteins needed in calcium channels, in order to channel ATP. Both genes display similar expression profiles in LC and Gorab^{Prx1} samples. In both, no response to loading was detected, which leads to the conclusion of unimpaired ATP channeling in Gorab^{Prx1} animals. Channel based ATP release as a mechanotransduction mechanism should therefore not be impaired.

4.14 Possible roles of altered TGF-β signaling in *Gorab*^{Prx1} mutants

Our group has published data showing, that active TGF-β is massively upregulated in Gorab^{Prx1} animals. Using RNAseq, active TGF-β cannot be detected. Only total TGF-β was measured, showing no difference between LC and Gorab^{Prx1} mRNA expression profiles. This matched the data our group collected for total TGF-β in our previous studies. Therefore, the effect found in 4 week old mutants cannot be ruled out, nor neglected, using these methods. Western blot analysis would have to be executed to quantify the amount of active TGF-β. No response to loading in Gorab^{Prx1} tibiae was detected in Smad9 expression levels, but in LC animals. Studies showed that Smad9 is a transcriptional regulator of BMP signaling[323]. BMP's are the largest subfamily of the TGF-β family. Smad9 expression is normally increased by BMP signaling, which in return reduces BMP activity, acting like a feedback mechanism[323]. Therefore, in loaded LC mice higher BMP activity may be possible, which would in turn match the documented bone formation response to loading in LC. In addition, the missing bone formation response in Gorab^{Prx1} animals could be explained by a non-elevated Smad9 expression.

4.15 Possible roles of altered WNT signaling in *Gorab*^{Prx1} mutants

Differential expression profiles between LC and Gorab^{Prx1} samples in Smad9, Wnt7b, Wnt4, Lrp5 and Dkk1 where evident, when analyzing the most important genes, whose gene products take part in the Wnt pathway. Sost, Ctnnb1, Axin1 and GSK3a/b did not exhibit differing expressing profiles in non-loaded and loaded samples.

Wnt4 is under debate as to whether it favors bone formation by inhibiting the RANKL-induced phosphorylation of TGF activated kinase 1, which results in suppression of osteoclast differentiation[324]. Therefore, the in LC loaded tibiae elevated expression level can be explained *via* the physiological bone remodel response to mechanical loading. The missing response in Gorab^{Prx1} tibiae is in line with the rest of the non-responding Wnt target genes. Nevertheless, the number of osteoclasts do not differ significantly in LC and Gorab^{Prx1} bone, even in loaded LC animals, where Wnt4 is elevated after mechanical loading. Both groups still show a tendency of increased osteoclast numbers per bone area. Therefore, the numbers of osteoclasts are not influenced exclusively by Wnt4.

Wnt7b has been shown to be a crucial factor for bone formation *in vivo via the activation of mTORC1*[325]. The massive upregulated Wnt7b expression level in loaded LC matches with the cited studies, which award Wnt7b the induction of bone formation. Furthermore, the consistent high expression level of Wnt7b in Gorab^{Prx1} tibiae matches the higher endocortical and periosteal Ct.BFR/BS.

Also, the similar expression level in Gorab^{Prx1} non-loaded and loaded tibiae points to the loss of mechanoresponsiveness. Upstream mechanisms must to be investigated in further studies, in order to understand why the positive Wnt pathway response is missing.

Studies implied that Lrp5 plays a role in bone responsiveness to mechanical loading. Lrp$^{-/-}$ mice show almost no bone formation to loading[114]. Mechanistic details remain to be fully understood.

In our RNAseq data, Lrp5 exhibited a higher expression profile in the loaded LC tibia compared to the non-loaded LC tibia. This finding matches the increased bone formation found in LC mice after two weeks of loading. RNAseq was completed after a single loading session. Bone formation was measured during a two week loading program, and so it can be speculated that the effect of continuous loading causes the Lrp5 levels to further elevate. Therefore, the positive Lrp5 correlation to loading, described by other groups, such as Johnson et al., was documented on RNA level[326]. In both Gorab^{Prx1} tibia,

the expression level is comparable to the non-loaded LC sample. Therefore, a general expression level is not impaired, but the non-loaded Gorab^{Prx1} sample does not show any difference to the loaded. This could be a hint towards an upstream impairment, which is not transduced in osteocytes, which would lead to Lrp5 upregulation due to mechanical loading. In addition, the non-upregulation of Lrp5 could be partwise responsible for the missing mechanoresponsiveness.

Interestingly Dkk1, which normally inhibits Lrp5, which in turn promotes bone formation shows similar expression pattern in LC tibiae. Dkk1 therefore controls the Lrp5 induction of bone formation to circumvent an exorbitant bone formation. Expression of Dkk1 in Gorab^{Prx1} tibiae is not changed after loading, but is constant on the loaded level of LC. Therefore, Dkk1 is inhibiting Lrp5 in an over-proportional manner and could explain the low bone formation rate in Gorab^{Prx1}.

Overall, the Wnt/TGF-β pathway seems non-responsible to mechanical loading in Gorab^{Prx1} tibiae.

If the strain amplification within the lacunar-canalicular network does not threshold the mechanosensation, nor is an impaired mechanosensation itself, then being by any cellular mechanosensors could explain the non-responsiveness of Wnt/TGF-β pathway.

4.16 Conclusions

The mechanism behind the loss of mechanoresponsiveness cannot be narrowed down to one specific impairment or target. Similar to most pathomechanisms several factors interact and reinforce each other. Figure 55 and Figure 56 show that the loss of Gorab impairs the osteocyte differentiation, retrograde vesicular transport and proteoglycan glycosylation. Furthermore, all of these mechanism are tightly related to each other, influencing and bolstering each other. Even if other mechanisms or pathways are under further investigation to uncover the holistic mechanisms of Gorab, which lead to GO's pathology, Figure 55 shows a possible scenario leading to one of GO phenotypes, the early onset osteoporosis. Our group focused especially on Gorab's capacity in the Golgi-apparatus trafficking, which is connected directly to two out of the three proposed causes of the loss of mechanoresponsiveness.

This study revealed a crucial loss of mechanoresponsiveness in Gorab^{Prx1} animals. As a mouse model of the progeroid disorder *Gerodermia osteodysplastica,* exhibiting osteoporotic bones ,we were thereby able to shed a light on the cause for this phenotype. Additionally, we were able to exclude osteoblasts and osteoclasts as GO therapeutic targets. Furthermore, we showed that the lacunar-canalicular network is heavily impaired in connectivity and canaliculi length. As research targets for new therapies for GO and other bone related diseases the ECM and therefore the osteocyte lacunar-canalicular network should move further into focus.

Our results provide an invaluable and detailed description of loss of mechanoresponsiveness and its morphological foundation. Furthermore, we were able to eliminate several cellular mechanotransduction and signal transmission processes as agent. Additionally, we are well placed to advise of the need for analysis of several possible pathomechanisms.

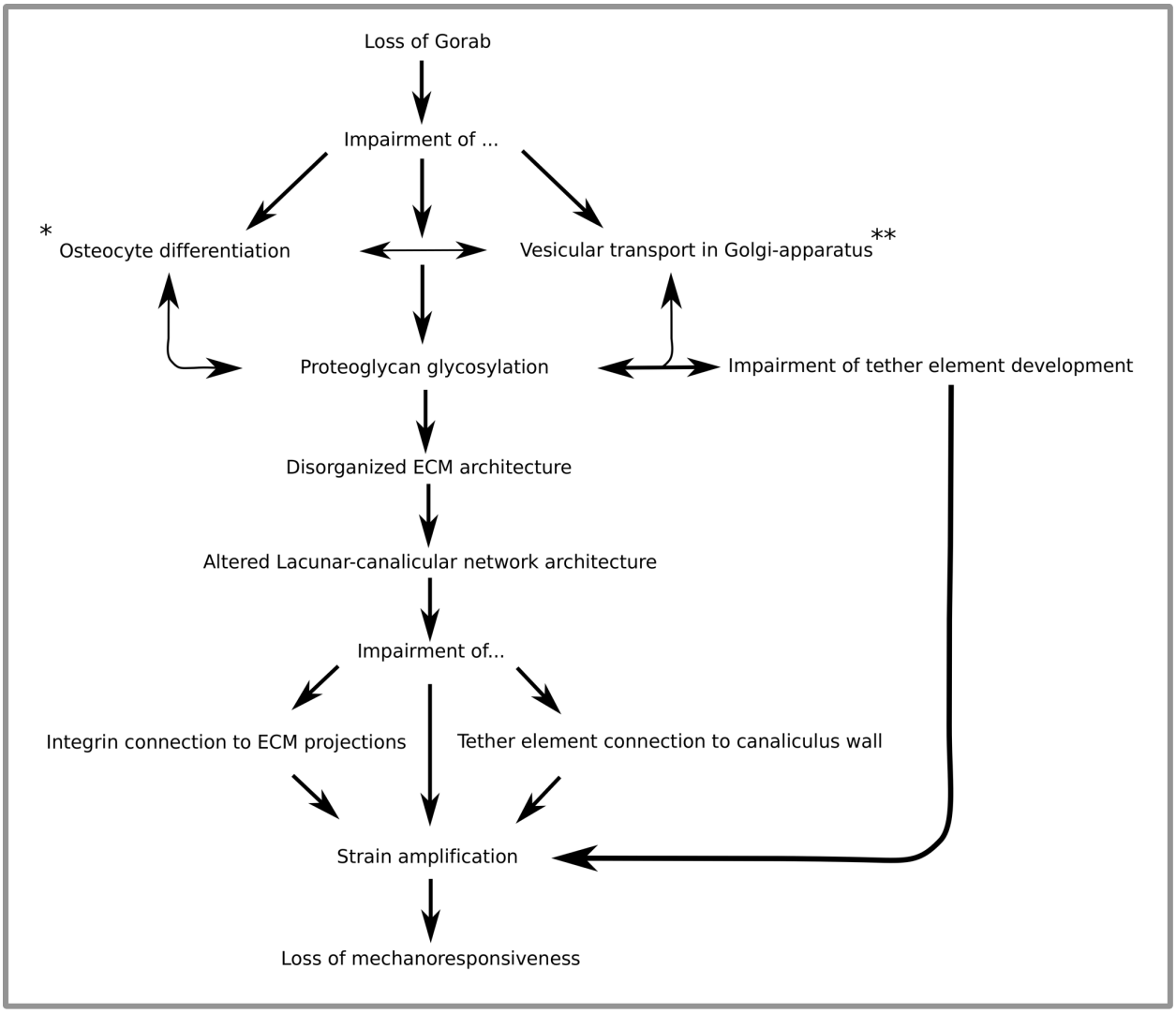

*Figure 55 Proposed mechanism, how the loss of Gorab leads to the loss of mechanoresponsiveness. * and ** will be shown in figure 56, which acts as add-on to this figure.*

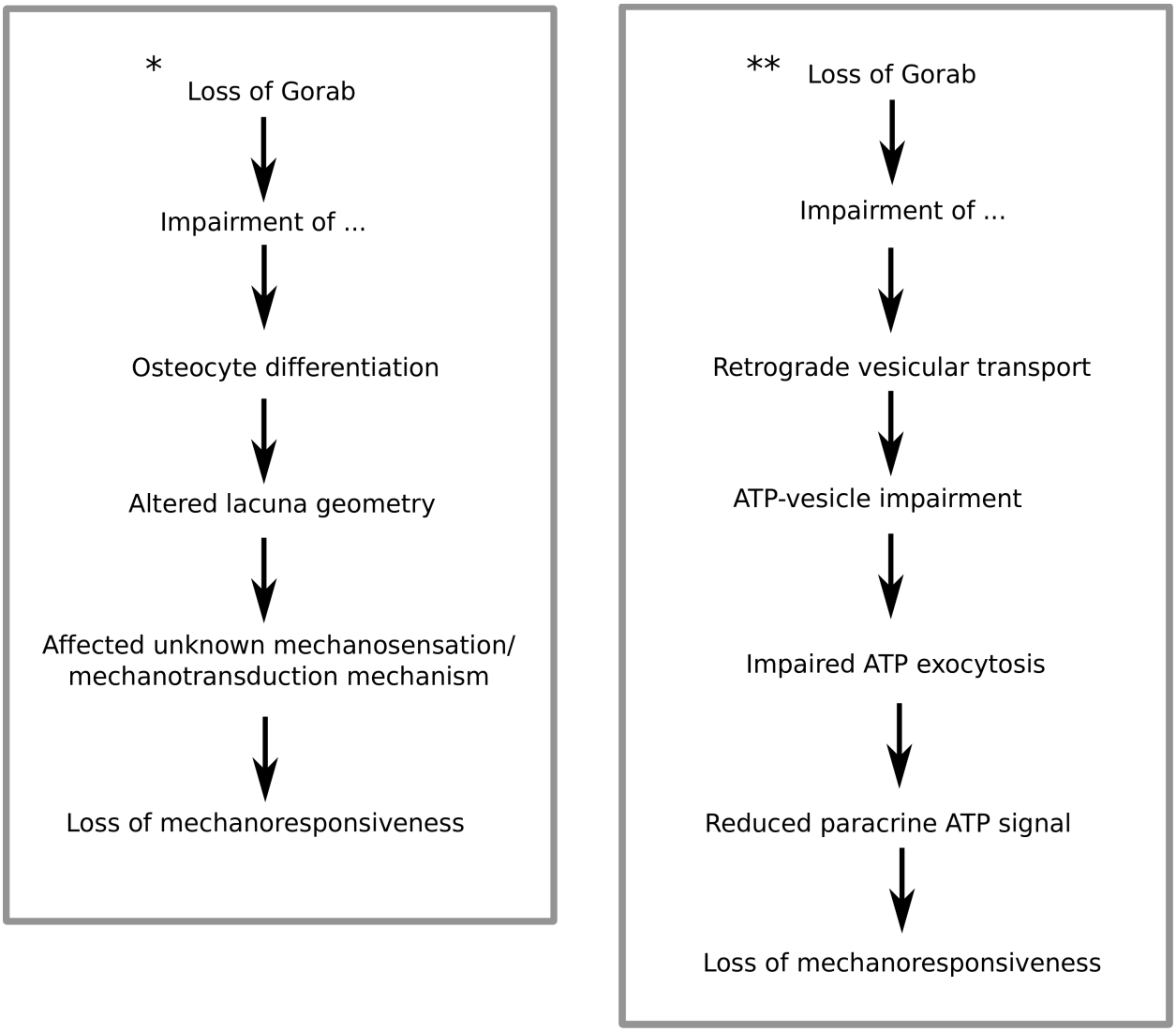

Figure 56 Proposed mechanism, how the loss of Gorab a) leads due the osteocyte differentiation impairment and b)impairment of the retrograde transport to the loss of mechanoresponsiveness.

5 Outlook

Until today, very little is known about the composition and physical characteristics of pericellular matrix and fluid. Investigating the physiologic *in vivo* conditions of the lacunar-canalicular network, and therefore the environment osteocytes are residing in, would help to better understand mechanoresponse-process in general. After revealing the wildtype conditions, further studies of genetically induced impairments of mechanoresponsiveness would be logical.

Until that happens, in order to further the actual studies, the following experiments are recommended to illuminate the specific mechanism behind the loss of mechanoresponsiveness in Gorab^{Prx1} mice.

To distinguish which target is more impaired, osteocytes themselves, or the interaction with the ECM, a follow-up study has already been designed, and the animal proposal already approved. This study involves the analysis of an inducible cre conditional knockout mouse line, termed Gorab^{iCre}. This mouse line is genetically designed to induce the identical knockout as in Gorab^{Prx1}, after supplementation of tamoxifen. By tamoxifen supplementation the cre-recombinase is induced, which is in turn responsible for the Gorab conditional knockout. The particular characteristic of this mouse line, is that a physiologic normal ECM and lacunar-canalicular network can be formed during the early weeks of life. After developing the bone structure, tamoxifen can be administered which induces the knockout, and therefore the osteocytes will lack Gorab.

Under those conditions (a normal ECM and lacunar-canalicular network) no loss of mechanoresponsiveness is expected. Correctly glycosylated proteoglycans will give the osteocytes the perfect environment for connection and adjustment within the lacunar-canalicular network. Furthermore, with a higher connectivity in canaliculi and dendrites leading to the fluid flow not being impaired, it would be possible to enable ATP signaling, and the strain could be amplified at the correctly spanned tether elements.

Furthermore, I highly recommend to investigate the cytoskeleton - executing immunofluorescence stainings for actin/fimbrin and other architectural components would be the method of choice[327].

Transmission electron microscopy would give the chance to quantify the number of hillocks projecting from the canaliculus wall.

A possible altered composition of proteoglycans in the pericellular space should be investigated by immunofluorescence. This would give less opportunity for the osteocyte dendrite to connect or stabilize, jeopardizing the physical environment of the network.

Perlecan, an osteocyte secreted proteoglycan, is assumed to be part of tether element, which connects the osteocyte process to the surrounding canaliculus wall, suspected to play a role in strain amplification. This should be investigated for glycolisation properties[79,86]. Western Blotting for quantity, immunofluorescence stainings for quality, and electron microscopy on grinded and polished sections to potentially reveal the architectural patterning.

A possible impaired fluid flow within the network needed for strain amplification and paracrine signaling should be investigated in the GO mouse model, supposedly showing a reduced flow capacity. To this end, load induced fluid flow should be analyzed by beforehand locally injected dye, as described by Wang et al.[254, 328].

6 Bibliography

1. Fuchs, R.K., Bauer, J.J. & Snow, C.M. Jumping improves hip and lumbar spine bone mass in prepubescent children: a randomized controlled trial. *J Bone Miner Res* **16**, 148-156 (2001).
2. Heinonen, A. et al. Randomised controlled trial of effect of high-impact exercise on selected risk factors for osteoporotic fractures. *Lancet* **348**, 1343-1347 (1996).
3. Kato, T. et al. Effect of low-repetition jump training on bone mineral density in young women. *J Appl Physiol (1985)* **100**, 839-843 (2006).
4. Chan, W.L. et al. Impaired proteoglycan glycosylation, elevated TGF-beta signaling, and abnormal osteoblast differentiation as the basis for bone fragility in a mouse model for gerodermia osteodysplastica. *PLoS Genet* **14**, e1007242 (2018).
5. Hennies, H.C. et al. Gerodermia osteodysplastica is caused by mutations in SCYL1BP1, a Rab-6 interacting golgin. *Nat Genet* **40**, 1410-1412 (2008).
6. Steele, D.G. & Bramblett, C.A. The anatomy and biology of the human skeleton, Edn. 1st. (Texas A&M University Press, College Station; 1988).
7. Bonewald, L.F. Mechanosensation and Transduction in Osteocytes. *Bonekey Osteovision* **3**, 7-15 (2006).
8. Meyers, M.A. & Chen, P.-Y. Biological materials science : biological materials, bioinspired materials, and biomaterials. (Cambridge University Press, New York; 2014).
9. Aszodi, A., Bateman, J.F., Gustafsson, E., Boot-Handford, R. & Fassler, R. Mammalian skeletogenesis and extracellular matrix: what can we learn from knockout mice? *Cell Struct Funct* **25**, 73-84 (2000).
10. Christoffersen, J. & Landis, W.J. A contribution with review to the description of mineralization of bone and other calcified tissues in vivo. *Anat Rec* **230**, 435-450 (1991).
11. Yagami, K. et al. Matrix GLA protein is a developmental regulator of chondrocyte mineralization and, when constitutively expressed, blocks endochondral and intramembranous ossification in the limb. *J Cell Biol* **147**, 1097-1108 (1999).
12. Buckwalter, J.A., Glimcher, M.J., Cooper, R.R. & Recker, R. Bone biology. I: Structure, blood supply, cells, matrix, and mineralization. *Instr Course Lect* **45**, 371-386 (1996).
13. Downey, P.A. & Siegel, M.I. Bone biology and the clinical implications for osteoporosis. *Phys Ther* **86**, 77-91 (2006).
14. Datta, H.K., Ng, W.F., Walker, J.A., Tuck, S.P. & Varanasi, S.S. The cell biology of bone metabolism. *J Clin Pathol* **61**, 577-587 (2008).
15. Fritton, S.P., McLeod, K.J. & Rubin, C.T. Quantifying the strain history of bone: spatial uniformity and self-similarity of low-magnitude strains. *J Biomech* **33**, 317-325 (2000).
16. Green, J., Schotland, S., Stauber, D.J., Kleeman, C.R. & Clemens, T.L. Cell-matrix interaction in bone: type I collagen modulates signal transduction in osteoblast-like cells. *Am J Physiol* **268**, C1090-1103 (1995).
17. Miller, S.C., de Saint-Georges, L., Bowman, B.M. & Jee, W.S. Bone lining cells: structure and function. *Scanning Microsc* **3**, 953-960; discussion 960-951 (1989).
18. Capulli, M., Paone, R. & Rucci, N. Osteoblast and osteocyte: games without frontiers. *Arch Biochem Biophys* **561**, 3-12 (2014).
19. Damoulis, P.D. & Hauschka, P.V. Nitric oxide acts in conjunction with proinflammatory cytokines to promote cell death in osteoblasts. *J Bone Miner Res* **12**, 412-422 (1997).

20. Marks, S.C., Jr. & Popoff, S.N. Bone cell biology: the regulation of development, structure, and function in the skeleton. *Am J Anat* **183**, 1-44 (1988).
21. Dallas, S.L. & Bonewald, L.F. Dynamics of the transition from osteoblast to osteocyte. *Ann N Y Acad Sci* **1192**, 437-443 (2010).
22. Kapinas, K., Kessler, C., Ricks, T., Gronowicz, G. & Delany, A.M. miR-29 modulates Wnt signaling in human osteoblasts through a positive feedback loop. *J Biol Chem* **285**, 25221-25231 (2010).
23. Zhang, Y. et al. A program of microRNAs controls osteogenic lineage progression by targeting transcription factor Runx2. *Proc Natl Acad Sci U S A* **108**, 9863-9868 (2011).
24. Montero, A. et al. Disruption of the fibroblast growth factor-2 gene results in decreased bone mass and bone formation. *J Clin Invest* **105**, 1085-1093 (2000).
25. Buo, A.M. & Stains, J.P. Gap junctional regulation of signal transduction in bone cells. *FEBS Lett* **588**, 1315-1321 (2014).
26. Grigoriadis, A.E., Heersche, J.N. & Aubin, J.E. Differentiation of muscle, fat, cartilage, and bone from progenitor cells present in a bone-derived clonal cell population: effect of dexamethasone. *J Cell Biol* **106**, 2139-2151 (1988).
27. Fakhry, M., Hamade, E., Badran, B., Buchet, R. & Magne, D. Molecular mechanisms of mesenchymal stem cell differentiation towards osteoblasts. *World J Stem Cells* **5**, 136-148 (2013).
28. Ducy, P., Zhang, R., Geoffroy, V., Ridall, A.L. & Karsenty, G. Osf2/Cbfa1: a transcriptional activator of osteoblast differentiation. *Cell* **89**, 747-754 (1997).
29. Hu, H. et al. Sequential roles of Hedgehog and Wnt signaling in osteoblast development. *Development* **132**, 49-60 (2005).
30. Yoshiko, Y., Candeliere, G.A., Maeda, N. & Aubin, J.E. Osteoblast autonomous Pi regulation via Pit1 plays a role in bone mineralization. *Mol Cell Biol* **27**, 4465-4474 (2007).
31. Arana-Chavez, V.E., Soares, A.M. & Katchburian, E. Junctions between early developing osteoblasts of rat calvaria as revealed by freeze-fracture and ultrathin section electron microscopy. *Arch Histol Cytol* **58**, 285-292 (1995).
32. Anderson, H.C. Matrix vesicles and calcification. *Curr Rheumatol Rep* **5**, 222-226 (2003).
33. Boivin, G. & Meunier, P.J. The degree of mineralization of bone tissue measured by computerized quantitative contact microradiography. *Calcif Tissue Int* **70**, 503-511 (2002).
34. Boivin, G. et al. The role of mineralization and organic matrix in the microhardness of bone tissue from controls and osteoporotic patients. *Bone* **43**, 532-538 (2008).
35. Yavropoulou, M.P. & Yovos, J.G. Osteoclastogenesis--current knowledge and future perspectives. *J Musculoskelet Neuronal Interact* **8**, 204-216 (2008).
36. Yoshida, H. et al. The murine mutation osteopetrosis is in the coding region of the macrophage colony stimulating factor gene. *Nature* **345**, 442-444 (1990).
37. Boyce, B.F., Hughes, D.E., Wright, K.R., Xing, L. & Dai, A. Recent advances in bone biology provide insight into the pathogenesis of bone diseases. *Lab Invest* **79**, 83-94 (1999).
38. Sodek, J. & McKee, M.D. Molecular and cellular biology of alveolar bone. *Periodontol 2000* **24**, 99-126 (2000).
39. Boyce, B.F. & Xing, L. Functions of RANKL/RANK/OPG in bone modeling and remodeling. *Arch Biochem Biophys* **473**, 139-146 (2008).
40. Longhini, R., de Oliveira, P.A., de Souza Faloni, A.P., Sasso-Cerri, E. & Cerri, P.S. Increased apoptosis in osteoclasts and decreased RANKL immunoexpression in periodontium of cimetidine-treated rats. *J Anat* **222**, 239-247 (2013).

41. Longhini, R., Aparecida de Oliveira, P., Sasso-Cerri, E. & Cerri, P.S. Cimetidine reduces alveolar bone loss in induced periodontitis in rat molars. *J Periodontol* **85**, 1115-1125 (2014).
42. Phan, T.C., Xu, J. & Zheng, M.H. Interaction between osteoblast and osteoclast: impact in bone disease. *Histol Histopathol* **19**, 1325-1344 (2004).
43. Kobayashi, Y., Udagawa, N. & Takahashi, N. Action of RANKL and OPG for osteoclastogenesis. *Crit Rev Eukaryot Gene Expr* **19**, 61-72 (2009).
44. Miyamoto, T. The dendritic cell-specific transmembrane protein DC-STAMP is essential for osteoclast fusion and osteoclast bone-resorbing activity. *Mod Rheumatol* **16**, 341-342 (2006).
45. Teitelbaum, S.L. Osteoclasts: what do they do and how do they do it? *Am J Pathol* **170**, 427-435 (2007).
46. Lakkakorpi, P.T., Horton, M.A., Helfrich, M.H., Karhukorpi, E.K. & Vaananen, H.K. Vitronectin receptor has a role in bone resorption but does not mediate tight sealing zone attachment of osteoclasts to the bone surface. *J Cell Biol* **115**, 1179-1186 (1991).
47. Saltel, F., Destaing, O., Bard, F., Eichert, D. & Jurdic, P. Apatite-mediated actin dynamics in resorbing osteoclasts. *Mol Biol Cell* **15**, 5231-5241 (2004).
48. Luxenburg, C. et al. The architecture of the adhesive apparatus of cultured osteoclasts: from podosome formation to sealing zone assembly. *PLoS One* **2**, e179 (2007).
49. Chabadel, A. et al. CD44 and beta3 integrin organize two functionally distinct actin-based domains in osteoclasts. *Mol Biol Cell* **18**, 4899-4910 (2007).
50. Teitelbaum, S.L., Tondravi, M.M. & Ross, F.P. Osteoclasts, macrophages, and the molecular mechanisms of bone resorption. *J Leukoc Biol* **61**, 381-388 (1997).
51. Blair, H.C., Kahn, A.J., Crouch, E.C., Jeffrey, J.J. & Teitelbaum, S.L. Isolated osteoclasts resorb the organic and inorganic components of bone. *J Cell Biol* **102**, 1164-1172 (1986).
52. Mattila, P.K. & Lappalainen, P. Filopodia: molecular architecture and cellular functions. *Nat Rev Mol Cell Biol* **9**, 446-454 (2008).
53. Destaing, O., Saltel, F., Geminard, J.C., Jurdic, P. & Bard, F. Podosomes display actin turnover and dynamic self-organization in osteoclasts expressing actin-green fluorescent protein. *Mol Biol Cell* **14**, 407-416 (2003).
54. Franz-Odendaal, T.A., Hall, B.K. & Witten, P.E. Buried alive: how osteoblasts become osteocytes. *Dev Dyn* **235**, 176-190 (2006).
55. Rochefort, G.Y., Pallu, S. & Benhamou, C.L. Osteocyte: the unrecognized side of bone tissue. *Osteoporos Int* **21**, 1457-1469 (2010).
56. Bonewald, L.F. The amazing osteocyte. *J Bone Miner Res* **26**, 229-238 (2011).
57. Zhao, W., Byrne, M.H., Wang, Y. & Krane, S.M. Osteocyte and osteoblast apoptosis and excessive bone deposition accompany failure of collagenase cleavage of collagen. *J Clin Invest* **106**, 941-949 (2000).
58. Holmbeck, K. et al. The metalloproteinase MT1-MMP is required for normal development and maintenance of osteocyte processes in bone. *J Cell Sci* **118**, 147-156 (2005).
59. P.A. Veno, D.P.N., I. Kalaizic, D.W. Rowe, L.F.Bonewald, S. Dallas Dynamic imaging in living calvaria reveals the motile properties of osteoblasts and osteocytes and suggests heterogeneity of osteoblasts in bone. *Journal of Bone and Mineral Research* **22** (2007).
60. Kamioka, H., Sugawara, Y., Honjo, T., Yamashiro, T. & Takano-Yamamoto, T. Terminal differentiation of osteoblasts to osteocytes is accompanied by dramatic changes in the distribution of actin-binding proteins. *J Bone Miner Res* **19**, 471-478 (2004).

61. Ohizumi, I. et al. Association of CD44 with OTS-8 in tumor vascular endothelial cells. *Biochim Biophys Acta* **1497**, 197-203 (2000).
62. Scholl, F.G., Gamallo, C., Vilaro, S. & Quintanilla, M. Identification of PA2.26 antigen as a novel cell-surface mucin-type glycoprotein that induces plasma membrane extensions and increased motility in keratinocytes. *J Cell Sci* **112 (Pt 24)**, 4601-4613 (1999).
63. Zhang, K. et al. E11/gp38 selective expression in osteocytes: regulation by mechanical strain and role in dendrite elongation. *Mol Cell Biol* **26**, 4539-4552 (2006).
64. Feng, J.Q. et al. Loss of DMP1 causes rickets and osteomalacia and identifies a role for osteocytes in mineral metabolism. *Nat Genet* **38**, 1310-1315 (2006).
65. Bonewald, L.F. & Johnson, M.L. Osteocytes, mechanosensing and Wnt signaling. *Bone* **42**, 606-615 (2008).
66. Bonewald, L.F. Osteocytes as dynamic multifunctional cells. *Ann N Y Acad Sci* **1116**, 281-290 (2007).
67. Igarashi, M., Kamiya, N., Ito, K. & Takagi, M. In situ localization and in vitro expression of osteoblast/osteocyte factor 45 mRNA during bone cell differentiation. *Histochem J* **34**, 255-263 (2002).
68. Rowe, P.S. et al. MEPE has the properties of an osteoblastic phosphatonin and minhibin. *Bone* **34**, 303-319 (2004).
69. Boskey, A.L. et al. MEPE's diverse effects on mineralization. *Calcif Tissue Int* **86**, 42-46 (2010).
70. Winkler, D.G. et al. Osteocyte control of bone formation via sclerostin, a novel BMP antagonist. *EMBO J* **22**, 6267-6276 (2003).
71. Balemans, W., Cleiren, E., Siebers, U., Horst, J. & Van Hul, W. A generalized skeletal hyperostosis in two siblings caused by a novel mutation in the SOST gene. *Bone* **36**, 943-947 (2005).
72. Li, X. et al. Targeted deletion of the sclerostin gene in mice results in increased bone formation and bone strength. *J Bone Miner Res* **23**, 860-869 (2008).
73. D. Guo, A.K., L. Barragan, J. Zhao, J. Guthrie, L. Bonewald Identification of Proteins Involved in Cytoskeletal Rearrangement, Anti-hypoxia, and Membrane Channels Enriched in Osteocytes over Osteoblasts. *Journal of Bone and Mineral Research* **21**, 1 (2006).
74. Hirao, M. et al. Oxygen tension is an important mediator of the transformation of osteoblasts to osteocytes. *J Bone Miner Metab* **25**, 266-276 (2007).
75. Sugawara, Y., Kamioka, H., Honjo, T., Tezuka, K. & Takano-Yamamoto, T. Three-dimensional reconstruction of chick calvarial osteocytes and their cell processes using confocal microscopy. *Bone* **36**, 877-883 (2005).
76. Buenzli, P.R. & Sims, N.A. Quantifying the osteocyte network in the human skeleton. *Bone* **75**, 144-150 (2015).
77. Wang, Y., McNamara, L.M., Schaffler, M.B. & Weinbaum, S. A model for the role of integrins in flow induced mechanotransduction in osteocytes. *Proc Natl Acad Sci U S A* **104**, 15941-15946 (2007).
78. Noonan, K.J. et al. Spatial distribution of CD44 and hyaluronan in the proximal tibia of the growing rat. *J Orthop Res* **14**, 573-581 (1996).
79. Thompson, W.R. et al. Perlecan/Hspg2 deficiency alters the pericellular space of the lacunocanalicular system surrounding osteocytic processes in cortical bone. *J Bone Miner Res* **26**, 618-629 (2011).

80. Kamioka, H., Honjo, T. & Takano-Yamamoto, T. A three-dimensional distribution of osteocyte processes revealed by the combination of confocal laser scanning microscopy and differential interference contrast microscopy. *Bone* **28**, 145-149 (2001).
81. You, L.D., Weinbaum, S., Cowin, S.C. & Schaffler, M.B. Ultrastructure of the osteocyte process and its pericellular matrix. *Anat Rec A Discov Mol Cell Evol Biol* **278**, 505-513 (2004).
82. Knothe Tate, M.L., Adamson, J.R., Tami, A.E. & Bauer, T.W. The osteocyte. *Int J Biochem Cell Biol* **36**, 1-8 (2004).
83. Kerschnitzki, M. et al. Architecture of the osteocyte network correlates with bone material quality. *J Bone Miner Res* **28**, 1837-1845 (2013).
84. McNamara, L.M., Majeska, R.J., Weinbaum, S., Friedrich, V. & Schaffler, M.B. Attachment of osteocyte cell processes to the bone matrix. *Anat Rec (Hoboken)* **292**, 355-363 (2009).
85. Dallas, S.L., Prideaux, M. & Bonewald, L.F. The osteocyte: an endocrine cell ... and more. *Endocr Rev* **34**, 658-690 (2013).
86. You, L., Cowin, S.C., Schaffler, M.B. & Weinbaum, S. A model for strain amplification in the actin cytoskeleton of osteocytes due to fluid drag on pericellular matrix. *J Biomech* **34**, 1375-1386 (2001).
87. Petrtyl, M., Hert, J. & Fiala, P. Spatial organization of the haversian bone in man. *J Biomech* **29**, 161-169 (1996).
88. Parfitt, A.M. Osteonal and hemi-osteonal remodeling: the spatial and temporal framework for signal traffic in adult human bone. *J Cell Biochem* **55**, 273-286 (1994).
89. Everts, V. et al. The bone lining cell: its role in cleaning Howship's lacunae and initiating bone formation. *J Bone Miner Res* **17**, 77-90 (2002).
90. Matsuo, K. & Irie, N. Osteoclast-osteoblast communication. *Arch Biochem Biophys* **473**, 201-209 (2008).
91. Fata, J.E. et al. The osteoclast differentiation factor osteoprotegerin-ligand is essential for mammary gland development. *Cell* **103**, 41-50 (2000).
92. Kobayashi, N. et al. Segregation of TRAF6-mediated signaling pathways clarifies its role in osteoclastogenesis. *EMBO J* **20**, 1271-1280 (2001).
93. Kim, H.H. et al. Receptor activator of NF-kappaB recruits multiple TRAF family adaptors and activates c-Jun N-terminal kinase. *FEBS Lett* **443**, 297-302 (1999).
94. Luo, J. et al. LGR4 is a receptor for RANKL and negatively regulates osteoclast differentiation and bone resorption. *Nat Med* **22**, 539-546 (2016).
95. Pfeilschifter, J. & Mundy, G.R. Modulation of type beta transforming growth factor activity in bone cultures by osteotropic hormones. *Proc Natl Acad Sci U S A* **84**, 2024-2028 (1987).
96. Kato, M. et al. Cbfa1-independent decrease in osteoblast proliferation, osteopenia, and persistent embryonic eye vascularization in mice deficient in Lrp5, a Wnt coreceptor. *J Cell Biol* **157**, 303-314 (2002).
97. Cui, Y. et al. Lrp5 functions in bone to regulate bone mass. *Nat Med* **17**, 684-691 (2011).
98. Bennett, C.N. et al. Wnt10b increases postnatal bone formation by enhancing osteoblast differentiation. *J Bone Miner Res* **22**, 1924-1932 (2007).
99. Miclea, R.L. et al. Adenomatous polyposis coli-mediated control of beta-catenin is essential for both chondrogenic and osteogenic differentiation of skeletal precursors. *BMC Dev Biol* **9**, 26 (2009).

100. Holmen, S.L. et al. Essential role of beta-catenin in postnatal bone acquisition. *J Biol Chem* **280**, 21162-21168 (2005).
101. Glass, D.A., 2nd et al. Canonical Wnt signaling in differentiated osteoblasts controls osteoclast differentiation. *Dev Cell* **8**, 751-764 (2005).
102. Kramer, I. et al. Osteocyte Wnt/beta-catenin signaling is required for normal bone homeostasis. *Mol Cell Biol* **30**, 3071-3085 (2010).
103. Maeda, K. et al. Wnt5a-Ror2 signaling between osteoblast-lineage cells and osteoclast precursors enhances osteoclastogenesis. *Nat Med* **18**, 405-412 (2012).
104. Santiago, F., Oguma, J., Brown, A.M. & Laurence, J. Noncanonical Wnt signaling promotes osteoclast differentiation and is facilitated by the human immunodeficiency virus protease inhibitor ritonavir. *Biochem Biophys Res Commun* **417**, 223-230 (2012).
105. Wei, W. et al. Biphasic and dosage-dependent regulation of osteoclastogenesis by beta-catenin. *Mol Cell Biol* **31**, 4706-4719 (2011).
106. Pederson, L., Ruan, M., Westendorf, J.J., Khosla, S. & Oursler, M.J. Regulation of bone formation by osteoclasts involves Wnt/BMP signaling and the chemokine sphingosine-1-phosphate. *Proc Natl Acad Sci U S A* **105**, 20764-20769 (2008).
107. Bennett, C.N. et al. Regulation of osteoblastogenesis and bone mass by Wnt10b. *Proc Natl Acad Sci U S A* **102**, 3324-3329 (2005).
108. Stevens, J.R. et al. Wnt10b deficiency results in age-dependent loss of bone mass and progressive reduction of mesenchymal progenitor cells. *J Bone Miner Res* **25**, 2138-2147 (2010).
109. Li, X. et al. Dickkopf-1 regulates bone formation in young growing rodents and upon traumatic injury. *J Bone Miner Res* **26**, 2610-2621 (2011).
110. Schulze, J. et al. Negative regulation of bone formation by the transmembrane Wnt antagonist Kremen-2. *PLoS One* **5**, e10309 (2010).
111. Robling, A.G. et al. Mechanical stimulation of bone in vivo reduces osteocyte expression of Sost/sclerostin. *J Biol Chem* **283**, 5866-5875 (2008).
112. Turner, C.H. et al. Mechanobiology of the skeleton. *Sci Signal* **2**, pt3 (2009).
113. Robinson, J.A. et al. Wnt/beta-catenin signaling is a normal physiological response to mechanical loading in bone. *J Biol Chem* **281**, 31720-31728 (2006).
114. Sawakami, K. et al. The Wnt co-receptor LRP5 is essential for skeletal mechanotransduction but not for the anabolic bone response to parathyroid hormone treatment. *J Biol Chem* **281**, 23698-23711 (2006).
115. Saxon, L.K., Jackson, B.F., Sugiyama, T., Lanyon, L.E. & Price, J.S. Analysis of multiple bone responses to graded strains above functional levels, and to disuse, in mice in vivo show that the human Lrp5 G171V High Bone Mass mutation increases the osteogenic response to loading but that lack of Lrp5 activity reduces it. *Bone* **49**, 184-193 (2011).
116. Keller, H. & Kneissel, M. SOST is a target gene for PTH in bone. *Bone* **37**, 148-158 (2005).
117. Bellido, T. et al. Chronic elevation of parathyroid hormone in mice reduces expression of sclerostin by osteocytes: a novel mechanism for hormonal control of osteoblastogenesis. *Endocrinology* **146**, 4577-4583 (2005).
118. Li, X. et al. Determination of dual effects of parathyroid hormone on skeletal gene expression in vivo by microarray and network analysis. *J Biol Chem* **282**, 33086-33097 (2007).
119. Wan, M. et al. Parathyroid hormone signaling through low-density lipoprotein-related protein 6. *Genes Dev* **22**, 2968-2979 (2008).

120. Lin, G.L. & Hankenson, K.D. Integration of BMP, Wnt, and notch signaling pathways in osteoblast differentiation. *J Cell Biochem* **112**, 3491-3501 (2011).
121. Kamiya, N. The role of BMPs in bone anabolism and their potential targets SOST and DKK1. *Curr Mol Pharmacol* **5**, 153-163 (2012).
122. Amedee, J. et al. Osteogenin (bone morphogenic protein 3) inhibits proliferation and stimulates differentiation of osteoprogenitors in human bone marrow. *Differentiation* **58**, 157-164 (1994).
123. Hughes, F.J., Collyer, J., Stanfield, M. & Goodman, S.A. The effects of bone morphogenetic protein-2, -4, and -6 on differentiation of rat osteoblast cells in vitro. *Endocrinology* **136**, 2671-2677 (1995).
124. Bain, G., Muller, T., Wang, X. & Papkoff, J. Activated beta-catenin induces osteoblast differentiation of C3H10T1/2 cells and participates in BMP2 mediated signal transduction. *Biochem Biophys Res Commun* **301**, 84-91 (2003).
125. Zimmerman, D., Jin, F., Leboy, P., Hardy, S. & Damsky, C. Impaired bone formation in transgenic mice resulting from altered integrin function in osteoblasts. *Dev Biol* **220**, 2-15 (2000).
126. Helfrich, M.H., Nesbitt, S.A., Dorey, E.L. & Horton, M.A. Rat osteoclasts adhere to a wide range of RGD (Arg-Gly-Asp) peptide-containing proteins, including the bone sialoproteins and fibronectin, via a beta 3 integrin. *J Bone Miner Res* **7**, 335-343 (1992).
127. Helfrich, M.H. et al. Beta 1 integrins and osteoclast function: involvement in collagen recognition and bone resorption. *Bone* **19**, 317-328 (1996).
128. Mbalaviele, G., Shin, C.S. & Civitelli, R. Cell-cell adhesion and signaling through cadherins: connecting bone cells in their microenvironment. *J Bone Miner Res* **21**, 1821-1827 (2006).
129. Han, Y., Cowin, S.C., Schaffler, M.B. & Weinbaum, S. Mechanotransduction and strain amplification in osteocyte cell processes. *Proc Natl Acad Sci U S A* **101**, 16689-16694 (2004).
130. Miyauchi, A. et al. AlphaVbeta3 integrin ligands enhance volume-sensitive calcium influx in mechanically stretched osteocytes. *J Bone Miner Metab* **24**, 498-504 (2006).
131. Piekarski, K. & Munro, M. Transport mechanism operating between blood supply and osteocytes in long bones. *Nature* **269**, 80-82 (1977).
132. Weinbaum, S., Cowin, S.C. & Zeng, Y. A model for the excitation of osteocytes by mechanical loading-induced bone fluid shear stresses. *J Biomech* **27**, 339-360 (1994).
133. Mammoto, T. & Ingber, D.E. Mechanical control of tissue and organ development. *Development* **137**, 1407-1420 (2010).
134. Dupont, S. et al. Role of YAP/TAZ in mechanotransduction. *Nature* **474**, 179-183 (2011).
135. McBeath, R., Pirone, D.M., Nelson, C.M., Bhadriraju, K. & Chen, C.S. Cell shape, cytoskeletal tension, and RhoA regulate stem cell lineage commitment. *Dev Cell* **6**, 483-495 (2004).
136. Engler, A.J., Sen, S., Sweeney, H.L. & Discher, D.E. Matrix elasticity directs stem cell lineage specification. *Cell* **126**, 677-689 (2006).
137. Gilbert, P.M. et al. Substrate elasticity regulates skeletal muscle stem cell self-renewal in culture. *Science* **329**, 1078-1081 (2010).
138. Chen, C.S., Mrksich, M., Huang, S., Whitesides, G.M. & Ingber, D.E. Geometric control of cell life and death. *Science* **276**, 1425-1428 (1997).
139. Azzolin, L. et al. Role of TAZ as mediator of Wnt signaling. *Cell* **151**, 1443-1456 (2012).

140. Varelas, X. et al. The Hippo pathway regulates Wnt/beta-catenin signaling. *Dev Cell* **18**, 579-591 (2010).
141. Halder, G., Dupont, S. & Piccolo, S. Transduction of mechanical and cytoskeletal cues by YAP and TAZ. *Nat Rev Mol Cell Biol* **13**, 591-600 (2012).
142. Xiong, J., Almeida, M. & O'Brien, C.A. The YAP/TAZ transcriptional co-activators have opposing effects at different stages of osteoblast differentiation. *Bone* **112**, 1-9 (2018).
143. Schwartz, Z., Schlader, D.L., Swain, L.D. & Boyan, B.D. Direct effects of 1,25-dihydroxyvitamin D3 and 24,25-dihydroxyvitamin D3 on growth zone and resting zone chondrocyte membrane alkaline phosphatase and phospholipase-A2 specific activities. *Endocrinology* **123**, 2878-2884 (1988).
144. Nahar, N.N., Missana, L.R., Garimella, R., Tague, S.E. & Anderson, H.C. Matrix vesicles are carriers of bone morphogenetic proteins (BMPs), vascular endothelial growth factor (VEGF), and noncollagenous matrix proteins. *J Bone Miner Metab* **26**, 514-519 (2008).
145. Creemers, E.E., Tijsen, A.J. & Pinto, Y.M. Circulating microRNAs: novel biomarkers and extracellular communicators in cardiovascular disease? *Circ Res* **110**, 483-495 (2012).
146. Lin, Z. et al. Selective enrichment of microRNAs in extracellular matrix vesicles produced by growth plate chondrocytes. *Bone* **88**, 47-55 (2016).
147. Biggs, M.J. & Dalby, M.J. Focal adhesions in osteoneogenesis. *Proc Inst Mech Eng H* **224**, 1441-1453 (2010).
148. Chen, G., Deng, C. & Li, Y.P. TGF-beta and BMP signaling in osteoblast differentiation and bone formation. *Int J Biol Sci* **8**, 272-288 (2012).
149. Baron, R. & Kneissel, M. WNT signaling in bone homeostasis and disease: from human mutations to treatments. *Nat Med* **19**, 179-192 (2013).
150. Wan, C. et al. Role of HIF-1alpha in skeletal development. *Ann N Y Acad Sci* **1192**, 322-326 (2010).
151. Tang, S.Y. & Alliston, T. Regulation of postnatal bone homeostasis by TGFbeta. *Bonekey Rep* **2**, 255 (2013).
152. Takeuchi, Y. et al. Differentiation and transforming growth factor-beta receptor down-regulation by collagen-alpha2beta1 integrin interaction is mediated by focal adhesion kinase and its downstream signals in murine osteoblastic cells. *J Biol Chem* **272**, 29309-29316 (1997).
153. Yasui, T. et al. Regulation of RANKL-induced osteoclastogenesis by TGF-beta through molecular interaction between Smad3 and Traf6. *J Bone Miner Res* **26**, 1447-1456 (2011).
154. Hsu, H.C. et al. Ultrasound induces cyclooxygenase-2 expression through integrin, integrin-linked kinase, Akt, NF-kappaB and p300 pathway in human chondrocytes. *Cell Signal* **19**, 2317-2328 (2007).
155. Gupta, V. & Grande-Allen, K.J. Effects of static and cyclic loading in regulating extracellular matrix synthesis by cardiovascular cells. *Cardiovasc Res* **72**, 375-383 (2006).
156. Chen, K.D. et al. Mechanotransduction in response to shear stress. Roles of receptor tyrosine kinases, integrins, and Shc. *J Biol Chem* **274**, 18393-18400 (1999).
157. Goldspink, G. Changes in muscle mass and phenotype and the expression of autocrine and systemic growth factors by muscle in response to stretch and overload. *J Anat* **194 (Pt 3)**, 323-334 (1999).
158. Li, Z. et al. Inflammatory response of human tendon fibroblasts to cyclic mechanical stretching. *Am J Sports Med* **32**, 435-440 (2004).

159. Rubin, C.T. & Lanyon, L.E. Regulation of bone formation by applied dynamic loads. *J Bone Joint Surg Am* **66**, 397-402 (1984).
160. Duncan, R.L. & Turner, C.H. Mechanotransduction and the functional response of bone to mechanical strain. *Calcif Tissue Int* **57**, 344-358 (1995).
161. Gardinier, J.D. et al. In situ permeability measurement of the mammalian lacunar-canalicular system. *Bone* **46**, 1075-1081 (2010).
162. Hughes-Fulford, M. Signal transduction and mechanical stress. *Sci STKE* **2004**, RE12 (2004).
163. Gusmao, C.V. & Belangero, W.D. How Do Bone Cells Sense Mechanical Loading? *Rev Bras Ortop* **44**, 299-305 (2009).
164. Lee, D.Y. et al. Integrin-mediated expression of bone formation-related genes in osteoblast-like cells in response to fluid shear stress: roles of extracellular matrix, Shc, and mitogen-activated protein kinase. *J Bone Miner Res* **23**, 1140-1149 (2008).
165. Haugh, M.G., Vaughan, T.J. & McNamara, L.M. The role of integrin alpha(V)beta(3) in osteocyte mechanotransduction. *J Mech Behav Biomed Mater* **42**, 67-75 (2015).
166. Jaasma, M.J., Plunkett, N.A. & O'Brien, F.J. Design and validation of a dynamic flow perfusion bioreactor for use with compliant tissue engineering scaffolds. *J Biotechnol* **133**, 490-496 (2008).
167. Forwood, M.R. Inducible cyclo-oxygenase (COX-2) mediates the induction of bone formation by mechanical loading in vivo. *J Bone Miner Res* **11**, 1688-1693 (1996).
168. Zaidel-Bar, R., Cohen, M., Addadi, L. & Geiger, B. Hierarchical assembly of cell-matrix adhesion complexes. *Biochem Soc Trans* **32**, 416-420 (2004).
169. Boutahar, N., Guignandon, A., Vico, L. & Lafage-Proust, M.H. Mechanical strain on osteoblasts activates autophosphorylation of focal adhesion kinase and proline-rich tyrosine kinase 2 tyrosine sites involved in ERK activation. *J Biol Chem* **279**, 30588-30599 (2004).
170. Scott, A., Khan, K.M., Duronio, V. & Hart, D.A. Mechanotransduction in human bone: in vitro cellular physiology that underpins bone changes with exercise. *Sports Med* **38**, 139-160 (2008).
171. Lee, H.S., Millward-Sadler, S.J., Wright, M.O., Nuki, G. & Salter, D.M. Integrin and mechanosensitive ion channel-dependent tyrosine phosphorylation of focal adhesion proteins and beta-catenin in human articular chondrocytes after mechanical stimulation. *J Bone Miner Res* **15**, 1501-1509 (2000).
172. Pommerenke, H. et al. The mode of mechanical integrin stressing controls intracellular signaling in osteoblasts. *J Bone Miner Res* **17**, 603-611 (2002).
173. Tang, C.H. et al. Ultrasound stimulates cyclooxygenase-2 expression and increases bone formation through integrin, focal adhesion kinase, phosphatidylinositol 3-kinase, and Akt pathway in osteoblasts. *Mol Pharmacol* **69**, 2047-2057 (2006).
174. Woods, A. & Couchman, J.R. Syndecan 4 heparan sulfate proteoglycan is a selectively enriched and widespread focal adhesion component. *Mol Biol Cell* **5**, 183-192 (1994).
175. Brighton, C.T. & Albelda, S.M. Identification of integrin cell-substratum adhesion receptors on cultured rat bone cells. *J Orthop Res* **10**, 766-773 (1992).
176. Thi, M.M., Suadicani, S.O., Schaffler, M.B., Weinbaum, S. & Spray, D.C. Mechanosensory responses of osteocytes to physiological forces occur along processes and not cell body and require alphaVbeta3 integrin. *Proc Natl Acad Sci U S A* **110**, 21012-21017 (2013).

177. Anderson, E.J. & Knothe Tate, M.L. Idealization of pericellular fluid space geometry and dimension results in a profound underprediction of nano-microscale stresses imparted by fluid drag on osteocytes. *J Biomech* **41**, 1736-1746 (2008).
178. Plotkin, L.I. et al. Mechanical stimulation prevents osteocyte apoptosis: requirement of integrins, Src kinases, and ERKs. *Am J Physiol Cell Physiol* **289**, C633-643 (2005).
179. Liedert, A., Kaspar, D., Blakytny, R., Claes, L. & Ignatius, A. Signal transduction pathways involved in mechanotransduction in bone cells. *Biochem Biophys Res Commun* **349**, 1-5 (2006).
180. Cornillon, J., Campos, L. & Guyotat, D. [Focal adhesion kinase (FAK), a multifunctional protein]. *Med Sci (Paris)* **19**, 743-752 (2003).
181. Kawamura, N. et al. Akt1 in osteoblasts and osteoclasts controls bone remodeling. *PLoS One* **2**, e1058 (2007).
182. Giancotti, F.G. & Ruoslahti, E. Integrin signaling. *Science* **285**, 1028-1032 (1999).
183. Geiger, B., Bershadsky, A., Pankov, R. & Yamada, K.M. Transmembrane crosstalk between the extracellular matrix--cytoskeleton crosstalk. *Nat Rev Mol Cell Biol* **2**, 793-805 (2001).
184. Yamada, K.M. & Geiger, B. Molecular interactions in cell adhesion complexes. *Curr Opin Cell Biol* **9**, 76-85 (1997).
185. Vatsa, A., Semeins, C.M., Smit, T.H. & Klein-Nulend, J. Paxillin localisation in osteocytes--is it determined by the direction of loading? *Biochem Biophys Res Commun* **377**, 1019-1024 (2008).
186. Abou Alaiwi, W.A., Lo, S.T. & Nauli, S.M. Primary cilia: highly sophisticated biological sensors. *Sensors (Basel)* **9**, 7003-7020 (2009).
187. Praetorius, H.A. & Spring, K.R. A physiological view of the primary cilium. *Annu Rev Physiol* **67**, 515-529 (2005).
188. Malone, A.M. et al. Primary cilia mediate mechanosensing in bone cells by a calcium-independent mechanism. *Proc Natl Acad Sci U S A* **104**, 13325-13330 (2007).
189. Temiyasathit, S. et al. Mechanosensing by the primary cilium: deletion of Kif3A reduces bone formation due to loading. *PLoS One* **7**, e33368 (2012).
190. Uzbekov, R.E. et al. Centrosome fine ultrastructure of the osteocyte mechanosensitive primary cilium. *Microsc Microanal* **18**, 1430-1441 (2012).
191. Vaughan, T.J., Mullen, C.A., Verbruggen, S.W. & McNamara, L.M. Bone cell mechanosensation of fluid flow stimulation: a fluid-structure interaction model characterising the role integrin attachments and primary cilia. *Biomech Model Mechanobiol* **14**, 703-718 (2015).
192. Yu, K. et al. Mechanical loading disrupts osteocyte plasma membranes which initiates mechanosensation events in bone. *J Orthop Res* **36**, 653-662 (2018).
193. Seref-Ferlengez, Z. et al. P2X7R-Panx1 Complex Impairs Bone Mechanosignaling under High Glucose Levels Associated with Type-1 Diabetes. *PLoS One* **11**, e0155107 (2016).
194. Thompson, W.R. et al. Association of the alpha(2)delta(1) subunit with Ca(v)3.2 enhances membrane expression and regulates mechanically induced ATP release in MLO-Y4 osteocytes. *J Bone Miner Res* **26**, 2125-2139 (2011).
195. Mikolajewicz, N., Zimmermann, E.A., Willie, B.M. & Komarova, S.V. Mechanically-stimulated ATP release from murine bone cells is regulated by a balance of injury and repair. *Elife* **7** (2018).

196. Genetos, D.C., Kephart, C.J., Zhang, Y., Yellowley, C.E. & Donahue, H.J. Oscillating fluid flow activation of gap junction hemichannels induces ATP release from MLO-Y4 osteocytes. *J Cell Physiol* **212**, 207-214 (2007).
197. Cooper, S.T. & McNeil, P.L. Membrane Repair: Mechanisms and Pathophysiology. *Physiol Rev* **95**, 1205-1240 (2015).
198. Lewis, K.J. et al. Osteocyte calcium signals encode strain magnitude and loading frequency in vivo. *Proc Natl Acad Sci U S A* **114**, 11775-11780 (2017).
199. Han, R. & Campbell, K.P. Dysferlin and muscle membrane repair. *Curr Opin Cell Biol* **19**, 409-416 (2007).
200. McDade, J.R., Archambeau, A. & Michele, D.E. Rapid actin-cytoskeleton-dependent recruitment of plasma membrane-derived dysferlin at wounds is critical for muscle membrane repair. *FASEB J* **28**, 3660-3670 (2014).
201. Abbracchio, M.P., Burnstock, G., Verkhratsky, A. & Zimmermann, H. Purinergic signalling in the nervous system: an overview. *Trends Neurosci* **32**, 19-29 (2009).
202. Rath, A.L. et al. Correlation of cell strain in single osteocytes with intracellular calcium, but not intracellular nitric oxide, in response to fluid flow. *J Biomech* **43**, 1560-1564 (2010).
203. Berridge, M.J., Lipp, P. & Bootman, M.D. The versatility and universality of calcium signalling. *Nat Rev Mol Cell Biol* **1**, 11-21 (2000).
204. Mogami, H., Tepikin, A.V. & Petersen, O.H. Termination of cytosolic Ca2+ signals: Ca2+ reuptake into intracellular stores is regulated by the free Ca2+ concentration in the store lumen. *EMBO J* **17**, 435-442 (1998).
205. Miyauchi, A. et al. Parathyroid hormone-activated volume-sensitive calcium influx pathways in mechanically loaded osteocytes. *J Biol Chem* **275**, 3335-3342 (2000).
206. Shapiro, F. Variable conformation of GAP junctions linking bone cells: a transmission electron microscopic study of linear, stacked linear, curvilinear, oval, and annular junctions. *Calcif Tissue Int* **61**, 285-293 (1997).
207. Yellowley, C.E., Li, Z., Zhou, Z., Jacobs, C.R. & Donahue, H.J. Functional gap junctions between osteocytic and osteoblastic cells. *J Bone Miner Res* **15**, 209-217 (2000).
208. McGarry, J.G., Klein-Nulend, J. & Prendergast, P.J. The effect of cytoskeletal disruption on pulsatile fluid flow-induced nitric oxide and prostaglandin E2 release in osteocytes and osteoblasts. *Biochem Biophys Res Commun* **330**, 341-348 (2005).
209. Tanaka-Kamioka, K., Kamioka, H., Ris, H. & Lim, S.S. Osteocyte shape is dependent on actin filaments and osteocyte processes are unique actin-rich projections. *J Bone Miner Res* **13**, 1555-1568 (1998).
210. Volkmann, N., DeRosier, D., Matsudaira, P. & Hanein, D. An atomic model of actin filaments cross-linked by fimbrin and its implications for bundle assembly and function. *J Cell Biol* **153**, 947-956 (2001).
211. Culty, M. et al. The hyaluronate receptor is a member of the CD44 (H-CAM) family of cell surface glycoproteins. *J Cell Biol* **111**, 2765-2774 (1990).
212. Weber, G.F., Ashkar, S., Glimcher, M.J. & Cantor, H. Receptor-ligand interaction between CD44 and osteopontin (Eta-1). *Science* **271**, 509-512 (1996).
213. Nakamura, H., Kenmotsu, S., Sakai, H. & Ozawa, H. Localization of CD44, the hyaluronate receptor, on the plasma membrane of osteocytes and osteoclasts in rat tibiae. *Cell Tissue Res* **280**, 225-233 (1995).

214. Anderson, E.J., Kaliyamoorthy, S., Iwan, J., Alexander, D. & Knothe Tate, M.L. Nano-microscale models of periosteocytic flow show differences in stresses imparted to cell body and processes. *Ann Biomed Eng* **33**, 52-62 (2005).
215. Bonivtch, A.R., Bonewald, L.F. & Nicolella, D.P. Tissue strain amplification at the osteocyte lacuna: a microstructural finite element analysis. *J Biomech* **40**, 2199-2206 (2007).
216. Wu, X.T. et al. The potential role of spectrin network in the mechanotransduction of MLO-Y4 osteocytes. *Sci Rep* **7**, 40940 (2017).
217. De Matteis, M.A. & Morrow, J.S. Spectrin tethers and mesh in the biosynthetic pathway. *J Cell Sci* **113 (Pt 13)**, 2331-2343 (2000).
218. Das, A., Base, C., Manna, D., Cho, W. & Dubreuil, R.R. Unexpected complexity in the mechanisms that target assembly of the spectrin cytoskeleton. *J Biol Chem* **283**, 12643-12653 (2008).
219. Machnicka, B. et al. Spectrins: a structural platform for stabilization and activation of membrane channels, receptors and transporters. *Biochim Biophys Acta* **1838**, 620-634 (2014).
220. Butcher, M.T., Espinoza, N.R., Cirilo, S.R. & Blob, R.W. In vivo strains in the femur of river cooter turtles (Pseudemys concinna) during terrestrial locomotion: tests of force-platform models of loading mechanics. *J Exp Biol* **211**, 2397-2407 (2008).
221. Eiichi Fukada, I.Y. On the Piezoelectric Effect of Bone. *Journal of the Physical Society of Japan* **12**, 5 (1957).
222. Qin, Y.X., Lin, W. & Rubin, C. The pathway of bone fluid flow as defined by in vivo intramedullary pressure and streaming potential measurements. *Ann Biomed Eng* **30**, 693-702 (2002).
223. Salter, D.M., Robb, J.E. & Wright, M.O. Electrophysiological responses of human bone cells to mechanical stimulation: evidence for specific integrin function in mechanotransduction. *J Bone Miner Res* **12**, 1133-1141 (1997).
224. Salter, D.M., Wallace, W.H., Robb, J.E., Caldwell, H. & Wright, M.O. Human bone cell hyperpolarization response to cyclical mechanical strain is mediated by an interleukin-1beta autocrine/paracrine loop. *J Bone Miner Res* **15**, 1746-1755 (2000).
225. Hunter, A.G. Is geroderma osteodysplastica underdiagnosed? *J Med Genet* **25**, 854-857 (1988).
226. Rajab, A. et al. Geroderma osteodysplasticum hereditaria and wrinkly skin syndrome in 22 patients from Oman. *Am J Med Genet A* **146A**, 965-976 (2008).
227. Freeze, H.H. Genetic defects in the human glycome. *Nat Rev Genet* **7**, 537-551 (2006).
228. Short, B., Haas, A. & Barr, F.A. Golgins and GTPases, giving identity and structure to the Golgi apparatus. *Biochim Biophys Acta* **1744**, 383-395 (2005).
229. Grigoriev, I. et al. Rab6 regulates transport and targeting of exocytotic carriers. *Dev Cell* **13**, 305-314 (2007).
230. Mallard, F. et al. Early/recycling endosomes-to-TGN transport involves two SNARE complexes and a Rab6 isoform. *J Cell Biol* **156**, 653-664 (2002).
231. Neill, T., Schaefer, L. & Iozzo, R.V. Decorin: a guardian from the matrix. *Am J Pathol* **181**, 380-387 (2012).
232. Grafe, I. et al. Excessive transforming growth factor-beta signaling is a common mechanism in osteogenesis imperfecta. *Nat Med* **20**, 670-675 (2014).
233. Fransson, L.A. et al. Biosynthesis of decorin and glypican. *Matrix Biol* **19**, 367-376 (2000).

234. Biewener, A.A. Allometry of quadrupedal locomotion: the scaling of duty factor, bone curvature and limb orientation to body size. *J Exp Biol* **105**, 147-171 (1983).
235. Al-Gazali, L.I., Sztriha, L., Skaff, F. & Haas, D. Gerodermia osteodysplastica and wrinkly skin syndrome: are they the same? *Am J Med Genet* **101**, 213-220 (2001).
236. Courtney, A.C., Wachtel, E.F., Myers, E.R. & Hayes, W.C. Age-related reductions in the strength of the femur tested in a fall-loading configuration. *J Bone Joint Surg Am* **77**, 387-395 (1995).
237. Brunkow, M.E. et al. Bone dysplasia sclerosteosis results from loss of the SOST gene product, a novel cystine knot-containing protein. *Am J Hum Genet* **68**, 577-589 (2001).
238. Willie, B.M. et al. Diminished response to in vivo mechanical loading in trabecular and not cortical bone in adulthood of female C57Bl/6 mice coincides with a reduction in deformation to load. *Bone* **55**, 335-346 (2013).
239. D.Pflanz, E.B., A. Birkhold, T. Thiele, C. Li, H.Z. Ke No additive effects of in vivo loading and sclerostin antibody treatment on bone anabolism in elderly mice. *Journal of Bone and Mineral Research* **27** (2012).
240. Sugiyama, T. et al. Mechanical loading enhances the anabolic effects of intermittent parathyroid hormone (1-34) on trabecular and cortical bone in mice. *Bone* **43**, 238-248 (2008).
241. Lynch, M.E. et al. Cancellous bone adaptation to tibial compression is not sex dependent in growing mice. *J Appl Physiol (1985)* **109**, 685-691 (2010).
242. Sugiyama, T. et al. Bones' adaptive response to mechanical loading is essentially linear between the low strains associated with disuse and the high strains associated with the lamellar/woven bone transition. *J Bone Miner Res* **27**, 1784-1793 (2012).
243. De Souza, R.L. et al. Non-invasive axial loading of mouse tibiae increases cortical bone formation and modifies trabecular organization: a new model to study cortical and cancellous compartments in a single loaded element. *Bone* **37**, 810-818 (2005).
244. Dempster, D.W. et al. Standardized nomenclature, symbols, and units for bone histomorphometry: a 2012 update of the report of the ASBMR Histomorphometry Nomenclature Committee. *J Bone Miner Res* **28**, 2-17 (2013).
245. Repp, F. et al. Spatial heterogeneity in the canalicular density of the osteocyte network in human osteons. *Bone Rep* **6**, 101-108 (2017).
246. Montes, G.S. & Junqueira, L.C. The use of the Picrosirius-polarization method for the study of the biopathology of collagen. *Mem Inst Oswaldo Cruz* **86 Suppl 3**, 1-11 (1991).
247. Woo, S.M., Rosser, J., Dusevich, V., Kalajzic, I. & Bonewald, L.F. Cell line IDG-SW3 replicates osteoblast-to-late-osteocyte differentiation in vitro and accelerates bone formation in vivo. *J Bone Miner Res* **26**, 2634-2646 (2011).
248. Brini, M., Cali, T., Ottolini, D. & Carafoli, E. Neuronal calcium signaling: function and dysfunction. *Cell Mol Life Sci* **71**, 2787-2814 (2014).
249. Nathanson, M.H. Cellular and subcellular calcium signaling in gastrointestinal epithelium. *Gastroenterology* **106**, 1349-1364 (1994).
250. Aido, M. et al. Effect of in vivo loading on bone composition varies with animal age. *Exp Gerontol* **63**, 48-58 (2015).
251. Robling, A.G., Castillo, A.B. & Turner, C.H. Biomechanical and molecular regulation of bone remodeling. *Annu Rev Biomed Eng* **8**, 455-498 (2006).
252. Robling, A.G. & Turner, C.H. Mechanical signaling for bone modeling and remodeling. *Crit Rev Eukaryot Gene Expr* **19**, 319-338 (2009).

253. Zhang, D., Weinbaum, S. & Cowin, S.C. Estimates of the peak pressures in bone pore water. *J Biomech Eng* **120**, 697-703 (1998).
254. Wang, L., Cowin, S.C., Weinbaum, S. & Fritton, S.P. Modeling tracer transport in an osteon under cyclic loading. *Ann Biomed Eng* **28**, 1200-1209 (2000).
255. Gururaja, S., Kim, H.J., Swan, C.C., Brand, R.A. & Lakes, R.S. Modeling deformation-induced fluid flow in cortical bone's canalicular-lacunar system. *Ann Biomed Eng* **33**, 7-25 (2005).
256. Hsieh, Y.F. & Turner, C.H. Effects of loading frequency on mechanically induced bone formation. *J Bone Miner Res* **16**, 918-924 (2001).
257. Warden, S.J. & Turner, C.H. Mechanotransduction in the cortical bone is most efficient at loading frequencies of 5-10 Hz. *Bone* **34**, 261-270 (2004).
258. Yang, H. et al. Examining tissue composition, whole-bone morphology and mechanical behavior of Gorab(Prx1) mice tibiae: A mouse model of premature aging. *J Biomech* **65**, 145-153 (2017).
259. Pereira, R.C., Bischoff, D.S., Yamaguchi, D., Salusky, I.B. & Wesseling-Perry, K. Micro-CT in the Assessment of Pediatric Renal Osteodystrophy by Bone Histomorphometry. *Clin J Am Soc Nephrol* **11**, 481-487 (2016).
260. Kraehenbuehl, T.P. et al. Effects of muCT radiation on tissue engineered bone-like constructs. *Biomed Tech (Berl)* **55**, 245-250 (2010).
261. Drifka, C.R. et al. Comparison of Picrosirius Red Staining With Second Harmonic Generation Imaging for the Quantification of Clinically Relevant Collagen Fiber Features in Histopathology Samples. *J Histochem Cytochem* **64**, 519-529 (2016).
262. Boerckel, J.D. et al. Effects of in vivo mechanical loading on large bone defect regeneration. *J Orthop Res* **30**, 1067-1075 (2012).
263. Lucero, H.A., Patterson, S., Matsuura, S. & Ravid, K. Quantitative histological image analyses of reticulin fibers in a myelofibrotic mouse. *J Biol Methods* **3** (2016).
264. Duval, K. et al. Modeling Physiological Events in 2D vs. 3D Cell Culture. *Physiology (Bethesda)* **32**, 266-277 (2017).
265. Bonewald, L.F. Establishment and characterization of an osteocyte-like cell line, MLO-Y4. *J Bone Miner Metab* **17**, 61-65 (1999).
266. Wang, F. et al. A comparison of CRISPR/Cas9 and siRNA-mediated ALDH2 gene silencing in human cell lines. *Mol Genet Genomics* **293**, 769-783 (2018).
267. Frost, H.M. From Wolff's law to the mechanostat: a new "face" of physiology. *J Orthop Sci* **3**, 282-286 (1998).
268. Frost, H.M. The Utah paradigm of skeletal physiology: an overview of its insights for bone, cartilage and collagenous tissue organs. *J Bone Miner Metab* **18**, 305-316 (2000).
269. Frost, H.M. The Utah Paradigm of Skeletal Physeology, Vol.
. (Athens, Greece: ISMNI, 2004).
270. Boskey, A.L., Spevak, L. & Weinstein, R.S. Spectroscopic markers of bone quality in alendronate-treated postmenopausal women. *Osteoporos Int* **20**, 793-800 (2009).
271. Kreider, J.M. & Goldstein, S.A. Trabecular bone mechanical properties in patients with fragility fractures. *Clin Orthop Relat Res* **467**, 1955-1963 (2009).
272. Chen, H., Washimi, Y., Kubo, K.Y. & Onozuka, M. Gender-related changes in three-dimensional microstructure of trabecular bone at the human proximal tibia with aging. *Histol Histopathol* **26**, 563-570 (2011).

273. Ding, M. & Hvid, I. Quantification of age-related changes in the structure model type and trabecular thickness of human tibial cancellous bone. *Bone* **26**, 291-295 (2000).
274. Ding, M., Odgaard, A., Linde, F. & Hvid, I. Age-related variations in the microstructure of human tibial cancellous bone. *J Orthop Res* **20**, 615-621 (2002).
275. Chen, H., Zhou, X., Fujita, H., Onozuka, M. & Kubo, K.Y. Age-related changes in trabecular and cortical bone microstructure. *Int J Endocrinol* **2013**, 213234 (2013).
276. Dalzell, N. et al. Bone micro-architecture and determinants of strength in the radius and tibia: age-related changes in a population-based study of normal adults measured with high-resolution pQCT. *Osteoporos Int* **20**, 1683-1694 (2009).
277. Burghardt, A.J., Kazakia, G.J., Ramachandran, S., Link, T.M. & Majumdar, S. Age- and gender-related differences in the geometric properties and biomechanical significance of intracortical porosity in the distal radius and tibia. *J Bone Miner Res* **25**, 983-993 (2010).
278. Macdonald, H.M., Nishiyama, K.K., Kang, J., Hanley, D.A. & Boyd, S.K. Age-related patterns of trabecular and cortical bone loss differ between sexes and skeletal sites: a population-based HR-pQCT study. *J Bone Miner Res* **26**, 50-62 (2011).
279. Nicks, K.M. et al. Relationship of age to bone microstructure independent of areal bone mineral density. *J Bone Miner Res* **27**, 637-644 (2012).
280. Launey ME, B.M., Ritchie RO On the mechanistic origins of toughness in bone. *Annu Rev Mater Res*, 25-53 (2010).
281. Sell, D.R. & Monnier, V.M. Structure elucidation of a senescence cross-link from human extracellular matrix. Implication of pentoses in the aging process. *J Biol Chem* **264**, 21597-21602 (1989).
282. Odetti, P. et al. Advanced glycation end products and bone loss during aging. *Ann N Y Acad Sci* **1043**, 710-717 (2005).
283. Saito, M., Marumo, K., Fujii, K. & Ishioka, N. Single-column high-performance liquid chromatographic-fluorescence detection of immature, mature, and senescent cross-links of collagen. *Anal Biochem* **253**, 26-32 (1997).
284. Wang, X., Shen, X., Li, X. & Agrawal, C.M. Age-related changes in the collagen network and toughness of bone. *Bone* **31**, 1-7 (2002).
285. Vashishth, D. et al. Influence of nonenzymatic glycation on biomechanical properties of cortical bone. *Bone* **28**, 195-201 (2001).
286. Garnero, P. et al. Extracellular post-translational modifications of collagen are major determinants of biomechanical properties of fetal bovine cortical bone. *Bone* **38**, 300-309 (2006).
287. K. Flurkey, J.M.C., D E. Harrison Mouse models in aging research, Vol. Volume 3. (Elsevier, 2007).
288. Beamer, W.G., Donahue, L.R., Rosen, C.J. & Baylink, D.J. Genetic variability in adult bone density among inbred strains of mice. *Bone* **18**, 397-403 (1996).
289. Brodt, M.D., Ellis, C.B. & Silva, M.J. Growing C57Bl/6 mice increase whole bone mechanical properties by increasing geometric and material properties. *J Bone Miner Res* **14**, 2159-2166 (1999).
290. Buie, H.R., Moore, C.P. & Boyd, S.K. Postpubertal architectural developmental patterns differ between the L3 vertebra and proximal tibia in three inbred strains of mice. *J Bone Miner Res* **23**, 2048-2059 (2008).
291. Ferguson, V.L., Ayers, R.A., Bateman, T.A. & Simske, S.J. Bone development and age-related bone loss in male C57BL/6J mice. *Bone* **33**, 387-398 (2003).

292. Glatt, V., Canalis, E., Stadmeyer, L. & Bouxsein, M.L. Age-related changes in trabecular architecture differ in female and male C57BL/6J mice. *J Bone Miner Res* **22**, 1197-1207 (2007).
293. Yeni, Y.N., Brown, C.U., Wang, Z. & Norman, T.L. The influence of bone morphology on fracture toughness of the human femur and tibia. *Bone* **21**, 453-459 (1997).
294. S., S. Longitudinal shear properties of human compact bone and its constituents, and the associated failure mechanism. *J Mater Sci* **12**, 1798 - 1806 (1977).
295. Doyle, J.J., Gerber, E.E. & Dietz, H.C. Matrix-dependent perturbation of TGFbeta signaling and disease. *FEBS Lett* **586**, 2003-2015 (2012).
296. F. Ramirez, E.A.-S. Marfan syndrome and related disorders. *C. Rosen* **7th Edition**, 450-454 (2008).
297. Ramirez, F., Caescu, C., Wondimu, E. & Galatioto, J. Marfan syndrome; A connective tissue disease at the crossroads of mechanotransduction, TGFbeta signaling and cell stemness. *Matrix Biol* **71-72**, 82-89 (2018).
298. Ramirez, F. & Rifkin, D.B. Extracellular microfibrils: contextual platforms for TGFbeta and BMP signaling. *Curr Opin Cell Biol* **21**, 616-622 (2009).
299. Tong, J. et al. Lamin A/C deficiency is associated with fat infiltration of muscle and bone. *Mech Ageing Dev* **132**, 552-559 (2011).
300. Bergo, M.O. et al. Zmpste24 deficiency in mice causes spontaneous bone fractures, muscle weakness, and a prelamin A processing defect. *Proc Natl Acad Sci U S A* **99**, 13049-13054 (2002).
301. Muir, P., Johnson, K.A. & Ruaux-Mason, C.P. In vivo matrix microdamage in a naturally occurring canine fatigue fracture. *Bone* **25**, 571-576 (1999).
302. Mori, S. & Burr, D.B. Increased intracortical remodeling following fatigue damage. *Bone* **14**, 103-109 (1993).
303. Prendergast, P.J. & Taylor, D. Prediction of bone adaptation using damage accumulation. *J Biomech* **27**, 1067-1076 (1994).
304. Carter, Y., Thomas, C.D.L., Clement, J.G. & Cooper, D.M.L. Femoral osteocyte lacunar density, volume and morphology in women across the lifespan. *J Struct Biol* **183**, 519-526 (2013).
305. emmatian H, L.M., Claessens F, Vanderschueren D, van Lenthe GH Age-related changes in the 3D microstructural mouse cortical bone using high resolution desktop micro-CT system. **38th**, 9-16 (2016).
306. Bacabac, R.G., Van Loon, J.J., Smit, T.H. & Klein-Nulend, J. Noise enhances the rapid nitric oxide production by bone cells in response to fluid shear stress. *Technol Health Care* **17**, 57-65 (2009).
307. Klein-Nulend, J., Bacabac, R.G. & Bakker, A.D. Mechanical loading and how it affects bone cells: the role of the osteocyte cytoskeleton in maintaining our skeleton. *Eur Cell Mater* **24**, 278-291 (2012).
308. Davies, P.F. Flow-mediated endothelial mechanotransduction. *Physiol Rev* **75**, 519-560 (1995).
309. Ingber, D.E. Tensegrity: the architectural basis of cellular mechanotransduction. *Annu Rev Physiol* **59**, 575-599 (1997).
310. Janmey, P.A. The cytoskeleton and cell signaling: component localization and mechanical coupling. *Physiol Rev* **78**, 763-781 (1998).

311. Anno, T., Sakamoto, N. & Sato, M. Role of nesprin-1 in nuclear deformation in endothelial cells under static and uniaxial stretching conditions. *Biochem Biophys Res Commun* **424**, 94-99 (2012).
312. Milovanovic, P. et al. Osteocytic canalicular networks: morphological implications for altered mechanosensitivity. *ACS Nano* **7**, 7542-7551 (2013).
313. Zhou, X., Novotny, J.E. & Wang, L. Anatomic variations of the lacunar-canalicular system influence solute transport in bone. *Bone* **45**, 704-710 (2009).
314. Wang, L. et al. In situ measurement of solute transport in the bone lacunar-canalicular system. *Proc Natl Acad Sci U S A* **102**, 11911-11916 (2005).
315. Prasadam, I. et al. Osteocyte-induced angiogenesis via VEGF-MAPK-dependent pathways in endothelial cells. *Mol Cell Biochem* **386**, 15-25 (2014).
316. Zebaze, R.M. et al. Intracortical remodelling and porosity in the distal radius and post-mortem femurs of women: a cross-sectional study. *Lancet* **375**, 1729-1736 (2010).
317. Dong, X.N. & Guo, X.E. The dependence of transversely isotropic elasticity of human femoral cortical bone on porosity. *J Biomech* **37**, 1281-1287 (2004).
318. Augat, P. & Schorlemmer, S. The role of cortical bone and its microstructure in bone strength. *Age Ageing* **35 Suppl 2**, ii27-ii31 (2006).
319. Schaffler, M.B. & Burr, D.B. Stiffness of compact bone: effects of porosity and density. *J Biomech* **21**, 13-16 (1988).
320. Liu, Y. et al. Gorab Is Required for Dermal Condensate Cells to Respond to Hedgehog Signals during Hair Follicle Morphogenesis. *J Invest Dermatol* **136**, 378-386 (2016).
321. Kringelbach, T.M. et al. Fine-tuned ATP signals are acute mediators in osteocyte mechanotransduction. *Cell Signal* **27**, 2401-2409 (2015).
322. Cenacchi, G., Fanin, M., De Giorgi, L.B. & Angelini, C. Ultrastructural changes in dysferlinopathy support defective membrane repair mechanism. *J Clin Pathol* **58**, 190-195 (2005).
323. Tsukamoto, S. et al. Smad9 is a new type of transcriptional regulator in bone morphogenetic protein signaling. *Sci Rep* **4**, 7596 (2014).
324. Yu, B. et al. Wnt4 signaling prevents skeletal aging and inflammation by inhibiting nuclear factor-kappaB. *Nat Med* **20**, 1009-1017 (2014).
325. Chen, J. et al. WNT7B promotes bone formation in part through mTORC1. *PLoS Genet* **10**, e1004145 (2014).
326. Johnson, M.L. LRP5 and bone mass regulation: Where are we now? *Bonekey Rep* **1**, 1 (2012).
327. Smith-Clerc, J. & Hinz, B. Immunofluorescence detection of the cytoskeleton and extracellular matrix in tissue and cultured cells. *Methods Mol Biol* **611**, 43-57 (2010).
328. Knothe Tate, M.L., Knothe, U. & Niederer, P. Experimental elucidation of mechanical load-induced fluid flow and its potential role in bone metabolism and functional adaptation. *Am J Med Sci* **316**, 189-195 (1998).

7 Appendix

7.1 Comparison of human and rodent (mouse) anatomy and histology of the tibia[17]

Most of this study's experiments were conducted *in vivo*. Therefore, all documented effects were investigated in mice tibiae. Mice represent a balanced compromise for researchers, analyzing bone. Similarities and differences between the human and mouse long bone will be explained. This chapter should illustrate, why the findings in rodents can be extrapolated to human.

7.1.1 Anatomy of human and mouse tibia

In human and mice the gross anatomy of long bones is identical, representing epiphyseal endings, a metaphyseal region, mostly housing the cartilage rich growth plate and the diaphyseal midshaft. In both systems, the cortex is most thick in the midshaft, whereas it is thinning to the diaphyseal ends. Trabecular bone is implemented in the diaphyseal and metaphyseal regions for support of the compressive forces.

As a crucial anatomical difference it has to be mentioned, that the fibula and tibia fuse right below midshaft in rodents. Humans show no fusion of these bones and the fibula extends till the ankle. Otherwise both models share most key features on the anatomic level.

7.1.2 Histology of human and mouse tibia

7.1.2.1 Epiphysis

In both human and rodent tibiae the epiphysis shows below the knee joint a subchondral plate. In mice this plate can vary in thickness and can be extremely thin in some areas, but in human it is usually thin and of same thickness.

7.1.2.2 Growth plate

The growth plate of humans and rodents can be divided in four layers, from the epiphyseal top to the diaphyseal bottom. From top to bottom an undifferentiated, resting zone, a proliferation zone, a hypertrophy zone and a zone for ossification and calcification, which leads to the subchondral bone.

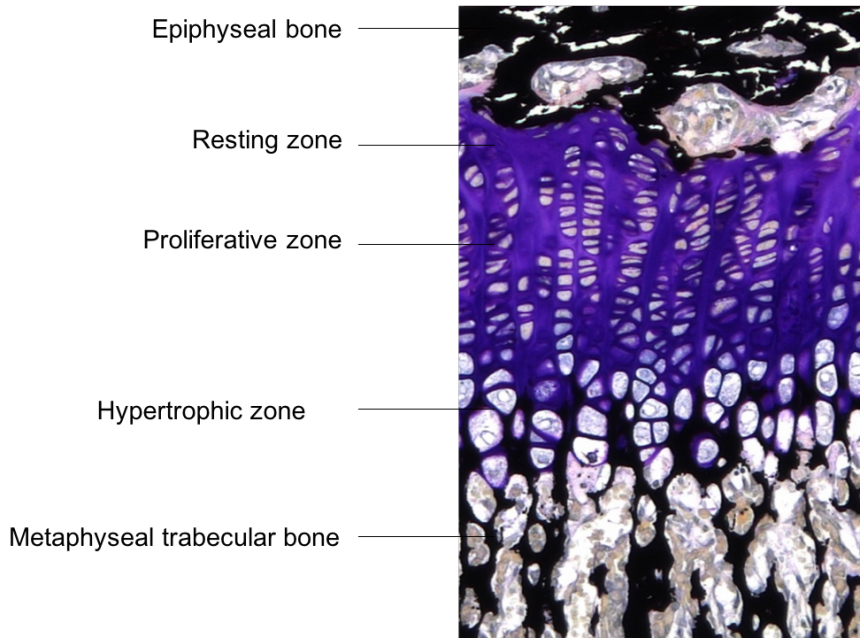

Figure 58 Growth plate of a LC mouse stained with toluidine blue and calcium stain, showing in black calcified bone and in purple cartilage. Exemplary for the different zones in the epiphyseal growth plate and the primary spongiosa at the metaphyseal end of the growth plate.

Below the resting zone chondrocytes massively proliferate and form cylindrical cell columns in which the cells enlarge and then undergo hypertrophy. Deep in the hypertrophic zone, the cartilage gets mineralized and arising from the metaphysis the chondrocyte cylinders get vascularized. During calcification the chondrocytes undergo apoptosis or differentiate to osteoblasts. The calcified cartilage is resorbed by osteoclasts and replaced by osteoid, which again becomes mineralized. The newly formed matrix becomes the trabecular bone of the primary spongiosa. It is not unusual for these structures still encasing a cartilage core. Undergoing constant remodeling the remaining cartilage is replaced, representing a thinner trabecular network as the secondary spongiosa.

Differences in the human and mouse growth plate are the varying periods of existing. In rodents the growth plate's thickness is proportional to their life span, but never disappears (560 µm max in thickness, decreases to less than 100 µm). In humans the growth plate has a constant thickness of 1-3 mm and vanishes at the age of 18, the age of skeletal maturation. The growth plate is undergoing endochondral ossification. The resulting bone, termed epiphyseal scar connects now the epiphysis and metaphysis.

7.1.2.3 Metaphysis

Both, human and mice show two sections of spongiosa in the metaphysis, primary and secondary spongiosa.
In mice the primary spongiosa is located within the first 250 nm below the growth plate cartilage and is represented by immature bone. Here we find most of the surface covered by osteoblasts and osteoclasts. With further distance to the growth plate the secondary spongiosa shows narrowing trabecular bone (less cartilage), a reduction in osteoblasts and osteoclasts but an increase in marrow space. The marrow space hosts primary hematopoietic marrow, which lasts a lifetime.

Human spongiosa has a similar structure. Like in mice the primary spongiosa is rising from the growth plate, pervaded by massive vascularization. Primary spongiosa is covered also with osteoblasts and osteoclasts. With further distance from the growth plate the amount of bone surrounding the cartilage is increasing around the cartilage cores in the secondary spongiosa. Despite the reduction of active bone cells on the trabecular bone surface, the remodeling process is still ongoing. During development hematopoietic marrow is present in the marrow space of the spongiosa. Afterwards it is replaced by fatty marrow.

Trabecular bone architecture in human can be described as osseous plates, which cross each other in a more or less 90° angle. Fine pores are present in the trabeculae guaranteeing communication between the marrow spaces. In rodents the architecture shows high similarity. In adult humans the trabecular bone is composed of lamellar bone, excluding Harvesian canals, in mice the cartilage core is decreasing throughout life.

Both show a thin metaphyseal cortex in comparison to their diaphysis.

7.1.2.4 Diaphysis

As a similarity in human and rodent long bones the shaft consists by a major part of cortical bone. At a very young age rodents show woven bone in a high proportion. During rodent growth the bone expands on the periosteal side with bone formation (circumferential lamellar bone) and bone resorption on the endosteal surface. During this process the medullar cavity enhances its diameter and at the same time the woven bone vanishes. After 12-16 weeks mice show mostly lamellar bone in the cortex. Harversian canals cannot be found numerously, therefore the mouse cortical bone does usually not contain osteon structures. Furthermore, the rodent cortical bone is rarely remodeled.
The human cortical bone in contrast shows osteon rich structure, delimited by circumferential lamella on the inner and outer surface. During development the cortex is formed via appositional growth of circumferential lamellae. Throughout bone development and growth these structures are remodeled to osteon structures. Only on the inner and outer surface circumferential lamellae can be found in adulthood. The human cortical bone undergoes remodeling processes throughout life.

Summarizing the comparison of human and rodent long bone as conclusion the anatomical and morphological similarities are, on a proportional level striking.
Mice represent a perfect compromise between the representation of human bone features and a fast developing, little breeding and housing space needing animal model.
Furthermore, no *in vitro*, nor *in silico* system by date are able to recreate such a complex system as the bone, therefore most of the experiments have to be executed *in vivo*.

7.2 Canadian Centre for Computational Genomics RNA-Seq Analysis Report

Home Contact

Canadian Centre for Computational Genomics

RNA-Seq Analysis Report

Introduction

This document contains the description of the current MUGQIC RNA-Seq analysis. The information presented here reflects the current state of the analysis as of 2015-12-04.

Analysis and Results

Read Trimming and Clipping of Adapters

Reads are trimmed from the 3' end to have a phred score of at least **30**. Illumina sequencing adapters are removed from the reads, and all reads are required to have a length of at least **32** bp. Trimming and clipping are performed using Trimmomatic (Bolger, Lohse, and Usadel 2014).

Trimming Statistics per Readset (download full table)

Sample	Readset	Raw Paired Reads #	Surviving Paired Reads #	Surviving Paired Reads %
BCU1053_TC_RNASeq_1	BCU1053_TC_RNASeq_1.MPS045232_PELib.0795.7	28,525,598	26,601,629	93.3
BCU1053_Mono_RNASeq_1	BCU1053_Mono_RNASeq_1.MPS045231_PELib.0795.6	26,887,722	24,888,096	92.6

- Raw Paired Reads #: number of Paired Reads obtained from the sequencer
- Surviving Paired Reads #: number of Remaining Paired Reads after the trimming step
- Surviving Paired Reads %: percentage of Surviving Paired Reads / Raw Paired Reads

Read Alignment to a Reference Genome

The filtered reads are aligned to a reference genome. The genome used in this analysis is ***Homo_sapiens*** assembly **GRCh37**. Each readset is aligned using STAR (Dobin et al. 2012) which creates a Binary Alignment Map file (.bam). Then, all readset BAM files from

the same sample are merged into a single global BAM file using Picard.

Trimming and Alignment Metrics per Sample

General summary statistics are provided per sample. Sample readsets are merged for clarity.

Trimming and Alignment Statistics per Sample (**partial table**; download full table)

Sample	Raw Reads #	Surviving Reads #	%	Aligned Reads	%	Alternative Alignments	%	rRNA Reads	%	Coverage	Exonic Rate	Genes
BCU1053_TC_RNASeq_1	57,051,196	53,203,258	93.3	52,140,159	98.0	7,125,766	13.7	0	0.0	27.48	0.58	22,176
BCU1053_Mono_RNASeq_1	53,775,444	49,776,192	92.6	48,701,076	97.8	6,523,514	13.4	0	0.0	27.98	0.63	20,389

- Raw Reads: total number of reads obtained from the sequencer
- Surviving Reads: number of remaining reads after the trimming step
- %: Surviving Reads / Raw Reads
- Aligned Reads: number of aligned reads to the reference
- %: Aligned reads / Surviving reads
- Alternative Alignments: number of duplicate read entries providing alternative coordinates
- %: Alternative Alignments / Aligned Reads
- rRNA Reads: number of reads aligning to rRNA regions as defined in the transcript model definition
- %: rRNA Reads / Surviving Reads
- Coverage: mean coverage = number of bp aligning to reference / total number of bp in the reference
- Exonic Rate: fraction mapping reads within exons
- Genes: number of Genes with at least 5 reads

Additional metrics can be found in the original RNAseqQC report available here

Wiggle Graphs/Tracks Generation

Wiggle tracks format files are generated from the aligned reads using BedGraphToBigWig. This file is a representation of read alignments that can be easily downloaded in browsers like IGV or UCSC (for UCSC, some naming conventions and/or coordinate limits may cause some problems; in this case, please contact us for file re-formatting).

The wiggle tracks are available here

FPKM Analysis

FPKM Values Generation

The Cufflinks program (Roberts et al. 2011) is used to assemble aligned RNA-Seq reads into transcripts and to estimate their abundance (FPKM). In RNA-Seq experiments, cDNA fragments are sequenced and mapped back to genes and ideally, individual transcripts. Properly normalized, the RNA-Seq fragment counts can be used as a measure of the relative abundance of transcripts, and Cufflinks measures transcript abundances in **Fragments Per Kilobase of exon per Million fragments mapped (FPKM)**, which is analogous to single-read "RPKM". In paired-end RNA-Seq experiments, fragments are sequenced from both ends, providing two reads for each fragment. To estimate isoform-level abundances, one must assign fragments to individual transcripts, which may be difficult because a read may align to multiple isoforms of the same gene. Cufflinks uses a statistical model of paired-end sequencing experiments to derive a likelihood for the abundances of a set of transcripts given a set of fragments. Once transcripts are assembled and their corresponding FPKM estimated, these transcripts are annotated with the known reference set of transcripts obtained from the Ensembl database.

Metrics and Exploratory Analysis

We use several metrics and exploratory analyses to control data quality and biological reliability.

FPKM Metrics

The pairwise sample correlation analysis controls the general transcripts expression consistency between samples. It can also check sample mix-up or error in name assignment. Thus, samples belonging to the same design group/condition are expected to show higher level of correlation.

Pairwise Pearson's correlation value per sample (**partial table**; download full table)

Vs	BCU1053_TC_RNASeq_1	BCU1053_Mono_RNASeq_1
BCU1053_TC_RNASeq_1	1.00	0.90
BCU1053_Mono_RNASeq_1	0.90	1.00

Saturation plots show if there is enough sequencing depth to saturate gene expression at various ranges of expression. In RNA-Seq experiments, saturation would be reached when an increment in the number of reads does not result in additional true expressed transcripts being detected. The precision of any sample statistics (FPKM or RPKM) is affected by sample size (sequencing depth). The saturation analysis will resample a series of subsets from total RNA reads and then calculate RPKM values using each subset. By doing this, we are able to check if the current sequencing depth was saturated or not (or if the RPKM values were stable or not). For each sample we estimate the Percent Relative Error (PRE). The PRE measures how the RPKM estimated from a subset of reads deviates from real expression levels) and the median RPKM of the set of transcripts. Saturation plots are generated independently for four different set of transcripts: high, intermediate, moderate and low expressed transcripts (corresponding to quartiles Q1 to Q4 of median RPKM).

Saturation graphs are available here

Exploratory Analysis

Different exploratory data analysis (EDA) techniques are applied to gene and transcript expression levels, quantified respectively by the HT-seq calculated log2(CPM) (counts-per-million reads) and cufflinks estimated log2(FPKM) (fragments per kilobase of exon per million fragments mapped). Main goals of expression level EDA are the detection of outliers, potential mislabeling, to explore the homogeneity of biological replicates and to appreciate the global effects of the different experimental variables. EDA plots are therefore essential to insure clean data is sent to differential analysis.

First, we analyze how samples are connected to each other using hierarchical clustering on the log2(CPM) gene expression levels. The Ward method is applied to the matrix of Pearson's correlation distance.

Secondly, we perform principal component analysis (PCA) on gene expression levels (log2CPM). A PCA plot shows the projection of the samples onto a two-dimensional space spanned by the first and second principal components. These are the orthogonal directions in which the data exhibits the largest and second-largest variability. These two components are usually sufficient to differentiate groups of samples describing the principal effects of the experimental design.

Next, genes and transcripts with the most variable expression levels (log2CPM or log2FPKM standard deviation across all samples, usually the top 75) are used to cluster samples. The utility of such a plot is to get a rough overview of which genes or transcripts are contributing the most to the samples clustering pattern.

Description	File
PCA (first two components) of the gene log2CPM values	pdf
Heat map of most varying genes by log2(CPM) standard deviation	pdf
Heat map of most varying transcripts by log2(FPKM) standard deviation	pdf
All Figures	zip

Transcriptome Assembly with Cufflinks

In order to provide the most complete analysis results the entire set of Cufflinks files are provided in the following archive:

Complete Cuff suite analysis files are available here

A reference-based transcript assembly was performed, which allows the detection of known and novel transcripts isoforms. Transcript assembly is accomplished using Cufflinks (Roberts et al. 2011).

Cufflinks constructs a parsimonious set of transcripts that "explains" the reads observed in an RNA-Seq experiment. The assembly algorithm explicitly handles paired-end reads by treating the alignment for a given pair as a single object in the covering relation. Cufflinks tries to find the most parsimonious set of transcripts by performing a minimum-cost maximum matching. Reference annotation based assembly seeks to build upon available information about the transcriptome of an organism to find novel genes and isoforms. When a reference GTF is provided, the reference transcripts are tiled with faux-reads that will aid in the assembly of novel isoforms. These faux-reads are combined with the sequencing reads and are input into the regular Cufflinks assembler. The assembled transfrags are then compared to the reference transcripts to determine if they are different enough to be considered novel. Individual results of these assemblies are available in the `cufflinks/` folder in the archive.

Cuffmerge was then used to merge all assemblies gtf to a single one (`cufflinks/AllSamples/merged.gtf`).

The resulting merged assembly gtf file was used as a reference to estimate the abundance of each transcript and to subsequently perform a differential analysis for each design as provided in the design file using Cuffdiff. The entire set of result files for the Cuffdiff analysis is provided in the `cuffdiff/` folder of the archive.

As Cuffdiff generates normalized data using only the sample implicated in the design comparison, we additionally run the Cuffnorm tool to generate a normalized data set that includes all the samples. The resulting tables of normalized expression values are provided in the `cuffnorm/` folder of the archive.

Differential Expression Analysis - Methods

Differential Analysis Design

The experimental design resulted from a discussion with the client. The designs used in differential analysis are presented in the following table, which contains the sample names as well as the sample group membership per design. For each experimental design (column name), three conditions/groups are possible: 0, 1 and 2. If a sample is assigned 0, it is not included in a particular analysis. If a sample is assigned 1, the sample is considered as a member of the control group. If a sample is assigned 2, the sample is considered as a member of the test/case group.

Sample Names and Experimental Designs (**partial table**; download full table)

Sample	BCU1053_TC_vs_Mono
BCU1053_TC_RNASeq_1	1
BCU1053_Mono_RNASeq_1	2

Differential Gene Analysis Description

A primary task in the analysis of RNA-Seq data is the detection of differentially expressed genes. For this purpose, count data from RNA-Seq should be obtained for each non-overlapping gene. Read counts are found to be (to good approximation) linearly related to the abundance of the target transcript (Mortazavi et al. 2008). If reads were independently sampled from a population with given, fixed fractions of genes, the read counts would follow a multinomial distribution, which can be approximated by the Poisson distribution. Thus, we can use statistical testing to decide whether, for a given gene, an observed difference in read counts is significant, that is, whether it is greater than what would be expected just due to natural random variation. The differential gene expression analysis is done using DESeq (Anders and Huber 2010) and edgeR (Robinson, McCarthy, and Smyth 2010) R Bioconductor packages

Read counts are obtained using HTSeq and are represented as a table which reports, for each sample (columns), the number of reads

mapped to a given gene (rows).

Matrix of Raw Read Counts per Gene per Sample (**partial table**; download full table)

Gene	Symbol	BCU1053_TC_RNASeq_1	BCU1053_Mono_RNASeq_1
ENSG00000000003	TSPAN6	36	0
ENSG00000000005	TNMD	0	0
ENSG00000000419	DPM1	547	411
ENSG00000000457	SCYL3	573	258
ENSG00000000460	C1orf112	166	116
ENSG00000000938	FGR	275	10478

Differential Transcripts Analysis Description

FPKM values calculated by Cufflinks are used as input. The transcript quantification engine of Cufflinks, Cuffdiff (Roberts et al. 2011), is used to calculate transcript expression levels in more than one condition and test them for significant differences. To identify a transcript as being differentially expressed, Cuffdiff tests the observed log-fold-change in its expression against the null hypothesis of no change (i.e. the true log-fold-change is zero). Because measurement errors, technical variability, and cross-replicate biological variability might result in an observed log-fold-change that is nonzero, Cuffdiff assesses significance using a model of variability in the log-fold-change under the null hypothesis. This model is described in details in (Trapnell et al. 2012).

Gene Ontology (GO) Analysis of the Differential Expression Results

One simple, but extremely widely used, systems biology technique for highlighting biological processes is to look at gene category the show over-representation in the differential analysis results. In order to perform this analysis, genes are grouped into categories defined by the common biological properties and then tested to find categories that are over-represented amongst the differentially expressed genes. Gene Ontology (GO) terms are the most commonly used categories. RNA-Seq data suffers from a bias in detecting differential expression for long genes. This means that when using a standard analysis, any category containing a preponderance of long genes will be more likely to show up as being over-represented than a category containing genes of average lengths. Thus the GO analysis is performed using of the goseq (Young et al. 2010) R Bioconductor package which provides methods for performing Gene Ontology analysis of RNA-Seq data, taking this length bias into account.

Differential Expression Analysis - Results

The following sections provide the results of the differential gene expresssion and differential transcript expression per design.

The results of the differential gene expression analysis are generated using DESeq and edgeR. Raw read counts generated by HTSeq are used as input. The first column is the gene id; the second column is the gene symbol; the third column is the log2 fold change of the level of expression of each gene; the fourth column is the nominal p-value of the test; and the fifth column is the FDR adjusted p-value of the test.

The results of the differential transcript expression analysis are generated using Cuffdiff. FPKM values calculated by Cufflinks are used as input. The first column is the transcript id, the second column is the gene symbol, the third column is the log2 fold change of the level of expression of each transcript, the fourth column is the nominal p-value of the test and the fifth column is the FDR adjusted p-value of the test.

The results of the differential gene and transcript expression analyses are processed in a gene ontology analysis using goseq. There are two gene ontology analyses per design. The first one is based on the differentially expressed genes from the DESeq/edgeR results. Every gene having an FDR adjusted p-value under 0.05 is considered as differentially expressed. The second analysis is based on the differentially expressed transcripts from the cuffdiff results. The threshold for differentially expressed selection is the same as in the first analysis. The first column is the ID of the category enriched; the second column is the FDR adjusted p-value of category enrichment; the third column is the GO id; and the fourth column is a brief description of the GO term. **If there are no results for a particular design, it means the FDR adjusted GO enrichment was not significant (p-value too high)**.

BCU1053_TC_vs_Mono Results

Differential Gene Expression Results (**partial table**; download full table)

id	gene_symbol	log_FC	log_CPM	deseq.p-value	deseq.adj.pvalue	edger.p.value	edger.adj.p.value
ENSG00000158825	CDA	11.624	3.809	0.049	1	0.0013	0.67
ENSG00000178562	CD28	-8.405	7.473	0.055	1	0.0015	0.67
ENSG00000104725	NEFL	-11.57	3.784	0.059	1	0.0014	0.67
ENSG00000176928	GCNT4	-9.035	4.557	0.061	1	0.0016	0.67
ENSG00000182010	RTKN2	-8.632	5.075	0.062	1	0.0016	0.67
ENSG00000154027	AK5	-11.43	3.647	0.063	1	0.0016	0.67

Differential Transcript Expression Results (**partial table**; download full table)

test_id	gene_id	tss_id	nearest_ref_id	class_code	gene	locus	length
TCONS_00000001	XLOC_000001	TSS1	ENST00000456328	=	DDX11L1	1:11868-31109	1657
TCONS_00000002	XLOC_000001	TSS1	ENST00000450305	j	DDX11L1	1:11868-31109	1534
TCONS_00000003	XLOC_000001	TSS1	ENST00000450305	j	DDX11L1	1:11868-31109	1510
TCONS_00000004	XLOC_000001	TSS1	ENST00000450305	j	DDX11L1	1:11868-31109	1370
TCONS_00000005	XLOC_000001	TSS1	ENST00000450305	j	DDX11L1	1:11868-31109	1530
TCONS_00000006	XLOC_000001	TSS1	ENST00000515242	=	DDX11L1	1:11868-31109	1653

No FDR adjusted GO enrichment was significant (p-value too high) based on the differentially expressed gene results for this design.

Analysis Configuration Parameters

All analysis parameters are described in this configuration file.

References

Anders, S., and W. Huber. 2010. "Differential Expression Analysis for Sequence Count Data." *Genome Biology* 11 (10): R106. doi:10.1186/gb-2010-11-10-r106.

Bolger, A.M., M. Lohse, and B. Usadel. 2014. "Trimmomatic: A Flexible Trimmer for Illumina Sequence Data." *Bioinformatics* 30 (15): 2114–20. doi:10.1093/bioinformatics/btu170.

Dobin, A., C.A. Davis, F. Schlesinger, J. Drenkow, C. Zaleski, S. Jha, P. Batut, M. Chaisson, and T.R. Gingeras. 2012. "STAR: Ultrafast Universal RNA-Seq Aligner." *Bioinformatics* 29 (1): 15–21. doi:10.1093/bioinformatics/bts635.

Mortazavi, A., B.A. Williams, K. McCue, L. Schaeffer, and B. Wold. 2008. "Mapping and Quantifying Mammalian Transcriptomes by RNA-Seq." *Nature Methods* 5 (7): 621–28. doi:10.1038/nmeth.1226.

Roberts, A., H. Pimentel, C. Trapnell, and L. Pachter. 2011. "Identification of Novel Transcripts in Annotated Genomes Using RNA-Seq." *Bioinformatics* 27 (17): 2325–29. doi:10.1093/bioinformatics/btr355.

Robinson, M.D., D.J. McCarthy, and G.K. Smyth. 2010. "EdgeR: A Bioconductor Package for Differential Expression Analysis of Digital Gene Expression Data." *Bioinformatics* 26 (1): 139–40. doi:10.1093/bioinformatics/btp616.

Trapnell, C., D.G. Hendrickson, M. Sauvageau, L. Goff, J.L. Rinn, and L. Pachter. 2012. "Differential Analysis of Gene Regulation at Transcript Resolution with RNA-Seq." *Nature Biotechnology* 31 (1): 46–53. doi:10.1038/nbt.2450.

Young, M.D., M.J. Wakefield, G.K. Smyth, and A. Oshlack. 2010. "Gene Ontology Analysis for RNA-Seq: Accounting for Selection Bias." *Genome Biology* 11 (2): R14. doi:10.1186/gb-2010-11-2-r14.

C3G is supported by the following organizations:

McGill · GenomeCanada · GenomeQuébec · compute • calcul CANADA · canarie

7.3 List of Abbreviations

Abbreviation	
Akt	AKT Serine/Threonine Kinase
ALP	Alkaline phosphatase
AP-1	Activator protein 1
ARCL	autosomal recessive cutis laxa
ARF5	ADP Ribosylation Factor 5
ASARM	acidic serine aspartate-rich MEPE-associated motif
ATP	Adenosintriphosphate
BGLAP	Bone Gamma-Carboxyglutamate Protein
BMP	bone morphogenic protein
BMU	bone multicellular unit
BSP	Bone sialoprotein
c-myc	MYC Proto-Oncogene
Ca	Calium
CD	cluster of differentiation
cFMS	Colony-stimulating factor-1 receptor
Col1	Colagen type 1
Col1A1	Colagen type 1 alpha 1
COX	Cyclooxygenase
Ct.Po	Cortical porosity
DC-STAMP	Dendritic Cells (DC)-Specific Transmembrane Protein
DMP1	Dentin matrix protein 1
e.g.	for example
E11	podopanin
ECM	extracellular matrix
ERK	Mitogen-Activated Protein Kinase 1
FAK	Focal adhesion kinase
FGF	fibroblast growth factor
Fgf23	Fibroblast growth factor 23

Abbreviation	
wk	week
wnt	wingless-INT
Wwtr1	WW Domain Containing Transcription Regulator 1
YAP	Yes-associated protein
Yap1	Yes-associated protein 1
µm	micro meter
Cre	causes recombination
LC	Littermate control
LoxP	locus of X-over P1
FEM	Forschungseinrichtung für Experimentelle Medizin
LAGeSo	Landesamt für Gesundheit und Soziales
N	Newton
Hz	Herz
M	Monday
F	Friday
mg	milligram
kg	kilogram
µCT	micro computed tomography
VOI	volume of interest
ROI	Reion of interest
ms	millisecond
µA	micro ampere
kVp	peak kilovoltage
HA/cc	Hydroxyapatite density
Tb	trabecular
Ct	cortical
BV	bone volume
TV	total volume

FZD	frizzled
g	gram
GO	Gerodermia osteodysplastica
Grb2	Growth factor receptor-bound protein 2
GSK3	Glykogensynthase-Kinase 3
h	hour
HSC	hematopoietic stem cells
IGF1	insulin-like growth factor 1
IIAP	integrin intracellular anchoring protein
IP3R	inositol-1,4,5-triphosphate
IκK	inhibitor of nuclear factor kappa-B kinase
Kif5	Kinesin-related family member 5
km	kilometer
Krm2	Kringle Containing Transmembrane Protein 2
LGR4	Leucine Rich Repeat Containing G Protein-Coupled Receptor 4
Lrp5	lipoprotein receptor-related protein 5
M-CFS	macrophage colony-stimulating factor
MAP2K6	Mitogen-Activated Protein Kinase Kinase 6
MAPK	mitogen-activated protein kinase
MEPE	Matrix extracellular phosphoglycoprotein
MITF	Melanogenesis Associated Transcription Factor
ml	milliliter
MLO-Y4	Murine Long bone Osteocyte-Y4
MMP9	matrix metallopeptidase 9
MSC	mesenchymal stem cell
mTor	Mechanistic Target Of Rapamycin Kinase
MV	Matrix vesicles
NF-κB	Nuclear Factor Kappa B Subunit 1
NFATc1	Nuclear Factor Of Activated T Cells 1
Th	Thickness
N	Number
Sp	Spacing
v	voluminetric
TMD	tissue mineral density
min	minimum
max	maximum
I	principle moment of inertia
Ar	area
Tt	total
RT	room temperature
C	celsius
Al	aluminium
O	oxygen
PMMA	Polymethyl methacrylate
Ec	endocortical
Ps	Periosteal
sLS	Single labeled surface
BS	bone surface
dLS	Double labeled surface
MS	mineralizing surface
MAR	Mineral apposition rate
BFR	bone formation rate
PFA	Paraformaldehyd
EDTA	Ethylenediaminetetraacetic acid
DAB	3,3'-Diaminobenzidine
BSA	Bovine serum albumin
PBS	Phosphate-buffered saline
a.dest.	aqua destillata

NFATc1	Nuclear Factor Of Activated T Cells 1
ng	nanogram
nm	nano meter
OCN	Osteocalcin
OPG	osteoprotegerin
Osf2	osteoblast-specific factor
OSX	Osterix
P2RX7	Purinergic Receptor P2X 7
PGE_2	Prostaglandin E2
pH	potentia hydrogenii
Phex	Phosphate Regulating Endopeptidase Homolog X-Linked
PI3K	Phosphatidylinositol-4,5-Bisphosphate 3-Kinase Catalytic Subunit Alpha
PKC	phosphokinase C
PLC	phospholipase C
Po	Porosity
Prx1	Paired Related Homeobox 1
PTH	Parathyroid Hormone
PTH1R	parathyroid hormone 1 receptor
Rab6	Ras-related protein Rab-6A
Raf	rapidly accelerated fibrosarcoma
RANK	Receptor Activator of NF-κB
RANKL	Receptor Activator of NF-κB Ligand
Ras	RAS P21 Protein Activator 1
Rho	Rhodopsin
RNA	ribonucleic acid
RNAseq	RNA sequencing
ROCK	Rho Associated Coiled-Coil Containing Protein Kinase 1
ROR2	Receptor Tyrosine Kinase Like Orphan Receptor 2
Runx2	Runt-related transcription factor 2
RYK	FZD-receptor-like tyrosine kinas

ON	over night
pH	power of hydrogen
DANN	deoxyribonucleic acid
cDNA	complementary deoxyribonucleic acid
mRNA	messenger ribonucleic acid
siRNA	short interference ribonucleic acid
PCR	Polymerase chain reaction
IDG-SW3	immortomouse/Dmp1-GFP-SW3
FBS	Fetal Bovine Serum
α-MEM	Minimum Essential Medium Eagle - Alpha Modification
INF-ɣ	Interferon-gamma
DPBS	Dulbecco's Phosphate-Buffered Saline
ATP	Adenosine Triphosphate
J	polar moment of inertia
SD	standard deviation
B	bone
Pm	perimeter
Ob	osteoblast
Oc	Osteoclast
Ot	Osteocyte
Ad	Adipocyte
Lc	Lacuna
Axin1	Axis Inhibition Protein 1
Ctnnb1	Catenin Beta-1
Dkk1	Dickkopf WNT Signaling Pathway Inhibitor 1
Cacna1g	Calcium Voltage-Gated Channel Subunit Alpha1 G
Tuba1a	Tubulina1a
Tubg1	Tubuling1
Itgb1	Integrin Subunit Beta 1
Itgb3	Integrin Subunit Beta 3

RyR	ryanodine receptors
s	second
SIBLING	small integrin-binding ligand and N-linked glycoprotein
SLRP	Small leucin rich proteoglycans
Sos	SOS Ras/Rac Guanine Nucleotide Exchange Factor 1
SOST	Sclerostin
Sp7	Osterix
Src	SRC Proto-Oncogene, Non-Receptor Tyrosine Kinase
TAZ	transcriptional coactivator with PDZ-binding motif
TGF-ß	transforming growth factor beta
TRAF	TNF receptor-associated factor
TRAP	Tartrate-resistant acid phosphatase
vATPase	vacuolar-type H^+-ATPase
VEGF	vascular endothelial growth factor
VSCC	voltage sensitive calcium channels

Cav1	Calveolin1
Itpr3	Inositol 1,4,5-Trisphosphate Receptor Type 3
Gja1	GAP Junction Protein Alpha 1
Pls1	Plastin 1
Dysf	Dysferlin
Myof	Myoferlin
Prkd1	Protein Kinase C
D	dimension
FWHM	Ful width half maximum
AUC	area under curve
qBEI	quantitative backscattered electron microscopy
FPKM	Fragments per kilobase million
mTORC1	mammalian target of rapamycin complex 1
iCre	inducible cre

Vorveröffentlichungen

Journal of Biomechanics
Accepted 15 October 2017

Examining tissue composition, whole-bone morphology and mechanical behavior of GorabPrx1 mice tibiae: A mouse model of premature aging

Co-Autorenschaften:
Haisheng Yang, Laia Albiol, Wing-Lee Chan, Dag Wulsten, Anne Seliger, Michael Thelen, Tobias Thiele, Lyudmila Spevak, Adele Boskey, Uwe Kornak, Sara Checa, Bettina M. Willie

Includes data of the executed strain gauging experiments.